Volume 14, Number 8, 2023 ISSN 1847-6996

FERIT
FACULTY OF ELECTRICAL ENGINEERING, COMPUTER SCIENCE AND INFORMATION TECHNOLOGY **OSIJEK**

IJECES International Journal of Electrical and Computer Engineering Systems

International Journal of Electrical and Computer Engineering Systems

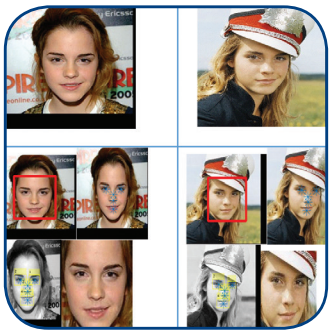

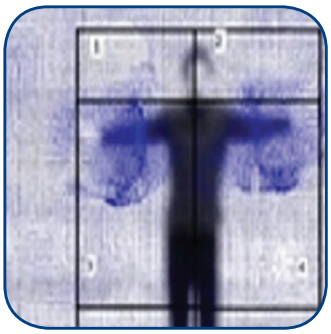

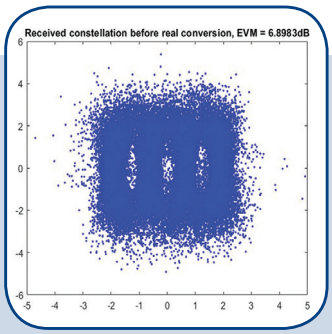

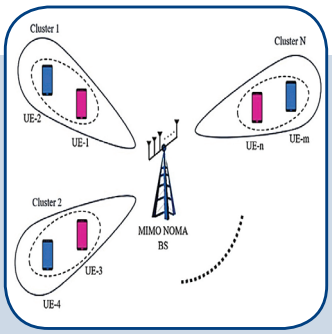

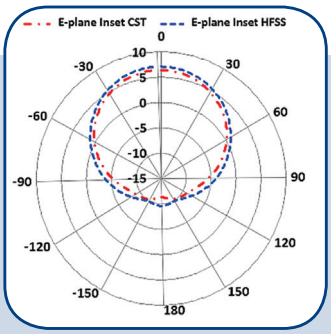

ISSN: 1847-6996

INTERNATIONAL JOURNAL OF ELECTRICAL AND COMPUTER ENGINEERING SYSTEMS

Published by Faculty of Electrical Engineering, Computer Science and Information Technology Osijek, Josip Juraj Strossmayer University of Osijek, Croatia

Osijek, Croatia | Volume 14, Number 8, 2023 | Pages 821 - 958

The International Journal of Electrical and Computer Engineering Systems is published with the financial support of the Ministry of Science and Education of the Republic of Croatia

CONTACT

International Journal of Electrical and Computer Engineering Systems (IJECES)

Faculty of Electrical Engineering, Computer Science and Information Technology Osijek,
Josip Juraj Strossmayer University of Osijek, Croatia
Kneza Trpimira 2b, 31000 Osijek, Croatia
Phone: +38531224600, Fax: +38531224605
e-mail: ijeces@ferit.hr

Subscription Information

The annual subscription rate is 50€ for individuals, 25€ for students and 150€ for libraries.
Giro account: 2390001 - 1100016777,
Croatian Postal Bank

Journal is referred in:

- Scopus
- Web of Science Core Collection (Emerging Sources Citation Index - ESCI)
- Google Scholar
- CiteFactor
- Genamics
- Hrčak
- Ulrichweb
- Reaxys
- Embase
- Engineering Village

Bibliographic Information

Commenced in 2010.
ISSN: 1847-6996
e-ISSN: 1847-7003
Published: quarterly
Circulation: 300

IJECES online

https://ijeces.ferit.hr

TABLE OF CONTENTS

Beamforming Array Antenna Technique Based on Partial Update Adaptive Algorithms

Original Scientific Paper

Zahraa A. Shubber
University of Technology- Iraq
Department of Electrical and Electronics Engineering
Baghdad, Iraq
eee.20.50@grad.uotechnology.edu.iq

Thamer M. Jamel
University of Technology- Iraq
Department of Communications Engineering
Baghdad, Iraq
thamer.m.jamel@uotechnology.edu.iq

Ali. K. Nahar
University of Technology- Iraq
Department of Electrical and Electronics Engineering
Baghdad, Iraq
30081@uotechnology.edu.iq

Abstract *–The most important issues for improving the performance of modern wireless communication systems are interference cancellation, efficient use of energy, improved spectral efficiency and increased system security. Beamforming Array Antenna (BAA) is one of the efficient methods used for this purpose. Full band BAA, on the other hand, will suffer from a large number of controllable elements, a long convergence time and the complexity of the beamforming network. Since no attempt had previously been made to use Partial Update (PU) for BAA, the main novelty and contribution of this paper was to use PU instead of full band adaptive algorithms. PU algorithms will connect to a subset of the array elements rather than all of them. As a result, a common number of working antennas for the system's entire cells can be reduced to achieve overall energy efficiency and high cost-effectiveness. In this paper, we propose a new architectural model that employs PU adaptive algorithms to control and minimize the number of phase shifters, thereby reducing the number of base station antennas. We will concentrate on PU LMS (Least Mean Square) algorithms such as sequential-LMS, M-max LMS, periodic-LMS, and stochastic-LMS. According to simulation results using a Uniform Linear Array (ULA) and three communications channels, the M-max-LMS, periodic LMS, and stochastic LMS algorithms perform similarly to the full band LMS algorithm in terms of square error, tracking weight coefficients, and estimation input signal, with a quick convergence time, low level of error signal at steady state and keeping null steering's interference-suppression capability intact.*

Keywords*: Beamforming Array Antenna, Partial Update Adaptive Algorithm, Full band LMS, M-max PU LMS, sequential PU LMS, periodic PU LMS and stochastic PU LMS algorithms.*

1. INTRODUCTION

In next-generation cellular communication networks, numerous antennas are used to improve spectral and energy efficiency, as well as performance against interference caused by constrained spectrum. This is possible through the use of various antenna designs, one of which is Beamforming Array Antenna (BAA). The development of 5G and upcoming wireless communication systems is anticipated to depend mainly on BAA technology [1].

Signals are correctly controlled in adaptive array beamforming at wireless communication link base stations (BSs) and mobile stations with the aim of enhancing the wireless mobile link and boosting system performance. The antenna boosts the capacity of wireless communication networks by effectively decreasing multipath fading and channel interference. This is accomplished by employing beamforming techniques to focus signal radiation in the desired direction and adapt it to the signal environment. [1, 2]. The most well-known and powerful beamforming scheme is the

well-known Phased Array Antenna (PAA), which is an array of antenna elements driven by signals with well-defined phase relationships between those elements [1]. ULA with N-antenna elements required N phase shifters or other active control units. There are only a few papers in the literature that propose algorithms or techniques for reducing the number of ULA elements and thus the number of phase shifters [2-10].

To achieve high cost-effectiveness and total energy efficiency, the system can reduce the number of operational antennas for all of the cells. [2-10] The overall energy efficiency of the cell is mostly influenced by how many functioning antenna elements there are in the cell for each BS's stipulated power consumption. As novel ideas, the authors of [2] proposed the cascaded angle offset phased array antenna (CAO-PAA) and the dimensionality reduced CAO-PAA (DRCAO-PAA). They represent phase shift steering in all directions using a coefficient matrix. The dimensionality of the coefficient matrix is then lowered by reducing the number of phase shifters [2].

Other strategies for reducing the active number of antennas have been proposed [3-9], including reduced active controller-based vector synthesis. Another method is sub-array compression, which employs a different phase shifter for each sub-array. The author of [10] proposed that an adaptive algorithm (such as LMS, RLS, CG, or CMA) be connected to only a small number of the array elements located in the center of the array rather than all elements, leaving the other elements that have less of an impact on the pattern of the array unaffected by the adaptation process.

The Partial Update (PU) algorithms have gained significant attention in recent years, both in terms of research and practical applications [11-24], but they have yet to be applied to array beamforming systems. According to our knowledge, no previous studies have used adaptive partial update (PU) methods for beamforming array antennas. This study proposes using PU techniques for beamforming array antennas by proposing a new architecture system model, which was thought to be the paper's main innovation, in order to reduce the number of antennas used. Rather than connecting to the entire set of antenna elements, partial update adaptive methods will connect to a subset of them.

Then, we will be applying PU LMS algorithms such as sequential-LMS, M-max-LMS, periodic-LMS, and stochastic-LMS algorithms.

As a result, in terms of convergence time and ability to suppress interference signals via null steering, the performance of these methods will be comparable to that of full band adaptive arrays. The performance of the proposed model will then be compared to three different multipath fading propagation LTE channel models.

The reminder for this paper will be as follows: Section 2 covers beamforming theory and Partial Update LMS adaptive algorithms. Section 3 describes the proposed model's architecture. Section 4 presents simulation results, Section 5 compare results with previous work and Section 6 concludes the study.

2. BACKGROUND

2.2. BEAMFORMING ARRAY SIGNAL MODEL

The use of beamforming antennas by mobile carriers is crucial for the development of next-generation networks. Beamforming antennas dynamically shape their main and null beam directions based on the location of their connected users, in contrast to older antennas that could only transmit and receive on set radiation patterns.

Because of this, these futuristic antennas are often referred to as "beamformers" In addition to greatly enhancing the signal-to-interference-and-noise ratio (SINR) and the end user experience, beamforming antennas stand out for their ability to successfully minimize interference.

By lowering the amount of signal interference from other users, maximizing the signal strength received by each user, and transmitting beamforming aims to boost capacity. By entirely constructing the processed signals in the direction of the desired terminals and canceling the beams of competing signals, the goal of the beamforming process is to construct an antenna's radiated beam patterns.

ULA is the most commonly studied method in array signal processing due to its simplicity. Consider an N-element uniform linear antenna array (ULA), as depicted in figure 1. Let the spacing between each antenna element be d = 0.5 λ, where λ is the wavelength of incoming signals.

This diagram shows how the weight vector $w=[w_1\ w_2\ \ldots.w_N]^H$ can be changed to reduce errors as much as possible when iterating the array weights [25]. The signal s(n) and interferers $i_1(n)$, $i_2(n)$,$\ldots i_N(n)$ are received by a collection of N elements, each having N potential weights. Additionally, there is additive Gaussian noise in every element. Each of the n_{th} time samples are a representation of time.

2.2. FULL BAND LEAST MEAN SQUARES (LMS)

The LMS beamforming method is simple and widely used in wireless communication applications. As a result, this method is frequently used as an adaptive beamforming technique in a variety of applications. The weighted array output in Fig. (1) is written as follows: [25].

$$y(n)= w^H(n)\, x(n) \tag{1}$$

$$\begin{aligned} x(n) &= a_0\, s(n) + [a_1\ a_2 \ldots a_N]\ .\ [i_1(n)\ i_1(n) \vdots \\ &\quad i_N(n)] + z(n) \\ &= x_s(n) + x_i(n) + z(n) = input\ signal \end{aligned} \tag{2}$$

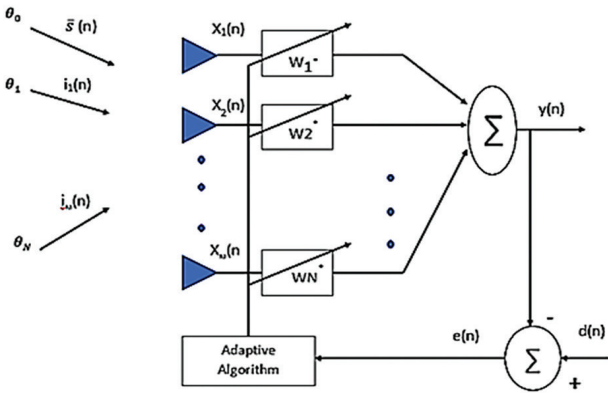

Fig. 1. Adaptive Array Beam forming System

With:

$w=[w_1\ w_2\ \ldots.w_N]^T$= array weights

$x_s(n)$ = desired signal vector

$x_i(n)$ = interfere signals vector

$z(n)$ = Gaussian noise with a zero mean for each channel

$s(n)$ is desired signal

θ_0 is desired signal direction

θ_1 ..... θ_N is interfere signals direction

a = steering vector forθ_i direction of arrival using an N-element array.

The difference between the desired signal $d(n)$ (eq. (1)) and the output signal $y(n)$ is the error signal $e(n)$ [25]:

$$e(n)=d(n)-w^H(n)\,x(n) \tag{3}$$

The weight vector of LMS is calculated using the gradient of the cost function [1]:

$$w(n+1)=w(n)+\mu\, e(n)\, x(n) \tag{4.1.}$$

If update vector $f(n)=\mu\, e(n)\, x(n)$, then:

$$w(n+1)=w(n)+f(n) \tag{4.2.}$$

The parameter μ is a step-size directly influences the LMS algorithm's convergence in equation (4.1).

2.3. PU LMS ALGORITHMS

Processing work can be reduced during the adaptive filter update phase using a technique called partial updates (PU). In recent years, these algorithms have drawn a lot of interest from both users and researchers [23].

The partial-update approach updates only the $M\times1$ coefficients, where $M < N$, as opposed to updating all of the N-1 coefficients. This paper considers fundamental partial update techniques such as (periodic, sequential, stochastic, and M-max) PU approaches. A general update equation can be used to characterize each PU algorithm studied in this study [14] [26]:

$$w(n+1)=w(n)+\mu\, I_M(n)\, e(n)\, x(n) \tag{5}$$

The matrix, $I_M(n)$, which is known as a weight selection matrix, represents the only distinction between PU techniques (5) and the full update LMS algorithm (4.1). It can be calculated as [14, 26]:

$$\begin{gathered} I_M(n)=[i_0(n)\ \cdots 0 \vdots \ddots \vdots 0 \cdots i_{L\text{-}1}(n)\ ], \\ i_k(n)\in\{0,1\},\quad \sum_{k=0}^{(L-1)} i_k(n)=M \end{gathered} \tag{6}$$

Hence, a diagonal matrix with entries of (0 or 1) makes up the weight selection matrix, where M denotes the sum of the number of 1s in the matrix indicating which M coefficients are to be updated at iteration n and the diagonal of the matrix, which has N-M zeros.

The number M, which represents how many adaptive filter weights are chosen for the update at each sampling interval, is likewise subscripted to the selection matrix. The selection matrix's diagonal elements are set to 0 or 1 in each consecutive sample interval using the procedure below: [14, 26]:

$$i_k(n)=\{1\ \text{ if } k\in I_M(n)\ 0\ \ otherwise \tag{7}$$

Where $I_M(n)$ stands for a collection of filter weight indices with a count of M, indicating the coefficients to be modified in the nth iteration. This set's definition changes based on which PU LMS algorithm is used.

The main advantage of the partial updates in (5) is that they minimize complexity to meet hardware complexity restrictions. The slower convergence speed of partial updates could be a drawback. Partial updates might be viewed in this situation as a trade-off between computational complexity and convergence speed.

2.4. PU SEQUENTIAL LMS ALGORITHM

By updating a piece of the adaptive filter coefficients at each iteration, sequential PU reduces the computation required for the adaptation process.

For each iteration of the sequential PU approach, a portion of the coefficient vector is modified to fit the complexity restrictions [14]. The adaptive filter coefficient vector is, in this sense, "decimated" by the use of consecutive PU.

Deterministically, the coefficient subsets to be updated are chosen in a round-robin fashion. As a result, regardless of the input signal, the updates follow a periodic pattern. The coefficient selection matrix $I_M(n)$ is computed as follows: (6).

For given N and M, $I_M(n)$ is not explicitly specified. Consider the distinct M-subsets of the coefficient index set (that is, subsets with M members) $S=\{1, 2, \ldots, N\}$, denoted by ($I_1, I_2, \ldots, I_C$)where $C=(N/M)$. The symbol S is the period of coefficient updates.

Suppose that ($B = N/M$) is an integer. The sequential partial update method can then be implemented by using any B M-subsets of S. The complexity of the adaptation process can be reduced by updating M coefficients in an adaptive filter of length N at every iteration. As a result, the algorithm has a number of flaws, such as

a slow rate of convergence, instability for cyclostationary input signals, and more [11-12].

2.5. PU M-MAX-LMS ALGORITHM

The M-max LMS selects M elements from the input vector $x(n)$ that cause the greatest changes in the magnitude of the filter weights. When partial updates are applied to the generic adaptive filter in (5), the result is [14]:

$$w(n+1)=w(n)+ I_M (n) f(n) \quad (8)$$

Where: $f(n)$ is update vector

$$f(n)= [f_1 (n),f_2 (n)m...,f_N (n)]^T \quad (9)$$

The entries in the selection matrix's diagonal of the coefficient selection matrix $I_M(n)$, specified in (6), are [14]:

$$i_k(n)= \{1 \quad if |f\_k (n)| \in (|f_l (n)|, M) \quad 0 \quad otherwise \quad (10)$$

where $\max_{0\le l\le N} (f_l, M)$ represents a set of M maxima of elements f_l [26]. M-max updates are similar to sequential partial updates in that they both 'decimate' the update vector.

2.6. PU PERIODIC LMS ALGORITHM

The updating weights vector is as follows when periodic partial updates are applied to the adaptive filter coefficients in (4.2.):

$$w((n+1)S)=w(nS)+ f(nS) \; n = 0, 1, 2, \quad (11)$$

$$w((nS+i))=w(nS) \quad i = 0, 1, \ldots, S-1 \quad (12)$$

The periodic PU method decimates the coefficient update w(n) by a factor of S. The coefficients of adaptive filter update every Sth iteration at k = 0, S, 2 S, 3 S, . . ., while the coefficients of adaptive filter are held constant between updates, i.e.,

$$w(n\,S) = w(n\,S + 1) = \cdots = w(n\,S + S - 1) .$$

The adaptation process can calculate the update vector in S iterations due to the decimation of updates by S. As a result, the typical processing demands of each iteration are reduced by S [14].

2.7. PU STOCHASTIC LMS ALGORITHM

To implement the stochastic method, a randomized variation of the sequential approach can be used, in which the coefficient of adaptive filter subsets is chosen at random rather than in a deterministic manner [14]. The stochastic PU method employs the following coefficient selection matrix:

$$I_M (n)= [i_0 (n)\cdots 0 \vdots \ddots \vdots 0 \cdots i_N (n) \;], \quad i_k (n)= \{1 \quad if\, k \in I_{m(n)} \quad 0 \quad otherwise \quad (13)$$

where $m(n)$ is an independent random process.

By using stochastic PU methods, complexity can be reduced to a level equivalent to that gained by sequential PU [26], if the overheads for producing the random signal m(k) are disregarded. Moreover, the stochastic partial update algorithm surpasses the sequential partial update technique in terms of network performance [19].

3. ARCHITECTURE OF THE PROPOSED MODEL

In next-generation networks with numerous antennas in the precoders and/or detectors, adaptive array beamforming is essential [27]. Next-generation networks have lower power consumption and amplifier costs due to lower power requirements of beamforming array antennas for sending signals to the intended user and cost reductions.

To achieve high cost-effectiveness and total energy efficiency, a common number of functional antennas for the system's cells might be decreased. The number of working antenna elements in the cell has a relatively significant impact on overall energy efficiency for the specified power consumption of each BS.

The most popular and effective method for providing adaptive array beamforming is the well-known phased array antenna (PAA), which is an array of antenna elements controlled by signals with well-defined phase relations between those elements [28].

A N-phased array antenna typically requires N phase shifters or other active control components. Many plans exist to reduce the use of phase shifters, but more active control units should be added as a substitute.

Although many ULA researchers have studied these issues, update partial (PU) adaptive filtering has never been used before. Fig. 2 depicts the architecture-proposing model, which employs update partial adaptive filtering to select or deselect the RF chain for each ULA element to increase or decrease the number of antennas (M), such that $M < N$.

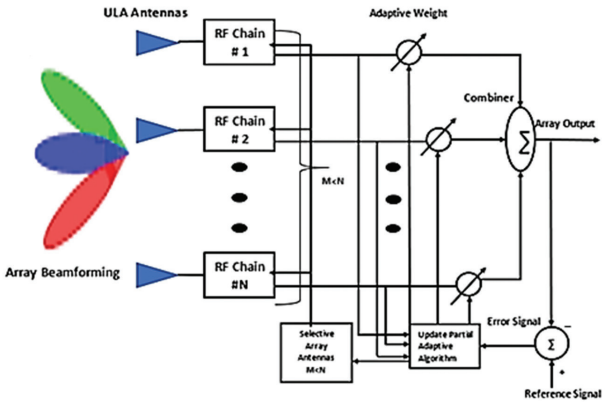

This selection process implies that at each coefficient update, M coefficients are updated while the remaining (N-M) coefficients remain unchanged. In theory, the chosen M coefficients should change with each iteration to allow all adaptive filter coefficients to be updated over time. This reduction also has important implications, such as minimizing each antenna element's radio frequency (RF) chain and reducing the total size and weight of the antenna array system. Another critical component is to streamline signal processing and reduce the amount of storage required as fewer signals are received. As a result, the overall cost of the system is reduced.

The process of reducing the number of antenna elements in antenna arrays while maintaining their radiation pattern features close to the full band, on the other hand, has a significant impact on wireless communication systems. When the number of elements is reduced, the radiation pattern exhibits minimal distortion and is symmetric in all orthogonal planes of the array.

4. SIMULATION RESULTS

The array beamforming base station, as depicted in Fig. (2), comprises a linear antenna array made up of eight (N=8). It is assumed that the x-axis contains all of the array's elements, and that each element is d=0.5 λ units apart. Three users broadcast at a specific elevation angle, with the intended user's angle being 00 and the other two users' angles being 300 and -200, respectively. There have been 400 iterations in total. Table 1 show the simulation parameters:

Table 1. The simulation parameters

Parameter	Value
Carrier Frequency (FC)	900 MHz
Signal Frequency	200 KHz
Spacing between element (d)	0.5 λ
Type of antenna	Uniform N element linear array antenna
Number of elements	N = 8 (full band) & (M = 1, 3 , and 5 for partial band)
Channel	EPA, EVA, and ETU

Given that all algorithms tested had the same step size μ value, which was calculated automatically within the MATLAB program according to (14). It was demonstrated that using this selection criterion would produce results that were as close as possible to the full band LMS algorithm's performance. The formula in (14) is dependent on the maximum eigenvalue λ_{max} of the input correlation matrix estimation $\hat{R}_{xx}$: [24]

$$0 \leq \mu \leq \frac{1}{2\lambda_{max}} \tag{14}$$

$$\text{Step size (LMS) } \mu = \frac{1}{(4*real(trace\ R_{xx})} \tag{15}$$

Were $\hat{R}_{xx}$, can be instantaneous estimates as:

$$\hat{R}_{xx}(n) \approx \underline{x}(n)\,\underline{x}^{H}(n) \tag{16}$$

The crucial design parameter is the number of filters taps that must be changed with each sampling interval. In the PU-LMS algorithms, M coefficients out of the adaptive filter's N coefficients are updated at each iteration. To select the suitable value of M parameter, several values of M will used which are 1,3 and 5 respectively. Then a comparison result obtained to choose the best value of M that perform the best performance of the algorithms. Then best value for M will used for the rest of the work. The chosen M coefficient values starts at 5 then 3 , then 1 which represents the worst case [23] using EPA channel.

4.1. SIMULATION RESULTS USING EPA (EXTENDED PEDESTRIAN MODEL) LTE CHANNEL MODEL

The Extended Pedestrian is the first model. A wireless channel model (EPA) with seven pathways and a gain of [0 -1 -2 -3 -8 -17.2 -20.8] dB with a delay of [0 30 70 90 110 190 410] *1e-9 for each path [29-30]. This channel simulates small cell size and low delay spread situations found inside buildings. Fig. (3 & 4 & 5) show the error square performance for all algorithms (EPA channel) at M=1 & M=3 & M=5, respectively.

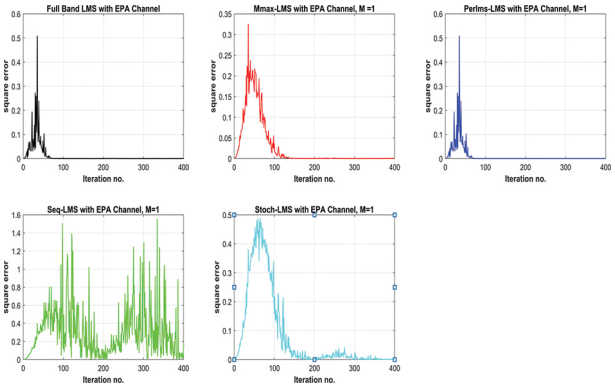

Fig. 3. Error Square performance for all algorithms (EPA channel) at M=1.

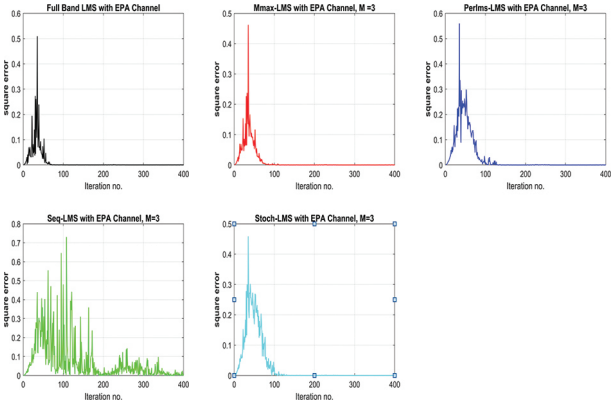

Fig. 4. Error Square performance for all algorithms (EPA channel) at M=3.

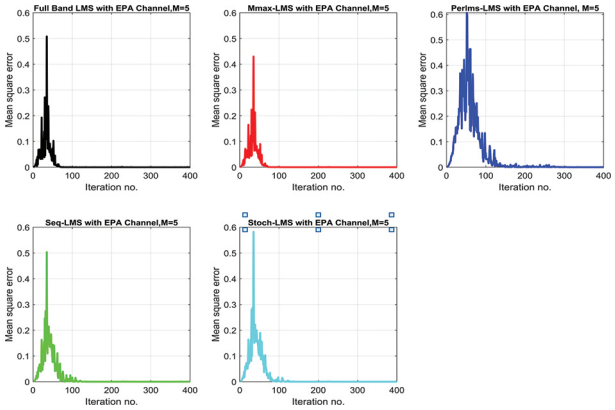

Fig. 5. Error Square performance for all algorithms (EPA channel) at M=5

Table 2 show square error convergence time comparison results for applying a different type of algorithms and EPA channel.

Table 2. Square error convergence time comparison EPA channel

Type of algorithm	Convergence time at iteration number		
	M=1	M=3	M=5
Full band-LMS(N=8)	60	60	60
M max-LMS	110	70	60
Periodic-LMS	60	100	110
Sequential-LMS	400	200	70
Stochastic-LMS	150	100	70

Fig. (6 ,7, and 8) show the performance for different values of M in terms of output estimation signal when the input desired signal is a pure sinewave.

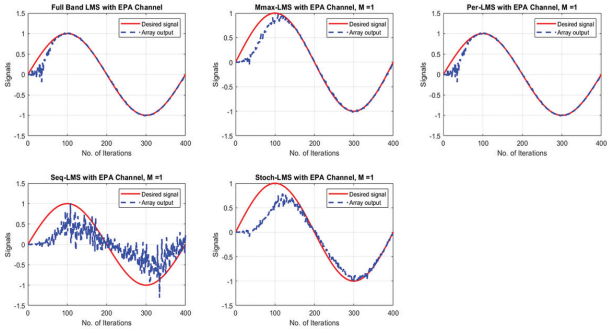

Fig. 6. Array output and desired signals of algorithms for EPA channel model, at $M = 1$

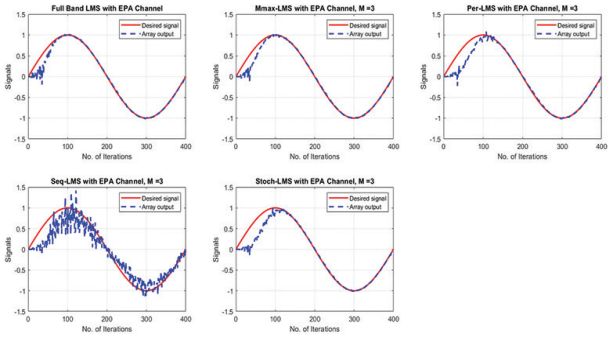

Fig. 7. Array output and desired signals of algorithms for EPA channel model, at $M = 3$

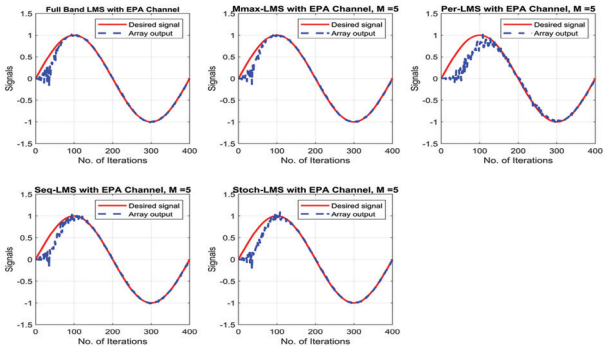

Fig. 8. Array output and desired signals of algorithms for EPA channel model, at $M = 5$

Table 3 show convergence time of estimation array output performance comparison of algorithms.

Table 3. Convergence time comparison of estimation array output over EPA channel

Type of algorithm	Convergence time at iteration number		
	M=1	M=3	M=5
Full band-LMS(N=8)	60	60	60
M max-LMS	100	70	60
Periodic-LMS	60	100	115
Sequential-LMS	Very slow	110	80
Stochastic-LMS	150	100	80

Convergence times and estimate accuracy of *M-max* algorithm are best at M=3,5, but decrease at M=1. In contrast, periodic algorithm provides reliable estimates at M=1, but starts to degrade around M = 3,5. In addition, the Stochastic method provides reliable forecasts when M=5, but it degrades when M=1, 2, or 3. The algorithm Sequential PU LMS decreases when M is equal to 1 and 3.

Fig. 9. shows the array pattern for algorithms when M equals 5.

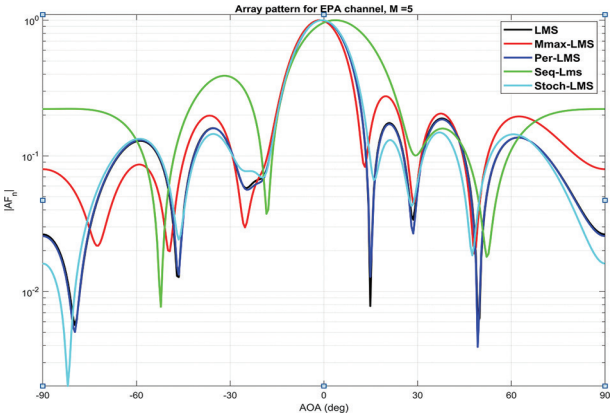

Fig. 9. The array pattern for algorithms with EPA channel model, M equals 5 elements

It is evident that in terms of steering the primary beam in the desired direction (0º) and nulling the beam in the direction of interference (-20º, 30º), for (M=5) the array structure of PU LMS algorithms is semi-similar to that of the full band LMS, except for the sequential PU algorithm.

We found that when the number of antennas was set to 5, the results were good and were more similar to the full band results than the other two options i.e., M=1 and 3.

4.3. SIMULATION RESULTS USING EVA (EXTENDED VEHICULAR MODEL) LTE CHANNEL MODEL

Extended Vehicular (EVA) was the paradigm for the second LTE channel. A wireless channel model (EVA) with nine pathways and matching gain values of [0 -1.5

-1.4 -3.6 -0.6 -9.1 -7 -12 -16.9] dB and [0 30 150 310 370 710 1090 1730 2510] *1e-9 for each path. This channel features a medium delay spread model and reflects metropolitan areas with big cells [29-30].

The error square performance of each algorithm is shown in Fig. 10 for EVA channel. This figure demonstrates that in terms of convergence rate and minimum error level in the steady state region, the performance of the *M-max*, Periodic, and Stochastic PU LMS algorithms is comparable to that of the respective full band LMS algorithms. In contrast, the performance of the sequential PU LMS algorithm has little more than them because of slow convergence rates and high steady state error levels. This decrease occurred as a result of the demand for more iterations (> 400 iterations) and for step size parameter selection by trial and error.

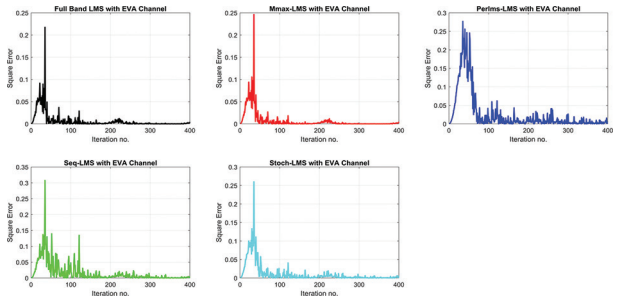

Fig. 10. Error Square performance for all algorithms (EVA channel)

Table 4 show the summary results for applying a different type of algorithms over EVA channel.

Table 4. Square error convergence time comparision (EVA channel)

Number of elements of antenna	Type of algorithm	Convergence time at iteration number
8	Full band-LMS	40
5	M max-LMS	40
5	Periodic-LMS	70
5	Sequential-LMS	150
5	Stochastic-LMS	50

Fig. 10. depicts the estimation output signal. It is evident that the *M-max*, Sequential and Stochastic PU LMS algorithms have accurate estimates, but they decline for the Periodic PU LMS algorithm.

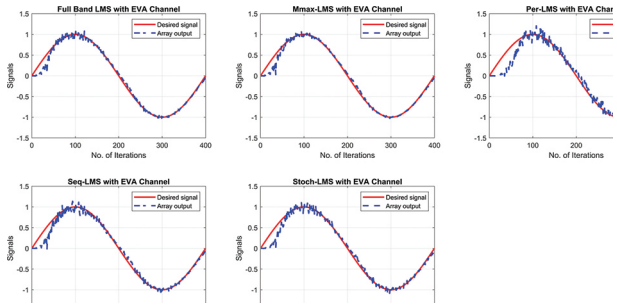

Fig. 11. Array output and desired signals of algorithms for EVA channel model

Table 5 show convergence time comparison when using EVA channel:

Number of elements of antenna	Type of algorithm	Convergence time (Iteration number)
8	Full band-LMS	40
5	M max-LMS	45
5	Periodic-LMS	80
5	Sequential-LMS	50
5	Stochastic-LMS	45

4.3. SIMULATION RESULTS USING ETU (EXTENDED TYPICAL URBAN MODEL) LTE CHANNEL MODEL

The third channel was the Extended Typical Urban Model (ETU) wireless channel model, which is used to simulate urban settings with large cells and has significant delay spread situations [14]. There are nine pathways in this channel model, each having a gain of [-1 -1 -1 0 0 0 -3 -5 -7] dB and a matching delay of [0 50 120 200 230 500 1600 2300 5000] *1e-9 [29-30].

The error square performance of each algorithm is shown in Fig. 12. This figure demonstrates that in terms of convergence rate and minimum error level in the steady state region, the performance of the M-max, Periodic, and Stochastic PU LMS algorithms is comparable to that of the respective full band LMS algorithms. In contrast, the performance of the Sequential PU LMS algorithm has little more than them because to slow convergence rates and high steady state error levels. This decrease occurred as a result of the demand for more iterations (> 400 iterations) and for step size parameter selection by trial and error.

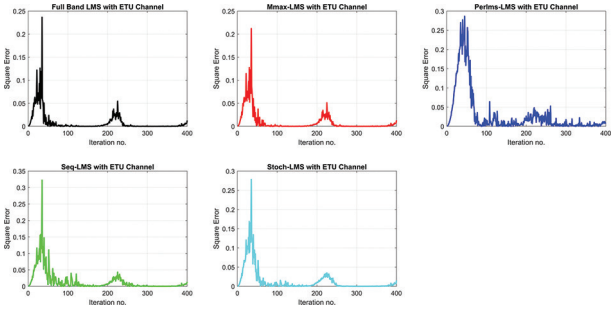

Fig. 12. Error Square performance for all algorithms (ETU channel)

Table 6 show the summary results for applying a different type of algorithms and ETU channel.

Table 6. Convergence time comparison of square error curves (ETU channel)

Number of elements of antenna	Type of algorithm	Convergence time (Iteration number)
8	Full band-LMS	45
5	M max-LMS	46
5	Periodic-LMS	80
5	Sequential-LMS	55
5	Stochastic-LMS	47

Fig. 13 depicts the accurate estimates output signal using M-max, Sequential and Stochastic PU LMS algorithms, but they decline for the Periodic PU LMS algorithm.

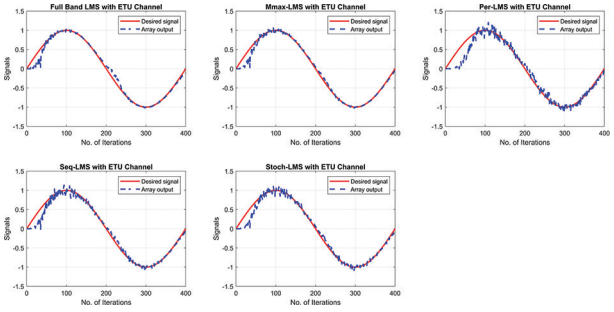

Fig.13. Array output and desired signals of algorithms for ETU channel model

Table 7 show convergence time comparison when using ETU channel.

Table 7. Convergence time comparison of estimation array output (ETU channel)

Number of elements of antenna	Type of algorithm	Steady state at iteration number
8	Full band-LMS	48
5	M max-LMS	48
5	Periodic-LMS	80
5	Sequential-LMS	50
5	Stochastic-LMS	50

The results of the simulation may indicate which PU LMS algorithm performs best in terms of error square and convergence time, and whether any of the PU LMS algorithms perform similarly to the full band LMS algorithm.

Periodic-partial-updates LMS are has slower convergence time than the LMS algorithm. Sequential partial updates aim to reduce computational complexity by updating a subset of the adaptive filter coefficients at each iteration. It is may not provide a satisfactory solution to the instability problem.

Stochastic partial updates are used to avoid instability issues with sequential partial updates for non-stationary inputs. Stochastic partial updates are desirable due to their stability implications.

M-max updates where the maximum absolute value of the filter coefficients is limited to a predefined value. This modification can improve the stability of the algorithm. It is the best PU LMS algorithm and comparable to the full band LMS algorithm.

5. RESULTS COMPARISON WITH PREVIOUS WORK

Our proposed paper will compare with very related and previously published paper in 2019 [10] that used adaptive algorithms also like LMS. Before make a comparison result, Table 8 shows the main comparison points between our proposed model and [10].

Table 8. the main comparison points between our proposed methods and [10].

Items	[10]	Our proposed model
N and M parameters	N =12, M =4	N= 8, M= 5 ,3, and 1
Communications channel	Did not mentioned, Unknown	EPA, EVA, and ETU channels
Number of Iterations K	K=100	K=400
Step size μ	Fixed (μ= 0.006)	Automatic selectable μ eq (14)
Input desired signal (S)	Did not mentioned, Unknown	Sinewave input desirable signal
Method for Selectable number of antennas (M)	Did not mentioned how they choose M=4 out from N=12	PU algorithms (M- *max*, Periodic, Sequential, and Stochastic)
Carrier frequency (FC)	Did not mentioned, Unknown	FC = 900 MHz

Figs. (14 and 15) shows comparison results between this paper and [10].

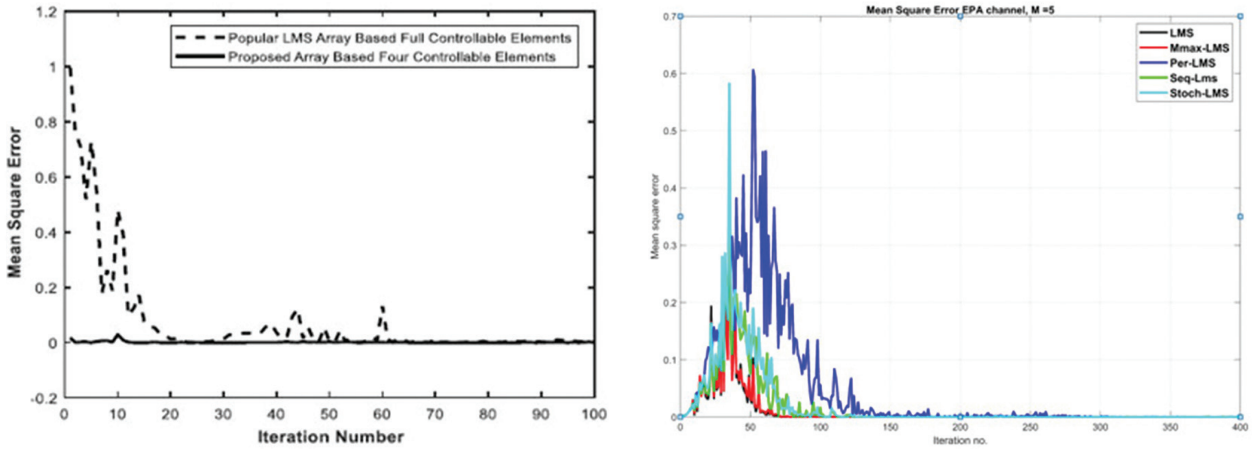

a) b)

Fig.14. MSE comparison; a) MSE [10] , b) Proposed

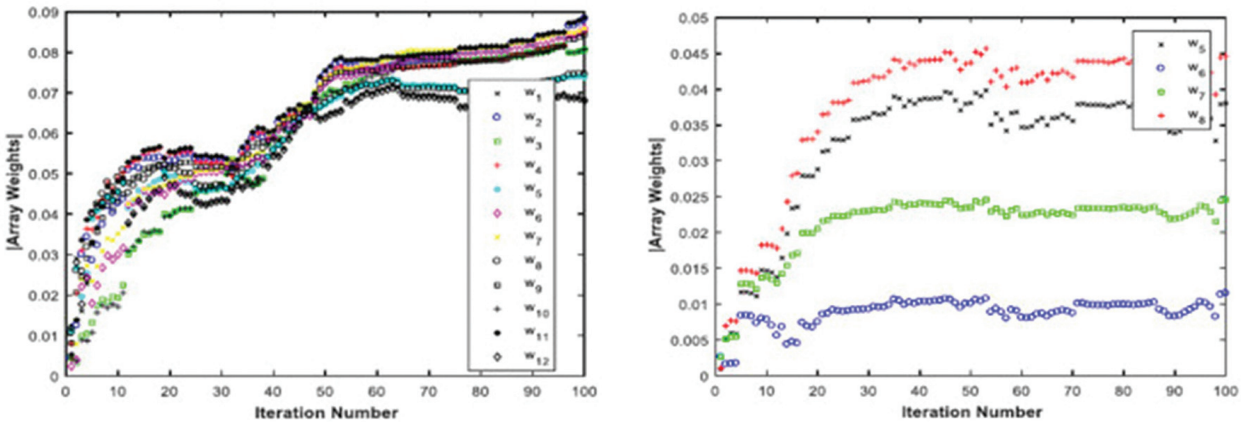

a)

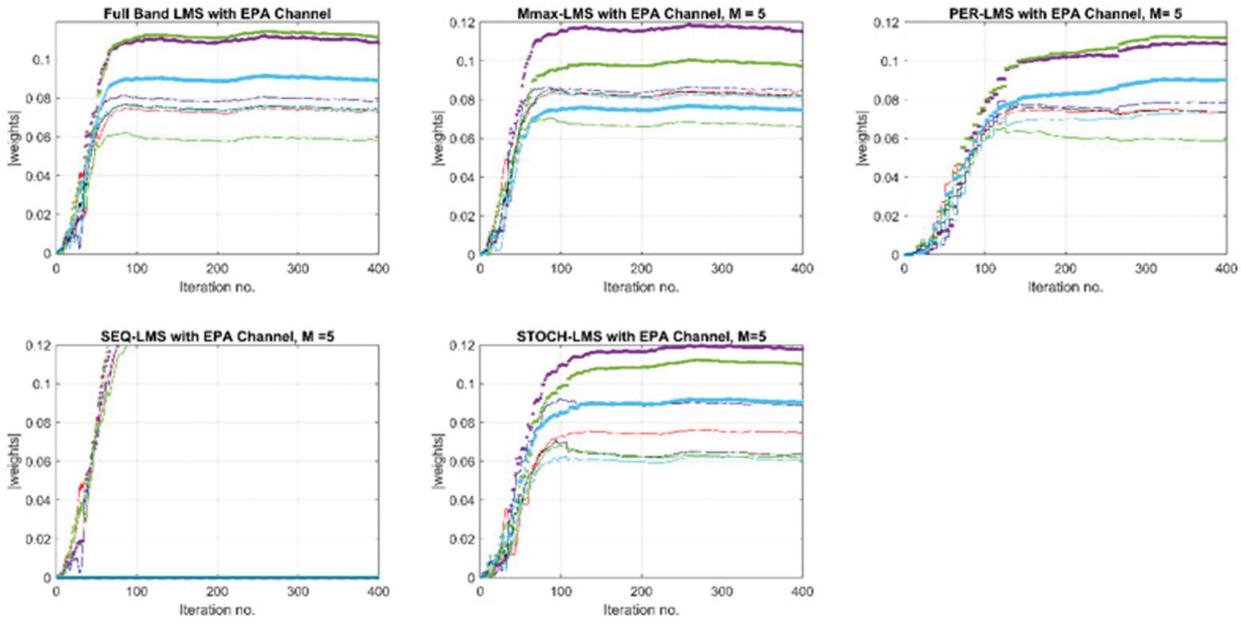

b)

Fig 15. Weights tracking comparison; a) [10] , b) Proposed

The research methodology employed in this study for reducing the number of antennas and consequent reduction in phase shifters is deemed more effective compared to research method [10]. This superiority can be attributed to the incorporation of intelligent decision-making in our approach, wherein the selection of antennas to be reduced is guided by the principles and equations of partial modernization. In contrast, method of [9] solely focuses on selecting antennas located in the center of the matrix, without providing a rationale for this choice or considering antennas situated elsewhere within the system.

The absence of a theoretical foundation and explanation for the exclusive selection of central antennas in method of [10] stands in contrast to our methodology, which adheres to the rules and equations of modernization to inform the antenna selection process. If our method demonstrates superior effectiveness and efficiency, and the selection of fixed antennas is not arbitrary but rather adheres to the prescribed laws and regulations of each respective method, then it can be concluded that this method is superior.

6. CONCLUSION

This paper's key contribution was the first attempt to apply PU adaptable methods for selecting or choosing the number of antennas (M) by selecting or deselecting the RF chain for each element in the ULA such that $M < N$, which in turn reduced the number of active components.

The total size and weight of the antenna array system are reduced, and each antenna element's radio frequency (RF) chain is minimized as a result of this decrease in size and weight. Another crucial element is to streamline signal processing and decrease the amount of storage needed as a result of fewer signals being received. As a result, the cost of the entire system has decreased.

The performance of PU algorithms, with the exception of Sequential PU LMS, is comparable to that of the full band LMS algorithm in terms of convergence time

and low level of minimal error in steady state. While the *M-Max* algorithm is significantly quicker than other PU methods, the Stochastic algorithm is considerably more reliable because it is not affected by cyclo-stationary input. When utilizing Periodic PU in the BAA system with LMS algorithm, it is sufficient to utilize a maximum of half of the coefficients. This is due to the fact that increasing the number of coefficients beyond this threshold does not result in a significant difference.

The nulling effect affects beam-forming array antenna radiation patterns. The null control was designed to emit low power in areas where unapproved listeners may be present. Adjusting excitation amplitude, phase, array distance spacing, and element number can achieve null control. Radiation patterns show a higher primary beam orientation and a lower secondary interference direction.

From simulation results, the convergence time by using the partial update (with exception of sequental one) is combarable or semicombarable to full band LMS. While convergence time of perodic PU algorithm became slow with increasing M as contrary to the others.

As for nulling, the array structure of PU LMS algorithms demonstrates clear effectiveness in directing the primary beam towards the desired direction (0^o) and nullifying the beam in the direction of interference (-20^o, 30^o), particularly for an array size of M=5. This array structure exhibits a semi-similarity to the full band LMS, with the exception of the sequential PU algorithm. the *M-max*-LMS, periodic LMS and stochastic LMS algorithms perform similarly to the full band LMS algorithm in terms of square error (SE), tracking weight coefficients and estimation input signal, with a quick convergence time and a low level of error signal at steady state.

Additionally, the PU algorithms retain the radiation patterns' minimal distortion and symmetrical properties, which have a big impact on wireless communication systems.

The total number of coefficients required was reduced by 62% (M=5) compared to the total number used by the full update method.

7. REFERENCES

[1] M. A. G. Al-Sadoon, M. N. Patwary, Y. Zahedi, N.O. Parchin, A. Aldelemy, R. A. Abd-Alhameed, "A New Beamforming Approach Using 60 GHz Antenna Arrays for Multi-Beams 5G Applications", Electronics, Vol. 1, No. 11, 2022, pp. 1739-1761.

[2] X. Shiyi et al. "Dimensionality Reduced Antenna Array for Beamforming/steering", arXiv:2210.16197, 2022.

[3] B. Avser, J. Pierro, G. M. Rebeiz, "Random Feeding Networks for Reducing the Number of Phase Shifters in Limited-Scan Arrays", IEEE Transactions on Antennas and Propagation, Vol. 64, No. 11, 2016, pp. 4648-4658.

[4] S. I. Abd Elrahman, A. M. Elkhawaga, A. H. Hussein, A. E. A. Shaalan, "Linear Antenna Array Sectorized Beam Scanning Approaches Using Element Position Perturbation in the Azimuth Plane", Sensors, Vol. 23, No. 14, 2023, pp. 6557-6591.

[5] B. Avser, R. F. Frazita, G. M. Rebeiz, "Interwoven Feeding Networks with Aperture Sinc-Distribution for Limited-Scan Phased Arrays and Reduced Number of Phase Shifters", IEEE Transactions on Antennas and Propagation, Vol. 66, No. 5, 2018, pp. 2401-2413.

[6] B. R. P. Uakula, A. H. Aljuhani, G. M. Rebeiz, "Limited Scan-Angle Phased Arrays Using Randomly Grouped Subarrays and Reduced Number of Phase Shifters", IEEE Transactions on Antennas and Propagation, Vol. 68, No. 1, 2019, pp. 70-80.

[7] E. Juárez, M. A. P. Mendoza, D. H. Covarrubias, A. R. Maldonado, B. Sanchez, C. D. Rio, "An Innovative Way of Using Coherently Radiating Periodic Structures for Phased Arrays with Reduced Number of Phase Shifters", IEEE Transactions on Antennas and Propagation, Vol. 70, No. 1, 2022, pp. 307-316.

[8] R. B. Sánchez, M. A. Panduro, D. H. Covarrubias, M. A. Reyna, E. Juárez, "Coherently Radiating Periodic Structures for Feeding Concentric Rings Array with Reduced Number of Phase Shifters", Sensors, Vol. 22, No. 23, 2022, pp. 9528-9545.

[9] F. Akbar, A. Mortazavi, "Design of a scalable phased array antenna with a simplified architecture", Proceedings of the 45th European Microwave Conference, Paris, France, 7-10 September 2015, pp. 1427-1430.

[10] J. R. Mohammed, "Interference Mitigation in the Wireless Communication Systems Using Adaptive Filters", Proceedings of the 1st International Conference on Engineering and Technology, Ninevah, Iraq, 5-6 April 2021, pp. 012001-012011.

[11] T. M. Jamel, F. F. Hammood, "A New Variable Length LMS Algorithm for Partial Update Adaptive Filtering Driven by Cyclostaionary Signal", International Journal of Computing and Digital Systems, Vol. 5, No. 5, 2016, pp. 411-419.

[12] T. M. Jamel, F. F. Hammood, "Performance enhancement of Echo Cancellation Using a Combination of Partial Update (PU) Methods and New Variable Length LMS (NVLLMS) Algorithm", Journal of Engineering, Vol. 24, No. 5, 2018, pp. 66-85.

[13] B. Xie, T. Bose, "Partial update EDS algorithms for adaptive filtering", Proceedings of the 24th IEEE International Conference on Acoustics, Speech and Signal Processing, Dallas, TX, USA,14-19 March 2010, pp. 3750-3753.

[14] K. Dogançay, "Partial-Update Adaptive Signal Processing: Design. Analysis and Implementation", 1st Edition, Academic Press, Burlington, 2008.

[15] A. W. Khong, W. S. Gan, P. A. Naylor, M. Brookes, "A low complexity fast converging partial update adaptive algorithm employing variable step-size for acoustic echo cancellation", Proceedings of the IEEE International Conference on Acoustics, Speech and Signal Processing, Las Vegas, NV, USA, 31 March - 4 April 2008, pp. 237-240.

[16] G. Mahesh, O. H. Alfred, "Partial Update LMS Algorithms", IEEE Transactions on Signal Processing, Vol. 53, No. 7, 2005, pp. 2382-2399.

[17] M. A. Ramdane, A. Benallal, M. Maamoun, I. Hassani, "Partial Update Simplified Fast Transversal Filter Algorithms for Acoustic Echo Cancellation", Traitement du Signal, Vol. 39, No. 1, 2022, pp. 11-19.

[18] S. A. Akinboro, A. Omotosho, E. A. Oluwatosin, "A Fractional Variable Partial Update Least Mean Square Algorithm (FVPULMS) for Communication Channel Estimation", Nigerian Journal of Technological Development, Vol. 15, No. 4, 2018, pp. 108-112.

[19] V. Barfa, R. P. Narwaria, "Partial Update Adaptive Strategies for Distributed Wireless Networks", International Journal of Electrical and Electronics Engineers, Vol. 07, No. 01, 2015, pp. 2321-2055.

[20] R. Arablouei, K. Dogancay, S. Perreau, "Partial Update Adaptive Decision Feedback Equalization", Proceedings of the 19th International Conference on European Signal Processing Conference, Barcelona, Spain, 29 August - 2 September 2011, pp. 2205-2209.

[21] R. P. Lorente, M. R. Ferrer, A. F. Martínez, P. G. Navarro, "Modified Filtered-X Hierarchical LMS Algorithm with Sequential Partial Updates for Active Noise Control", Applied Sciences, Vol. 11, No. 1, 2020, pp. 344-368.

[22] M. Grira, J. A. Chambers, "Adaptive Partial Update Channel Shortening in Impulsive Noise Environments", Proceedings of the 15th International Conference on Digital Signal Processing, Cardiff, UK, 1-4 July 2007, pp. 555-558.

[23] D. Bismor, "Simulations of Partial Update LMS Algorithms in Application to Active Noise Control", Proceedings of the 7th International Conference on Procedia Computer Science, 1-3 January 2016, pp. 1180-1190.

[24] R. Dewda, M. Gupta, V. Barfa," Adaptive Partial Update Algorithm Over Wireless Sensor Networks", International Journal of Innovative Research in Technology, Vol. 3, No. 1, 2016, pp. 2349-6002.

[25] F. B. Gross, "Smart Antenna for Wireless Communication", 1st Edition McGraw-Hill, 2005.

[26] X. Bei, T. Bose, "Partial update least-square adaptive filtering", Springer Nature, 2022.

[27] M. Reil, G. Lloyd, "Millimeter-Wave Beamforming: Antenna Array Design Choices & Characterization", Rohde & Schwarz GmbH & Co. KG, Munich, Germany, Technical Report TR- 1MA276_2e, 2016.

[28] L. M. Alnaggar, M. M. A. Elnaby, A. H. Hussein, "A New Beamforming Technique for the Synthesis of Uniform Circular Antenna Arrays Using Reduced Number of Antenna Elements", IEEE Access, Vol. 9, 2021, pp. 90306-90318.

[29] "Evolved Universal Terrestrial Radio Access (E-UTRA); Base Station (BS) radio transmission and reception (3GPP TS 36.104 version 14.3. 0 release 14)", ETSI Secretariat, Technical Report TR- RTS/TSGR-0436104ve30, 2017.

[30] V. S. AL-Doori, T. M. Jamel, B. M. Mansoor, "Space Division Multiple Access Base Station (SDMA) Based on Block Adaptive Euclidean Direction Search Algorithm", IEIE Transactions on Smart Processing and Computing, Vol. 11, No. 02, 2022, pp. 133-139.

Design and Performance Analysis of Rectangular Microstrip Patch Antennas Using Different Feeding Techniques for 5G Applications

Original Scientific Paper

Sattar Othman Hasan
Salahaddin University-Erbil, Iraq
College of Education, Department of Physics
sattar.hasan@su.edu.krd

Othman Salim Hammd
Salahaddin University-Erbil, Iraq
College of Education, Department of Physics
othman.hammd@su.edu.krd

Saman Khabbat Ezzulddin
Salahaddin University-Erbil, Iraq
College of Science, Department of Physics
saman.ezzulddin@su.edu.krd

Rashad Hassan Mahmud
Salahaddin University-Erbil, Iraq
College of Education, Department of Physics
rashad.mahmud@su.edu.krd

Abstract *– In this article, the design and performance of a novel rectangular microstrip patch antenna (RMPA) utilizing the dielectric substrate material FR4 of relative permittivity (ε_r = 4.3) and thickness (h = 0.254 mm) is proposed to operate at (f_r = 28 GHz). Three different feeding techniques (microstrip inset line, coaxial probe, and proximity coupled line) are investigated to improve the antenna radiation performance especially the antenna gain and bandwidth using Computer Simulation Technology (CST) and High Frequency Structure Simulator (HFSS). The simulated frequency responses generally reveal that the proximity-coupled fed provides extremely directive pattern and maintain higher radiation performance regardless of its antenna size which is larger than the other considered feeding ones. With the presence of the three feeding techniques, the gain is improved from 5.50 dB to 6.83 dB additionally, the antenna bandwidth is improved from 0.6 GHz to 3.60 GHz at f_r = 28 GHz when the reflection coefficient S_{11}= -10 dB. Compared to the previously designed RMPA, the proposed design has the advantages of reliable size, larger bandwidth and higher gain, which make it more suitable for many 5G application systems.*

Keywords*: Feed techniques, gain, broadband bandwidth, microstrip patch, 5G*

1. INTRODUCTION

In recent years, wireless applications have been involved in all aspects of our life. Wide bandwidth, high gain, and compactness are the properties of antennas that are extremely required in the 5G and millimeter wave applications [1, 2]. A rectangular microstrip patch antenna (RMPA) is a good candidate to employ in these applications. However, its poor gain and small bandwidth are considered the two main drawbacks. Many methods have been conducted in the literature to overcome these drawbacks.

Numerous studies have been conducted to enhance the gain and bandwidth of MPAs, for instance decreasing substrate thickness, increasing substrate permittivity, feeding methodologies, and using various optimization methods [3]. Moreover, the mode shift theory presented in [4] was mainly done to enhance the bandwidth of the dual-mode RMPA by exciting two resonant modes. Exciting the higher mode in the RMPA has improved the bandwidth and efficiency and reduced the antenna size. A pair of slots etched from the microstrip patch done in [5] was to excite the two radiative modes close to each other and enlarge the bandwidth of the MPA. On the other hand, a superstrate lens placed on a normal patch antenna, which uniformed the phase distribution of the electric field over the patch was studied by [6] and led to an improvement in the antenna gain up to 48%.

In addition, a ferrite ring realized into the hybrid substrate of the RMPA was proposed by [7] to create a constructive interference between the incident and reflective fields in the substrate, which leads to an enhanced 4.0 dB gain of the antenna without compromising the bandwidth. Subsequently, two sets of short-circuited patches introduced in [8] were to excite two sets of orthogonal electric and magnetic dipole modes and enhance the overall antenna performances. A switchable feed network, which was controlled by a microcontroller, was employed in the array to provide a reconfigurable polarization and a high gain to the RMPA [9]. A numerical method (so-called discrete mode matching method) was presented in [10] to overcome the

disadvantages of RMPA. A microstrip patch was fed optically via a vertical cavity surface emitting laser by [11]. Such an optically feed system removes the need of the transmission line to feed the radiation element to improve the antenna gain.

Different from the methods mentioned above, a dual circularly polarized radiation was obtained from an equilateral triangular patch antenna using an aperture-coupled and proximity feeds [12]. A circular microstrip patch antenna's bandwidth and gain were significantly enhanced using an L-shaped patch with coaxial probe feed and hybrid-feed techniques [13]. Similarly, the dual feed ports in the square microstrip patch antenna were utilized to excite two orthogonal modes [14]. As a result of that, linear and circular polarization can be resulted over a certain operating frequency point. A bow-tie slot, which was etched from a rectangular patch, was introduced to achieve dual polarization and widen the bandwidth of RMPA [15].

This article proposes a new design of RMPA using three feeding techniques: microstrip inset feed, coaxial probe feed, and proximity coupled feed. For this, the dielectric material FR4 is selected as a substrate and the return loss S11, VSWR, gain, radiation pattern, antenna size and bandwidth of the suggested RMPA are examined under the influence of these feeding techniques using the (HFSS) and (CST) simulation methods. Through these investigations, a reasonable feeding technique in terms of simplicity and providing reliable radiation performance suitable for 5G application systems is identified.

The remaining part of the article is arranged as follows. Section 2 presents the theory, calculation, and design of the RMPA in the light of the three feeding techniques. The computed results of the fundamental RMPA parameters with the using each mentioned feeding methods are displayed in section three. Finally, the remarkable outcome conclusions are presented in section four.

2. ANTENNA DESIGN

Generally, different methods existed in the literature to feed the radiation patch of RMPA. The role of which in enhancing the antenna input impedance and efficiency is significant [17]. The two most widely recognized feeding techniques are the contact and non-contact methods. In the case of the contacting method, the guided EM energy is fed immediately to the radiating patch via a conducting strip such as microstrip inset line feeding and/or a coaxial probe feeding. On the other hand, the guided EM energy can be guided to the radiating patch under the resonant condition via proximity coupling fed. In the following, the design of RMPA in the light of these feeding types is described.

2.1. THEORETICAL DESIGN

The three fundamental parameters for the design of RMPA are the resonant frequency (f_r), substrate thickness (h), and substrate relative permittivity ($\mathcal{E}_r$). For the proposed RMPA, the (f_r) value is chosen to be (28) GHz. The substrate material type is FR4 with dielectric constant ($\mathcal{E}_r$ = 4.3) and thickness (h = 0.254 mm). The remaining design parameters can be calculated using the following relations.

The patch width (Wp) can be obtained using the relation [18]:

$$W_{\mathrm{p}} = \frac{c}{2f_r}\sqrt{\frac{2}{\mathcal{E}_r+1}} \tag{1}$$

Where, (c) is the speed of light in free space. The effective relative permittivity ($\mathcal{E}_{reff}$) which is produced due to the creation of fringing field and is expressed for the advanced RMPA as follows [18]:

$$\mathcal{E}_{r\mathrm{eff}} = \frac{\mathcal{E}_r+1}{2} + \frac{\mathcal{E}_r-1}{2}\left[1 + 12\frac{h}{W_p}\right] \tag{2}$$

The extension patch length (ΔL), which arise due to substrate thickness fringing field effect can be determined by [18]:

$$\Delta L = \frac{0.412(\mathcal{E}_{r\mathrm{eff}}+0.3)\left(\frac{W_{\mathrm{p}}}{h}+0.264\right)}{(\mathcal{E}_{r\mathrm{eff}}-0.258)\left(\frac{W_{\mathrm{p}}}{h}+0.8\right)}\,\mathcal{E}_{\mathrm{eff}} \tag{3}$$

And, the effective patch length (L_{eff}) is computed by an expression given by [18] as:

$$L_{\mathrm{eff}} = \frac{c}{2f_{\mathrm{r}}\sqrt{\mathcal{E}_{r\mathrm{eff}}}} \tag{4}$$

Finally, the actual patch length (L_p) can be calculated in term of the L_{eff} and ΔL of the patch using the relation [18]:

$$L_{\mathrm{p}} = L_{\mathrm{eff}} - 2\Delta L \tag{5}$$

It is worth mentioning that the above relations have been utilized to obtain the initial physical dimensions of the proposed RMPA. These dimensions have been inserted into the CST and HFSS simulators so as to layout the actual RMPA as can be seen in the next section.

2.2. ANTENNA CONFIGURATION

Fig. 1 demonstrates the design of the recommended RMPA with the presence of the three feeding techniques using the (CST) simulator. Fig. 1 (a), represents the RMPA which is fed via the microstrip inset feed line. Such line is used to convert the edge impedance to a merit that matches to the input impedance characteristic. Two slots are etched around the microstrip line in order to maintain good impedance matching. The length of the microstrip feed line is a quarter wavelength within the transformed impedance value that can be computed using the relation [19]:

$$Z_T = \sqrt{Z_o Z_a} \tag{6}$$

Here, Z_0 is the applied source impedance, Z_a is the radiation patch input impedance, and Z_T is impedance of the microstrip feed line.

In Fig. 1 (b), the design of the proposed RMPA with the existence of the proximity-coupled feed is shown. In this case, the antenna compasses the two layers of

dielectric medium with the same substrate thickness and dielectric constant. In Fig. 1 (c), the radiation patch is powered by a coaxial feed technique. This technique requires a probe feed line (mainly a 50 Ω coaxial connector) to link the radiation patch to the input port. The edge position of the port can be computed using the expression given by [17] as:

$$y(y_\circ) = \cos^2\left(\frac{\pi y_\circ}{L}\right) \quad (7)$$

Where, ($y_\circ$) is the y-position of the fed point at which the impedance matching is occur.

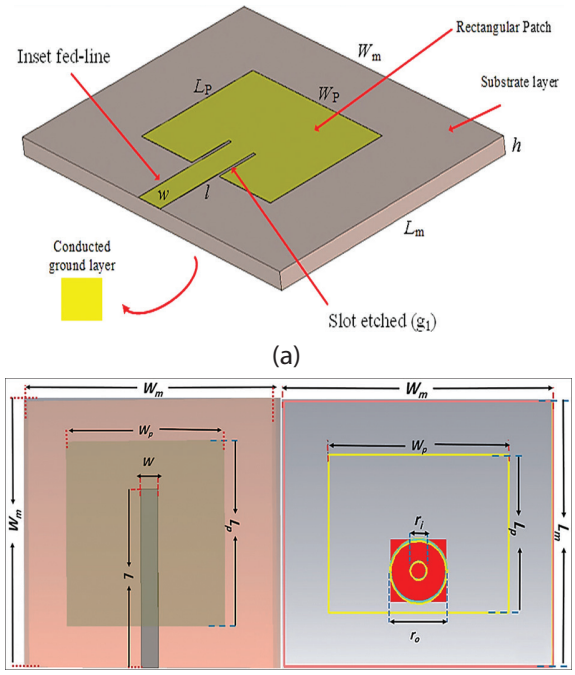

Fig. 1. Three-dimension view of the simulated RMPA with their specified layer representation for (a) microstrip line, (b) Proximity coupled and (c) Coaxial probe fed

It is essential to observe that the initial values of the dimensions labeled on the RMPA in Fig. 1 have been obtained using the relations given in section 2.1. Then, the genetic algorithm optimization method in CST has been performed on these dimensions in order to make the antenna resonate at (f_r = 28 GHz). The optimized dimensions of the proposed RMPA with each mentioned feeding techniques are summarized in Table 1.

Table 1. Optimized physical dimensions of the proposed RMPAs with each feeding techniques

Parameters (mm)	Discerption	Feed Types		
		Microstrip line	Coaxial probe	Proximity coupled
W_p	Patch Width	3.92	4.41	4.13
L_p	Patch Length	2.42	3.54	4.0
W_m	Width of ground Plane	6.58	6.58	6.58
L_m	Length of ground Plane	5.79	5.79	5.79
g_1	Slot etched	0.08	--	--
L	Length of Feed Line	0.88	--	3.86
h	Substrate Hight	0.254	0.254	0.508
W	Feed line with	0.49	--	0.44
r_o	Outer conductor diameters	--	1.40	--
r_i	Inner conductor diameter	--	0.40	--

3. RESULTS AND DISCUSSIONS

This section exhibits the proposed RMPA simulation results with the mentioned feeding technique using the CST and HFSS simulators. It can be indicated that good agreement between the simulated results of the CST and HFSS are obtained, validating the accuracy of the suggested RMPAs.

Fig. 2 represents the simulated results of the advanced RMPA feeding with the microstrip inset feed line. As can be observed form Fig. 2 (a) that the reflection coefficient (S11) is well matched at fr = 28 GHz having about 0.60 GHz bandwidth at (S11 = 10 dB). The first peak gain value is 5.50 dB at (28) GHz, while, the second peak gains value is 4.61 dB appeared at (37) GHz, as can be noticed in Fig. 2 (b). The radiation pattern for both the electric (E) and magnetic (H) planes are shown in Fig. 2 (c) and (d) at which the main beam is extremely directive with having small back lobes.

Moreover, the computed results obtained with both HFSS and CST simulation techniques of the recommended RMPA, when the coaxial feed probe feed is employed are displayed in Fig. 3. A very good matching of S11 is achieved at (28) GHz as shown in Fig. 3 (a). Also, about 0.6 GHz bandwidth is obtained at frequency of (28) GHz when (S11 = -10 dB). The maximum gain is 6.73 dB at (27) GHz as can be noticed in Fig. 3 (b). Moreover, the antenna radiation patterns are very directive for both the E- and H-planes at (28) GHz having only one back lobe as clearly seen in Fig. 3 (c) and (d). The existence of the back lobe here is appear due to the coaxial probe feed located beneath the RMPA which could distort the electric field distribution.

The proposed RMPA, when the proximity coupled probe is employed, is also simulated in both the CST and HFSS simulators. The calculated results are presented in Fig. 4. It can be observed from Fig. 4 (a) that the proposed RMPA provides a very large bandwidth, which is more than 3.60 GHz at fr = 28 GHz with the implementation of proximity coupled fed.

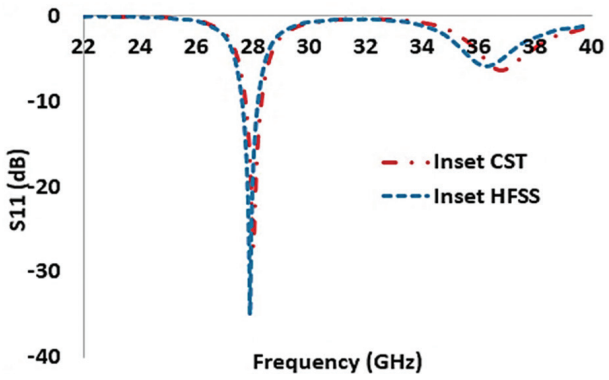

(a)

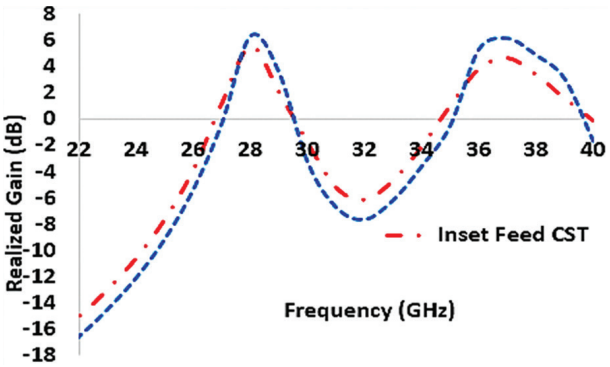

(b)

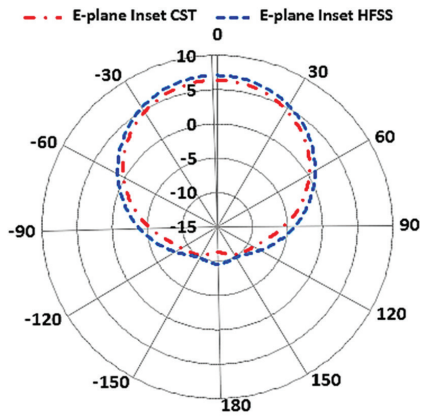

(c)

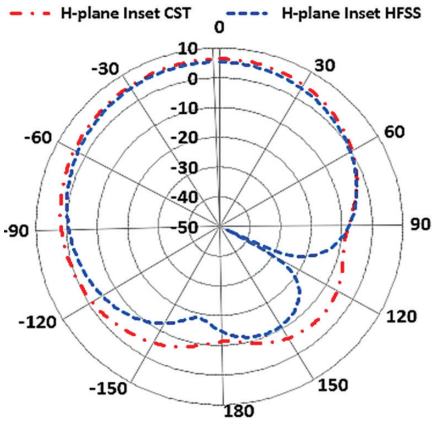

(d)

Fig. 2. Demonstrates results of the (**a**) Reflection coefficient (S11), (**b**) Realized gain, (**c**) E-plane and (**d**) H-plane for RMPA with the microstrip inset feed line

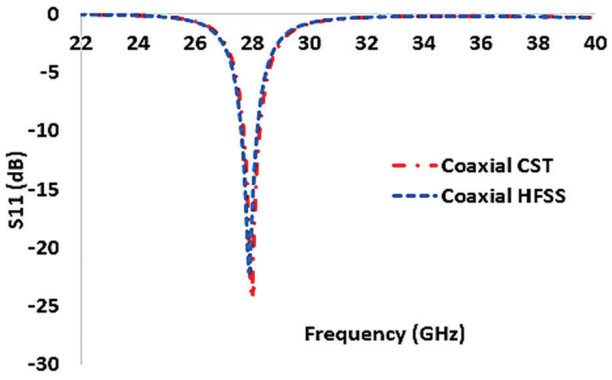

(a)

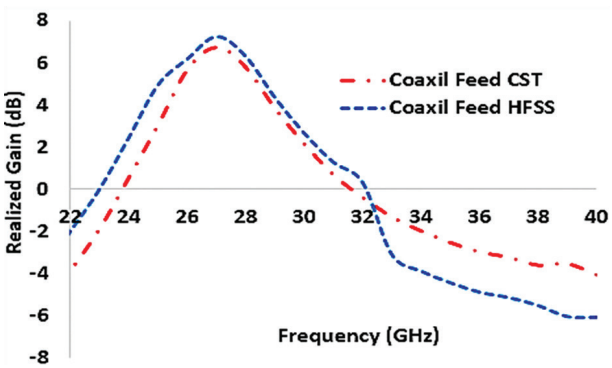

(b)

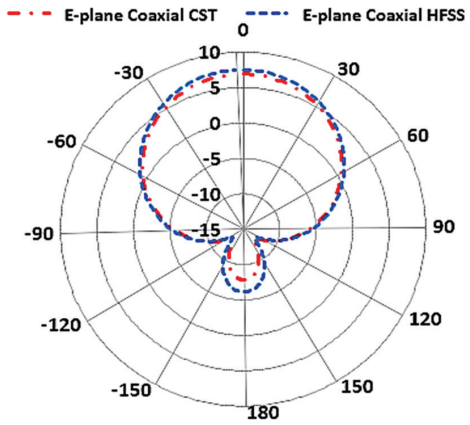

(c)

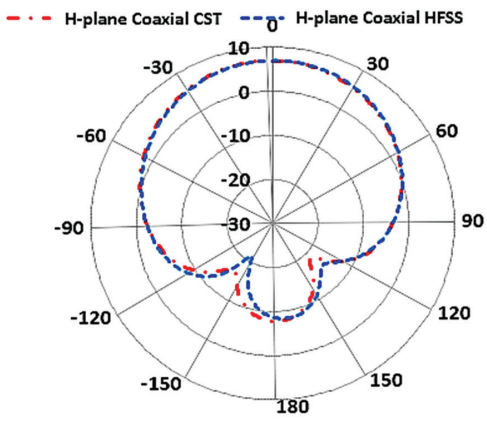

(d)

Fig. 3. Represents results of the (**a**) Reflection coefficient (S11), (**b**) Realized gain, (**c**) E-plane and (**d**) H-plane for RMPA with the coaxial probe feed

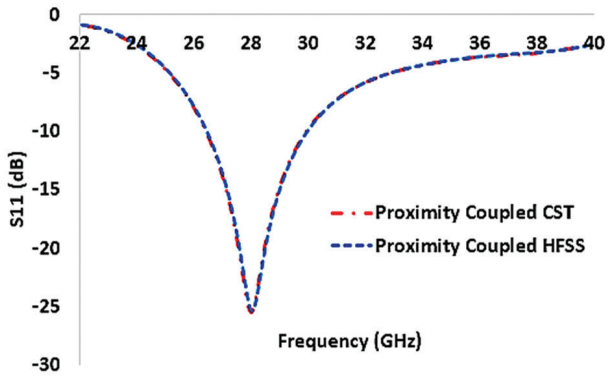

(a)

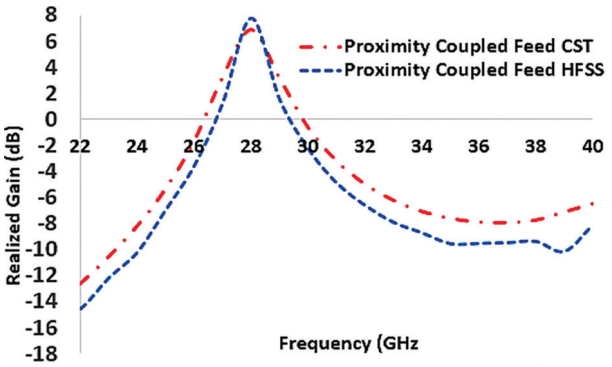

(b)

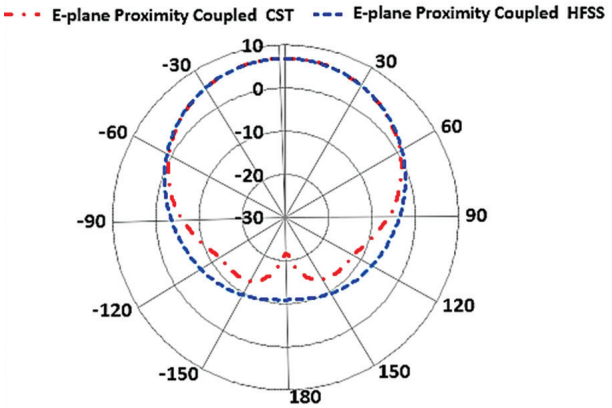

(c)

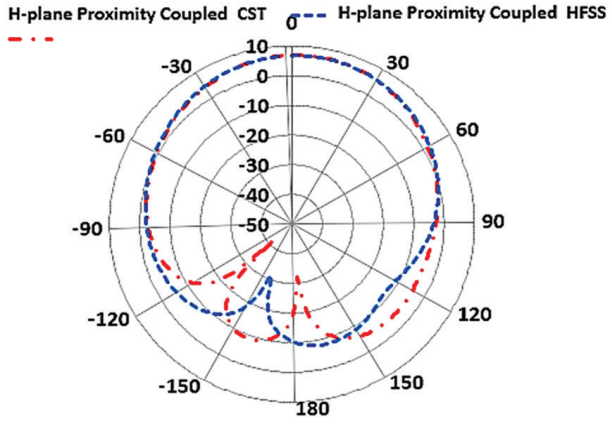

(d)

Fig. 4. displays results of the (**a**) Reflection coefficient (S11), (**b**) Realized gain, (**c**) E-plane and (**d**) H-plane for RMPA with the proximity coupled feed

Also, Fig. 4 (b) indicates that the peak gain value is 6.86 dB at fr = 28 GHz. Besides, extremely directive E- and H-planes radiation pattern with low side lobe level are observed with the proximity coupled fed as shown in Fig. 4 (c) and (d).

In addition, both CST and HFSS simulators are employed to compute the antenna directivity. The results of these computation for each considered feeding technique are shown in 3D view in Fig. 5. The HFSS simulator results reveal that the directivity values are (5.690, 6.860 and 7.980) dB for inset, coaxal and proximity-coupled feed, respectively for RMPA operating at (28) GHz. Additionally, the directivity values achieved for microstrip inset line, coaxal probe and proximity coupled feed with the implementation of CST simulator, are (5.515, 6.905 and 7.075) dB, respectively.

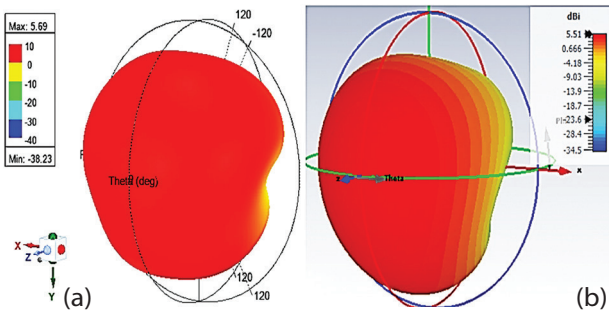

(a) (b)

(A)

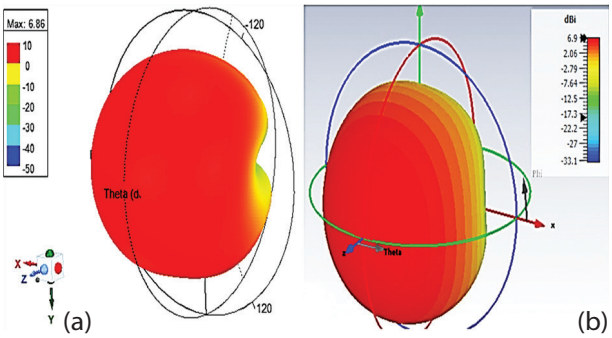

(a) (b)

(B)

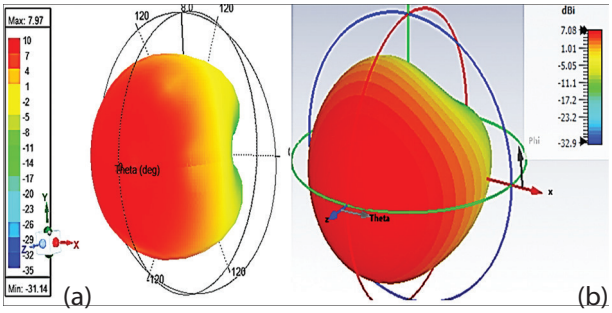

(a) (b)

(C)

Figs. 5. 3D view of RMPA directivity obtained by (**a**) HFSS and (**b**) CST for (**A**) microstrip inset fed, (**B**) coaxial probe fed and (**C**) proximity coupled fed.

The achieved values from both modeling techniques well agree with each other and the best values of antenna directivity are recorded with the proximity-cou-

pled feed technique, while it can be seen that directivity for both the inset and coaxial feeding methods are nearly equal [17].

On the other hand, the calculated bandwidth obtained with both simulation methods and for each aforementioned feeding techniques reveal that the proximity coupled feed technique has enlarged the bandwidth from 0.6 GHz to 3.60 GHz when S_{11} = -10 dB at f_r = 28 GHz as represented in Fig. 6. Besides, the maximum value of realized gain is equal to 6.86 dB, which is achieved with using proximity coupled technique as observed in Fig. 7.

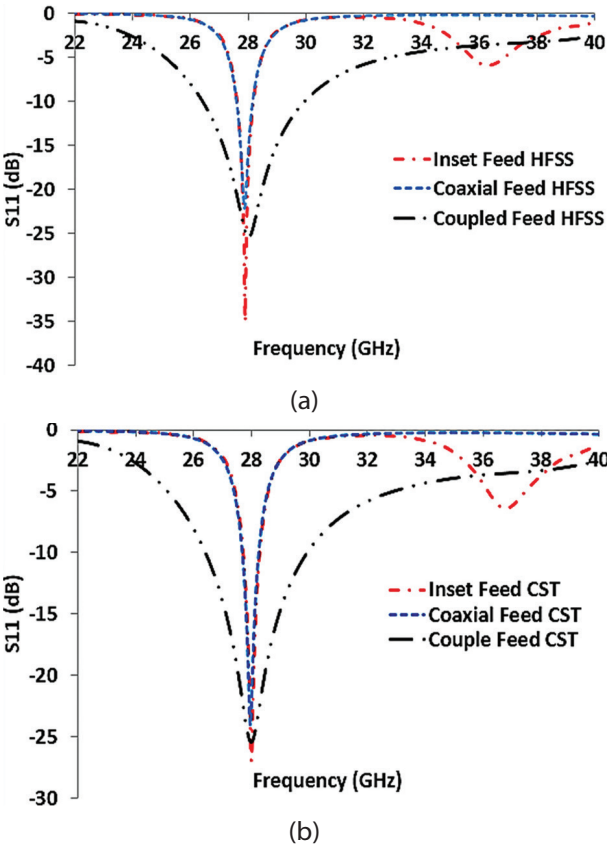

Figs. 6. The simulated antenna returns loss of the proposed RMPA with the presence of aforementioned feeding techniques with the use of (**a**) HFSS and (b) CST

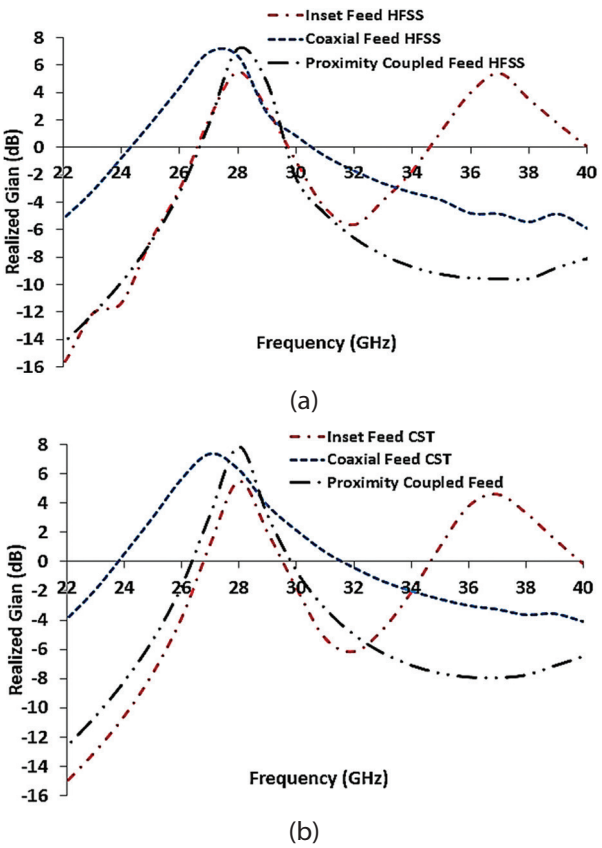

Figs. 7. The simulated antenna realized gain of the proposed RMPA with the presence of aforementioned feeding techniques with the use of (**a**) HFSS and (**b**) CST.

Finally, the overall calculated RMPA parameters obtained with both HFSS and CST simulation methods are summarized in Table 2 and compared with previous investigation by other researchers using different feeding methods. Table 2 exhibits the advantages of the proposed design, when the proximity coupled probe is employed, over the previously designed RMPA in the literature. It can be seen that our design is very competitive to the cited works, particularly in terms of the total size and overall radiation performances.

Table 2. Overall calculated RMPA parameters obtained with both HFSS and CST simulation methods

Simulation method	S11 (dB)	VSWR	Gain (dB)	BW(GHz)	fr(GHz)	Size mm3	Reference
Inset HFSS	-14.00	1.499	1.890	0.540	28.00	-	[20]
Inset HFSS	-40.08	1.020	4.060	-	27.50	324.958	[21]
Inset HFSS	-22.20	1.340	6.850	-	28.00	22.365	[22]
Inset HFSS	-24.50	1.127	6.430	0.900	27.65	23.400	[23]
Inset HFSS	-20.64	1.20	6.290	0.369	28.00	-	[24]
Inset HFSS	-20.00	1.222	8.020	1.300	28.00	22.702	[25]
Inset HFSS	-32.86	1.047	3.590	1.450	28.00	-	[26]
Inset HFSS	**-35.03**	**1.028**	**6.690**	**0.595**	**27.98**	**9.676**	**Present work**
Inset CST	-12.59	1.613	6.690	0.582	27.91	29.517	[27]
Inset CST	-20.53	1.020	6.210	0.400	27.98	119.07	[28]

Inset CST	-14.15	1.488	6.060	0.800	28.00	185.80	[29]
Inset CST	-36.17	1.310	6.710	0.462	27.98	19.124	[30]
Inset CST	-22.50	1.162	7.200	1.610	26.00	59.695	[31]
Inset CST	-28.68	1.076	5.820	0.452	28.00	-	[24]
Inset CST	-67.37	1.001	7.750	0.660	28.20	-	[32]
Inset CST	-26.00	1.160	4.430	2.900	28.02	17.050	[33]
Inset CST	-38.34	1.024	8.200	3.464	28.08	244.619	[34]
Inset CST	-20.09	1.197	7.500	1.060	28.00	46.350	[35]
Inset CST	**-27.04**	**1.095**	**5.515**	**0.573**	**28.00**	**9.676**	**Present work**
Coaxial HFSS	-27.00	1.094	7.800	1.700	27.23	23.400	[23]
Coaxial HFSS	-21.95	1.170	7.110	0.259	28.00	-	[24]
Coaxial HFSS	-20.00	1.222	6.510	2.200	28.10	22.702	[25]
Coaxial HFSS	-36.60	1.030	4.170	0.800	28.00	-	[26]
Coaxial HFSS	**-24.72**	**1.123**	**6.860**	**0.557**	**27.94**	**9.676**	**Present work**
Coaxial CST	-24.00	1.135	7.500	2.610	26.00	59.695	[31]
Coaxial CST	-43.23	1.014	7.690	0.792	28.30	-	[32]
Coaxial CST	-21.26	1.180	6.050	0.356	28.00	-	[24]
Coaxial CST	**-24.02**	**1.134**	**6.904**	**0.589**	**27.98**	**9.676**	**Present work**
Proximity HFSS	**-25.44**	**1.112**	**7.075**	**3.616**	**28.00**	**19.350**	**Present work**
Proximity CST	**-28.39**	**1.113**	**7.980**	**3.586**	**27.46**	**19.350**	**Present work**

4. CONCLUSIONS

In this work, a new configuration of RMPA operating at 28 GHz has been proposed using three different feeding techniques: the microstrip inset, the coaxial probe, and the proximity coupled. The characteristics of the simulated RMPA have been determined using the HFSS and CST simulators. Although the proximity coupled feed is some complex in terms of manufacturing, but generally gives higher radiation performance compared to the other considered feeding techniques. Since, the simulated results of the proximity coupled fed reveal that the RMPA can provide a gain and bandwidth of the order of (6.86 dB and 3.60 GHz), respectively, with no side and back lobes compared to the other considered feeding techniques. Besides, the proposed design has a very small size and competitive gain and bandwidth when compared to the other works cited here. In addition, it should be observed that the presented RMSAs are acceptable for use in 5G wireless communication systems.

5. REFERENCES

[1] B. A. Rahman, S. O. Hasan, "Simulation Design of Low-Profile Equilateral Triangle Microstrip Patch Antenna Operating at 28 GHz", International Journal on Communications Antenna and Propagation, Vol. 12, 2022, pp. 74-82.

[2] D. H. Patel, G. D. Makwana, "A Comprehensive Review on Multi-band Microstrip Patch Antenna Comprising 5G Wireless Communication", International Journal of Computing and Digital System, Vol. 11, 2022, pp. 942-953.

[3] A. Bansal, R. Gupta, "A review on microstrip patch antenna and feeding techniques", International Journal of Information Technology, Vol. 12, 2020, pp. 149-154.

[4] A. Bhattacharyya, J. Pal, K. Patra, B. Gupta, "Bandwidth-enhanced miniaturized patch antenna operating at higher order dual-mode resonance using modal analysis", IEEE Antennas and Wireless Propagation Letters, Vol. 20, 2020, pp. 274-278.

[5] J. Wen, D. Xie, L. Zhu, "Bandwidth-Enhanced High-Gain Microstrip Patch Antenna Under TM Dual-Mode Resonances", IEEE Antennas and Wireless Propagation Letters, Vol. 18, 2019, pp. 1976-1980.

[6] M. S. M. Mollaei, E. Zanganeh, M. F. Farahani, "Enhancement of patch antenna gain using cylindrical shell-shaped superstrate", IEEE Antennas and Wireless Propagation Letters, Vol. 16, 2017, pp. 2570-2573.

[7] A. Rivera-Albino, C. A. Balanis, "Gain enhancement in microstrip patch antennas using hybrid substrates", IEEE Antennas and Wireless Propagation Letters, Vol. 12, 2013, pp. 476-479.

[8] Y. Liu, Z. Yue, Y. Jia, Y. Xu, Q. Xue, "Dual-band dual-circularly polarized antenna array with printed

ridge gap waveguide", IEEE Transactions on Antennas and Propagation, Vol. 69, 2021, pp. 5118-5123.

[9] C. Liu, Y. Li, T. Liu, Y. Han, J. Wang, S. Qu, "Polarization reconfigurable and beam-switchable array antenna using switchable feed network", IEEE Access, Vol. 10, 2022, pp. 29032-29039.

[10] A. Ioffe, M. Thiel, A. Dreher, "Analysis of microstrip patch antennas on arbitrarily shaped multilayers", IEEE Transactions on Antennas and Propagation, Vol. 51, 2003, pp. 1929-1935.

[11] F. Peressutti, B. Poussot, L. Rousseau, C. Viana, J.-M. Laheurte, J.-L. Polleux, "Optically-Fed 5GHz Patch Antennas Excited by Vertical-Cavity Surface-Emitting Lasers", Journal of Lightwave Technology, Vol. 39, 2021, pp. 6768-6773.

[12] Q. Luo, S. Gao, M. Sobhy, J. T. S. Sumantyo, J. Li, G. Wei, J. Xu, C. Wu, "Dual circularly polarized equilateral triangular patch array", IEEE Transactions on Antennas and Propagation, Vol. 64, 2016, pp. 2255-2262.

[13] S.-L. Yang, K.-M. Luk, "Design of a wide-band L-probe patch antenna for pattern reconfiguration or diversity applications", IEEE Transactions on Antennas and Propagation, Vol. 54, 2006, pp. 433-438.

[14] J.-F. Tsai, J.-S. Row, "Reconfigurable square-ring microstrip antenna, IEEE Transactions on Antennas and Propagation", Vol. 61, 2013, pp. 2857-2860.

[15] C. Deng, Y. Li, Z. Zhang, Z. Feng, "A wideband high-isolated dual-polarized patch antenna using two different balun feedings", IEEE Antennas and Wireless Propagation Letters, Vol. 13, 2014, pp. 1617-1619.

[16] S. K. Ezzulddin, S. O. Hasan, M. M. Ameen, "Microstrip patch antenna design, simulation and fabrication for 5G applications", Simulation Modelling Practice and Theory, Vol. 116, 2022, p. 102497.

[17] P. Kuravatti, "Comparison of different parameters of the edge feed and the inset feed patch antenna", International Journal of Applied Engineering Research, Vol. 13, 2018, pp. 11285-11288.

[18] Y. Huang, "Antennas: from theory to practice", John Wiley & Sons, 2021.

[19] C. A. Balanis, "Antenna Theory Analysis and Design", 4th Edition, John Wiley & Sons, 2016.

[20] Y. S. Khraisat, "Increasing microstrip patch antenna bandwidth by inserting ground slots", Journal of Electromagnetic Analysis and Applications, Vol. 10, 2018, pp. 1-11.

[21] K. Neha, S. Sunil, "A 28-GHz U-slot microstrip patch antenna for 5G applications", International Journal of Engineering Development and Research, Vol. 6, 2018, pp. 363-368.

[22] A. Sivabalan, S. Pavithra, R. Selvarani, K. Vinitha, "Design of microstrip patch antenna for 5G", International Journal of Control and Automation, Vol. 13, 2021, pp. 546-552.

[23] I. Gharbi, R. Barrak, M. Menif, H. Ragad, "Design of patch array antennas for future 5G applications", Proceedings of the 18th International Conference on Sciences and Techniques of Automatic Control and Computer Engineering, Monastir, Tunisia, 21-23 December 2017, pp. 674-678.

[24] B. A. Rahman, S. O. Hasan, "Radiation Performance of Different Triangular Microstrip Patch Antenna Configuration Shapes Operating at 28 GHz", Zanco Journal of Pure and Applied Sciences, Vol. 34, 2022, pp. 45-55.

[25] P. Yugandhar, P. M. Rao, "Design And Performance Analysis of Single Patch Antenna, Slotted Patch Antenna And 1x2 Antenna Array For 5G Applications", International Research Journal of Modernization in Engineering Technology and Science, Vol. 4, 2022, pp. 1272-1279.

[26] K. Lalitha, K. L. Bhavani, P. Siddaiah, "Performance Analysis of Hybrid Microstrip Patch Antenna at Ka-Band", International Journal of Advanced Research in Computer and Communication Engineering, Vol. 5, 2016, pp. 161-165.

[27] D. Mungur, S. Duraikannan, "Microstrip patch antenna at 28 GHz for 5G applications", Journal of Science Technology Engineering and Management-Advanced Research & Innovation, Vol. 1, 2018, pp. 20-22.

[28] S. Johari, M. A. Jalil, S. I. Ibrahim, M. N. Mohammad, N. Hassan, "28 GHz microstrip patch antennas for future 5G", Journal of Engineering and Science Research, Vol. 2, 2018.

[29] M. Kavitha, T. D. Kumar, A. Gayathri, V. Koushick, "28GHz printed antenna for 5G communication

with improved gain using array", International Journal of Scientific and Technology Research, Vol. 9, 2020, pp. 5127-5133.

[30] M. Darsono, A. Wijaya, "Design and simulation of a rectangular patch microstrip antenna for the frequency of 28 GHz in 5G technology", Journal of Physics: Conference Series, Vol. 1469, 2020, pp. 1-7.

[31] H. Ai, C. Wu, S. Zhou, "Design and simulation of rectangular microstrip patch antenna with 5Gmm-wave coaxial line back-feed and microstrip line side-feeds", Proceedings of the 5th International Conference on Information Science, Computer Technology and Transportation, Shenyang, China, 13-15 November 2020, pp. 179-182.

[32] S. Kumar, A. Kumar, "Design of circular patch antennas for 5G applications", Proceedings of the 2nd International Conference on Innovations in Electronics, Signal Processing and Communication, Shillong, India, 1-2 March 2019, pp. 287-289.

[33] A. A. Ibrahim, H. Zahra, O. M. Dardeer, N. Hussain, S. M. Abbas, M. A. Abdelghany, "Slotted Antenna Array with Enhanced Radiation Characteristics for 5G 28 GHz Communications", Electronics, Vol. 11, 2022, pp. 1-13.

[34] M. S. Rana, M. M. R. Smieee, "Design and analysis of microstrip patch antenna for 5G wireless communication systems", Bulletin of Electrical Engineering and Informatics, Vol. 11, 2022, pp. 3329-3337.

[35] S.-E. Didi, I. Halkhams, M. Fattah, Y. Balboul, S. Mazer, M. El Bekkali, "Design of a microstrip antenna patch with a rectangular slot for 5G applications operating at 28 GHz", TELKOMNIKA (Telecommunication Computing Electronics and Control), Vol. 20, 2022, pp. 527-536.

AI-Based Q-Learning Approach for Performance Optimization in MIMO-NOMA Wireless Communication Systems

Original Scientific Paper

Ammar A. Majeed
Middle Technical University, Kut Technical Institute
Baghdad, Iraq
Ammar.alaa@mtu.edu.iq

Douaa Ali Saed
University of Wasit, Electrical engineering department
Wasit, Iraq
dsaed@uowasit.edu.iq

Ismail Hburi
University of Wasit, Electrical engineering department
Wasit, Iraq
isharhan@uowasit.edu.iq

Abstract *– In this paper, we investigate the performance enhancement of Multiple Input, Multiple Output, and Non-Orthogonal Multiple Access (MIMO-NOMA) wireless communication systems using an Artificial Intelligence (AI) based Q-Learning reinforcement learning approach. The primary challenge addressed is the optimization of power allocation in a MIMO-NOMA system, a complex task given the non-convex nature of the problem. Our proposed Q-Learning approach adaptively adjusts power allocation strategy for proximal and distant users, optimizing the trade-off between various conflicting metrics and significantly improving the system's performance. Compared to traditional power allocation strategies, our approach showed superior performance across three principal parameters: spectral efficiency, achievable sum rate, and energy efficiency. Specifically, our methodology achieved approximately a 140% increase in the achievable sum rate and about 93% improvement in energy efficiency at a transmitted power of 20 dB while also enhancing spectral efficiency by approximately 88.6% at 30 dB transmitted Power. These results underscore the potential of reinforcement learning techniques, particularly Q-Learning, as practical solutions for complex optimization problems in wireless communication systems. Future research may investigate the inclusion of enhanced channel simulations and network limitations into the machine learning framework to assess the feasibility and resilience of such intelligent approaches.*

Keywords*: MIMO-NOMA Networks, Power Allocation Strategies, Optimization of Wireless Communication Systems, Reinforcement Learning Techniques, Q-Learning Approach*

1. INTRODUCTION

The exponential proliferation of wireless devices, accompanied by a commensurate increase in data generation, has imposed unparalleled demands on contemporary wireless networks. This evolving landscape mandates a fundamental paradigmatic shift in the design and optimization strategies for forthcoming wireless communication systems, emphasizing maximizing Spectral efficiency (SE) and Energy Efficiency (EE) [1, 2]. NOMA has emerged as a seminal technology to address these burgeoning challenges. Unlike conventional Orthogonal Multiple Access (OMA) schemes, NOMA enables the concurrent utilization of identical time-frequency resources by multiple users, thereby substantially augmenting both SE and system connectivity [3, 4].

MIMO-NOMA systems, which integrate MIMO technology into NOMA, further enhance system capacity and efficiencies, providing an advanced solution for next-gen wireless networks [5]. Utilizing Spatial Data Multiplexing and Signal Diversity techniques, MIMO-NOMA systems are capable of realizing considerable improvements in data rate and EE. Nevertheless, the augmented complexity of MIMO-NOMA, particularly concerning power allocation and user grouping strategies, introduces formidable challenges that must be meticulously addressed. [6, 7]. NOMA offers key advantages like enhanced connectiv-

ity, reduced latency, and improved QoS, contributing to a more efficient wireless network [8, 9]. A salient constraint in the field of wireless communications is the stipulation that the quantity of user entities must not surpass the count of Radio Frequency (RF) Chains. However, NOMA overcomes this drawback by allowing various users to utilize the equivalent frequency and time resource, which results in higher SE and improved quality of service [6]. Fig. 1 demonstrates the NOMA system scheme [10].

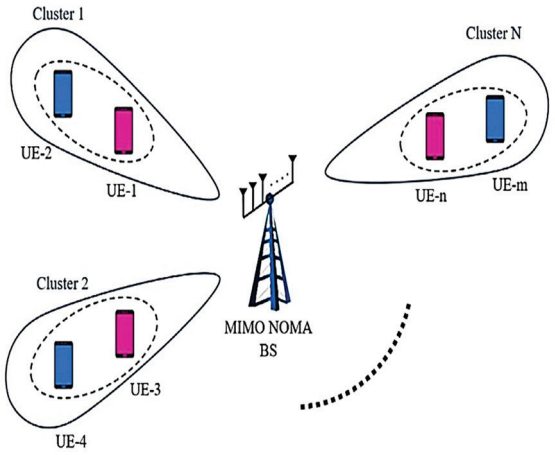

Fig. 1. MIMO-NOMA wireless system scheme [4]

Reinforcement Learning (RL) offers a promising avenue for addressing the complexities of optimizing MIMO-NOMA systems. RL enables an agent to learn optimal strategies through trial-and-error interactions with the environment, receiving feedback as rewards or punishments. Based on this feedback, the algorithm adapts its actions to maximize long-term rewards [11]. Q-learning has garnered considerable focus within the domain of RL algorithms owing to its straightforward implementation and robust performance in addressing intricate challenges. [12].

This study contributes significantly to the field of wireless communication systems, particularly in the optimization of MIMO-NOMA systems through these points:

1. We propose an affordable methodology, employing Q-Learning methodologies to refine power management strategies within the MIMO-NOMA wireless communication systems framework. By applying the Q-learning approach, Our goal is to identify the best power allocation policy to maximize the total data rate while ensuring sufficient levels of EE and SE.
2. We present a detailed system model that articulates the complexities of power allocation within the context of MIMO-NOMA, Which provides a solid foundation for understanding the intricacies of the problem and the motivation behind employing Q-learning as a solution.
3. We delve into the Q-learning approach particularities and demonstrate its application to the power allocation challenge in MIMO-NOMA configurations. Our research highlights the capacity of Q-learning to address complex optimization challenges in diverse network environments.
4. We validate our proposed approach through extensive simulations, providing illustrative results demonstrating significant improvements in the system's performance compared to traditional methods. For example, our methodology achieves an approximate 140% increase in the achievable sum rate compared to conventional NOMA with identical transmitted Power and traditional methods such as that proposed in [13].

The literature review highlights various studies on MIMO-NOMA using RL, such as Q-learning and other approaches, pinpoints areas of incomplete understanding, assesses methodological approaches, and situates our study in the broader field landscape.

This study [14] proposes a novel resource allocation (RA) scheme for massive systems of MIMO-NOMA, leveraging a deep Q-learning network (DQN) and a neural network, which utilizes backpropagation to optimize power management, user grouping, and beamforming. The authors address the significant challenge of downlink RA, aiming to enhance the system's SE while guaranteeing the constraint on the performance of the least efficient user. Their simulated tests indicate that the suggested approach can attain elevated SE for the system, closely mirroring the outcomes of comprehensive searches. This potentially impactful approach could lead to more efficient and reliable wireless communication networks, although the authors acknowledge that further real-world testing is necessary to validate these findings.

The study [15] introduces a deep learning methodology, SARSA λ, for optimizing uplink random access in NOMA-assisted URLLC networks. The algorithm is designed to mitigate decoding inaccuracies in dynamic communication setups and tackles issues related to user grouping, RA optimization, and instantaneous feedback mechanisms. The method reaches convergence within a span of 200 episodes and attenuates the extended average error rate to an order of 10-2. Compared to conventional OMA systems, NOMA-URLLC significantly outperforms error probability and mean error performance over temporal intervals, exhibiting a superiority margin of 70%. The application of Deep RL (DRL) yields superior outcomes compared to both classical and SARSA Q-Learning, manifesting in enhancements of 37% and 38% in average error execution, respectively.

This survey paper [16] explores the role of deep learning (DL) methods in overcoming the limitations of NOMA, a technology pivotal to 5G and beyond 5 G (B5G) development. Despite NOMA's potential for enhancing user connectivity and system efficiency, its practical deployment is constrained by an inflexible design scheme and disparate signal-processing strategies. However, DL-based NOMA can improve key per-

formance indicators such as bit-error rate, throughput, latency, and RA. This analysis underscores DL's transformative capacity to address complex communication challenges and the benefits of its integration with emerging technologies. Future research directions point towards refining DL algorithms for optimized performance, lower latency, and more efficient RA, sparking interest in academic and industrial circles.

Reference [17] the use of RL in managing resources within wireless communication networks, specifically in a single-cell MIMO-NOMA network. The researchers address the challenge of optimizing the total sum rate, a problem complicated by its non-convex nature. They propose an innovative solution that integrates joint beamforming and power allocation by the use of deep DRL. The proposed methodology entails partitioning users into two distinct clusters and formulating an algorithm designed to augment the cumulative data rate for one cluster, while concurrently preserving a minimum threshold rate for the alternate cluster. The authors employ DQN and Double DQN-based algorithms to address this optimization challenge. Empirical findings validate the efficacy of the proposed algorithmic framework, resulting in marked improvements in the cumulative data throughput and rapid stabilization to a steady-state equilibrium.

Authors in [12] suggest a new RA scheme for massive antenna MIMO-NOMA systems using a multi-agent deep Q-network (DQN) algorithm. This approach addresses the slow convergence and suboptimal optimization of traditional algorithms. The researchers create an integrated optimization framework for beamforming, power allocation, and user grouping. Various RL networks are used to allocate Power smartly and group users to improve the system's overall rate. The RA results are fed back into each DQN for iterative optimization. Simulations show that multi-agent DQN improves SE. The study focuses on optimizing both user grouping and power management in massive MIMO-NOMA systems, achieving a balance between power allocation and user clustering while maintaining good performance for weaker users.

In [18], the article explores the susceptibility of NOMA systems to intelligent interference-based attacks using a zero-sum game framework. The base station (BS) determines the transmission power across several antennas as the leader. Conversely, in the follower role, the jammer A Stackelberg equilibrium is attained within the context of the game, considering variables such as the impact of numerous antennas and the states of the radio channels. An RL-based power control strategy is introduced to enhance communication efficiency against intelligent jammers. The hotbooting technique and Dyna architecture are used to speed up the Q-learning-based power management, maximizing NOMA transmission efficiency. Simulations show significant increases in total sum rates of data and user utilities compared to the standard approach. Future work will extend this research to practical situations involving smart interference with multiple jamming policies.

This paper [19] introduces a unique solution for Random Access (RA) optimization in ultra-dense Machine Type Communications (MTC), a central use case for 5G and beyond. The method employs Q-Learning and NOMA, facilitating dynamic RA slot allocation to MTC devices and enhancing network throughput significantly compared to existing techniques. The proposed solution necessitates a minimal increase in complexity on the device end and limited feedback from the BS. Simulations show that a larger discount factor results in better performance, particularly in many-device scenarios, offering faster convergence and improved throughput. This method outperforms existing solutions, promising substantial gains in network performance.

The paper [20], introduces a deep Q-learning (DQL) framework to boost the efficiency of an internal NOMA of Visible Light Communication (NOMA-VLC) downlink network, a crucial component in future wireless communication networks. The focus is on joint power management and Light Emitting Diode (LED) transmission angle tuning, improving challenge, aiming to optimize the average sum rate and EE. Findings suggest that the recommended method substantially enhances the efficiency of NOMA-VLC systems, notably for increased user counts, requiring less computational complexity compared to the "Genetic Algorithm" (GA) and "Differential Evolution" (DE) techniques. Moreover, the combined optimization of power distribution and LED transmission angle gains more effectiveness with growing users, surpassing the traditional solely optimal power allocation method.

This paper [21] proposes a deep Q-learning-based RA approach for uplink NOMA in a cognitive radio network (CRN) to maximize long-term throughput. This work focuses on secondary users (SUs) with limited battery capacity, which can extend their operations using energy harvested from solar sources. The method combines NOMA and "Time Division Multiple Access" (TDMA) to reduce system complexity. As an agent, the Secondary BS (SBS) aims to optimally allocate transmission energy to single users in each time slot through interaction with the system environment. Simulation results indicate that this approach outperforms conventional schemes, enhancing the performance of energy harvesting-powered CRNs over extended operations. The proposed method offers a solution for systems with large state space and action space, presenting the SBS with an optimal power allocation policy learned from environmental dynamics.

Subsequent to this introduction, Section 2 expounds upon our proposed methodology, delineating the Q-Learning approach and its applicability in optimizing power management within a MIMO-NOMA framework. This segment rigorously articulates the problem formulation and its associated mathematical constructs. Section 3 depicts an exhaustive compilation of discussions and results, substantiating the efficacy of our intended scheme in elevating the attainable aggregate data rate, EE, and SE. Comparative analyses with conventional

power management mechanisms are introduced to underscore the merits of integrating Q-learning. In Section 4, we synthesize our conclusions and suggest avenues for prospective research that could further fortify AI techniques' contribution in optimizing wireless communication paradigms. Finally, Section 5 enumerates all the references cited in this manuscript.

2. METHODOLOGY

This section outlines the research methodology, which entails the utilization of the Q-Learning algorithm for power assignment within the scheme of a MIMO-NOMA system.

2.1. THE SYSTEM MODEL OF MIMO-NOMA

In the scrutinized downlink MIMO-NOMA schemes, a multi-antenna is installed at the BS to facilitate serve for multi-user equipment sharing the same frequency and temporal resources. The users are partitioned into two distinct categories: proximal and distant, based on their distance to the BS. For efficacious allocation of transmitted Power, the BS employs a power allocation schema that apportions the available Power among these two classifications of users. The signals the user terminals receive are afflicted by path loss and contaminated by "Additive White Gaussian Noise" (AWGN). Figure 2 represents the system model under discussion of the proposed MIMO-NOMA scheme.

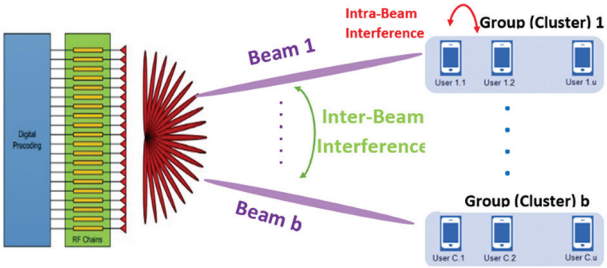

Fig. 2. The system model of the proposed work

2.2. PROBLEM FORMULATION

The intended paradigm seeks to fine-tune the power distribution among proximal and distant users within the wireless communication infrastructure of the MIMO-NOMA system. The overarching goal is to maximize the attainable aggregate data rate of the system. This optimization objective must be realized while concurrently preserving adequate levels of EE and SE.

Let's denote the assigned Power for the proximal and distant users as a_1 and a_2, such that $a_1 + a_2 = 1$. The proximal user also defines the channel gain as g_1 and the distant user as g_2. The Power of noise is represented as no. The achievable rate for the proximal user (R_{1n}) and the distant user (R_{2n}) are determined by the subsequent formulas of Shannon Capacity [3, 22]:

$$R_{1n} = log_2\left(\frac{1+p_t*a_1*g_1}{p_t*a_2*g_1+n_o}\right) \quad (1)$$

$$R_{2n} = log_2\left(\frac{1+p_t*a_2*g_2}{n_o}\right) \quad (2)$$

Where p_t is the total transmitted power from the BS, and log_2 represents the base-2 logarithm.

The total sum-rate (R_n) of the system can be calculated as the sum of R_{1n} and R_{2n} [23]:

$$R_n = R_{1n} + R_{2n} \quad (3)$$

The EE and SE of the system are defined as [13]:

$$EE = \frac{R_n}{p_t+p_c} \quad (4)$$

$$SE = \frac{R_n}{BW} \quad (5)$$

where the circuit power is denoted by P_c is, and the bandwidth (BW) is represented by BW.

The maximization challenge is thus defined as:

Maximize: Optimize the function involving variables a_1, a_2 given a fixed transmission power pt while adhering to constraints C_1, C_2.This can be formally expressed as [23]:

$$Maximize \quad R_n = log_2\left(\frac{1+p_t*a_1*g_1}{p_t*a_2*g_1+n_o}\right) + log_2\left(\frac{1+p_t*a_2*g_2}{n_o}\right) \; subjected\ to\ C_1, C_2 \quad (6)$$

Where C_1 Indicates that the aggregate of the transmitted Power across all user entities must equate to one. $a_1 + a_2$ =1. C_2 guarantees that the allocated power value of any user in the system must be a positive value.

The issue delineated in Eq. (6) constitutes a non-convex optimization quandary, particularly when the system encompasses more than two user entities. Under such circumstances, the problem escalates in complexity and becomes intractable through conventional optimization techniques. To address this challenge, the present study advocates the employment of the Q-Learning algorithm, a model-free RL methodology, as a viable solution strategy.

2.3. Q-LEARNING ALGORITHM

The Q-Learning algorithm serves as a model-free RL mechanism devised to address the maximization mentioned above challenge. The fundamental premise of the Q-Learning paradigm is to cultivate a policy that directs an agent in choosing apt actions contingent upon particular conditions or scenarios. The Q-learning methodology incorporates a Q-table, a data structure that retains the projected rewards associated with executing specific actions in defined states. The entries within the Q-table undergo iterative modification guided by a predetermined update equation [24]:

$$Q\,[s,a] = Q\,[s,a] + \alpha * (r + y * max\,Q\,[\dot{s},\dot{a}] - Q\,[s,a]) \quad (7)$$

Where,

- Q[s, a] designates the quantified Q-factor corresponding to a specific state-action pair (s, a) encompassing the aggregated reward accrued

through the execution of action (a) within the context of state (s).

- The learning coefficient, symbolized as α, stipulates the extent to which newly assimilated data supersedes extant information throughout the learning trajectory.
- The instant reward, annotated as r, constitutes the value realized subsequent to the state transition from (s) to (s') facilitated by the enactment of action (a).
- The discount coefficient, denoted by y, delineates the relative importance or weighting conferred upon prospective rewards within the framework of the RL procedure.
- The expression "$max\ Q[s', a']$" ignifies the maximal projected subsequent reward attainable upon transition to the subsequent state (s'), given the consideration of all plausible actions (a'). This corresponds to the peak Q-value amongst the set of feasible actions in the ensuing state.

Our Q-Learning approach in MIMO-NOMA systems is based on varying power allocation coefficients, path loss exponents, and critical system performance determinants. The reward structure is centered on the achievable sum rate, incentivizing the algorithm to optimize performance. The Q-Learning framework, a model-free RL technique, learns by interacting with the MIMO-NOMA system environment and updating the Q-table based on the received rewards. This process progressively guides future action selection, culminating in maximizing cumulative reward.

2.4. PERFORMANCE METRICS

The Q-learning performance is evaluated using three main measurements: achievable data rate, EE, and SE. These metrics help quantify how effectively the algorithm improves the system's performance.

Achievable Sum Rate: This metric denotes the total data rate the MIMO-NOMA scheme can uphold, computed as the sum of individual rates for proximal and distant users as per Eq. (3). The main goal is to maximize this sum rate.

Energy Efficiency (EE): This metric evaluates the system's effectiveness in utilizing energy for data transmission. It is calculated as the ratio of the achievable sum rate to the total power expenditure, encompassing both transmit Power and circuit power, as specified in Equation (4). An elevated EE value indicates the system's capability to sustain a greater data rate while maintaining identical power consumption.

Spectral Efficiency (SE): This metric gauges the system's adeptness in capitalizing on the available frequency spectrum for data transmission. Specifically, it evaluates the system's ability to use the allocated BW for information conveyance judiciously. It is mathematically determined as the ratio of the attainable aggregate data rate to the BW, in accordance with Equation (5). A superior SE index signifies the system's proficiency in supporting an elevated data rate while operating within identical BW constraints.

These performance indicators are computed for each conventional MIMO-NOMA system and the intended MIMO-NOMA framework incorporating the Q-Learning methodology. The enhancement observed in these measurements substantiates the efficacy of the advanced Q-Learning-driven power allocation schema. Algorithm 1, delineated below, furnishes a structured procedure for implementing Q-Learning to optimize power allocation and the path loss exponent within the confines of a MIMO-NOMA system. By systematically selecting actions that elevate the Q-value across multiple episodes, the algorithm is poised to identify a policy that could potentially augment the system's performance in the domains of achievable data rates, EE, and SE.

Algorithm 1: Q-Learning Optimization for MIMO-NOMA System

1. Initialization:

- Set the simulation parameters, including distances d_1, d_2, number of users N transmission power p_t, Bandwidth BW, noise power n_o, and circuit power p_c.
- Initialize the Q-learning parameters: learning rate α, discount factor γ, exploration rate ϵ, and number of episodes for Q-learning $n_{episodes}$.
- Define the action space as the product of possible values for the power allocation coefficient a_1 and the path loss exponent η.
- Initialize the Q-table with zero values.

2. For each episode in $n_{episodes}$:

- Initialize the cumulative reward to zero.
- For each user in N
  - Select an action using the epsilon-greedy policy.
  - Extract the power allocation coefficient a_1 and the path loss exponent η from the selected action.
  - Compute the channel gains h_1, h_2 for each user.
  - Calculate the square of the absolute value of the channel gain g_1, g_2.
  - Calculate the achievable sum rate R_1, R_2 for each user and store the mean of the rates.
  - Compute the reward as the mean of the achievable rates.
  - Update the Q-table using the Q-learning update rule.
  - Add the reward to the cumulative reward.
- Store the cumulative reward for the episode.

3. After all episodes:

- Select the optimal action as the one with the maximal Q-value.
- Extract the optimal power allocation coefficient $a_{1_{opt}}$. and the optimal path loss exponent $\eta_{opt.}$ from the optimal action.

- Using the optimal action, calculate the achievable rates, energy efficiency, SE, and signal-to-noise ratio.
- Plot the results and compare them with the system without Q-learning.

3. RESULTS AND DISCUSSION

The ensuing section will elucidate and critically evaluate the results garnered from our investigation, focusing specifically on the efficacy of the Q-Learning paradigm in improving the MIMO-NOMA system. In the context of our examination, we make reference to the system parameters encapsulated in Table 1, enumerating the values for diverse parameters. We postulate that the BS is endowed with flawless Channel State Information (CSI) for all constituents of the user network. This assumption signifies that the BS possesses precise awareness of the CSI for each user, thereby facilitating optimum decision-making and RA paradigms.

Table 1. The simulation system parameters of the proposed system

Parameter	Description	Value(s)
d_1	Separation metric among user '1' and BS	200
d_2	Separation metric among user '2' and BS	500
N	The system's user count	1000
P_t	Transmission power magnitudes expressed in dBm	[-30, -25, -20, -15, -10, -5, 0, 5, 10, 15, 20, 25, 30]
BW	Bandwidth	1 MHz
N_o	The power of Noise Magnitude Specified in dBm	-114 dBm
P_c	Circuit consumed Power	100 W
alpha	The learning rate of Q-learning	0.5
gamma	Discount coefficient of Q-learning	0.95
epsilon	The Exploration rate of Q-learning	0.1
episodes	Number of Q-learning episodes	1000
etas	Path loss exponent (eta) discretized values	[2.0, 3.0, 4.0, 5.0, 6.0]
a_{1s}	Power allocation coefficient (a1) discretized values	[0.5, 0.6, 0.7, 0.8, 0.9]
Original	The conventional NOMA standard from reference [13] is used as the benchmark for comparing our results.	-

Our Q-learning approach for MIMO-NOMA systems provides adaptability through learning from system experiences, simplifies complex optimization by learning a policy mapping states to actions, and ensures scalability by efficiently handling large action spaces.

3.1. ACHIEVABLE SUM RATE

The inaugural graph delineates the attainable aggregate data rates corresponding to each of the conventional and Q-Learning methodologies, plotted corresponding to transmission power. Examination of the graphical representation reveals a direct correlation between the sum rates and transmit Power levels for both methods. Notably, the Q-Learning algorithm consistently surpasses the performance metrics of the conventional approach across the entire spectrum of transmission power magnitudes. This observation substantiates the efficacy of the Q-Learning paradigm in the realm of power assignment for sum-rate optimization. Figure 3 elucidates the achievable data rate corresponding to varying magnitudes of transmission power; the intended scheme manifests a convergent augmentation of 140% in comparison to conventional NOMA techniques when evaluated at identical transmitted power levels.

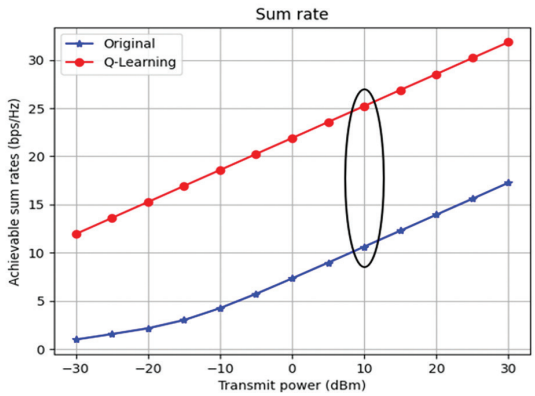

Fig. 3. The achievable data rate parameterized corresponding to the Power transmitted

3.2. SIGNAL-TO-NOISE RATIO

The following diagram illustrates the SNR for each conventional and Q-Learning scheme, plotted against transmit Power, assuming perfect CSI for all users. Both plots reveal a comparable direct correlation between transmitted Power and SNR, with no significant differences in SNR between the methods. Fig. 4 compares the SNR for the benchmark and proposed systems, confirming that SNR is predominantly contingent upon the transmission power and channel conditions, variables that remained invariant across both methodologies. This suggests that the Q-Learning approach can improve specific performance metrics without negatively affecting other metrics.

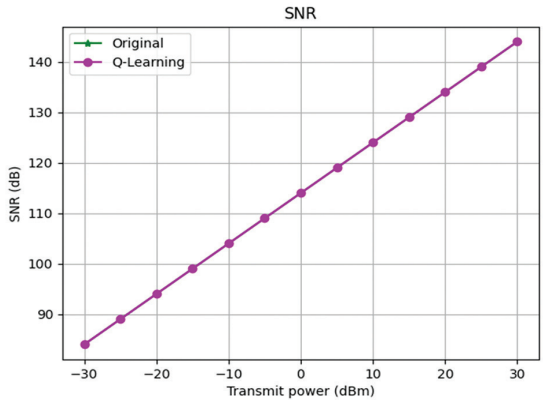

Fig. 4. SNR parameterized as a function of Power transmitted

3.3. ENERGY EFFICIENCY

The third chart compares the EE for the conventional and Q-Learning methods, with EE plotted against transmit Power in Fig. 5. The empirical findings reveal that the Q-Learning methodology uniformly eclipses the traditional approach in the realm of EE, irrespective of the magnitude of transmit Power. This suggests that the Q-Learning-based power management yields higher data rates while keeping power consumption constant. Notably, at 20 dB of transmission power, the intended Q-Learning method outstrips the conventional by an appreciable performance differential of approximately 93%. These outcomes underscore the advantages of integrating Q-Learning into power management, enabling more efficient power utilization while achieving superior data rates.

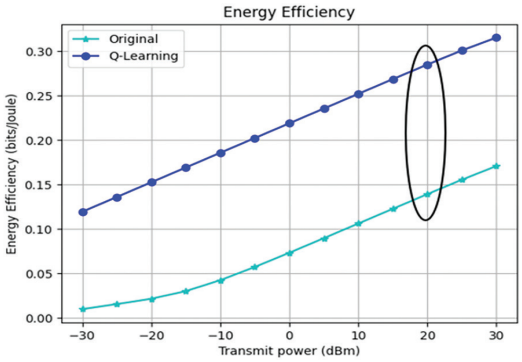

Fig. 5. The EE of the proposed scheme in contrast to Traditional NOMA

3.4. SPECTRAL EFFICIENCY

The next diagram delineates the SE metrics for both the benchmark and proposed systems employing the Q-Learning algorithm. Figure 6 portrays that the Q-Learning methodology consistently registers higher SE across all levels of transmitted Power. This attests to the efficacy of the Q-Learning algorithm in maximizing the data-rate within the identical BW allocation, highlighting its utility in improving MIMO-NOMA systems. Specifically, at a transmit power setting of 30 dB, the SE of the proposed Q-Learning framework surpasses that of the conventional NOMA approach by an appreciable margin of approximately 88.6%.

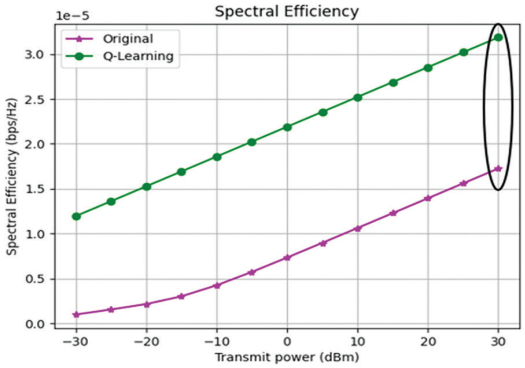

Fig. 6. The SE of the Intended Paradigm in Comparison with Conventional NOMA

3.5. IMPROVEMENT WITH Q-LEARNING

Two graphical representations, shown in Figs. 7 and 8, elucidate the advancements achieved via the Q-Learning algorithm. These figures empirically corroborate the pronounced improvements in both performance metrics, juxtaposing the Q-Learning methodology with the conventional approach across a diverse range of transmit power levels. The Q-Learning algorithm manifests the most salient augmentation in EE within the power range of 0 to 20 dB. Concurrently, the most notable enhancement in the sum rate is observed within the power spectrum of -5 to 30 dB.

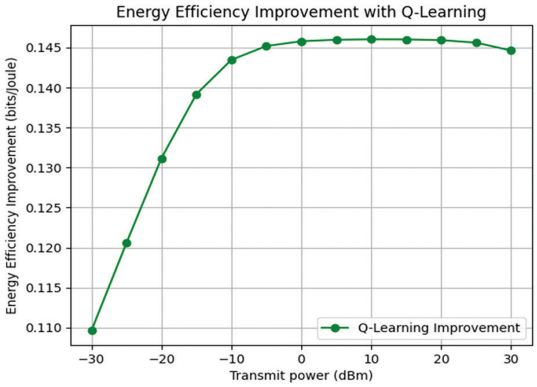

Fig. 7. The EE Enhancement Attributable to the Implementation of the Q-Learning Algorithm

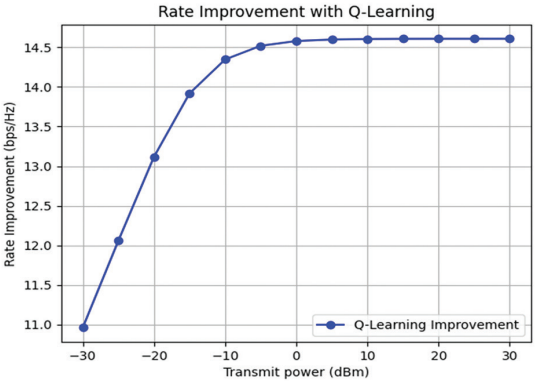

Fig. 8. The Increment in Achievable Sum Rate by Adopting the Q-Learning Algorithm

3.6. ACCUMULATED REWARD PER EPISODE

The final figure, denoted as Fig. 9, exhibits the accumulated reward accrued per episode within the context of the Q-Learning methodology. The figure reveals an ascending trajectory of rewards as a function of the episode count, substantiating that the algorithm is undergoing a learning process and progressively enhancing its operational performance. The incremental trend in the cumulative reward serves as empirical evidence of the Q-Learning algorithm's effectiveness in discerning an optimal power allocation strategy.

To sum up, the intended Q-Learning-based power management methodology engenders substantial enhancements in the operational execution of the MIMO-

NOMA paradigm, particularly in the domains of achievable data-rates, EE, and SE. Despite the constancy in SNR, this attribute does not undermine the merits of the Q-Learning Algorithm. Prospective study initiatives may contemplate the investigation of alternative RL algorithms or scrutinize diverse architectural variations of MIMO-NOMA systems.

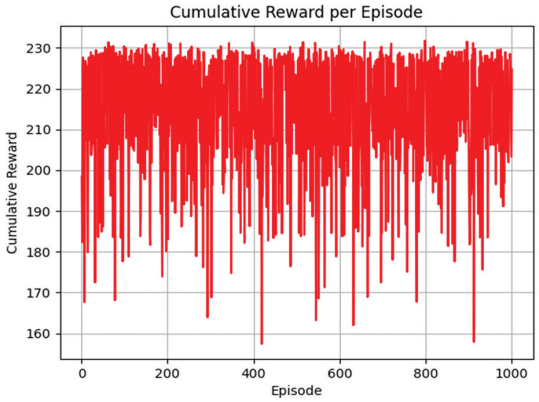

Fig. 9. The number of cumulative rewards per episode

4. CONCLUSION

In this research, we proposed and meticulously investigated an AI-based reinforcement Q-Learning approach for performance optimization in MIMO-NOMA wireless communication systems. Our Q-Learning approach in MIMO-NOMA systems is based on varying power allocation coefficients, path loss exponents, and key system performance determinants. The reward structure is centered on the achievable sum rate, incentivizing the algorithm to optimize performance. The Q-Learning framework, a model-free RL technique, learns by interacting with the MIMO-NOMA system environment and updating the Q-table based on the received rewards. This process progressively guides future action selection, culminating in maximizing cumulative reward.

Our results showed a substantial enhancement in the achievable sum rate, EE, and SE, compared to traditional MIMO-NOMA systems. We got 140%, 93%, and 88.6% higher performance for each previously mentioned performance metric, respectively, compared with traditional NOMA systems; this underscores the capacity of our Q-Learning approach to adaptively manage power between users, effectively optimizing the trade-off between these critical system performance metrics.

Based on the successes of this study, future work could expand in several potential directions. Investigating other RL methodologies beyond Q-Learning, including deep reinforcement learning or policy gradient techniques, could be compelling in improving the performance of MIMO-NOMA systems to a greater extent. Second, our approach could be applied to more complex communication scenarios, including massive MIMO systems or cooperative NOMA networks, offering insights into the scalability and adaptability of AI-based power allocation. Lastly, with the advent of 5G and beyond wireless networks, integrating our AI-based methodology with other emerging technologies like edge computing or the Internet of Things (IoT) could be examined to foster comprehensive and efficient solutions for future wireless communication systems. Furthermore, The implications of the research on practical applications and real-world deployments could be explored.

5. REFERENCES

[1] S. P. Yadav, "Performance Optimization of Universal Filtered Multicarrier Technique for Next Generation Communication Systems", International Journal of Electrical and Computer Engineering Systems, Vol. 14, No. 2, 2023, pp. 119-127.

[2] L. Dai, B. Wang, Z. Ding, Z. Wang, S. Chen, L. Hanzo, "A Survey of Non-Orthogonal Multiple Access for 5G", IEEE Communications Surveys & Tutorials, Vol. 20, No. 3, 2018, pp. 2294-2323.

[3] A. A. Majeed, I. Hburi, "Beamspace-MIMO-NOMA Enhanced mm-Wave Wireless Communications: Performance Optimization", Proceedings of the International Conference on Computer Science and Software Engineering, Dohuk, Iraq, 15-17 March 2022, pp. 144-150.

[4] A. F. Banob, F. W. Zaki, M. M. Ashour, "The effect of quantized ETF, grouping, and power allocation on non-orthogonal multiple accesses for wireless communication networks", International Journal of Electrical and Computer Engineering Systems, Vol. 13, No, 8, 2022, pp. 681-693.

[5] C. Ben Issaid, C. Anton-Haro, X. Mestre, M.-S. Alouini, "User Clustering for MIMO NOMA via Classifier Chains and Gradient-Boosting Decision Trees," IEEE Access, Vol. 8, 2020, pp. 211411-211421.

[6] A. A. Majeed, I. Hburi, "Energy-Efficient Optimization of mm-Wave Communication Using a Novel Approach of Beamspace MIMO-NOMA", Wasit Journal of Engineering Sciences, Vol. 10, No. 2, 2022, pp. 223-239.

[7] Z. Shi, H. Wang, Y. Fu, G. Yang, S. Ma, F. Hou, T. A. Tsiftsis, "Zero-Forcing Based Downlink Virtual MIMO-NOMA Communications in IoT Networks", IEEE Internet of Things Journal, Vol. 7, No. 4, 2020, pp. 2716-2737.

[8] U. Ghafoor, M. Ali, H. Z. Khan, A. M. Siddiqui, M. Naeem, "NOMA and future 5G & B5G wireless networks: A paradigm", Journal of Network and Computer Applications, Vol. 204, 2022.

[9] S. Mahyar, M. Dohler, S. J. Johnson, "Massive Non-Orthogonal Multiple Access for Cellular IoT: Potentials and Limitations", IEEE Communications Magazine, Vol. 55, No. 9, 2017, pp. 55-61.

[10] A. Akbar, S. Jangsher, F. A. Bhatti, "NOMA and 5G emerging technologies: A survey on issues and solution techniques", Computer Networks, Vol. 190, 2021.

[11] J. Clifton, E. Laber, "Q-Learning: Theory and Applications", Annual Review of Statistics and Its Application, Vol. 7, No. 1, 2020, pp. 279-301.

[12] C. Yanmei, W. Lin, L. Jiaqing, Z. Jun, Y Lin, Z, Guomei, "Joint Resource Allocation Scheme Based Multi-agent DQN for Massive MIMO-NOMA Systems", Proceedings of the 14th International Conference on Communication Software and Networks, Chongqing, China, 10-12 June 2022, pp. 51-55.

[13] I. Hburi, H. F. Khazaal, N. M. Mohson, T. Abood, "MISO-NOMA Enabled mm-Wave: Sustainable Energy Paradigm for Large Scale Antenna Systems", Proceedings of the International Conference on Advanced Computer Applications, Missan, Iraq, 25-26 July 2021, pp. 45-50.

[14] Y. Cao, G. Zhang, G. Li, J. Zhang, "A Deep Q-Network Based-Resource Allocation Scheme for Massive MIMO-NOMA", IEEE Communications Letters, Vol. 25, No. 5, 2021, pp. 1544-1548.

[15] W. Ahsan, W. Yi, Y. Liu, A. Nallanathan, "A Reliable Reinforcement Learning for Resource Allocation in Uplink NOMA-URLLC Networks", IEEE Transactions on Wireless Communications, Vol. 21, No. 8, 2022, pp. 5989-6002.

[16] S. A. H. Mohsan, Y. Li, A. V. Shvetsov, J. V. Aldás, S. M. Mostafa, A. Elfikky, "A Survey of Deep Learning Based NOMA: State of the Art, Key Aspects, Open Challenges and Future Trends", Sensors, Vol. 23, No. 6, 2023.

[17] T. Lu, H. Zhang, K. Long, "Joint Beamforming and Power Control for MIMO-NOMA with Deep Reinforcement Learning", Proceedings of the IEEE International Conference on Communications, Montreal, Canada, 14-23 June 2021, pp. 1-5.

[18] L. Xiao, Y. Li, C. Dai, H. Dai, H. V. Poor, "Reinforcement Learning-Based NOMA Power Allocation in the Presence of Smart Jamming", IEEE Transactions on Vehicular Technology, Vol. 67, No. 4, 2018, pp. 3377-3389.

[19] M. V. da Silva, R. D. Souza, H. Alves, T. Abrão, "A NOMA-Based Q-Learning Random Access Method for Machine Type Communications", IEEE Wireless Communications Letters, Vol. 9, No. 10, 2020, pp. 1720-1724.

[20] A. A. Hammadi, L. Bariah, S. Muhaidat, M. Al-Qutayri, P. C. Sofotasios, M. Debbah, "Deep Q-Learning-Based Resource Allocation in NOMA Visible Light Communications", IEEE Open Journal of the Communications Society, Vol. 3, 2022, pp. 2284-2297.

[21] H. T. Huong Giang, P. Duy Thanh, I. Koo, "Dynamic Power Allocation Scheme for NOMA Uplink in Cognitive Radio Networks Using Deep Q Learning", Proceedings of the International Conference on Information and Communication Technology Convergence, Jeju Island, Korea, 21-23 October 2020, pp. 137-142.

[22] C. L. Wang, Y. C. Wang, P. Xiao, "Power Allocation Based on SINR Balancing for NOMA Systems with Imperfect Channel Estimation", Proceedings of the International Conference on Signal Processing and Communication Systems, Surfers Paradise, Australia, 16-18 December 2019, pp. 1-6.

[23] D. Tse. P. Viswanath, " Fundamentals of Wireless Communication", Cambridge University Press, 2005, pp. 228-289.

[24] B. H. Abed-Alguni, D. J. Paul, S. K. Chalup, F. A. Henskens, "A comparison study of cooperative Q-learning algorithms for independent learners", International Journal of Artificial Intelligence, Vol. 14, No. 1, 2016, pp. 71-93.

Compensating Chromatic Dispersion and Phase Noise using Parallel AFB-MBPS For FBMC-OQAM Optical Communication System

Original Scientific Paper

Ahmed H. Abbas
Communication Engineering Department,
University of Technology- Iraq
coe.21.01@grad.uotechnology.edu.iq

Thamer M. Jamel
Communication Engineering Department,
University of Technology- Iraq
thamer.m.jamel@uotechnology.edu.iq

Abstract *– Filter Bank Multi-Carrier Offset-QAM (FBMC-OQAM) is one of the hottest topics in research for 5G multi-carrier methods because of its high efficiency in the spectrum, minimal leakage in the side lobes, zero cyclic prefix (CP), and multiphase filter design. Large-scale subcarrier configurations in optical fiber networks need the use of FBMC-OQAM. Chromatic dispersion is critical in optical fiber transmission because it causes different spectral waves (color beams) to travel at different rates. Laser phase noise, which arises when the phase of the laser output drifts with time, is a major barrier that lowers throughput in fiber-optic communication systems. This deterioration may be closely related among channels that share lasers in multichannel fiber-optic systems using methods like wavelength-division multiplexing with frequency combs or space-division multiplexing. In this research, we use parallel Analysis Filter Bank (AFB) equalizers in the receiver part of the FBMC OQAM Optical Communication system to compensate for chromatic dispersion (CD) and phase noise (PN). Following the equalization of CD compensation, the phase of the carriers in the received signal is tracked and compensated using Modified Blind Phase Search (MBPS). The CD and PN compensation techniques are simulated and analyzed numerically and graphically to determine their efficacy. To evaluate the FBMC's efficiency across various equalizers, 16-OQAM is taken into account. Bit Error Rate (BER), Optical Signal-to-Noise Ratio (OSNR), Q-Factor, and Mean Square Error (MSE) were the primary metrics we utilized to evaluate performance. Single-tap equalizer, multi-tap equalizer (N=3), ISDF equalizer with suggested Parallel Analysis Filter Banks (AFBs) (K=3), and MBPS were all set aside for comparison. When compared to other forms of Nonlinear compensation (NLC), the CD and PN tolerance attained by Parallel AFB equalization with MBPS is the greatest.*

Keywords*: Keywords- FBMC, OQAM, Optical fiber communication, chromatic dispersion (CD) compensation, multi carrier modulation, Phase Noise, Nonlinear Effects, Nonlinear Compensation (NLC)*

1. INTRODUCTION

For coherent fiber optical communication (FOC), FBMC-OQAM has emerged as the multi-carrier modulation (MCM) of choice because to its enormous spectral efficiency [1]. Out-of-band leakage is significantly reduced in FBMC-OQAM [2], making it more adaptive in its adjustment of wave dispersion. Reduced guard band interval and zero CP in FBMC improve the system's spectral efficiency even more than in traditional OFDM [3]. The cladding and core of a fiber optic transmission system often have a differing refractive index, which may impede or speed up communication depending on the wavelength of light being sent. This is because the colors of light behave differently as they travel through a fiber optic [4]. Using number of subcarriers in the FBMC OQAM transmission is the only solution to tolerate the CD flatten the channel coefficients up to the level of subcarriers. But increasing the subcarrier to transmit for a desired bandwidth increases the duration of symbol which induce the phase noise of fiber channel [5].

The spectrum of the laser's emitted light must be a delta function. However, phase shifts in the laser's output optical field make this impossible [6]. Due to the oscillations' origin in the laser's own spontaneous emission, a statistical correlation is impossible to establish. They provide a time-varying disturbance in the carrier phase, known as phase noise (PN). The chromatic dis-

persion (CD) and phase noise (PN) may be minimized at the shortest possible transmission distance by using a single-tap equalization technique. When the number of subcarriers in long-distance communications became large enough, it began to have an effect on the equalization used to tolerate CD. Therefore, even for long-haul communication, an improved and effective equalization approach is required to carry out the CD compensation [7]. Furthermore, the optimum spectrum efficiency in optical communication depends on multi tap and time domain-based equalizations. For optical systems based on FBMC-OQAM, this is a major area of attention for researchers. In this study, we provide a design for a parallel AFB and MBPS equalization for FBMC-OQAM optics, which may be used to compensate for CD and PN. Simulation of each approach with various settings is also used to study and evaluate the FBMC OQAM's efficiency. In order to verify the equalizers in an optical system, a sampling rate of 30 GHz is taken into account.

The forthcoming section of the paper is structured as follows: Review of literature is presented in section II for multiple equalizers which we taken for the analysis of CD and PN compensation in FBMC-OQAM. In section III FBMC OQAM in optical system model and section IV for proposed equalizer design as mathematical model. In section V we concentrate on the performance analysis. Conclusion of this paper is discussed in section VI.

2. CD AND PN COMPENSATION EQUALIZER TECHNIQUES

i. Iterative Soft Decision Feedback Equalization

Inter symbol interference (ISI) caused by CD may be mitigated using a single tap equalizer. Although some inter-carrier-interference (ICI) and inter-symbol interference (ISI) residuals are present in the received data. Iterative Soft Decision Feedback Equalizer (ISDFE) was presented to further enhance the system by [10]. The N-Tap frequency sampling equalization is used in this technique. Nonlinear phase noise in the optical FBMC-OQAM system's back propagation was also adjusted by ISDFE, as shown in Fig. 1.

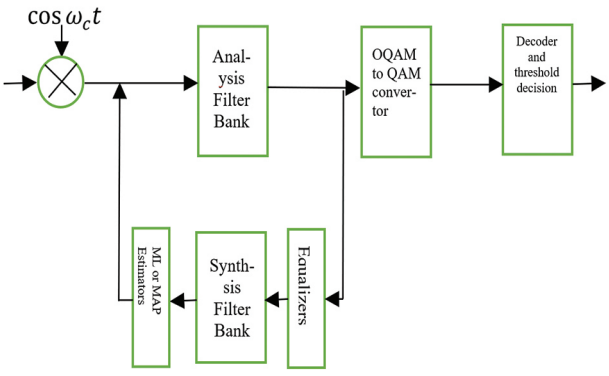

Fig. 1. ISDF equalizer

In the frequency domain, CD is a phase distortion, but in the time domain, NLP is a phase distortion.

The CD compensator (CDC) is used in the frequency domain to offset the effects of CD and NLP in the receiver.

$$H_{CD}(\omega) = \mathrm{e}^{-\left(\frac{jD}{2}\omega^2 L\right)+\delta} \tag{1}$$

where, D is second order dispersion known as group velocity dispersion (GVD) of fiber chromatic dispersion, L is fiber length, δ is phase shift and ω is angular frequency.

Repeatedly equalizing the CD by applying soft decision symbols (CDC output) and returning them to the SFB is how standard optical FBMC/OQAM achieves equalization of the CD. This is seen in Fig. 5. All leftover ISI is removed by passing to AFB several times during the operation, allowing the original signal to be reconstructed.

ii. Fourth-Order Nonlinearity

To eliminate the phase modulation in QPSK, the carrier phase may be approximated using a fourth-order nonlinearity, providing the estimate of the phase as follows:

$$\delta_{est}(n) = \left\{\frac{1}{2L+1}\sum_{q=-L}^{L} P(q)x_i^4(q+n)\right\} \tag{2}$$

where $P(q)$ is a weighting function that changes depending on how much laser phase noise is added to the additive white Gaussian noise [11]. For $P(q)$=1, Viterbi and Viterbi's estimator [12] is used as the estimator. A Wiener filter is used as a consequence of the weighting function to estimate the phase noise [13], which may perform almost as well as an ideal MAP estimator of the phase.

iii. Barycenter Algorithm

One particularly hardware-efficient phase estimator is the Barycenter algorithm [14] in which the order of the operations in Eq. (2) are reversed to give,

$$\delta_{est}(n) = \frac{1}{2L+1}\sum_{q=-L}^{L} P(q)\{x_i^4(q+n)\} \tag{3}$$

iv. Binary Phase Search (BPS)

Instead, the feedforward and parallelizable binary phase search (BPS) method may be utilized. The carrier phase is scanned from (0 to π/2 for square QAM), with the Euclidean distance between the rotating symbol and the final symbol being used to determine the mean square error for each trial phase. The iteration of the trial that yields the lowest MSE is chosen as the estimation iteration. In order to account for the ASE noise effect, the MSE is calculated by adding the distances between 2L symbols rotated by the same angle. As the decoding has already been completed during the testing step, the minimal mean squared error (MSE) index may be used to pick the decoded symbol through a toggle. Despite BPS's impressive tolerance for laser phase noise, the computational cost rises with the modulation order since more and more test phases are needed.

Because of the fourfold uncertainties of square QAM, the mentioned blind algorithms may result in cycle slip due to inaccurate phase estimation by a factor of π/2.

Nevertheless, differential encoding/decoding may be used to circumvent this issue, although at the cost of a little reduction in sensitivity. However, the higher computing cost is not always necessary to justify the gain [15].

v. Frequency Spreading (Fs) Equalization

In [8], author designed the novel equalization algorithm especially for multi carrier systems. The pictorial representation of this equalizer for FBMC OQAM is shown in Fig. 2.

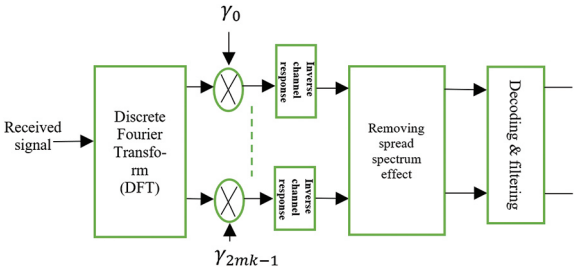

Fig. 2. Frequency Spreading equalizer

Input symbols propagated through the sub channel is spreader for number of sub carriers only if the corresponding samples of prototype filter (frequency domain) is non-zero. Spectral characteristics of the signal has been equalized after the received signal reach. Estimation of signal will not affect if the equalization done proper. Main advantage of this FS FBMC is no extra delay for computation.

vi. Overlap and Save Equalization

Researcher [9], proposed an overlap-save algorithm for equalization of single and multi-carrier systems. This algorithm provides the high efficiency in prediction of highest number of subcarriers from the finite impulse response (FIR). The procedure of the OS method is to prune the number of subcarriers for performing the convolution of FIR with each division of subcarriers in the frequency domain. In the initial stage, FFT is applied for each fragment, and it is convolved with frequency domain converted FIR signal. Once the convolution performed, the resultant will again convert back to time domain by IFFT and verified to $Kov/2$ overlapped symbols are included. Equalization is used to remove Inter Symbol Interference (ISI) from the received symbols, and Each symbol should be able to be recovered individually by the receiver [16]. Once equalized, the symbols are filtered by the FBMC prototype filter.

3. OPTICAL SYSTEM MODEL FOR THE FBMC-OQAM

Fig. 3 is a block diagram showing the FBMC OQAM Optical Communication system. The technology may be expanded to support dual polarization in addition to its single-polarization mode [17]. This method takes into account a subcarrier index of n, a QAM symbol time of T, and a subcarrier count of $2M$. The transmission of light across optical fibers may be affected by chromatic dispersion and AWGN channels [18].

FBMC transmitted signal with the rate of Fs=T/2M is generated as,

$$X(t) = \sum_{l=1}^{2N_s} \sum_{m=0}^{2M-1} q_{m,l} s_{m,l}(t) \tag{4}$$

where, $q_{m,l}$ is the OQAM modulated symbols, $s_{m,l}$ is the prototype filter response of FBMC synthesis filter and Ns is number of real multi carrier modulated symbols. Prototype filter is considered with the length of $L_p=2MO_k$. O_k is the overlapping factor of the filter with maximum energy and zero reconstruction error settings [19].

The chromatic dispersion frequency response of the channel propagation is defined as,

$$H(f) = e^{-j\frac{\pi D_c \lambda^2 F_l}{c} f^2} \tag{5}$$

where, F_l is Fiber length, D_c is Dispersion Coefficient, λ is laser wavelength, c is light speed and f is relative optical carrier frequency [20].

Distorted received signal after channel by impact of CD, Phase noise and additive noise is written as,

$$y(t) = \left(\int X(t) H(f) e^{j2\pi f t T_s} \, df + N(t) \right) e^{j\delta(t)} \tag{6}$$

Additive noise is representation of optical amplifier noise, thermal noise and short noise. Phase noise $\delta(t)$ is modelled as with linewidth of $\Delta\vartheta$ is,

$$\delta(t) = \delta(t-1) + \xi(t) \tag{7}$$

where, $\xi(t)$ is real Gaussian random value with zero mean and variance of $\sigma_\xi^2 = (\pi \Delta\vartheta T)/M$. The nonlinear phase noise shift effect is given as,

$$\delta(t) = \gamma L_{NF} \sum_{i=1}^{N_{span}} | X(t) + \sum_{j}^{O_k} N_A^j(t) |^2 \tag{8}$$

where, γ is the nonlinear coefficient and L_{NF} is nonlinear effective fiber length and is represented as,

$$L_{NF} = N_{span} \frac{(1 - e^{-\alpha L_{span}})}{\alpha} \tag{9}$$

α is fiber loss, L_{span} is fiber span length and N_{span} is number of 80km fiber spans. $N_A^j(t)$ is a noise of amplified spontaneous emission (ASE) and it is generated using AWGN with variance of σ^2 and zero mean. Hence the received signal after FBMC demodulation is given by,

$$Y_{m,l} = H_m \left(X_{m,l} + j\, r_{m,l} \right) e^{j\delta_l} + n_{m,l} \tag{10}$$

where, $r_{m,l}$ is the intrinsic interference of nearby symbols and $n_{m,l}$ is filtered additive noise. So the equalized symbol is formatted as,

$$\overline{X_{m,l}} = \sum_{l=0}^{N_{taps}} Y_{m,l} \, W_l \tag{11}$$

where, W_l is the equalization coefficients of the symbol using the proposed parallel analysis filter bank (AFB) equalization combined with Modified Blind Phase Search (MBPS) algorithm which detailed in section IV.

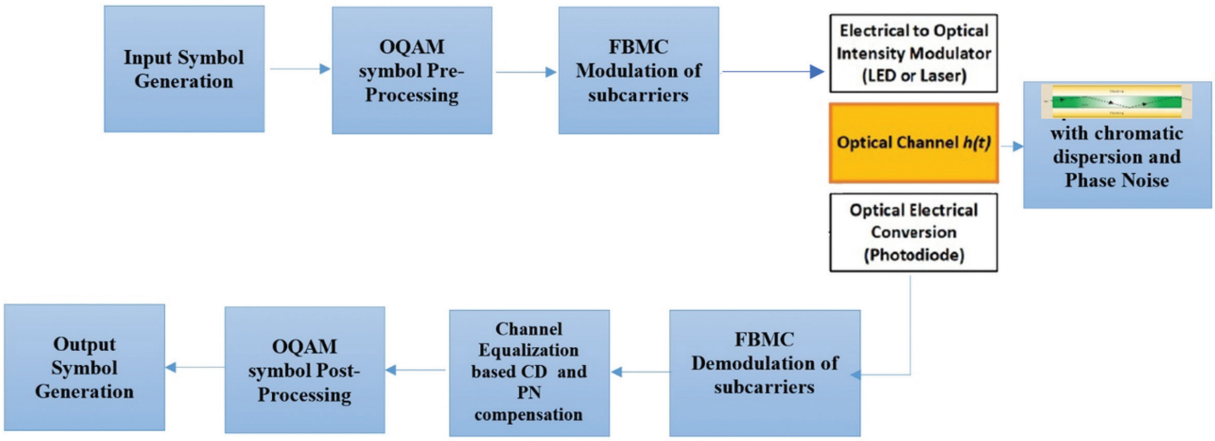

Fig. 3. Block Diagram of FBMC-OQAM Optical System

4. M-BPS WITH PARALLEL AFB FOR PHASE NOISE AND CHROMATIC DIFFUSION

Following the time-domain by using inverse fast Fourier transform process of frame synchronization, the received signal is sent on to the AFB block, where it will undergo frequency-domain processing. Similar to the approach used in [23, 24], a finite impulse response (FIR) filter is applied independently to each subcarrier to achieve CD correction. The core concept of the filter design is based on the frequency sampling method, which is extensively discussed in [25]. By manipulating the equalizer's coefficients, one may have the equalizer's frequency response "pass through" certain locations in the targeted subchannel. It is possible to calculate the equalizer's frequency response at certain frequencies using the zero-forcing criteria.

The configuration of parameters is listed in Table I. To show the exact performance of CD and PN compensation via proposed equalizers, For Each equalization some configurations are included as mentioned in Table 1. MSE and BER of received signal is calculated and compared for each subcarrier which taken as in Table 2, then we show the result in section v.

Table 1. Equalizer Parameters Configuration

Equalizer Type	Parameters and Values	
Multi Tap Equalizer	N_{taps}	3
ISDF Equalizer	N_{iter}	5
Parallel Equalization	K	3

Table 2. Constants Used in Simulations Configuration

Parameter	Value
Optical Fiber Length	1000 km
Dispersion Coefficient	17 ps/nm/km
Phase Noise Linewidth	200 KHz
Nonlinear coefficient	1.317 (1/W.km)
Fiber Type	SSMF
Core Effective Area	80μm²
Nonlinear Refractive Index	2.6×10^{-20} m²/W
Carrier Wavelength	1550 nm
Reference Bandwidth	12.5 GHz
Local Oscillator	Laser Source
Number of Subcarriers	128
FBMC overlapping factor	4
Modulation Order	16

The research suggests several different approaches to PN tracking [26-31]. Blind feedforward PN compensation gets our attention since it does not need the employment of pilots, which degrade spectral efficiency. The modified-blind phase search (M-BPS) technique has been found to give greater performance than the others [32], particularly when the number of subcarriers is considerable, despite its significant computing effort. The CD compensation block is by far the most difficult DSP step, therefore even while the complexity of the M-BPS increases with the order of the modulation, it has little impact on the complexity of the whole system [21]. As a result, we conduct this study with the M-BPS technique. You can read more about this method in [22]. Keep in mind that the little lingering CFO is also accounted for by the phase noise tracking.

A. Correction for Phase Noise using M-BPS

In order to fix the PN in the frequency domain, M-BPS is suggested [37]. The analysis filter bank (AFB) output data for all subcarriers are utilized to estimate the PN at each symbol time. The suggested methodology is so distinct from per-subcarrier PN compensation techniques. Using an analytical derivation, we demonstrate the algorithm's maximum likelihood (ML) optimality [38]. By just taking into account the distance in the real plane, M-BPS simplifies the computation of distance in the complex plane in comparison to other M-BPS algorithms. This drastically reduces the need for multiplication, which frees up more processing power for other tasks.

For the described system model in section III, a simple estimator for the absence of phase noise is made with removing the imaginary part to completely elimi-

nate the interference and considering only the real part of the equalized signal $\overline{X_{m,l}}$ as in (11).

When the phase noise presence the reconstruction of transmitted signal from the parallel AFB based equalized signal as,

$$\widehat{X_l} = \overline{X_l} \otimes \overline{\delta_l} + \overline{n_l} \tag{12}$$

where, $\widehat{X_l}$ is phase noise compensated signal after the MBPS algorithm and it is represented as,

$$\widehat{X_l} = \left[\widehat{X_{1,l}^R} \ \widehat{X_{1,l}^I} \ \widehat{X_{2,l}^R} \ \widehat{X_{2,l}^I} \ \ldots\ldots\ldots\ldots \widehat{X_{M,l}^R} \ \widehat{X_{M,l}^I} \right]^T \tag{13}$$

where $\widehat{X_{m,l}^R}$ and $\widehat{X_{m,l}^I}$ is real and imaginary part of phase noise compensated signal of m-th subcarrier and l-th modulated carrier. The phase noise signal $\overline{\delta_l}$ represented as,

$$\overline{\delta_l} = (\cos\delta_l \sin\delta_l)^T \tag{14}$$

$\bar{n}_l$ is denotes the equalized noise elements included with AWGN noise and interferences which represented by,

$$\overline{n_l} = \left[\overline{n_{1,l}^R} \ \overline{n_{1,l}^I} \ \overline{n_{2,l}^R} \ \overline{n_{2,l}^I} \ \ldots\ldots\ldots\ldots \overline{n_{M,l}^R} \ \overline{n_{M,l}^I} \right]^T \tag{15}$$

were,

$$\overline{n_{m,l}^R} = -r_{m,l}\sin\delta_l + n_{m,l}^R \tag{16}$$

$$\overline{n_{m,l}^I} = r_{m,l}\cos\delta_l + n_{m,l}^I \tag{17}$$

Where $\overline{n_{m,l}^R}$ and $\overline{n_{m,l}^I}$ is a real and imaginary elements of equalizers noise, Hence, we suggest testing all possible values of the phase, δ_K, on a predefined grid, and then choosing the value that minimizes the sum of distances between the projections on the real axis of the received samples after phase compensation testing and their hard decision counterparts [39]. The estimate and correction of phase noise is shown in Fig. 4.

The hard choice is done by picking the closest one between the projected values of the received sample and the optimal points of the pulse-amplitude modulation (PAM). The phase rotation used for a 4OQAM constellation is shown in Fig. 5. It is possible to express the expected phase rotation as,

$$\widehat{\delta_K} = \min_{\delta_K} \sum_{i=1}^{M} R[\overline{X_{\iota,l,K}}\ ] - H_d\left(R\left[\overline{X_{\iota,l,K}}\ \right]\right) \tag{18}$$

where, $R[.]$ denotes the real part of the signal and $H_d(.)$ represents the hard decision of phase search points. $\overline{X_{\iota,l,K}}$ is the rotated version of $\overline{X_{\iota,l}}$ given by,

$$\overline{X_{\iota,l,K}} = \overline{X_{\iota,l}}\, e^{-j\delta_K} \tag{19}$$

The phase search grid is defined as,

$$\delta_K = \frac{b}{B}\pi - \frac{\pi}{2} \tag{20}$$

Where B is the total number of phase tests and $b = 1, 2, B$. In order to lessen the effect of the additive noise, we average the cost function over M subcarriers. The switch then chooses the appropriate phase rotation to reduce the effect of phase noise by sending the samples' rotated versions in response to each phase test.

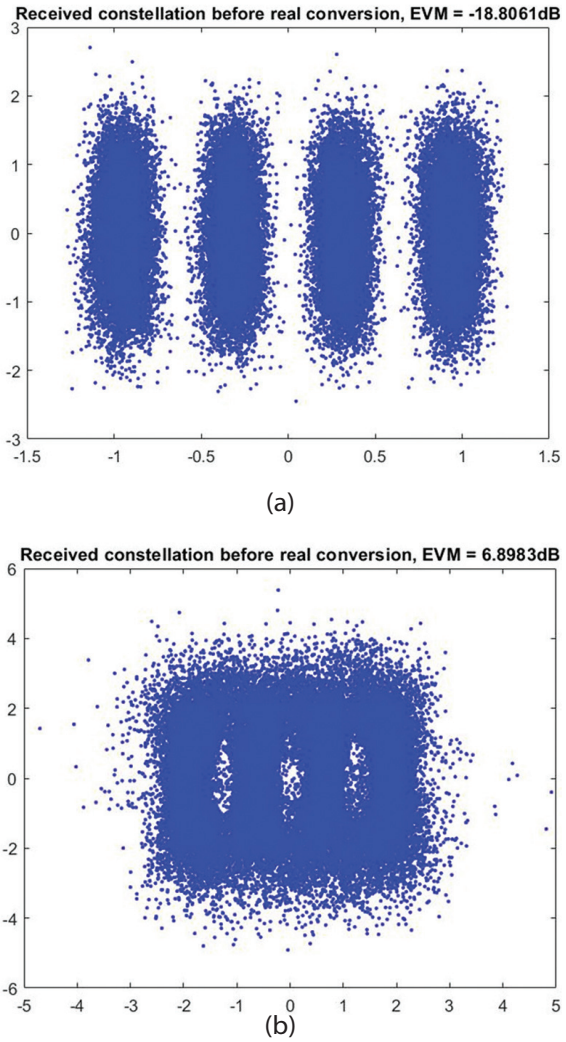

Fig. 4. modified blind phase search (M-BPS) (**a**) before and (**b**) after phase noise compensation

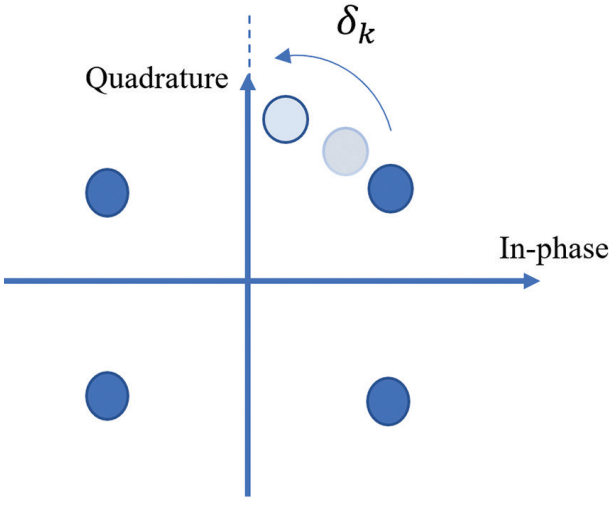

Fig. 5. Rotating the 4-OQAM constellation to measure the phase noise.

B. Features of M-BPS Estimation:

1. MBPS has a low computing cost and produces accurate phase noise estimations. In real-time systems [42], and this is important.

2. Due to its greater capture range, the MBPS approach can estimate phase noise even when the initial phase is far off [43]. This makes it resistant to severe channel faults such phase deviations or uncertain starting phases.

3. M-BPS estimator phase noise is accurate compering with other estimators such as maximum likelihood (ML), and Adaptive Maximum Likelihood (AML). M-BPS using iterative search. Through careful repetitions, the phase estimate approaches the true phase value. Phase noise may degrade FBMC performance, but this accuracy can compensate. As shown in Fig. 6.

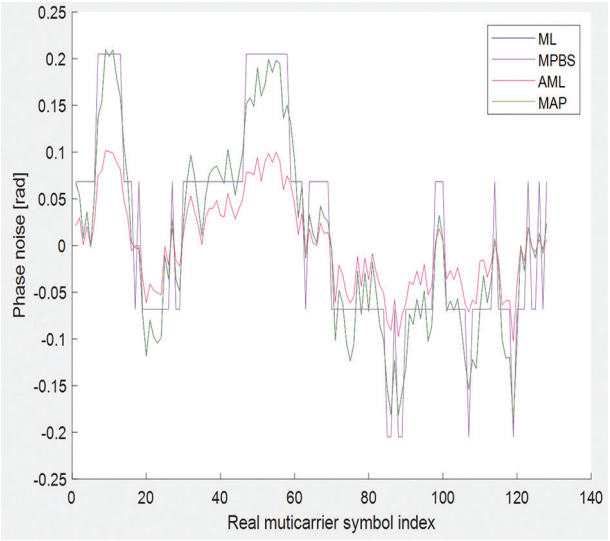

Fig. 6. Trackers By ML~MAP, AML, and M-BPS Estimators

4. The MBPS estimate is unaffected by fiber dispersion, temperature, or other channel variables. Due to its high channel flexibility, it can adjust for phase noise in many operational scenarios [44].

5. Modulation Format Independence MBPS works with several FBMC system configurations. It can be utilized in many optical fibers based FBMC topologies since it can compensate for phase noise in many system designs and handle many carrier frequencies.

C. Chromatic Dispersion Compensation Techniques

i. Single Tap Equalization

Low Complex single tap equalization is designed by [33], in which pre-equalization and equalization matrices are constructed. In general, multi-carrier systems split the bandwidth to number of narrow bands. Subcarrier counts in depends on the channel delay spread of FBMC OQAM. With the assumption of flat channel and slow varying phase noise single tap equalization is performed for the level of subcarrier [34]. Equalizer frequency response (FR) is calculated for the number of frequency points with the application of FIR filter and ZF reconstruction as shown in Fig. 7.

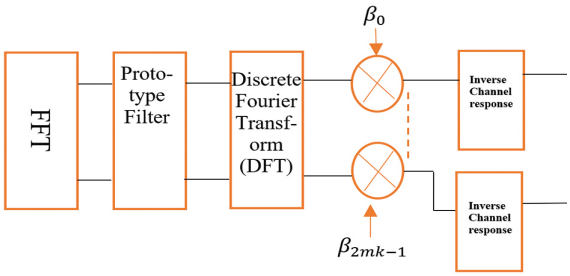

Fig. 7. Single Tap Equalization

Equalizer coefficient of one tap is given as,

$$\bar{z} = \frac{X_{m,n}}{H_m} e^{-j\beta_{m,n}} \tag{21}$$

where, $\beta_{m,n}$ is phase shift in prototype filter given by,

$$\beta_{m,n} = \frac{\pi}{2}(m+n) \tag{22}$$

$X_{m,n}$ is transmitted symbol of mth subcarrier and nth non equalized symbol, H_m is channel frequency response.

ii. The Equalization of multiple taps

The multi-tap equalization strategy models the secondary channel equalizers using a frequency sampling technique informed by channel information in the frequency space. The equalizer's coefficients are optimized such that the desired frequency filter response is attained. The transfer function of the filter is optimized to attain these predetermined values along the sub-channel frequency data. MMSE equalizer is one of the multi tap method which deals with the time domain coefficients which induce the successive interference cancellation (SIC) in throughput the system. For FBMC OQAM system frequency sampling based multi tap equalization is introduced by [35] as shown in Fig. 8. Equalizer coefficient is obtained for specific frequency points only by using channel impulse response (CIR) and is derived as,

$$\bar{z} = \left(\sum_{L=1}^{N_{taps}} W_{m,L} X_{m,n} \right) e^{-j\beta_{m,n}} \tag{23}$$

where, $W_{m,L}$ is weight of N_{taps} equalizer coefficients and it is derived for Zero Forcing (ZF) and Minimum Mean Square Error (MMSE) function in frequency sampling methodologies.

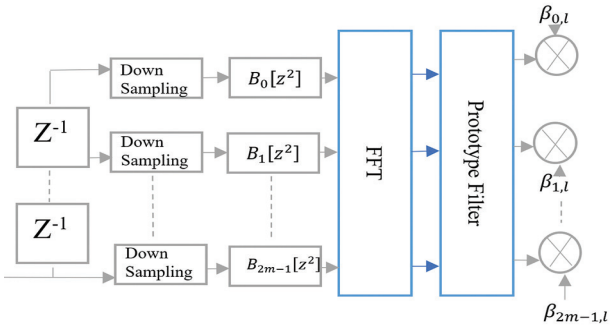

Fig. 8. Multi Tap Equalization

For ZF based equalization, W is described as,

$$W_Z = D_w^{-1} E_{zf} \tag{24}$$

where, E_{zf} is equalizer matrix for zeroforcing and is given by,

$$E_{zf} = (R_m^H R_m)^{-1} R_m^H \tag{25}$$

where, R_m is the frequency response matrix of N_t transmit antenna and Nr receive antenna at specific target points ϕ derived from Fourier transform of channel impulse response G_m and normalized impulse response G^n_m.

$$R_{m(N_t,N_r)} = \frac{\mathbb{F}(G_m)_\phi}{\mathbb{F}(G_m^n)_\phi} \tag{26}$$

Frequency target points of ϕ is calculated from the number of taps N_{taps} as,

$$\phi = \frac{2\pi}{N_{taps}+1}[-P, -P+1, \ldots\ldots, P] \tag{27}$$

Were,

$$P = \frac{(N_{taps}-1)}{2} \tag{28}$$

And Dw is equalizer weigh matrix calculated as,

$$D_{w(N_t,N_r)} = e^{jP\phi_{(N_t,N_r)}} \tag{29}$$

iii. Equalization using Parallel Analysis Filter Banks (AFBs)

A parallel multi tap equalizer is proposed by [36] to reduce the complexity of conventional multi tap equalization of FBMC OQAM. The graphical representation of this equalizer is depicted in Fig. 9. In this parallel AFBs equalization number of parallel receiver stage is structured in combiner part and all symbols are gathered based on per-subcarrier.

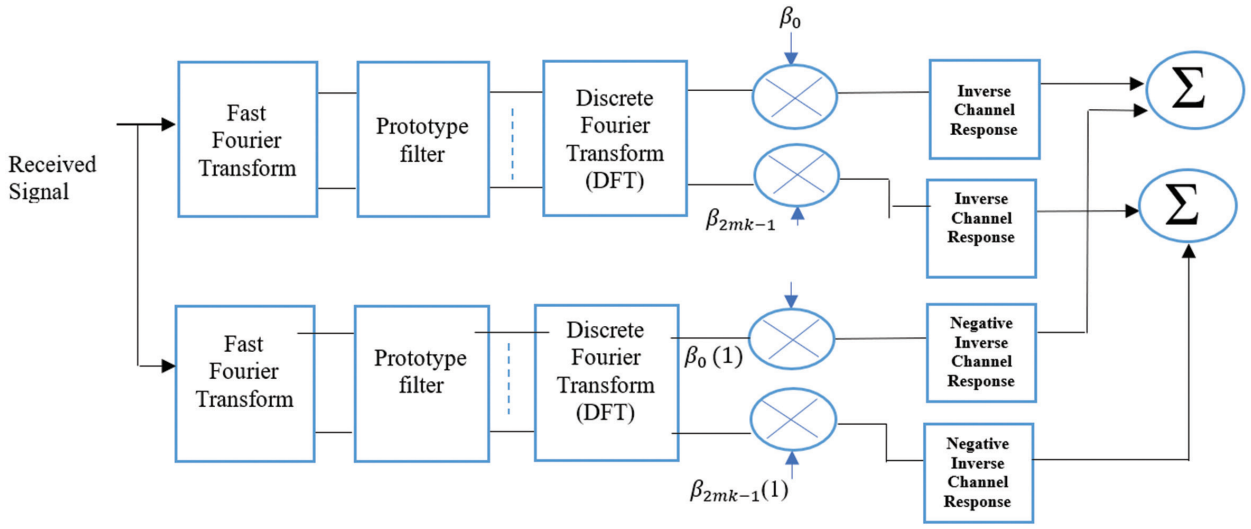

Fig. 9. Parallel AFB equalizer

For each K stages of equalization AFBs functions individualistically in parallel and principally filters the source signal by a polyphase network (PPN). This filter signal is derived from the received AFBs prototype pulse signal derivatives. Finally, the results from each stage are merged up to subcarrier level after performing the FFT. The equalization matrix is given by,

$$W_P = \sum_{k=0}^{K-1} \frac{J^k (H_m^{-1})^k}{(2M)^k} \tag{30}$$

5. RESULTS AND ANALYSIS

To prove the efficiency of multiple equalization for the purpose of CD and phase noise compensation in FBMC OQAM optical communication, in this section we perform the validation in terms of MSE, BER and Q-factor parameter. In this we are considering modulation of 16-OQAM. we are including the effects of phase noise (PN) and additive noise.

Using an optical amplifier with a noise figure anywhere from 0 to 30, Fig. 10 shows the bit error rate (BER) as a function of OSNR across a resolution bandwidth of 0.1 nm. As the OSNR increased BER getting reduced to $10^{-3.8}$ for our proposed parallel AFB with MBPS and for the same OSNR in ISDF-3-Tap reaches the $10^{-2.8}$. The Q-factor is computed from the bit error rate (BER) as [41].

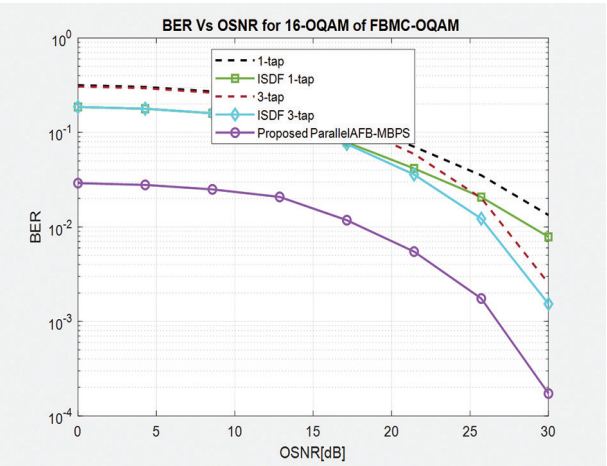

Fig. 10. BER Vs OSNR for 16-OQAM

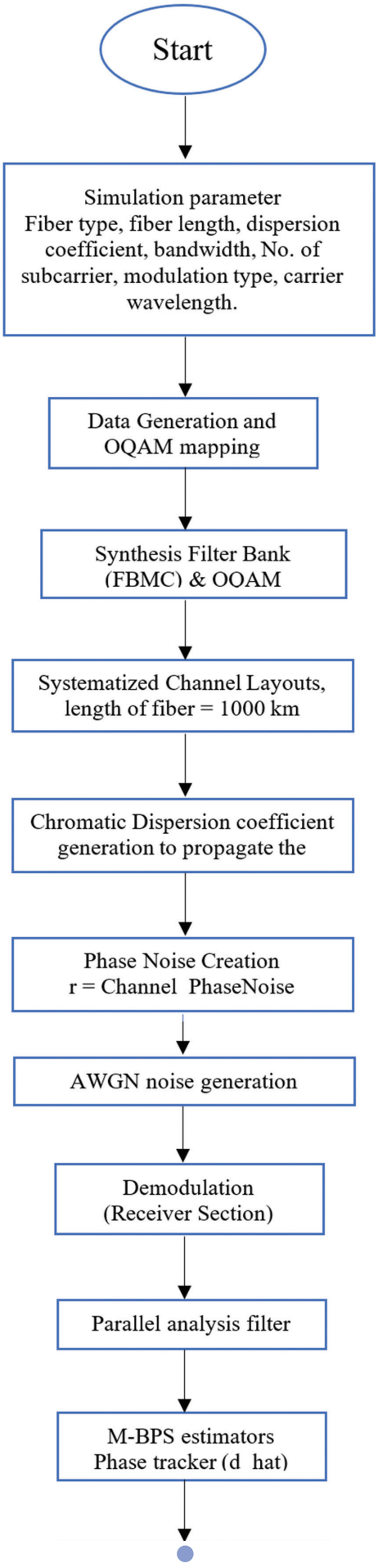

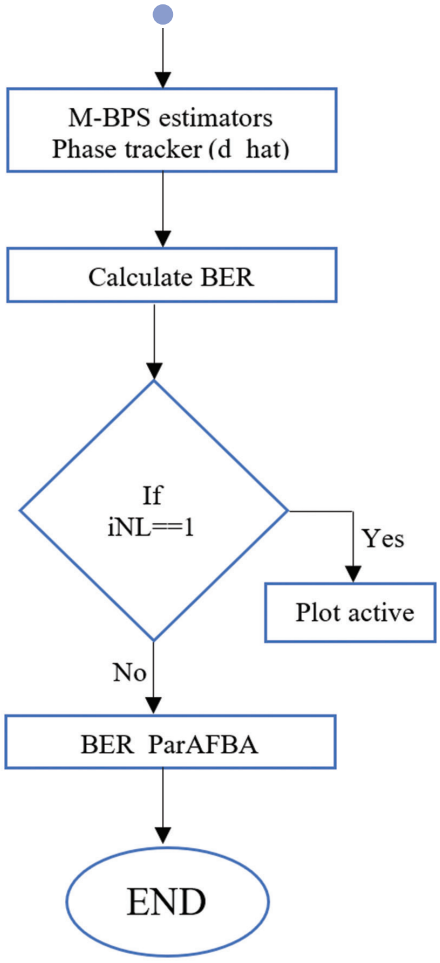

Fig. 11. flow chart of simulation FBMC/OQAM

$$Q_f(dB) = 20\log_{10}[\sqrt{2}\, erfc^{-1}(2 * BER)\,] \quad (31)$$

Q-factor is plotted versus OSNR with two separate Figs. of 11 and 12. Fig 12. shows the performance of Q-factor of different equalizers with fixed fiber length of 320 km.

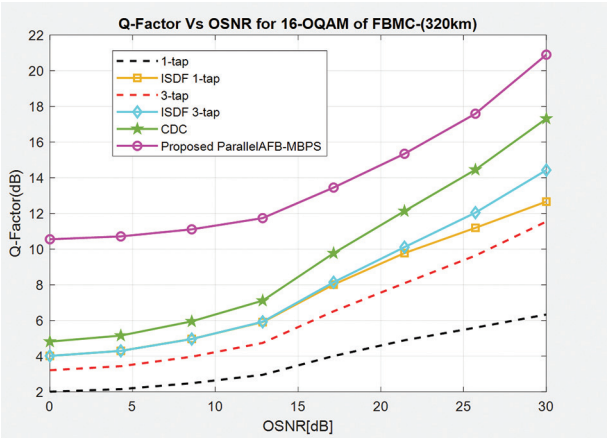

Fig. 12. Q-factor Vs OSNR for different Equalizer

Impact of different fiber length in Q-factor is reconnoitered for different equalizers and with consideration of OSNR metric with 0.1 nm resolution bandwidth as shown in Fig. 13, Fig. 14 and Fig. 15 respectively for

1-Tap ISDF, 3-Tap ISDF and Proposed Parallel AFB with MBPS equalizers.

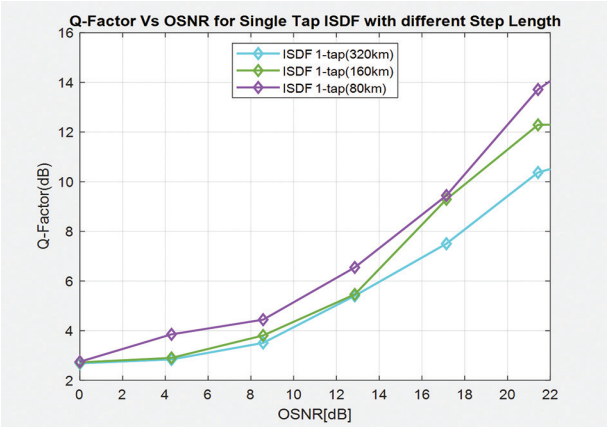

Fig.13. Q-factor Vs OSNR for different fiber length of ISDF-1-Tap equalizer

Fiber Length is configured with 320 km,160 km and 80 km for the implemented three equalizers of 1-Tap with ISDF, 3-Tap with ISDF and proposed Parallel AFB with MBPS. When the fiber length decreases the Q-factor getting increase as the information loss due to nonlinear effects are balances in short distance.

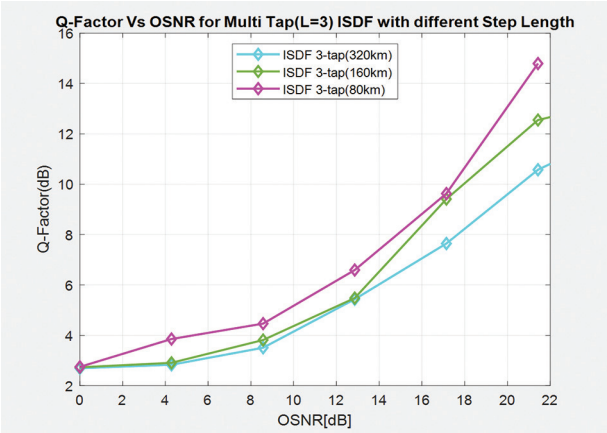

Fig. 14. Q-factor Vs OSNR for different fiber length of ISDF-3-Tap equalizer

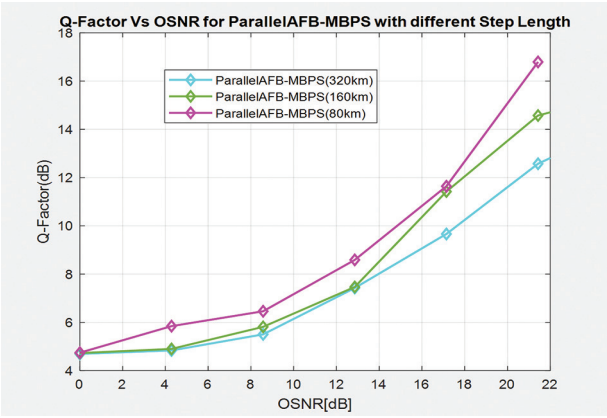

Fig. 15. Q-factor Vs OSNR for different fiber length of Parallel AFB with MBPS equalizer

BER Fig. 16 shows the results for varying fiber lengths and equalization settings. Fig. 16 depicts how the transmission distance of the fiber affects the BER performance of 16-QAM FBMC/OQAM. The anticipated fiber length is between 100 and 960 kilometers, with an 100-kilometer span. There were 24.19 dB, 21.18 dB, 19.42 dB, 18.17 dB, 17.2 dB, 16.41 dB, 15.74 dB, 15.16 dB, 14.19 dB, 13.78 dB, and 13.4 dB in received OSNR (0.1 nm resolution bandwidth) at various times. The findings are based on using a step length equal to the span length (80 km/step) or the entire fiber length (L/step) for equalization, and an input power of -10 dBm and an optical amplifier with a noise figure of 4 dB. Proposed parallel AFB with MBPS illustrated the improvement over other equalizers of ISDF and conventional multi tap equalizers for the entire fiber distance of low range to high range.

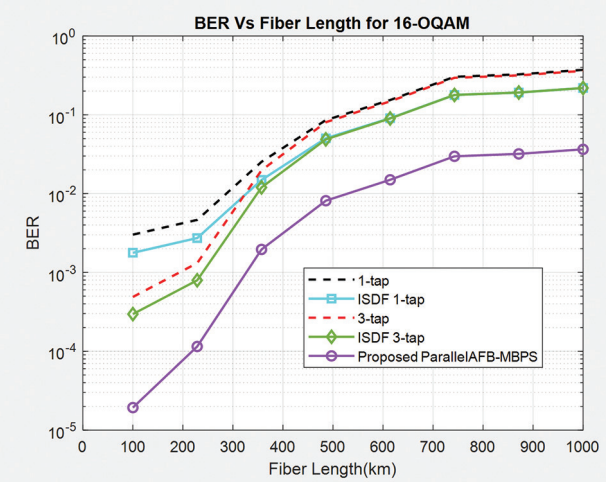

Fig.16. BER Vs Fiber Distance for different equalizer

The effect of carrier frequency offset lead to degradation the performance of the entire system which include interference between subcarriers, and intercarrier interference (ICI), and hence, lead to increase the BER.

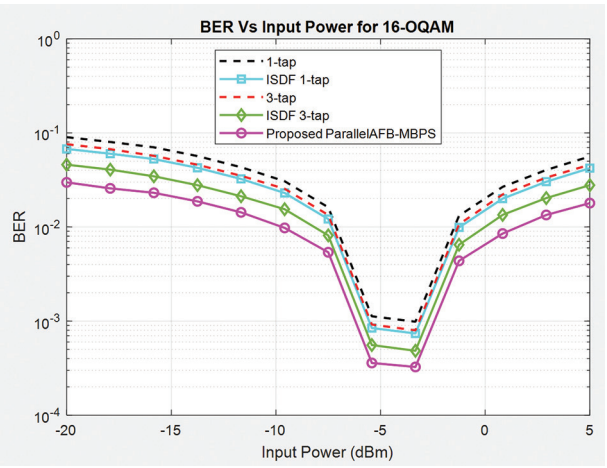

Fig. 17. BER Vs Input Power for different equalizer

Considering the SPM's interaction with ASE noise, as shown in Fig. 18, allows for an assessment of the FBMC/OQAM system's performance.

The bit error rate (BER) is shown vs signal strength. An optical amplifier with a noise figure of 4 dB is utilized to make up for the fiber loss in a 320-kilometer-long SSMF cable's transmission.

Figs. 18, 19, and 20 demonstrate that the BER performance of the ISDF-1-Tap equalization, ISDF-3-Tap equalizer, and the Parallel AFB with MBPS equalizer all increase with increasing input power when the system is running in the linear zone where the input power is less than 0 dBm. On the other hand, when input power is increased, nonlinear phase (NLP) noise degrades equalizer performance, leading to a lower bit error rate (BER). As a result, when nonlinear impairment is predominating, increasing the input power has a negative effect on the performance of the FBMC/OQAM system. Because of cumulative distortion from CD and NLP noise effects and the absence of a nonlinear compensator (NLC), a 1-tap equalizer cannot succeed. As compared to an ISDF-1-tap equalizer, the Parallel AFB with MBPS equalizer shows better results with optimal power at approximately -4 dBm.

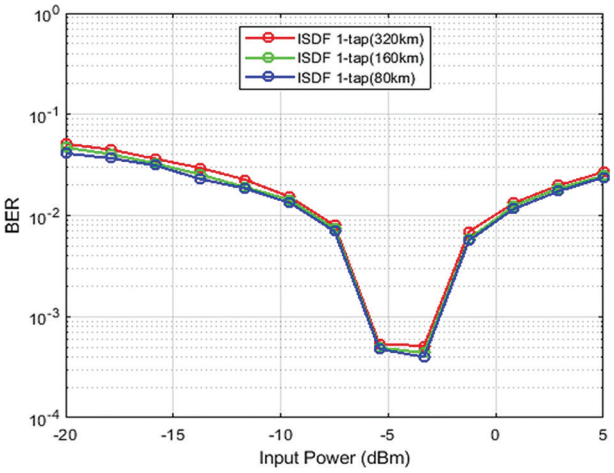

Fig. 18. BER Vs Input Power for ISDF-1-Tap equalizer

The ISDF and Parallel AFB equalizer with 80km/step length performs similarly to the case with 160km/step length at low input power.

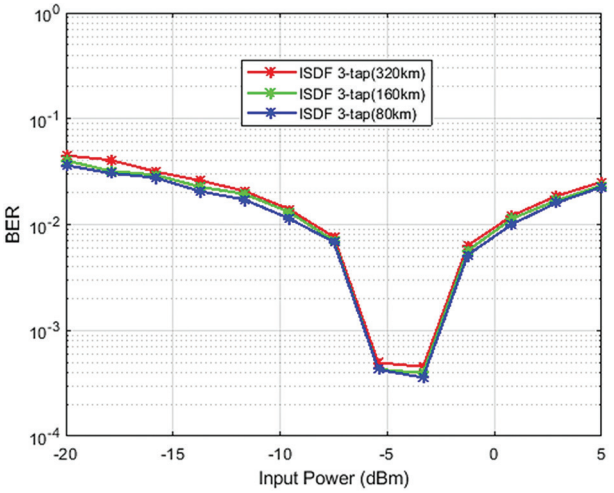

Fig. 19. BER Vs Input Power for ISDF-3-Tap equalizer

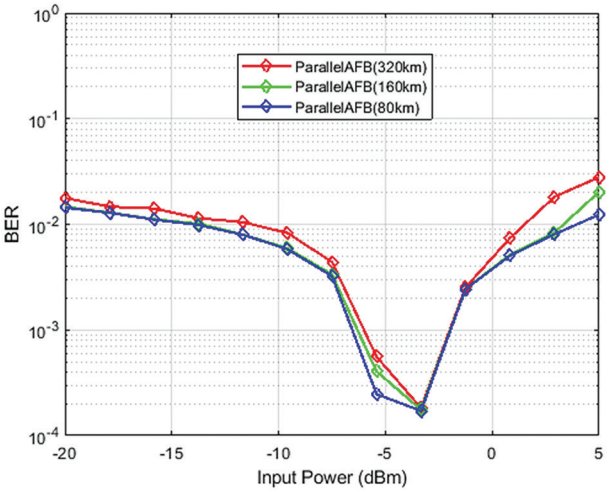

Fig. 20. BER Vs Input Power for Parallel AFB-MBPS equalizer

In summary, CD and nonlinear interference can be effectively removed by ISDF-1Tap (80 km/step) and parallel AFB with MBPS (80 km/step) equalizers. To enhance performance, though, they need to use a shorter step length.

When the transmitted power is huge, compensating just for the linear degradation is not enough. The fiber nonlinearity also plays a considerable role. When the fiber transmission distance is long, a system with a lot of power is required. The suggested equalizer is used to jointly adjust for the CD and phase noise (PN), and the results are compared to those obtained using the standard and benchmark equalizers. Filtering the CD-equalized signal using PN may help reduce the effects of fiber's nonlinear degradation.

To get the most out of your FBMC/OQAM setup, you'll need to optimize your NLC first. Several nonlinear (NL) scaling factors are shown in Fig. 21 to demonstrate the effect on the performance of the proposed parallel AFB with MBPS equalizers. The calculations use a noise figure of 4 dB per span and a transmission distance of 4 x 80 km.

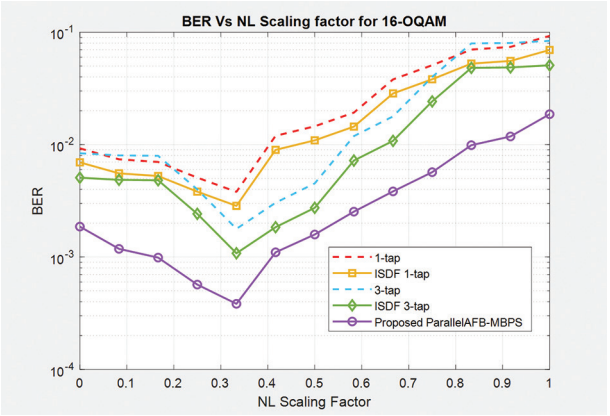

Fig. 21. BER Vs NL Scaling Factor for different equalizer

The nonlinearity area of the equalizers of ISDF-1-Tap, ISDF-3-Tap, and Parallel AFB with MBPS is shown in Fig. 22,

Fig. 23, and Fig. 24 to show the BER performance at a high input power of 2 dBm.

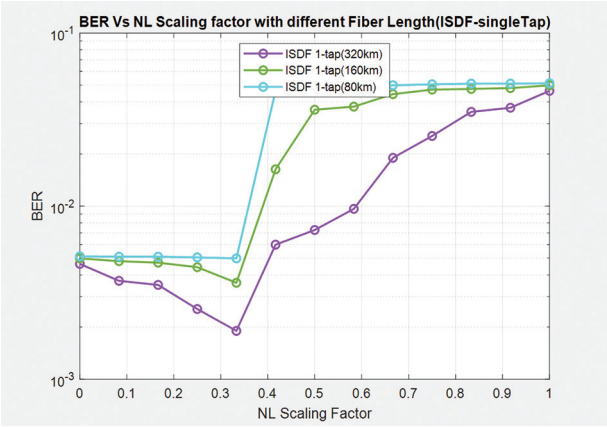

Fig. 22. BER Vs NL Scaling Factor for ISDF-1-Tap equalizer

As can be seen in Fig. 22, both the ISDF-1Tap (320km/step) and the ISDF-3Tap (320km/step) equalizers work optimally at a scale factor of 0.33.

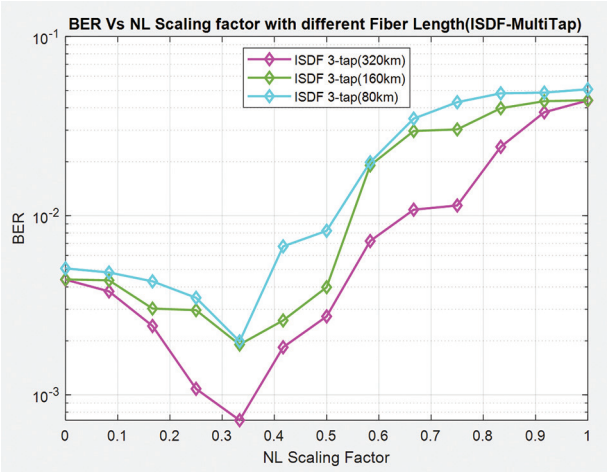

Fig. 23. BER Vs NL Scaling Factor for ISDF-3-Tap equalizer

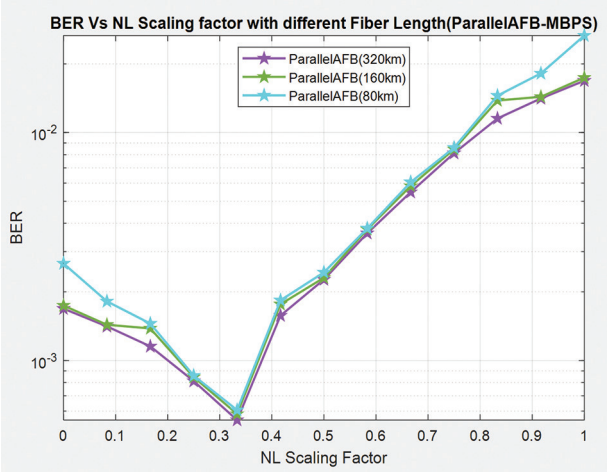

Fig. 24. BER Vs NL Scaling Factor for Parallel AFB-MBPS equalizer

Around 0.34 is the best scaling factor for the Parallel AFB-MBPS equalizer (80 km/step). For the Parallel AFB-MBPS equalizer to function at its best in terms of BER performance, as illustrated in Fig. 24, the NL scaling factor must be adjusted to its ideal value.

Fig. 25 displays MSE performance for a variety of equalizers and setups, all of which can be found in Table 1. At the bandwidth's edge, where the MSE is most extreme, the channel phase disparity is likewise the greatest. As the number of subcarriers increases, the system-wide chromatic dispersion is compensated for, leading to a decrease in MSE. We choose the often-used case of perfect CDC equalization for a single carrier [40] as our baseline for comparison. Fig. 25 shows that when the number of taps and the number of iterations in the ISDF both grow, the MSE's performance improves. However, these elements will add to the complexity of the system overall. Therefore, with its low complexity and little transmission latency, M-BPS based parallel AFB achieves the highest performance when compared to all these equalizers. ISDF-1-Tap technique provides MSE of difference of -14.1 dB, which is much better than one tap equalization. The MSE performance of ISDF with 3-Tap is -14.3 dB better than that of a 1-Tap equalizer. The findings of Parallel AFB with MBPS, however, show an improvement in MSE performance of -16.2 dB compared to that of 1-Tap.

By utilizing the different methodology that including AFB with MBPS, the experimental setup or simulation scenarios using the configuration parameter examine the performance metrics of each study to evaluate the effectiveness of the compensation technique to enhance MSE, BER, Power input, Q-factor and OSNR. Table (below) showing the difference finding studies.

Table 1. Comparison results between different studies

Parameters	Khaled A. Alaghbari 2020 [1]	Our Proposed Method
Mean square error	-13 dB	-16.2 dB
BER Vs. NL scaling factor for various equalizers (80,160,320) km	$10^{-1.5}$	$10^{-3.5}$
BER Vs. input power (80,160,320) km	~ 10^{-3} for various equalizers	$10^{-3.95}$
BER Vs. fiber length for 100 km	$10^{-3.7}$	$10^{-4.8}$
Q-factor Vs. OSNR for 0dB	~ 4 dB for different equalization	10.2 dB
Q-factor Vs. OSNR for 15 dB	~ 5.8 dB	12.2 dB

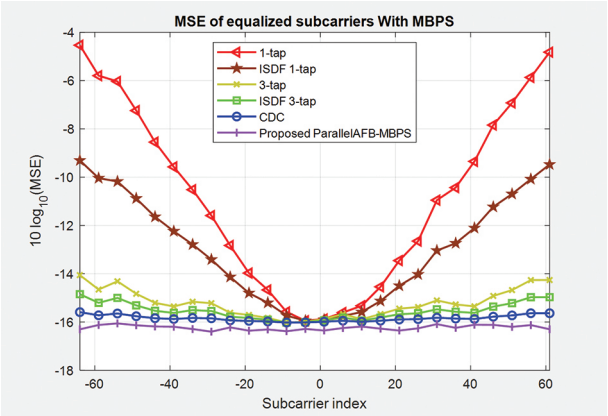

Fig. 25. MSE Vs Subcarrier Index

The 960 km ISDF-1Tap (L/step), ISDF-3Tap equalizers and parallel AFB-MBPS output are shown in Fig. 25, Fig. 26, and Fig. 27 respectively . High inter-symbol interference from CD, inherent interference, and optical channel noise distorts the constellation diagram at 960 km.

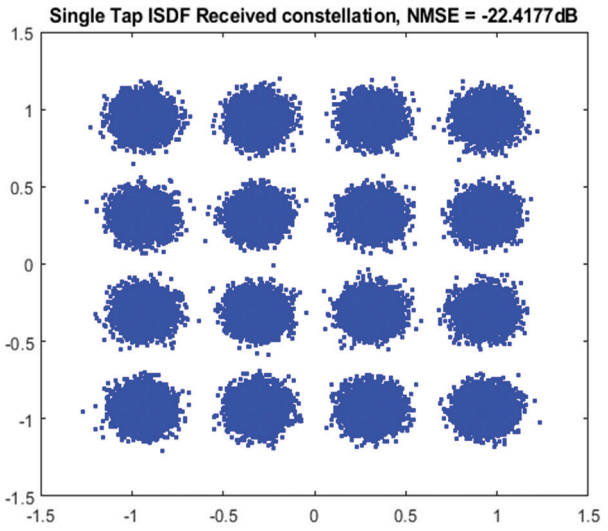

Fig. 25. 16-OQAM constellation of ISDF-1-Tap

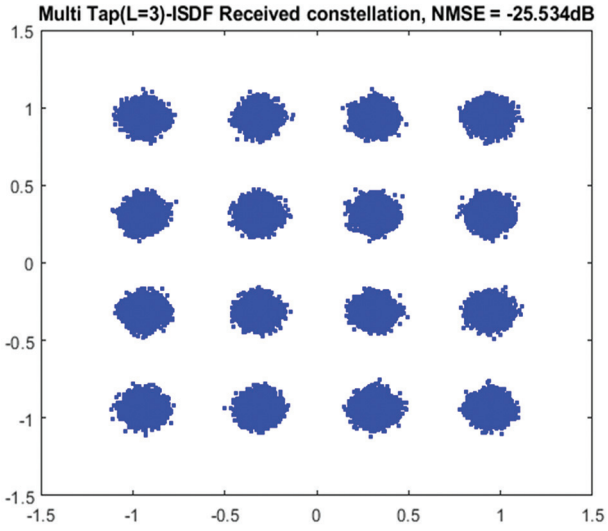

Fig. 26. 16-OQAM constellation of ISDF-3-Tap

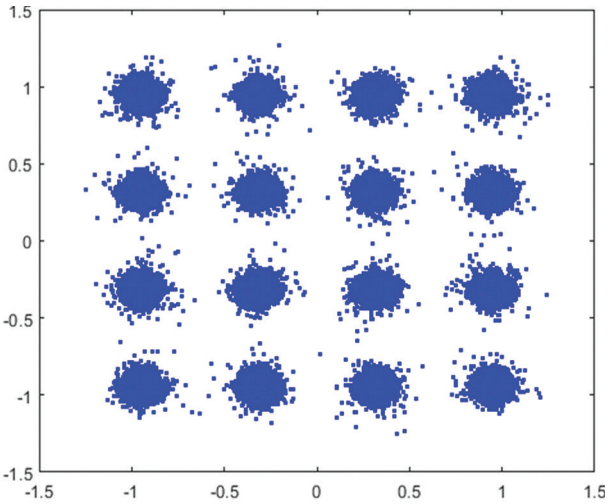

Fig. 27. 16-OQAM constellation of Parallel AFB-MBPS equalizer

6. CONCLUSION

Chromatic dispersion and phase noise in optical fiber communication with FBMC-OQAM protocol is compensated using parallel AFB with MBPS equalization method in this implementation. For comparison of proposed with previous equalizers of ISDF with single tap and multi tap is considered. These numerous equalizers are initially used in wireless transmission. In this work we are utilizing the concept of these equalizers in optical fiber FBMC OQAM. By increasing the number of subcarriers in the system will lead to phase noise. So here we achieve the best performance of both PN compensation and CD compensation in frequency and time domain with moderate subcarriers. Increasing the fiber length will affect the phase noise and degrade the BER performance of the system. After 700 km, the noise reaches the value where no data detection and BER approximately reaches the 0.5 value. The scaling factor affects the BER performance. The best scaling factor is obtained at 0.34 for the Parallel AFB-MBPS equalizer (80km/step).

In this we analyzed the complexity and performance for all compensation methods. Low complexity is achieved in proposed parallel AFB with modified blind phase search without any additional delay.

7. REFERENCES

[1] K. A. Alaghbari, H. S. Lim, T. A. Eltaif, "Compensation of chromatic dispersion and nonlinear phase noise using iterative soft decision feedback equalizer for coherent optical FBMC/OQAM systems", Journal of Lightwave Technology, Vol. 38, 2020, pp. 3839-3849.

[2] D. W. M. Guerra, T. Ab, "Efficient multitap equalization for FBMC-OQAM systems", Transactions on

Emerging Telecommunications Technologies, Vol. 30, No. 12, 2019, p. e3775.

[3] R. J. Essiambre, G. Kramer, P. J. Winzer, G. J. Foschini, B. Goebel, "Capacity limits of optical fiber networks", Journal of Lightwave Technology, Vol. 28, No. 4, 2010, pp. 662-701.

[4] F. Rottenberg, X. Mestre, F. Horlin, J. Louveaux, "Single-Tap Precoders and Decoders for Multi-User MIMO FBMC-OQAM under Strong Channel Frequency Selectivity", IEEE Transactions on Signal Processing, Vol. 65, No. 3, 2016, pp. 587-600.

[5] F. Rottenberg, T.-H. Nguyen, S.-P. Gorza, F. Horlin, J. Louveaux, "Advanced Chromatic Dispersion Compensation in Optical Fiber FBMC-OQAM Systems", IEEE Photonics Journal, Vol. 9, No. 6, 2017.

[6] Y.-F. Huang, C.T. Tsai, C.-Y. Chi, D.-W. Huang, G.-R. Lin, "Filtered Multicarrier OFDM Encoding on Blue Laser Diode for 14.8-Gbps Seawater Transmission", Journal of Lightwave Technology, Vol. 36, 2018, pp. 1739-1745

[7] H. Jamal, D. W. Matolak, "Dual-Polarization FBMC for Improved Performance in Wireless Communication Systems", IEEE Transactions on Vehicular Technology, Vol. 68, No. 1, 2019.

[8] H. Wang, W. Du, X. Wang, G. Yu, L. Xu, "Channel Estimation Performance Analysis of FBMC/OQAM Systems with Bayesian Approach for 5G-Enabled IoT Applications", Wireless Communications and Mobile Computing, Vol. 2020, 2020.

[9] J. Fickers, A. Ghazisaeidi, M. Salsi, G. Charlet, P. Emplit, F. Horlin, "Multicarrier Offset-QAM for Long-Haul Coherent Optical Communications", Journal of Lightwave Technology, Vol. 32, No. 24, 2014.

[10] Z. Li, "Experimental demonstration of 110-Gb/s unsynchronized band-multiplexed superchannel coherent optical OFDM/OQAM system", Optics Express, Vol. 21, No. 19, 2013, pp. 21924-21931.

[11] M. Bellanger, "FS-FBMC: an alternative scheme for filter bank based multicarrier transmission", Proceedings of the 5th International Symposium on Communications, Control and Signal Processing, Rome, Italy, 2-4 May 2012.

[12] T.-H. Nguyen, J. Louveaux, S. P. Gorza, F. Horlin, "Simple feedforward carrier phase estimation for optical FBMC/OQAM systems", IEEE Photonics Technology Letters, Vol. 28, No. 24, 2016, pp. 2823-2826.

[13] T.-H. Nguyen, F. Rottenberg, S. P. Gorza, J. Louveaux, F. Horlin, "Efficient chromatic dispersion compensation and carrier phase tracking for optical fiber FBMC/OQAM systems", Journal of Lightwave Technology, Vol. 35, No. 14, 2017, pp. 2909-2916.

[14] T.-H. Nguyen et al. "Experimental Demonstration of the Tradeoff Between Chromatic Dispersion and Phase Noise Compensation in Optical FBMC/OQAM Communication Systems", Journal of Lightwave Technology, Vol. 37, 2019, 4340-4348.

[15] S. Chimmalgi, A. Rode, L. Schmid, L. Schmalen, "Approximate Maximum a Posteriori Carrier Phase Estimator for Wiener Phase Noise Channels using Belief Propagation", arXiv:2307.03517, 2023.

[16] X. Mestre, M. Majoral, S. Pfletschinger "An Asymptotic Approach to Parallel Equalization of Filter Bank Based Multicarrier Signals", IEEE Transactions on Signal Processing, Vol. 61, No. 14, 2013.

[17] L. Zhang, P. Xiao, A. Zafar, A. Quddus, R. Tafazolli, "FBMC system: an insight into doubly dispersive channel impact", IEEE Transactions on Vehicular Technology, Vol. 66, No. 5, 2016, pp. 3942-3956.

[18] M. Ionescu, D. Lavery, A. Edwards, E. Sillekens, L. Galdino, D. Semrau, R. I. Killey, W. Pelouch, S. Barnes, P. Bayvel, "74.38 Tb/s transmission over 6300 km single mode fiber with hybrid EDFA/Raman amplifiers", Proceedings of the Optical Fiber Communication Conference, San Diego, CA, USA, 3-7 March 2019.

[19] P. J. Winzer, D. T. Neilson, A. R. Chraplyvy, "Fiber-optic transmission and networking: the previous 20 and the next 20 years", Optics Express, Vol. 26, No. 18, 2018, pp. 24190-24239.

[20] K. Zanette, J. C. Cartledge, M. O'Sullivan, "Correlation properties of the phase noise between pairs of lines in a quantum-dot optical frequency comb source", Proceedings of the Optical Fiber Communication Conference, Los Angeles, CA, USA, 19-23 March 2017.

[21] G. Vedala, M. Al-Qadi, M. O'Sullivan, J. Cartledge, R. Hui, "Phase noise characterization of a QD-based

diode laser frequency comb", Optics Express, Vol. 25, No. 14, 2017, pp. 15890-15904.

[22] C. Antonelli, O. Golani, M. Shtaif, A. Mecozzi, "Nonlinear interference noise in space-division multiplexed transmission through optical fibers", Optics Express, Vol. 25, No. 12, 2017, pp. 13055-13078.

[23] C. Li, Q. Yang, "Optical OFDM/OQAM for the future ber optics communications", Procedia Engineering, Vol. 140, 2016, pp. 99-106.

[24] M. Bi, L. Zhang, L. Liu, G. Yang, R. Zeng, S. Xiao, Z. Li, Y. Song, "Experimental demonstration of the OQAM-OFDM-based wavelength stacked passive optical networks", Optics Communications, Vol. 394, 2017, pp. 129-134.

[25] D. Petrovic, W. Rave, G. Fettweis, "Effects of phase noise on OFDM systems with and without PLL: Characterization and compensation", IEEE Transactions on Communications, Vol. 55, No. 8, 2007, pp. 1607-1616.

[26] F. Rottenberg, T.-H. Nguyen, S.-P. Gorza, F. Horlin, J. Louveaux, "ML and MAP phase noise estimators for optical fiber FBMC-OQAM systems", Proceedings of the IEEE International Conference on Communications, Paris, France, 21-25 May 2017, pp. 1-6.

[27] T. T. Nguyen, S. T. Le, R. Nissel, M. Wuilpart, L. Van Compernolle, P. Megret, "Pseudo-pilot coding-based phase noise estimation for coherent optical FBMC-OQAM transmissions", Journal of Lightwave Technology, Vol. 36, No. 14, 2018, pp. 2859-2867.

[28] B. You, L. Yang, F. Luo, S. Fu, S. Yang, B. Li, D. Liu, "Joint carrier frequency offset and phase noise estimation based on pseudo-pilot in CO-FBMC/OQAM system", IEEE Photonics Journal, Vol. 11, No. 1, 2019, pp. 1-11.

[29] X. Yan et al. "Low-complexity carrier phase estimation for M-ary quadrature amplitude modulation optical communication based on dichotomy", Optics Express, Vol. 28, No. 17, 2020, pp. 25263-25277.

[30] T.-H. Nguyen, C. Peucheret, "Kalman Filtering for Carrier Phase Recovery in Optical Offset-QAM Nyquist WDM systems", IEEE Photonics Technology Letters, Vol. 29, No. 12, 2017, pp. 1019-1022.

[31] J. Zhao, "Format-transparent phase estimation based on KL divergence in coherent optical systems", Optics Express, Vol. 28, No. 14, 2020, pp. 20016-20031.

[32] T. Sasai, A. Matsushita, M. Nakamura, S. Okamoto, F. Hamaoka, Y. Kisaka, "Laser phase noise tolerance of uniform and probabilistically shaped QAM signals for high spectral efficiency systems", IEEE/OSA Journal of Lightwave Technology, Vol. 38, No. 2, 2020, pp. 439-446.

[33] P. Zhang, H. Ren, M. Gao, J. Lu, Z. Le, Y. Qin, W. Hu, "Low-complexity blind carrier phase recovery for C-mQAM coherent systems", IEEE Photonics Journal, Vol. 11, No. 1, 2019, p. 7200214.

[34] Q. Xiang, Y. Yang, Q. Zhang, Y. Yao, "Low complexity, modulation transparent and joint polarization and phase tracking scheme based on the nonlinear principal component analysis", Optics Express, Vol. 27, No. 13, 2019, pp. 17968-17978.

[35] M. Nouri, M. G. Shayesteh, N. Farhangian, "Chromatic Dispersion and Nonlinear Phase Noise Compensation Based on KLMS Method", Optics Communications, Vol. 351, 2015, pp. 149-154.

[36] J. Louveaux "Equalization and Demodulation in the Receiver (Single Antenna)", PHYDYAS Technical Report, ICT-211887, 2008.

[37] T. Ihalainen, A. Ikhlef, J. Louveaux, M. Renfors "Channel Equalization for Multi-Antenna FBMC/OQAM Receivers", IEEE Transactions on Vehicular Technology, Vol. 60, No. 5, 2011, pp. 2070-2085.

[38] K. A. Alaghbari, H. S. Lim, T. Eltaif, N. Alsowaidi, "Chromatic Dispersion Compensation for Offset-QAM/FBMC Based Coherent WDM Using Digital Filter", Proceedings of the IEEE 7th International Conference on Photonics, Kuah, Malaysia, 9-11 April 2018, pp. 1-3.

[39] P. Duhamel, M. Vetterli, "Fast Fourier Transforms: A Tutorial Review and a State of the Art", Signal Processing Journal, Vol. 19, No. 4, 1990, pp. 259-299.

[40] A. Viholainen, M. Bellanger, M. Huchard, "Prototype Filter and Structure Optimization", PHYDYAS Technical Report, 2009.

[41] A. Zaidi, F. Athley, J. Medbo, U. Gustavsson, G. Durisi, X. Chen, "5G Physical Layer: Principles, Models and Technology Components", 1st Edition, Academic Press, 2018.

[42] Y. Shao et al. "Phase noise model for continuous-variable quantum key distribution using a local local oscillator", Physical Review A, Vol. 104, No. 3, 2021.

[43] B. You et al. "Joint carrier frequency offset and phase noise estimation based on pseudo-pilot in CO-FBMC/OQAM system", IEEE Photonics Journal, Vol. 11, No. 1, 2019, pp. 1-11.

[44] E. Börjesson, "Implementation of Blind Carrier Phase Recovery for Coherent Fiber-Optical Receivers", University of Gothenburg, Gothenburg, Sweden, 2018, Master thesis.

Survivability with Adaptive Routing and Reactive Defragmentation in IP-over-EON after A Router Outage

Original Scientific Paper

Ridwansyah
Electrical Engineering Department, Universitas Hasanuddin, Gowa, Indonesia
Electronic Engineering Study Program, Universitas Negeri Makassar, Makassar, Indonesia
ridwansyah@unm.ac.id

Syafruddin Syarif
Electrical Engineering Department, Universitas Hasanuddin, Gowa, Indonesia
syafruddin.s@eng.unhas.ac.id

Dewiani
Electrical Engineering Department, Universitas Hasanuddin, Gowa, Indonesia
dewiani@unhas.ac.id

Wardi
Electrical Engineering Department, Universitas Hasanuddin, Gowa, Indonesia
wardi@unhas.ac.id

Abstract *–The occurrence of a router outage in the IP layer can lead to network survivability issues in IP-over-elastic-optical networks with consequent effects on the existing connections used in transiting the router. This usually leads to the application of a path to recover any affected traffic by utilizing the spare capacity of the unaffected lightpath on each link. However, the spare capacity in some links is sometimes insufficient and thus needs to be spectrally expanded. A new lightpath is also sometimes required when it is impossible to implement the first process. It is important to note that both processes normally lead to a large number of lightpath reconfigurations when applied to different unaffected lightpaths. Therefore, this study proposes an adaptive routing strategy to generate the best path with the ability to optimize the use of unaffected lightpaths to perform reconfiguration and minimize the addition of free spectrum during the expansion process. The reactive defragmentation strategy is also applied when it is impossible to apply spectrum expansion because of the obstruction of the neighboring spectrum. This proposed strategy is called lightpath reconfiguration and spectrum expansion with reactive defragmentation (LRSE+RD), and its performance was compared to the first Shortest Path (1SP) as the benchmark without a reactive defragmentation strategy. The simulation conducted for the two topologies with two traffic conditions showed that LRSE+RD succeeded in reducing the lightpath reconfigurations, new lightpath number, and additional power consumption, including the additional operational expense compared to 1SP.*

Keywords*: adaptive routing, spectrum expansion, reactive defragmentation, router outage, lightpath reconfiguration, IP-over-EON*

1. INTRODUCTION

The increasingly diverse use of internet-based applications is observed to have led to rapid traffic growth. Some of these application services include online gaming, video streaming, and smart systems requiring large and dynamic traffic, making it important to ensure efficient utilization of optical networks [1]. One of the promising solutions offered by transport network technology for efficient spectrum utilization is the elastic optical network (EON) [2]. The efficiency is associated with the possibility of dividing the spectrum in the EON into smaller spectra called frequency slots (FSs), which are adjustable based on demand [3]. The EON flexibility is linked to the capability of sliceable bandwidth variable transponders (SBVTs) to generate diverse optical flows that can be directed to different destinations [4]. Moreover, SBVTs have the capacity to accommodate dynamic traffic changes by expanding and contracting the slot width on a lightpath [5]. This shows that EON and IP technology are promising solutions to integrate the next IP-over-optical backbone networks [6].

Multilayer IP-over-EON offers flexibility and adaptivity in exchanging huge amounts of traffic. The existence of failure in one of the layers, either the IP or optical/EON layer, has the ability to cause data loss on the user side and decrease operator revenue. This is the reason it is very important to consider the survivability in IP-over-optical networks [7]. It is important to note that failures in the optical/EON layer can be caused by fiber optic cable cuts and those in the IP layer by router outages, which is more common than fiber optic failure [8]. Generally, a backup router is usually set up when the primary router experiences a problem [9], but this is not economical from the perspective of operators.

Network survivability in IP-over-EON is established in a multilayer manner by utilizing unused capacity in each layer after a failure in order to reduce the provision of backup routers [7, 10]. The process of handling survivability with a focus only on each layer causes an increase in network costs and results in inefficient use of network resources [7, 10]. The failure of routers can influence traffic flows, but they can be restored to unaffected lightpaths using the multilayer restoration (MLR) mechanism [11]. This usually leads to the selection of the path utilizing the spare capacity on the unaffected lightpath in each link. The determination of the best routing is necessary to obtain a path that can reduce the occurrence of lightpath reconfiguration to allow the optimization of network resources [12].

The shortest-path routing is often used because of its simplicity in pathfinding. It is normally applied offline based on network information, specifically in fixed and fixed alternate routing [13, 14]. However, this path sometimes does not provide optimal results due to the possibility of another path producing a better outcome. This means there is a need to consider all potential paths connecting the source to the destination for a better objective value. Therefore, adaptive routing is considered a solution to find the best path dynamically according to the current conditions of the network [15].

In addition to resolving routing issues, there is a need to consider maximizing the utilization of spare capacity for restoring affected traffic. This minimizes the need for setting up a new lightpath during the lightpath reconfiguration procedure. The MLR strategies [11] outline the lightpath reconfiguration procedure in IP-over-EON networks, which occurs under two conditions. The first involves the unaffected lightpath utilizing its spectrally expanded spare capacities to recover the affected traffic. The second arises when a new lightpath is established due to neighboring spectrum blocks hindering the spectrum expansion process. This occurs when the demand for spectrum from the affected traffic exceeds the spare capacity on the unaffected lightpath and the free spectrum. It is crucial to acknowledge that the second condition leads to a higher increase in the operational expense (OPEX) of the operator.

For this reason, spectrum defragmentation has to be performed reactively to ensure sufficient spectrum width for the expansion process. A typical example of the reactive defragmentation (RD) technique for avoiding traffic disruption is push-pull (PP) defragmentation [16]. This technique gradually shifts the unaffected spectrum step by step without making any spectrum leaps.

This work proposes two strategies for optimizing resource usage in IP-over-EON networks. The first strategy involves performing the best path selection to optimize the usage of unaffected lightpaths and minimize the need for spare spectrum expansion. To achieve this, we propose the lightpath reconfiguration and spectrum expansion (LRSE) algorithm, an extension of our previous work in [12]. The second strategy focuses on executing the RD algorithm using the PP defragmentation technique, specifically when the neighboring spectrum blocks hinder the expansion process. The primary goals of these strategies are to reduce lightpath reconfigurations, minimize the establishment of new lightpaths, decrease power consumption, and lower OPEX.

By implementing the LRSE+RD strategies, network operators can optimize the use of existing resources, which are often over-provisioned to handle peak traffic. This delay in adding network resources can have a positive impact on increasing operator revenue in the long run.

2. RELATED WORK

Adaptive routing in EONs has been proposed in several papers. In [13], a routing method was introduced by using distance-adaptive modulation and bit rate-adaptive techniques to enhance spectrum utilization efficiency. Another study by [17] focused on improved adaptive routing and proposed two algorithms to minimize rejected demands or the probability of bandwidth blocking. Additionally, [18] presented an adaptive routing algorithm that finds a path based on the maximum available free FSs. In the context of survivable EONs, [19] addressed adaptive routing for various traffic classes. The work by [20] took into account aspects of survivability during connection requests in EONs and employed several strategies to solve routing, spectrum allocation, and scheduling problems for multi-class traffic. To minimize the spectrum fragmentation problem for dynamic traffic conditions in EONs, [21] introduced an adaptive routing scheme with first-last-mixed-fit spectrum assignment. Combining distance and hop, [22] proposed a method to overcome the problem of dynamic traffic grooming by determining the route for each traffic demand based on the path length threshold.

Spectrum defragmentation strategy for EONs was explained in [16, 23-29]. Specifically, in [23], dynamic spectrum defragmentation was explored based on the current condition of the routing network. The study by [24] introduced a hitless reconfiguration strategy using the PP defragmentation mechanism to relocate existing lightpaths and accommodate incoming requests efficiently. By using the hop tuning technique, [25] studied reactive defragmentation to improve spectral efficiency. Moreover,

[26] presented a route partitioning strategy that utilizes the PP defragmentation technique to maximize allowed traffic in EONs. Proactive and reactive defragmentation processes were proposed to enhance spectrum utilization efficiency [16]. A metaheuristic approach was also suggested to simplify connection reconfiguration and FSs index realignment [27]. The work by [28] focused on reactive defragmentation and spectrum conversion, illustrating situations where a connection request cannot be fulfilled due to the unavailability of the same spectrum allocation on the selected path. In such cases, the existing connection was re-established on a shorter path, or the FSs allocation was shifted. Furthermore, [29] discussed optimal defragmentation and split spectrum techniques for serving connection requests. When spectrum allocation on a single path was insufficient, traffic demand was split across the shortest link-disjoint paths.

Table 1. The notations listed in this paper

Notation	Description
$G(V,E)$	the topology of the IP-over-EON, V symbolizes all routers, and E symbolizes all IP layer logical links.
B	the total number of FS on each EON layer link.
m	the lightpath modulation level is used to carry a logical link in the IP layer between two routers, where u and $v \in V$.
$tp_{u,v}$	the indicator is set to 1 if routers u and v can be connected by lightpaths; otherwise, it is set to 0 (u and $v \in V$).
R	the matrix is utilized to save all of the affected flow.
r	an affected traffic flow, $r = (s_r, d_r, t_r, ts_r) \in R$, where s_r and d_r are source and destination routers, t_r is the bit rate, and the number of FSs for t_r is ts_r.
P	the matrix is utilized to save all of the unaffected flow.
p	an unaffected traffic flow, $p = (s_p, d_p, FC_p, SC_p, FCs_p, SCs_p) \in P$, where sp and dp are source and destination routers, full and spare (unused) capacity in bit rate are FC_p and SC_p, and the number of FSs for FC_p and SC_p are FCs_p and SCs_p.
fsp	the number of free FSs that exist between any p and its neighbors.
$fsp_{t\text{-}n}$	the number of free FSs that exist between p_{target} (p is used to recover r) and $p_{neighbor}$ (p is exactly on the left and right of p_{target}).
PSC_p	the potential spare capacity of p, namely the sum of spare capacity and free FSs ($SCs_p + fsp_{t\text{-}n}$)
$\Delta fsp_{t\text{-}n}$	the number of free FSs that is still needed to recover t_r, where: $\Delta fsp_{t\text{-}n} = PSCp - ts_r$ (for spectrum expansion), or $\Delta fsp_{t\text{-}n} = fsp - ts_r$ (for setting up a new lightpath), if $\Delta fsp_{t\text{-}n} \geq 0$, $FSvalueList = 0$, and if $\Delta fsp_{t\text{-}n} < 0$, $FSvalueList = \Delta fsp_{t\text{-}n}$ (Algorithm 2).
rl	the indicator that returns 1 if the reconfigured lightpath is reused and 0 otherwise.
nrl	the number of reconfigured lightpaths (rl).
nLR	the number of lightpath reconfigurations in a path that is caused by spectrum expansion or setting up a new lightpath.
$ratioLR$	the ratio between nrl and nLR in a path.
$sumFSv$	the total number of negative values of all $\Delta fsp_{t\text{-}n}$ in a path.
$maxm$	the highest modulation level value in a path.
ro	the broken router, router outage (ro), $ro \in V$.
n	the number of FSs that have just been recently assigned.
W_m	the power consumed by a frequency slot with modulation level (m) (Table 2).
W_0	a constant representing an SBVT's static power consumption ($W_0 = 100$ W).
α	the unit of the power consumption cost ($\alpha = 1$)
c_l	the additional cost of reconfiguring a lightpath
$\|R\|$	the number of affected flows due to a router outage.

Studies on spectrum expansion in EONs were covered in [30-34]. In [30], a dynamic traffic grooming algorithm was proposed, allowing the lightpath to expand and contract based on traffic conditions. The discussion in [31] revolved around the utilization of spectrum spacing between lightpaths to generate free adjacent FSs, accommodating new traffic requests by performing spectrum expansion through traffic grooming. Furthermore, [32] focused on survivable RSA and spectrum expansion or contraction under time-varying traffic conditions. Spectrum expansion or contraction could be simultaneously performed on primary and backup lightpaths when problems occurred in the optical layer. It is important to note that the path selection was based on weighted hop count. The problem of spectrum sharing and defragmentation to address dynamic traffic demands in EON was studied in [33]. Spectrum expansion or contraction was performed to adapt to traffic changes, and when neighboring spectra blocked the expansion process, spectrum defragmentation was executed to generate a free spectrum. The work by [34] proposed several path selection techniques to address the spectrum expansion/contraction problem with delay-variation constraints and multipath routing.

Several multilayer survivability algorithms have been proposed to overcome failures in IP-over-EON. In [10], multilayer survivability techniques were introduced to optimize primary and backup resources under various failure conditions. The work in [7] investigated integrated protection planning, preparing spare capacity between layers to address failures in the optical and IP layers. The study by [11] focused on cost-effective MLR to overcome IP router outages in IP-over-EONs through cross-layer orchestration. A paper [35] analyzed an MLR mechanism in IP-over-EONs, ensuring high-priority traffic was quickly recovered in the IP layer while best-efforts traffic was unloaded to the optical layer. Some MLR methods concentrated solely on the failure problem in the optical layer [36]. In [37], integer linear programming was used to design a multilayer survivability technique in IP-over-EON to overcome latency problems in multi-class traffic.

Table 2. Parameters related to lightpath modulation formats [11].

Modulation Format	Modulation level (m)	Optical reach (km)	Capacity per FS (Gb/s)	Dynamic power usage (W_m) (W)
16QAM	4	600	50	175.5
8QAM	3	1200	37.5	154.4
QPSK	2	2400	25	133.4
BPSK	1	4800	12.5	112.4

Multilayer optimization in IP-over-EON was studied in [12, 38-40]. For example, [38] presented an algorithm for reconfiguring multilayer networks to accommodate periodic IP traffic changes, utilizing spectrum expansion and reduction processes during adaptive bandwidth resizing. A study in [39] investigated dynamic

traffic grooming and proposed adaptive modulation and topology integration based on cross-layer routing and spectrum allocation. In [40], cross-layer spectrum defragmentation was employed to improve spectrum usage in IP-over-EON. The process occurred in both layers by rearranging traffic flows in the IP layer as well as making routing and spectrum utilization changes in the optical layer. The study by [12] proposed adaptive routing to recover traffic after an IP router failure and introduced an ALRP routing strategy that reduced lightpath reconfigurations compared to conventional schemes.

This paper is the development of previous work [12], with a focus on optimizing the reconfigured lightpath usage and implementing a spectrum expansion process that involves reactive defragmentation to obtain sufficient free FSs with minimal addition. It is crucial to acknowledge that this approach differs from what was carried out in [18, 22]. In the reactive defragmentation technique, the PP defragmentation is used without spectrum conversion, and the best path is specifically chosen for recovering affected traffic, as opposed to [25, 28, 29]. When compared to [31, 34, 33], the proposed strategies do not require preparing spectrum spacing; rather, it utilizes existing free FSs to perform spectrum expansion on a selected path. To optimize remaining resources in both layers and reduce the setup of new lightpaths and the process of lightpath reconfiguration, various modulation formats and an adaptive routing strategy are employed, achieving better results than the ones presented in [11]. Furthermore, the approach differed from [39, 10, 35], and [37], as all affected traffic is restored using the same strategies (adaptive routing and reactive defragmentation). There is no prioritization of specific traffic, and the spare capacity of unaffected lightpath is utilized for MLR.

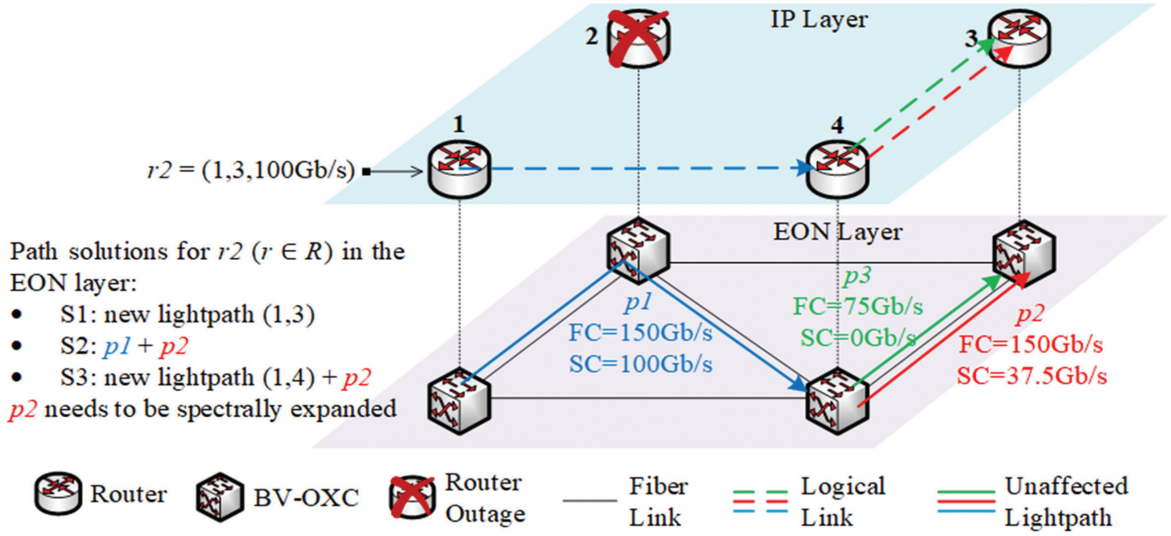

Fig. 1. IP-over-EON architecture after a router outage and three path solutions to recover affected traffic *r*2.

The main objective of the proposed strategies is to minimize lightpath reconfigurations, new lightpaths, power consumption, and OPEX. This study is necessary because the strategies can effectively reduce additional OPEX, leading to increased operator profitability. It is crucial to acknowledge that no recent study has integrated adaptive routing, spectrum expansion, and reactive defragmentation in IP-over-EON, specifically for recovering affected traffic caused by a router outage.

3. ADAPTIVE ROUTING AND REACTIVE DEFRAGMENTATION

3.1. NETWORK MODEL AND ARCHITECTURE

Figure 1 depicts an IP-over-EON multilayer network architecture with two layers interconnected using short-reach fibers. The notation $G(V,E)$ represents the IP-over-EON topology, where V corresponds to the set of IP routers, and E indicates the set of logical links. Two routers (u and $v \in V$) in the IP layer can be connected to one or more logical links, and a lightpath in the EON layer supports each logical link ($e \in E$). These logical links possess essential properties such as router pairs (source and destination), total capacity, spectrum allocation, and modulation level, providing crucial information about the EON layer.

In addition to serving as a destination router, an IP router can also function as an intermediate router. Data packets entering an IP router are then forwarded to the fiber optic cable in the EON layer for transmission until they reach the destination router, where further processing occurs [37]. In case an IP router experiences a failure, the operator removes the affected IP router ($v \in V$). Consequently, the IP-over-EON network state is updated, and all affected traffic is stored in R if the router outage occurs at an intermediate router. Spare capacities of the unaffected lightpaths are utilized to recover all this affected traffic. Due to the unpredictable nature of IP traffic, the utilization of these spare capacities may not have been fully optimized. Conversely, if the

outage happens at the destination or source router, the impacted traffic can only be recovered once the IP router is repaired.

The affected traffic ($r \in R$) is groomed into an unaffected lightpath with sufficient spare capacity. However, when there is insufficient spare capacity to accommodate the impacted traffic, two recovery processes are employed, namely spectrum expansion or the establishment of a new lightpath [11]. This leads to the initiation of the lightpath reconfiguration procedure. Setting up a new lightpath is generally more common when the affected traffic is heavy or when limited available FSs exist between an unaffected spectrum and its neighbors, making it impossible to achieve maximum spectral expansion on the unaffected lightpath. Consequently, this causes increased OPEX due to lightpath reconfiguration procedures and higher use of SBVTs and FSs.

To minimize the recovery cost for each affected traffic, the LRSE+RD strategies are adopted. This approach helps to reduce the lightpath reconfiguration procedures and facilitates the process of spare spectrum expansion. This is made possible by leveraging the reactive defragmentation technique, which ensures sufficient free spectrum to meet the traffic demands. The notations utilized in this paper are shown in Table 1.

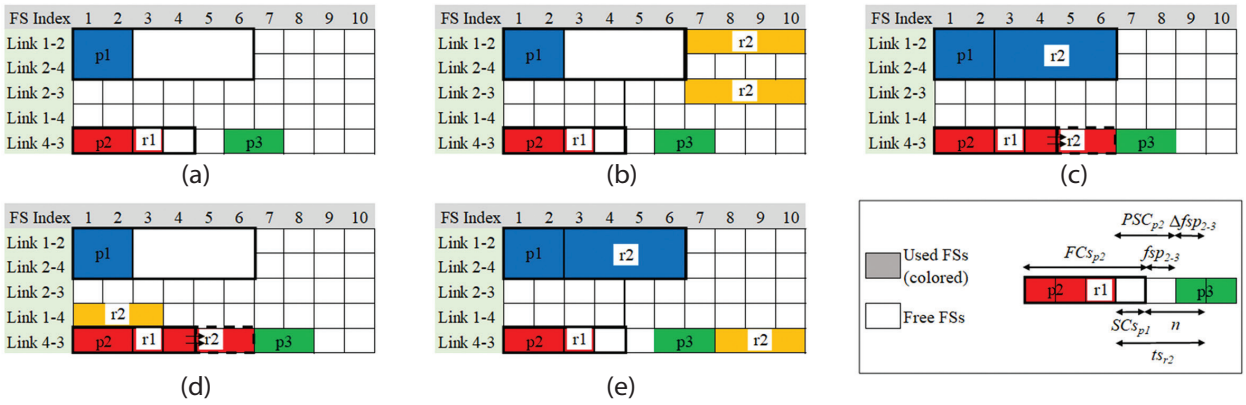

Fig. 2. Spectrum management of $r2$ for the three path solutions: (a) Initial condition; (b) $S1$ with LRSE+RD; (c) $S2$ with LRSE+RD; (d) $S3$ with LRSE+RD; and (e) $S2$ with LRSE-O.

3.2. PROPOSED STRATEGIES

This section elaborates on the mechanisms of both the LRSE and RD strategies. For example, Figs. 1 and 2 show the condition of the IP-over-EON network after a router outage (ro = 2) and the spectrum allocation of the three path solutions. In the EON layer, three unaffected lightpaths ($p1$, $p2$, and $p3$) possess varying full and spare capacities. Specifically, in router 1, an affected flow ($r2$) is being recovered to router 3, with affected traffic of 100 Gb/s. Based on the network condition in Fig. 1, three path solutions ($S1$, $S2$, and $S3$) are available for $r2$. All links are assumed to have a uniform distance of 1000 km. Fig. 2(a) shows the initial spectrum assignment condition of the three unaffected lightpaths and an affected flow $r1$, which has been recovered using the spare capacity of $p2$, amounting to 1 FS.

For the first path solution ($S1$), a new lightpath is established starting from BV-OXC 1, passing through BV-OXC 2, and terminating in BV-OXC 3. The distance of the new lightpath in the EON layer is 2000 km, and its modulation level (m) is 2, as seen in Table 2. This leads to one lightpath reconfiguration (nLR = 1) and a $ratioLR$ = 0 (nrl = 0 since there is no reuse of the reconfigured lightpath). Furthermore, to recover affected traffic $r2$ (ts_{r2} = 4) on path $S1$, a minimum of four free FSs (fsp ≥ 4) is required to fulfill the spectrum continuity and contiguity requirements. In case this condition is satisfied ($fsp \geq ts_{r2}$), a new lightpath can be established (Δfsp = 0, $sumFSv$ = 0). Finally, $maxm$ is equal to 2, as only one modulation level is generated by one lightpath reconfiguration in $S1$. It should be noted that $S1$ only uses the LRSE strategy, and the RD strategy is not implemented. This is because, for setting up a new lightpath, there has to be sufficient free spectrum width that matches the needs of the affected traffic. If $S1$ is selected as the path solution, the result of allocating the spectrum for $r2$ can be seen in Fig. 2(b).

On the alternative path ($S2$), two unaffected lightpaths ($p1$ and $p2$) are used. Meanwhile, this spare capacity of $p1$ is sufficient to recover traffic $r2$, and $p2$ (distance = 1000 km, m = 3) has a smaller spare capacity (SCs_{p2} = 1) than traffic $r2$ (ts_{r2} = 3), necessitating spectral extension (nLR = 1). Figure 2(a) shows that between $p2$ and $p3$, only one free FS ($fsp_{2\text{-}3}$ = 1) is available, leading to a shortage of 1 free FS ($\Delta fsp_{2\text{-}3}$ = -1; $SCs_{p2} + fsp_{2\text{-}3} - ts_{r2}$ = 1 + 1 - 3). The values for $maxm$ and $sumFSv$ are 3 and -1, respectively, indicating the need for only one lightpath reconfiguration procedure. Both LRSE and RD strategies are employed in $S2$, of which if $S2$ is selected as the best path in *Algorithm* 2, the PP defragmentation technique will be performed (*Algorithm* 3), leading to the shifting of spectrum $p3$ to the right by 1 FS. Successful reactive defragmentation allows spectrum expansion to recover traffic $r2$ into $p2$.

The result of $ratioLR$ in $S2$ is 1, resulting from the reuse of $p2$, which is previously utilized for traffic groom-

ing $r1$ (nlr =1). Figure 2(c) shows the final spectrum assignment result of recovering traffic $r2$ into $p1$ and $p2$ using LRSE and RD strategies. In contrast, Fig. 2(e) shows the result if the path from $S2$ used only the LRSE strategy without the RD strategy (LRSE-O).

The path in $S3$ finally results from setting up a new lightpath from BV-OXC 1 to BV-OXC 4 (following a similar procedure to $S1$) and using $p2$ (as in $S2$). Based on these results, there are two lightpath reconfigurations (nLR = 2), $ratioLR$ = 0.5 (nlr = 1), $sumFSv = \Delta fsp_{2\text{-}3}$ = -1 (obtained from using $p2$), and $maxm$ = 3 (both lightpath reconfigurations use the same modulation level). Figure 2(d) shows the spectrum assignment result of the affected flow $r2$ in $S3$. In this regard, the LRSE and RD strategies are executed.

Table 3. The results of the multiple criteria for the three path solutions are in Fig. 1.

Path Solution	*nLR*	*ratioLR*	*sumFSv*	*maxm*	Figure
$S2$	1	1/1	-1	3	2(c)
$S1$	1	0/1	0	2	2(b)
$S3$	2	1/2	-1	3	2(d)

Table 3 shows the outcome of the criteria for each path solution in Fig. 1, and after sorting (according to *Algorithm* 2, *Line* 25), $S2$ is determined to be the best path solution. The explanation of *Algorithm* 2 is provided in the following subsection.

3.3. PROPOSED ALGORITHMS

Algorithm 1 provides an overview of the entire procedure implemented in this study. This involves sorting all affected traffic (R) in descending order, and the recovery of each affected traffic utilizes a path obtained from *Algorithm* 2, while *Algorithm* 3 employs the reactive defragmentation strategy.

***Algorithm* 1**: Overall Procedure

1. **while** use the MLR algorithm in [11] **do**
2. use *Algorithm* 2 to find a path solution;
3. **if** $PSC_p < ts_r$ **then**
4. use *Algorithm* 3 to perform the PP defragmentation technique;
5. **if** the defragmentation process is successful **then**
6. spectrum expansion process can be executed to restore ts_r;
7. **else**
8. **continue** the MLR algorithm;
9. **end**
10. **end**
11. **end**

The LRSE strategy in *Algorithm* 2 is designed to find the best path using multiple criteria. The procedure is as follows: all alternative paths are obtained from the pair of routers s_r and d_r, then searched for the combination of links (u, v) for each path s ($s \in S$) (*Line* 4). In this process, it is ensured that u or v is not a router outage on each link (u, v), and both can be connected ($tp_{u,v}$ = 1). The specific link combinations of each path solution are shown in Fig. 1. In *Line* 6, each link (u, v) is compared with the existing ones in P. In case the result is blank (indicating the need to set up a new lightpath) or if it already existed but SCs_p is less than ts_r (representing the need to expand the spectrum p ($p \in P$)), an additional lightpath reconfiguration (nLR) is performed. Moreover, the modulation level (m) value in $maxm$ is adjusted when m is greater (*Lines* 7-9). Lower values for the variables nLR and $maxm$ lead to reduced additional OPEX costs. These variables are then sorted in ascending order (*Line* 25). Furthermore, in *Lines* 11-13, if a lightpath on the link (u, v) has been reconfigured before (for example, in Figs. 2(c) and 2(d), where $p2$ is used to recover $r1$), the same lightpath is re-selected to recover the next affected traffic (resulting in an increase in the value of nrl) and to save the difference of FSs ($\Delta fsp_{t\text{-}n}$) that are still needed to recover ts_r.

Lines 16 and 18 store the value of $\Delta fsp_{t\text{-}n}$ in preparation for setting up a new lightpath. Specifically, in *Line* 16, when there are not enough free FSs (fsp) to recover ts_r (the value of *FSvalueList* was *-Inf*), and in *Line* 18, when fsp is greater than or equal to ts_r In the case of multiple conditions ($fsp \geq ts_r$), the fsp with the largest number of free FSs is selected. This ensures that when the lightpath is reused to recover the next affected traffic, some free FSs are still available for traffic grooming. After obtaining the results of both $ratioLR$ and $sumFSv$ variables (*Lines* 22-23), they are sorted in descending order in *Line* 25. The $ratioLR$ variable is prioritized using the reconfigured lightpath in the path selection, while the variable $sumFSv$ (sorted from smallest to largest negative values) aims to minimize $p_{neighbor}$ shift when the PP defragmentation technique (*Algorithm* 3) is executed on the links of the path.

***Algorithm* 2**: LRSE Strategy

Input: $G(V,E)$ after router outage, ro, $tp_{u,v}$, $r \in R$, and $p \in P$

Output: a path solution

1. find all paths between s_r and d_r, store them in matrix of path solutions S;
2. **for** each path $s \in S$ **do**
3. set nLR, $ratioLR$, $sumFSv$, $maxm$, nrl, $FSvalueList$ = 0;
4. find and select the link combination (u, v) for path s, which does not originate from or end at ro with $tp_{u,v}$ =1;
5. **for** each link (u,v) $\in s$ **do**

6. save p $(p \in P)$, which has the same link as (u,v) to *OptionList*;
7. **if** *OptionList* == Ø or *OptionList* does not have $SCs_p \geq ts_r$ **then**
8. $nLR = nLR + 1$;
9. calculate m and update *maxm* if it is higher;
10. **end**
11. **if** rl ==1 **then**
12. $nrl = nrl + 1$;
13. save $\Delta fsp_{t\text{-}n}$ to *FSvalueList*;
14. **else**
15. **if** *OptionList* == Ø and $fsp < ts_r$ then
16. save -*Inf* to *FSvalueList*;
17. **else**
18. save $\Delta fsp_{t\text{-}n}$ to *FSvalueList*;
19. **end**
20. **end**
21. **end**
22. calculate the ratio between *nrl* and *nLR*, and store them in *ratioLR*;
23. calculate the total negative values in *FSvalueList*, and store them in *sumFSv*;
24. **end**
25. sort S by *nLR*(min), *ratioLR*(max), *sumFSv*(max), and *maxm*(min);

Algorithm 3 represents the reactive defragmentation (RD) strategy that utilizes the PP defragmentation technique. Typically, it is executed whenever the spectrum expansion of p_{target} in the link (u, v) is obstructed by $p_{neighbor}$ due to a lack of free FSs ($\Delta fsp_{t\text{-}n} < 0$). In such cases, if there are $p_{neighbor}$ to the left and/or right of the p_{target}, their spectrum is shifted step by step towards the left and/or right until sufficient free FSs are obtained to recover ts_r (*Lines* 3-9). However, if the $p_{neighbor}$ shift fails to produce $\Delta fsp_{t\text{-}n} = 0$ ($PSC_p = ts_r$), the PP defragmentation technique is deemed unsuccessful, and the algorithm stops (*Lines* 10-13). In this scenario, the process continues by establishing a new lightpath in *Algorithm* 1.

***Algorithm* 3**: RD Strategy

Input: $G(V,E)$ after router outage, $r \in R$, and $p \in P$

Output: enough free FSs for ts_r

1. find p_{target}, $p_{neighbor}$, and calculate $\Delta fsp_{t\text{-}n}$
2. **while** $\Delta fsp_{t\text{-}n} < 0$ **do**
3. **if** $p_{neighbor}$ is on the left of p_{target} **then**
4. shift $p_{neighbor}$ one step to the left;
5. **end**
6. **if** $p_{neighbor}$ is on the right of p_{target} then
7. shift $p_{neighbor}$ one step to the right;
8. **end**
9. update $p_{neighbor}$, and $\Delta fsp_{t\text{-}n}$;
10. **if** $p_{neighbor}$ cannot be shifted and $\Delta fsp_{t\text{-}n} < 0$ then
11. *DefragProcess* = **False**;
12. **break**;
13. **end**
14. **end**

The optimization algorithm aims to minimize the additional OPEX (C) as shown in (1), where α represents the unit cost of power consumption, and its value is set to 1 for power cost normalization. Meanwhile, the additional power consumption is expressed as $W_m \cdot n + W_0$. In this aspect, W_m denotes the power consumption for using an FS at a modulation level (m), and its values can be seen in Table 2. W_0 represents a static value derived from the power usage of an SBVT [5]. When a new lightpath is established, W_0 is equal to 100 W; otherwise, the value is 0.

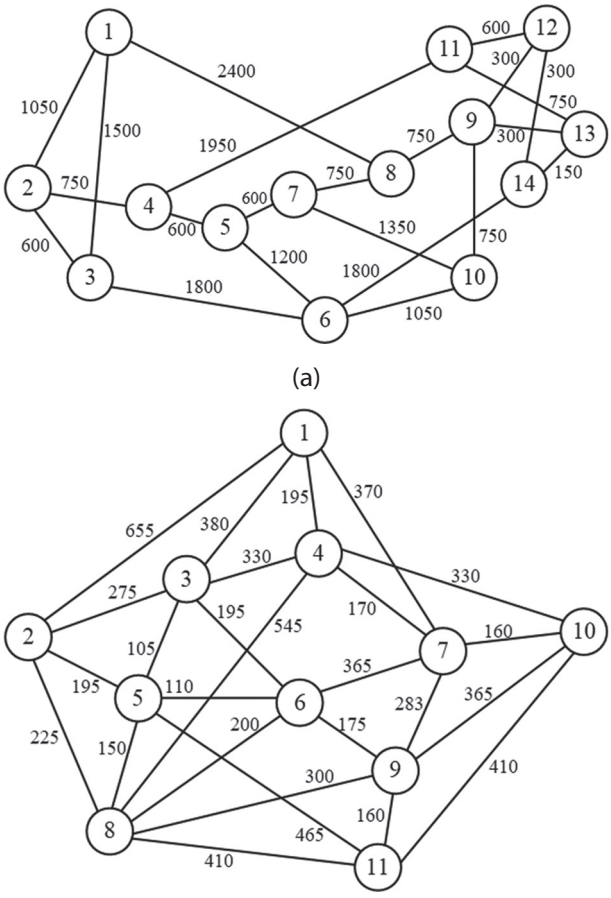

Fig. 3. IP-over-EON topologies (optical fiber length measured in kilometers); (a) NSFNET topology (14 nodes, 22 links), and (b) Cost239 topology (11 nodes, 26 links).

$$C = \alpha \cdot (W_m \cdot n + W_0) + c_l \quad (1)$$

$$n = ts_r - SCs_p \quad (2)$$

Equation (2) shows the number of newly used FSs (n), which is obtained from the difference in FSs between the affected traffic (ts_r) and the unaffected spare capacity (SCs_p). To calculate the number of FSs for an affected traffic t_r (in Gbps), (3) is used [39]. The same equation can also be used to determine the value of SCs_p. The value 12.5 represents the width of an FS (in GHz), and m denotes the modulation level of a lightpath (in bps/Hz). The value of m is significantly influenced by the transmission distance of the lightpath, as shown in Table 2.

$$ts_r = \left\lceil \frac{t_r}{12.5 \cdot m} \right\rceil \quad (3)$$

$$c_l = |R| \cdot \left(\sum_{u,v \in V} tp_{u,v} \right) \cdot \left(\sum_{r \in R} \left\lceil \frac{t_r}{12.5} \right\rceil \cdot \max(W_m) + W_0 \right) \quad (4)$$

In view of the upper limit of the total power cost (cl) in (4) and the primary objective of minimizing lightpath reconfiguration, various parameters are examined. The number of affected flows is denoted as $|R|$, and $\sum_{u,v \in V} tp_{u,v}$ represents the sum of all router pair indicators. Additionally, $\sum_{r \in R} [t_r / (12.5)]$ indicates the sum of all affected traffic divided by the width of an FS, which is the highest value of the number of FSs for all affected traffic. $max(W_m)$ refers to the highest value of W_m when recovering affected traffic requires more than one lightpath with varying power consumption. It is important to note that α, (1), (2), and (4) pertain to [11]. Sufficient resources are assumed to be available to recover all affected traffic (R) using the strategies in this current study.

4. PERFORMANCE EVALUATION

4.1. SIMULATION PARAMETERS

For testing the algorithms, the NSFNET topology [11] and the Cost239 topology [41] were employed as IP-over-EON, as shown in Figs. 3(a) and 3(b), respectively. To simulate the existing network conditions before a router outage occurred, several parameters were utilized. The maximum number of FSs for each fiber link was set to 358 FSs, with each FS having a bandwidth of 12.5 GHz. The capacity of the FS was determined by the modulation level, as shown in Table 2.

In the IP layer, connections for each router pair u-v ($tp_{u,v}$) were randomly selected from the range [0,1]. When both routers (u and v) could be connected ($tp_{u,v}$ = 1), one or more existing lightpaths in the EON layer were presented, with each consisting of several FSs. The number of existing lightpaths and their FSs were randomly chosen from the sets [1,4] and [1,10], respectively. It was noted that all existing lightpaths for the same router pair utilized the same physical routing path, which was randomly chosen from several path options in the EON layer.

For example, in the NSFNET topology, a pair of routers 1 and 4 could be connected ($tp_{1,4}$ = 1). From the random results, two existing lightpaths were obtained, each having a full capacity of 8 FSs. If the chosen physical path was 1-2-4, the first and second lightpaths connected routers 1-2 and routers 2-4, respectively, provided that $tp_{1,2}$ = 1 and $tp_{2,4}$ = 1. The configuration of each existing lightpath followed a first-fit spectrum assignment [14].

To simulate dynamic IP traffic conditions, spare capacity was randomly assigned to each existing lightpath. Two traffic conditions, namely heavy and moderate, were used to generate the spare capacity. Under heavy traffic conditions, each lightpath, on average, had 20% spare capacity, while the moderate condition had 40%. These values of 20% and 40% were determined by averaging the spare capacity of all existing lightpaths, leading to a more varied distribution of spare capacity (including the used capacity) for each existing lightpath.

After establishing the existing network conditions, a router outage was randomly selected, and all affected traffic in R was generated with fixed total traffic volumes ranging from 1 to 3 Tb/s (in increments of 0.5 Tb/s). The traffic in R was then sorted from largest to smallest, and each affected traffic ($r \in R$) was recovered using the aforementioned algorithms. Ten iterations were performed for each fixed total traffic volume, and the final data was obtained by averaging the results. The simulation program was developed using Matlab software and executed on a computer equipped with an Intel i7-7500U processor (clock speed of 2.7GHz), 8GB of RAM, and a Windows 10 operating system.

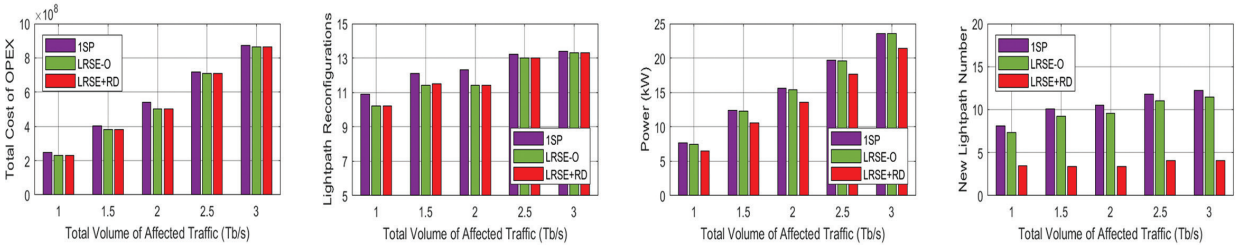

Fig. 4. The results of the heavy traffic simulation in NSFNET topology: (a) total cost of OPEX; (b) lightpath reconfigurations; (c) power consumption; and (d) new lightpaths

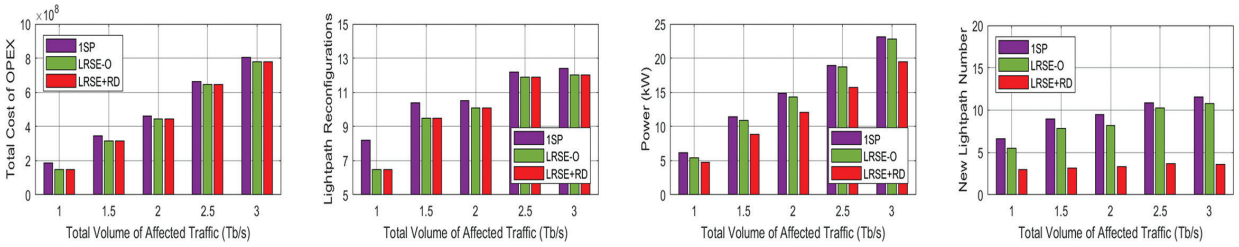

Fig. 5. The results of the moderate traffic simulation in NSFNET topology: (a) total cost of OPEX; (b) lightpath reconfigurations; (c) power consumption; and (d) new lightpaths

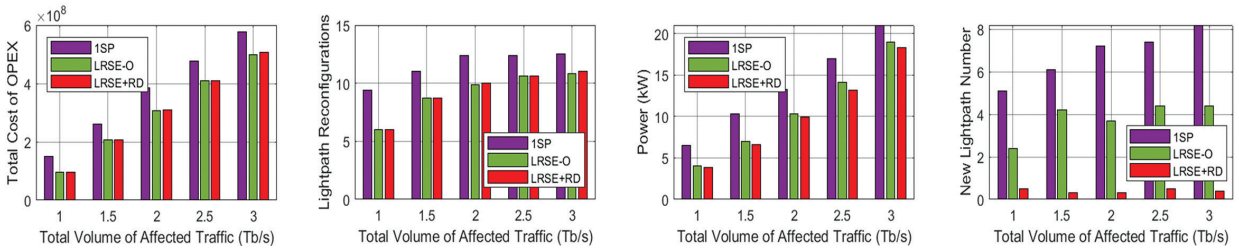

Fig. 6. The results of the heavy traffic simulation in Cost239 topology: (a) total cost of OPEX; (b) lightpath reconfigurations; (c) power consumption; and (d) new lightpaths

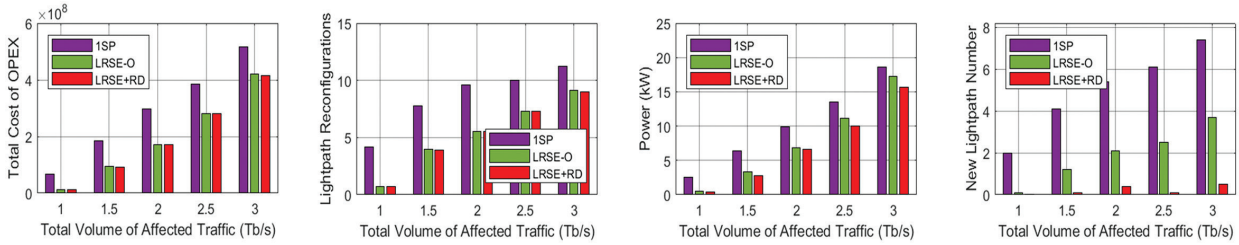

Fig. 7. The results of the moderate traffic simulation in Cost239 topology: (a) total cost of OPEX; (b) lightpath reconfigurations; (c) power consumption; and (d) new lightpaths

The LRSE strategy utilized all the existing data to determine the best alternative path for recovering the traffic of the affected flow. In *Algorithm* 1, the LRSE path was processed with the RD strategy in *Algorithm* 3 (LRSE+RD) and without the RD strategy (LRSE-O). Additionally, *Algorithm* 1 was run without the RD strategy, using the first shortest path (1SP) as a benchmark [11]. All strategies were able to execute the spectrum expansion process to recover all affected traffic.

4.2. NSFNET TOPOLOGY SIMULATION RESULTS

During the simulation, 1SP, LRSE-O, and LRSE+RD were compared using the NSFNET topology. The results of the simulation under heavy traffic conditions are shown in Fig. 4. Figs. 4(a) and 4(b) show the total cost of OPEX as well as the number of lightpath reconfigurations, respectively. Both figures indicated that LRSE-O and LRSE+RD yielded similar results due to their use of the same path solution. However, the outcomes of both strategies were still lower than the benchmark, 1SP. As the total volume of affected traffic increased, the performance gap between LRSE-O and LRSE+RD with 1SP narrowed, as shown in Fig. 4(a), which is understandable since the gap in Fig. 4(b) also generated a similar trend.

At 1 Tb/s, the LRSE algorithm effectively identified a path that optimally utilized spare capacities on unaffected lightpaths in each link, allowing for the accommodation of some affected traffic and minimizing lightpath reconfigurations, as shown in Fig. 4(b). However, at 3 Tb/s, the gap became smaller as the heavier traffic of affected flows could no longer be accommodated within spare capacities on unaffected lightpaths, often necessitating reconfiguration procedures (such as spectrum expansion or setting up a new lightpath). It should be noted that the algorithm utilized still outperformed 1SP in Fig. 4(b).

Figure 4(c) shows the additional power consumption result, with LRSE-O slightly outperforming 1SP, while LRSE+RD achieved even lower power consumption. The same trend was observed in the number of new lightpaths shown in Fig. 4(d), with LRSE+RD obtaining the lowest result. This indicated that the lightpath

reconfiguration number between LRSE-O and LRSE+RD was comparable in Fig. 4(b), but in Fig. 4(d), the number of new lightpaths created by LRSE+RD was further minimized, leading to reduced additional power consumption as seen in Fig. 4(c). As the total volume of affected traffic in Fig. 4(d) increased, the gap between LRSE+RD and the other two strategies also increased, suggesting that the use of the LRSE path and RD strategy maximized the spectrum expansion process, resulting in minimal increases in the number of new lightpaths at each data point.

Fig. 5 shows the simulation results under moderate traffic conditions, revealing similar graphical patterns to those shown in Fig. 4. However, in Fig. 5(b), a smaller lightpath reconfiguration number was observed compared to Fig. 4(b). This difference resulted from the larger average spare capacities of unaffected lightpaths in moderate traffic, which could be used to recover some affected traffic. All the simulations presented in Fig. 5 showed that LRSE+RD consistently generated lower values than 1SP.

4.3. COST239 TOPOLOGY SIMULATION RESULTS

Figs. 6 and 7 show the simulation results after the router outage occurred under heavy and moderate traffic conditions in the Cost239 topology. Specifically, Fig. 6 shows a trend similar to that in Fig. 4 but with lower values for all four test parameters. This result stemmed from the lower number of nodes in the Cost239 topology compared to the NSFNET topology, which resulted in the number of router pairs decreasing, leading to a higher number of available free FSs.

The abundance of free FSs impacted the number of new lightpaths generated by LRSE+RD in Fig. 6(d), which was substantially lower than that of LRSE-O and 1SP. In other words, the LRSE+RD strategy optimized the lightpath reconfigurations with a spectrum expansion process when there were more free FSs. Similar conditions are also observed in Fig. 7. The simulation results in Fig. 7 further confirmed the advantages of the LRSE+RD strategies over 1SP and LRSE-O.

5. CONCLUSION

This paper focuses on strategies for recovering all affected traffic following the failure of an IP router in IP-over-EON. Two key strategies were employed: adaptive routing and reactive defragmentation. The adaptive routing strategy utilized LRSE to optimize the utilization of unaffected lightpaths and expanded their spare spectrum minimally, generating the best path based on various criteria in the EON layer. Simultaneously, the RD strategy was applied to ensure sufficient free FSs through the push-pull defragmentation technique, which was triggered when the neighboring spectrum blocked the spectrum expansion process. The LRSE+RD strategies aimed to minimize lightpath reconfigurations, additional power consumption, and the setup of new lightpaths, leading to reduced OPEX. Through simulations conducted in both topologies (NSFNET and Cost239) under heavy and moderate traffic conditions, it became evident that the LRSE+RD strategies consistently exhibited the lowest values among all four test parameters compared to the 1SP benchmark. In comparison to LRSE-O, the LRSE+RD strategies achieved lower values in the number of new lightpaths and additional power consumption parameters, while the same positive results were obtained for the other two test parameters. Looking ahead, the future study will focus on applying a metaheuristic approach to enhance the proposed strategies.

6. REFERENCES

[1] N. Kitsuwan, P. Pavarangkoon, A. Nag, "Elastic Optical Network with Spectrum Slicing for Fragmented Bandwidth Allocation", Optical Switching and Networking, Vol. 38, 2020, pp. 1-14.

[2] E. Gandhimathi, A. Swarnalatha, B. Sowmya, G. Palani, "Spectrum Resource Optimization in Elastic Optical Networks using Dynamic RMSA", Optical and Quantum Electronics, Vol. 54, No. 4, 2022, pp. 1-16.

[3] Y. Qiu, "Spectrum Defragmentation in Flexible Grid Optical Networks", Proceedings of SPIE International Conference on Optical Instruments and Technology: Optical Communication and Optical Signal Processing, Beijing, China, 26-28 October 2019, pp. 1-9.

[4] S. M. H. Ghazvini, A. G. Rahbar, B. Alizadeh, "Load Balancing, Multipath Routing and Adaptive Modulation with Traffic Grooming in Elastic Optical Networks", Computer Networks, Vol. 169, 2020, pp. 1-21.

[5] N. Sambo et al. "Next Generation Sliceable Bandwidth Variable Transponders", IEEE Communications Magazine, Vol. 53, No. 2, 2015, pp. 163-171.

[6] Q. Zhu, X. Yu, Y. Zhao, A. Nag, J. Zhang, "Auxiliary-Graph-Based Energy-Efficient Traffic Grooming in IP-Over-Fixed/Flex-Grid Optical Networks", Journal of Lightwave Technology, Vol. 39, No. 10, 2021, pp. 3011-3024.

[7] W. Lu, X. Yin, X. Cheng, Z. Zhu, "On Cost-Efficient Integrated Multilayer Protection Planning in IP-Over-EONs", Journal of Lightwave Technology, Vol. 36, No. 10, 2018, pp. 2037-2048.

[8] R. Govindan, I. Minei, M. Kallahalla, B. Koley, A. Vahdat, "Evolve or Die: High-Availability Design Principles Drawn from Google's Network Infrastructure", Proceedings of the ACM SIGCOMM Conference, Florianopolis, Brazil, 22-26 August 2016, pp. 58-72.

[9] M. Ruiz, O. Pedrola, L. Velasco, D. Careglio, J. Fernández-Palacios, G. Junyent, "Survivable IP/MPLS-Over-WSON Multilayer Network Optimization", Journal of Optical Communications and Networking, Vol. 3, No. 8, 2011, pp. 629-640.

[10] S. Iyer, "Investigation of Cost and Spectrum Utilization in Internet Protocol- over-Elastic Optical Networks", Journal of Optics, Vol. 49, 2020, pp. 279-290.

[11] S. Liu, W. Lu, Z. Zhu, "On the Cross-Layer Orchestration to Address IP Router Outages With Cost-Efficient Multilayer Restoration in IP-over-EONs", Journal of Optical Communications and Networking, Vol. 10, No. 1, 2018, pp. A122-A132.

[12] Ridwansyah, S. Syarif, Dewiani, Wardi, "Minimizing the additional costs due to Router Outage in IP-over-EON using Adaptive Routing", Proceedings of the 10th IEEE International Conference on Communication, Networks and Satellite, Purwokerto, Indonesia, 17-18 July 2021, pp. 146-151.

[13] A. Agrawal, V. Bhatia, S. Prakash, "Spectrum Efficient Distance-Adaptive Paths for Fixed and Fixed-Alternate Routing in Elastic Optical Networks", Optical Fiber Technology, Vol. 40, 2018, pp. 36-45.

[14] L. Ruiz, R. J. D. Barroso, I. D. Miguel, N. Merayo, J. C. Aguado, E. J. Abril, "Routing, Modulation and Spectrum Assignment Algorithm Using Multi-Path Routing and Best-Fit", IEEE Access, Vol. 9, 2021, pp. 111633-111650.

[15] B. C. Chatterjee, N. Sarma, E. Oki, "Routing and Spectrum Allocation in Elastic Optical Networks: A Tutorial", IEEE Communications Surveys & Tutorials, Vol. 17, No. 3, 2015, pp. 1776-1800.

[16] S. Fernandez-Martínez, B. Baran, D. P. Pinto-Roa, "Spectrum Defragmentation Algorithms in Elastic Optical Networks", Optical Switching and Networking, Vol. 34, 2019, pp. 10-22.

[17] I. Olszewski, "Improved dynamic routing algorithms in elastic optical networks", Photonic Network Communications, Vol. 34, 2017, pp. 323-333.

[18] A. N. Khan, "A Constrained Maximum Available Frequency Slots on Path Based Online Routing and Spectrum Allocation for Dynamic Traffic in Elastic Optical Networks", International Journal of Electronics and Telecommunications, Vol. 66, No. 4, 2020, pp. 707-714.

[19] M. Aibin, K. Walkowiak, "Adaptive Survivability Algorithm for Path Protection with Various Traffic Classes in Elastic Optical Networks", Proceedings of the 7th International Workshop on Reliable Networks Design and Modeling, Munich, Germany, 5-7 October 2015, pp. 56-62.

[20] E. E. Moghaddam, H. Beyranvand, J. A. Salehi, "Routing, Spectrum and Modulation Level Assignment, and Scheduling in Survivable Elastic Optical Networks Supporting Multi-Class Traffic", Journal of Lightwave Technology, Vol. 36, No. 23, 2018, pp. 5451-5461.

[21] A. N. Khan, "Online Routing, Distance-Adaptive Modulation, and Spectrum Allocation for Dynamic Traffic in Elastic Optical Networks", Optical Fiber Technology, Vol. 53, 2019, pp. 1-8.

[22] P. Majumdar, T. De, "A Distance-Based Adaptive Traffic Grooming Algorithm in Large EON Under Dynamic Traffic Model", Proceedings of the 2nd International Conference on Computing, Analytics and Networking, Bhubaneswar, India, 14-15 December 2019, pp. 225-236.

[23] M. Zhang, C. You, H. Jiang, Z. Zhu, "Dynamic and Adaptive Bandwidth Defragmentation in Spectrum-Sliced Elastic Optical Networks With Time-Varying Traffic", Journal of Lightwave Technology, Vol. 32, No. 5, 2014, pp. 1014-1023.

[24] R. Wang, B. Mukherjee, "Provisioning in Elastic Optical Networks with Non-Disruptive Defragmentation", Journal of Lightwave Technology, Vol. 31, No. 15, 2013, pp. 2491-2500.

[25] S. K. Posam, S. K. Bhyri, R. Gowrishankar, V. N. Challa, S. S. S. Sanagapati, "Reactive Hitless Hop tuning based Defragmentation Algorithm for Enhanced Spectrum Efficiency in Elastic Optical Networks", Proceedings of the IEEE International Conference on Advanced Networks and Telecommunication Systems, New Delhi, India, 14-17 December 2020, pp. 1-6.

[26] S. Ba, B. C. Chatterjee, S. Okamoto, N. Yamanaka, A. Fumagalli, E. Oki, "Route Partitioning Scheme for Elastic Optical Networks With Hitless Defragmentation", Journal of Optical Communications and Networking, Vol. 8, No. 6, 2016, pp. 356-370.

[27] S. Selvakumar, S. S. Manivannan, "A Spectrum Defragmentation Algorithm Using Jellyfish Optimization Technique in Elastic Optical Network (EON)", Wireless Personal Communications, Vol. 127, 2022, pp. 1187-1205.

[28] D. S. Yadav, "RDRSA: A Reactive Defragmentation based on Rerouting and Spectrum Assignment (RDRSA) for Spectrum Convertible Elastic Optical Network", Optics Communications, Vol. 496, 2021, pp. 1-8.

[29] Ujjwal, J. Thangaraj, R. kumar, "Multi-Path Provisioning in Elastic Optical Network with Dynamic On-Request Optimal Defragmentation Strategy", Optical Switching and Networking, Vol. 41, 2021, pp. 1-14.

[30] P. Majumdar, A. Pal, T. De, "Extending Light-trail into Elastic Optical Networks for Dynamic Traffic Grooming", Optical Switching and Networking, Vol. 20, 2016, pp. 1-15.

[31] I. G. S. Santos, J. A. S. Monteiro, A. C. B. Soares, A. C. Fontinelle, D. R. Campelo, "A Spectrum Spacing Mechanism to Enhance Traffic Grooming in Elastic Optical Networks", Photonic Network Communications, Vol. 42, 2021, pp. 49-59.

[32] D. R. Din, "Spectrum Expansion/Contraction and Survivable Routing and Spectrum Assignment Problems on EONs with Time-Varying Traffic", Computer Communications, Vol. 148, 2019, pp. 152-164.

[33] I. Stiakogiannakis, E. Palkopoulou, D. Klonidis, O. Gerstel, I. Tomkos, "Dynamic Cooperative Spectrum Sharing and Defragmentation for Elastic Optical Networks", Journal of Optical Communications and Networking, Vol. 6, No. 3, 2014, pp. 259-269.

[34] D. R. Din, "Delay-Variation Constrained Spectrum Extraction and Contraction Problem for Multipath Routing on Elastic Optical Networks", Journal of Information Science and Engineering, Vol. 36, No. 1, 2020, pp. 109-125.

[35] D. Amar, E. Le Rouzic, N. Brochier, C. Lepers, "Multilayer Restoration in Elastic Optical Networks", Proceedings of the 19th International Conference on Optical Network Design and Modeling, Pisa, Italy, 11-14 May 2015, pp. 239-244.

[36] A. Castro, L. Velasco, J. Comellas, G. Junyent, "Dynamic Restoration in Multi-Layer IP/MPLS-over-Flexgrid Networks", Proceedings of the 9th International Conference on the Design of Reliable Communication Networks, Budapest, Hungary, 4-7 March 2013, pp. 155-162.

[37] E. Etezadi, H. Beyranvand, J. A. Salehi, "Latency-Aware Service Provisioning in Survivable Multilayer IP-over-Elastic Optical Networks to support Multi-Class of Service Transmission", Computer Communications, Vol. 183, 2022, pp. 161-170.

[38] T. Tanaka, T. Inui, A. Kadohata, W. Imajuku, A. Hirano, "Multiperiod IP-Over-Elastic Network Reconfiguration With Adaptive Bandwidth Resizing and Modulation", Journal of Optical Communications and Networking, Vol. 8, No. 7, 2016, pp. A180-A190.

[39] J. Zhao, Y. Xu, D. Ren, J. Hu, "A Cross-Layer Traffic Grooming Algorithm in Joint Optimization of the IP over Elastic Optical Network", Journal of Optical Communications, Vol. 41, No. 1, 2020, pp. 73-82.

[40] Y. Zhang, Y. Zhang, Y. Li, G. Shen, Y. Yan, W. Chen, "Cross-Layer Spectrum Defragmentation for IP over Elastic Optical Network", Proceedings of the Asia Communications and Photonics Conference, Hangzhou, China, 26-29 October 2018, pp. 1-4.

[41] D. S. Yadav, A. Chakraborty, B. S. Manoj, "A Multi-Backup Path Protection Scheme for Survivability in Elastic Optical Networks", Optical Fiber Technology, Vol. 30, 2016, pp. 167-175.

A Hierarchical Framework for Video-Based Human Activity Recognition Using Body Part Interactions

Original Scientific Paper

Milind Kamble
Department of Electronics and Telecommunication Engg.,
G. H. Raisoni College of Engineering and Management
Pune, Maharashtra, India
Email: milind.kamble@vit.edu

Rajankumar S. Bichkar
Vidya Pratishthan's Kamalnayan Bajaj Institute of Engineering and Technology
Baramati, Maharashtra, India
Email: bichkar@yahoo.com

Abstract *–Human Activity Recognition (HAR) is an important field with diverse applications. However, video-based HAR is challenging because of various factors, such as noise, multiple people, and obscured body parts. Moreover, it is difficult to identify similar activities within and across classes. This study presents a novel approach that utilizes body region relationships as features and a two-level hierarchical model for classification to address these challenges. The proposed system uses a Hidden Markov Model (HMM) at the first level to model human activity, and similar activities are then grouped and classified using a Support Vector Machine (SVM) at the second level. The performance of the proposed system was evaluated on four datasets, with superior results observed for the KTH and Basic Kitchen Activity (BKA) datasets. Promising results were obtained for the HMDB-51 and UCF101 datasets. Improvements of 25%, 25%, 4%, 22%, 24%, and 30% in accuracy, recall, specificity, Precision, F1-score, and MCC, respectively, are achieved for the KTH dataset. On the BKA dataset, the second level of the system shows improvements of 8.6%, 8.6%, 0.85%, 8.2%, 8.4%, and 9.5% for the same metrics compared to the first level. These findings demonstrate the potential of the proposed two-level hierarchical system for human activity recognition applications.*

Keywords*: Human Activity Recognition(HAR);Hierarchical Model, Hidden Markov Model(HMM); Support Vector Machine(SVM)*

1. INTRODUCTION

Human activity recognition using video signals is a rapidly evolving field with applications in various domains, such as surveillance systems [1], human-computer interaction, and healthcare monitoring [2]. The ability to automatically analyze and understand human activities from video data has significant implications for improving safety, enhancing user experiences, and enabling intelligent systems [3]. In this study, we present a comprehensive approach for human activity recognition that leverages spatial-temporal features and a two-level hierarchical method, integrating hidden Markov models (HMM) [4] and support vector machines (SVM) to achieve accurate and robust activity classification.

Our research aims to develop a practical framework that captures the dynamic nature of human activities by extracting meaningful features from video frames and modeling the temporal dependencies between different activity states. We employ a step-by-step process from extracting spatial-temporal features to the final classification of human activities to accomplish this.

The first step in our approach involves extracting spatial-temporal features from the video frames. Recognizing that human appearance and motion play crucial roles in activity recognition, we begin by identifying humans in each frame using the method proposed in [5]. This technique combines a support vector machine (SVM) classifier and a histogram of oriented gradients (HOG) features to detect human regions accurately.

The SVM classifier effectively learns the decision boundaries between human and non-human regions, while the HOG features capture local shape and appearance information. By leveraging these techniques, we can robustly identify humans in the video frames, forming the basis for subsequent analysis.

To capture the spatial characteristics of human activities, we further divide the human region into six segments: the head region, the torso region, and the lower body part, as shown in Figure 3. This segmentation allows us to focus on specific body regions and extract region-specific features. For each body region, we compute the histogram of optical flow, which captures the motion information between consecutive video frames. The correlation between the histograms of optical flow for different body regions is then calculated, encoding the relationships and coordinated movements between these regions. This correlation-based approach results in a comprehensive feature vector that effectively represents the spatial interactions within the human body.

In addition to the spatial features, we recognize that temporal dynamics are essential for accurate activity recognition. We adopt a two-level hierarchical method to model and classify human activities accurately. In the first level, we employ hidden Markov models (HMMs) to capture the temporal dependencies and transitions between different activity states. HMMs are widely used in activity recognition tasks because they model sequential data well. HMMs can capture the underlying dynamics and temporal patterns by representing activities as a sequence of hidden states. In our approach, we train HMMs on labeled training sequences, allowing them to learn the emission and transition probabilities. We use these probabilities to recognize unseen activities in test sequences, as shown in Figure 1.

From the confusion matrix obtained through the HMM classification, similar activities are grouped based on their patterns and transitions. This grouping enhances the discriminability of the activity classes and provides a foundation for the second level of our hierarchical approach.

In the second level, as shown in Figure 2, we employ support vector machines (SVMs) for activity classification. SVMs are well-established supervised learning algorithms known for handling high-dimensional feature vectors and effectively separating data into different classes. The grouped activities from the first level serve as input to the SVM, allowing it to learn the discriminative patterns and decision boundaries between different activity classes. Training the SVM on the grouped activities can make fine-grained distinctions between similar activities and generalize well to unseen data. The SVM classification stage serves as a refinement step, further improving the accuracy and robustness of activity recognition.

To evaluate the effectiveness of our approach, we conducted extensive experiments on benchmark datasets in human activity recognition. We compared the performance of our framework against state-of-the-art methods, including those based on deep learning approaches. The results demonstrate that our approach achieves competitive or superior performance in terms of accuracy, robustness, and computational efficiency.

The key contribution of the proposed work are:

1. Two-level Hierarchical Structure: The paper introduces a novel hierarchical model to enhance system accuracy in human activity recognition, particularly in video-based scenarios.
2. Body Part Relationships: The research explores and leverages the interconnections among various body parts, enriching the feature set and leading to better recognition and classification of human activities.

The following is a general breakdown of the structure of this paper: Section 2 presents the methodology. Each component of the proposed system was elaborated from human detection in the video frame through activity modelling. The training of level one using HMM and level two using SVM is also described. The experiment and results analysis are described in Section 3. Finally, Section 4 concludes the study.

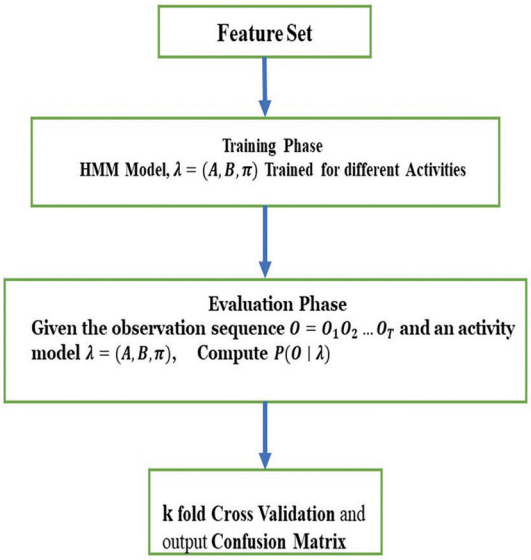

Fig. 1. Level 1, where activities are recognized based on HMM models

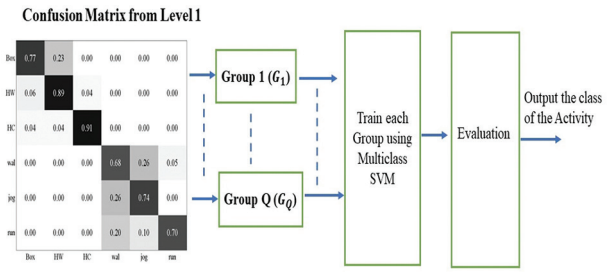

Fig. 2. At level 2, we group activities based on the confusion matrix of level 1 and use SVM as a classifier

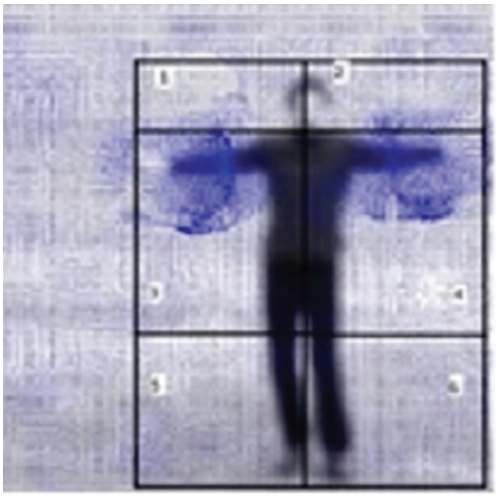

Fig. 3. The Region of Interest (ROI) in a video frame

1.1. RELATED WORK

Human activity recognition (HAR) using video signals is a rapidly evolving field, with numerous studies proposing innovative approaches and methodologies. This literature survey reviews influential works in this area, focusing on different aspects of human activity recognition.

In early research, spatial-temporal features played a significant role in human activity recognition, and researchers have explored various techniques to leverage these features effectively. In [6], which highlighted the inadequacy of direct 3D counterparts to commonly used 2D interest point detectors and proposed an alternative approach. In [7], the researcher presented a novel methodology that utilized local features to overcome the limitations of previous approaches of not detecting and localization of non-periodic activities. In [8], dense trajectories as features are used to enhance recognition accuracy. In [9], the authors proposed a novel method that uses local spatiotemporal color-depth information to enhance the robustness and accuracy of human action recognition in RGB-D videos. [10] proposed a sensing model capturing discriminative spatio-temporal features of human motion. In [11], they introduced a new paradigm for recognizing aggressive human behaviors, such as boxing action, using a fusion of Spatio Temporal Interest Point (STIP) and Histogram of Oriented Gradient (HoG) features. In [12], it aimed to improve the efficiency of optical flow feature extraction and explored spatio-temporal feature fusion methods.

To improve the recognition of human activities in real-world scenarios, researchers have proposed hierarchical models to address the challenges of activity recognition. In [13], the authors introduced the switching hidden semi-Markov model (S-HSMM). In [14], the authors applied the hierarchical hidden Markov model (HHMM) to capture the hierarchical nature of activities. In [15], they focused on detecting unstructured human activities in unstructured environments. In [16], authors proposed a spectral divisive clustering algorithm to extract hierarchies from tracklets. In [17], researchers developed a hierarchical sequence summarization approach for multi-temporal feature representations. In [18], deep hybrid models and active learning are combined in a continuous activity learning framework. [19] addressed group activity recognition with deep LSTM and 2-stage temporal models.

Recent advancements in HAR include the Progressive Skeleton-to-sensor Knowledge Distillation (PSKD) model [20] for wearable sensor-based HAR using smartwatch accelerometer data. In [21], the authors developed a methodology for automatic accident detection in surveillance videos to enhance safety and security systems. In [22], authors provided a comprehensive summary of deep neural network architectures in HAR, particularly convolutional neural networks (CNNs), offering insights into their advancements and applications.

Addressing key challenges in HAR, [23] introduced a rank-based fuzzy approach to capture transitional relationships between postures in temporal sequences. In [24], they introduced keypoint-MoSeq, an unsupervised machine-learning platform for identifying behavioral modules from keypoint data. In [25], the authors proposed SparseFormer, a method inspired by human sparse visual recognition, which focuses on key visual elements.

In conclusion, human activity recognition has witnessed significant advancements through exploring spatial-temporal features and hierarchical models. Recent research has addressed vital challenges and introduced innovative approaches for improved recognition, accuracy, and understanding of human actions. The integration of wearable sensors, deep neural networks, and human expertise shows promising directions for future research in this field.

2. METHODOLOGY

The initial steps in the proposed HAR approach involve pre-processing the video data and segmenting the region where the action occurs. Next, human detection is accomplished using HOG features calculated using Equation 1 and SVM as a classifier. We identify an active region by drawing a bounding box around the detected human in the frame, as shown in Figure 3. We subsequently partition the active region into six sub-blocks organized in a 3×2 grid, as depicted in Figure 3, and features are extracted from each sub-block. Feature extraction focuses on identifying the connection between a pixel and its surrounding pixels in space and time. We achieve this by computing the relative motion between the pixels and the Optical Flow (OF) for each pixel.

$$|\mathrm{GradientofI}| = \sqrt{x^2 + y^2}$$
$$\emptyset = \tan^{-1}\frac{I_y}{I_x} \quad (1)$$

2.1. OPTICAL FLOW

To extract features, a rectangular Region of Interest (ROI) is defined by a bounding box, which is further subdivided into two columns and three rows, as depicted in Figure 3. The Optical Flow (OF) is computed for each subblock using the Lucas-Kanade method [26], as illustrated in Figure 4. This method is robust to changes in lighting and background clutter and is computationally efficient. According to the Lucas-Kanade technique, the displacement of the visual content between subsequent frames in the vicinity of point p is low and roughly constant; thus, all pixels within a window with a center of p are expected to follow the OF equation, as given in Equation 2.

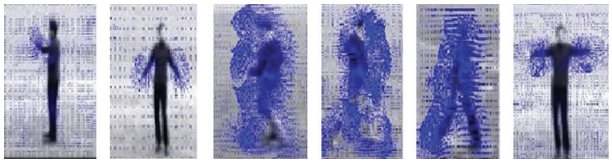

(a) (b) (c) (d) (e) (f)

Fig. 4. Optical flow of person who carries out the subsequent action a) Boxing b) Hand Waving c) Jogging d) Running e) Walking f) Hand Clapping

$$\begin{aligned} &I_x(q_1)V_x + I_y(q_1)V_y = -I_t(q_1)\\ &I_x(q_2)V_x + I_y(q_2)V_y = -I_t(q_2)\\ &\vdots\\ &I_x(q_n)V_x + I_y(q_n)V_y = -I_t(q_n) \end{aligned} \tag{2}$$

where $I_x(q_i)$, $I_y(q_i)$, $I_t(q_i)$ are the partial derivatives of image I with respect to x, y, and t, respectively, evaluated at pixel q_{-i}, (Vx, Vy) is the local image flow vector and q_1, q_2,…q_n represent the pixels inside the window.

Equation 2 can be expressed in matrix form $Av=b$, as shown in equation 3.

$$A = \begin{bmatrix} I_x(q_1) & I_y(q_1)\\ I_x(q_2) & I_y(q_2)\\ \vdots & \\ I_x(q_n) & I_y(q_n) \end{bmatrix}, v = \begin{bmatrix} V_x\\ V_y \end{bmatrix},$$
$$b = \begin{bmatrix} -I_t(q_1)\\ -I_t(q_2)\\ \vdots\\ -I_t(q_n) \end{bmatrix} \tag{3}$$

We obtain the solution to equation 3 using the least-square method.

$$v = (A^T A)^{-1} A^T b \tag{4}$$

where, v is a 2×1 dimension vector. The magnitude and phase components of v are given by Equation 5.

$$\begin{aligned} |v| &= \sqrt{Vx^2 + V_y^2}\\ \phi &= \tan^{-1}\frac{V_y}{V_x} \end{aligned} \tag{5}$$

where the components of v represent the velocities in x and y directions. From Equation 5, the optical flow histograms were calculated for each body segment using computer-vision techniques. Optical flow represents the motion of pixels between consecutive frames of a video, and the histogram summarizes the distribution of this motion in different directions and magnitudes. The algorithm can capture distinctive motion patterns associated with various human activities by calculating the optical flow histograms for each body segment. After calculating the histogram for all blocks in the ROI of a frame, they are concatenated to form a complete feature vector of size 1×54 for the video frame.

2.2. FEATURES BASED ON BODY PART INTERACTIONS

The proposed approach employs an autocorrelation strategy to capture the relationship and interaction between various body parts. The optical flow histograms for each body segment were cross-correlated with the histograms for all the other body segments to measure the similarity of their motion patterns. The resulting correlation matrix represents the inter-segment relationships and is used to build a hierarchical model that captures the overall structure of the human body and the relationships between its parts.

Cross-correlation was utilized to create feature vectors that link the six sub-blocks computed histograms. In addition, the cross-correlation determines the similarities between two series based on their separation from one another. Equation 6 defines the cross-correlation function for the two histograms $x[k]$ and $y[k]$, which correspond to the two body regions.

$$\begin{aligned} R_{xy} &= \sum_{m=-\infty}^{m=\infty} x[m]y[m-k]\\ R_{yx} &= \sum_{m=-\infty}^{m=\infty} y[m]x[m-k] \end{aligned} \tag{6}$$

where the value of k is $-\infty \le k \le \infty$. At $k=0$, $R_{xy}=R_{yx}$. The cross-correlation between one sub-block histogram and the remaining five sub-block histograms was calculated at $k=0$ to determine the similarity of each sub-histogram block to one another. The results are stored in a 1×6 vector. An identical approach was used for the remaining sub-blocks. A 1×6 vector is extracted from each sub-block, and this vector is combined with other vectors to form a 1×36 vector, which represents the feature vector of a single frame. The entire feature vector for a video sequence is created by applying this procedure to each video sequence frame and concatenating them. Once the feature vectors for all videos in a dataset are obtained, they are used to train the two-level proposed hierarchical model for HAR. In level one, each human activity is modelled using HMM. These feature vectors are used to train the HMM for each activity.

2.3. LEVEL ONE OF THE PROPOSED HIERARCHICAL MODEL

The proposed system utilizes the HMM to model each human action in the dataset at level one, as shown in Fig. 1. HMMs are generative probabilistic models that are used to generate hidden states based on observable data [26].

The proposed system employed an HMM in two stages. In the first stage, known as the training stage, each human activity is modelled by learning the model parameters $\lambda=(A,B,\pi)$ from the training data such that $P(O|\lambda)$, the probability of the observation sequence $O=O_1, O_2...O_T$ given the model λ, is maximized. The parameters of the HMM were A,B,π, where A represents the state transition probability matrix, B represents the observation symbol probability matrix, and π represents the initial state. The feature vectors derived from the video sequence frames create an observation sequence O.

In the second stage, referred to as the classification stage, the model that best captures the activity class for a particular observation sequence $O=O_1, O_2...O_T$ is chosen. We calculate the probability of the observation sequence given the activity model λ, denoted as $P(O|\lambda)$. An activity model that maximizes the probability $P(O|\lambda)$is selected.

Equation 7 illustrates the $P(O|\lambda)$ by adding the joint probabilities of all conceivable state sequences, q.

$$P(O|\lambda) = \sum_{allQ} P(O|Q,\lambda)P(Q|\lambda) = \sum_{q_1 q_2 \ldots q_T} b_{q_1}(O_1)a_{q_1 q_2}b_{q_2}(O_2) \quad \ldots a_{q_{T-1} q_T}b_{q_T}(O_T) \tag{7}$$

where, $q_1,q_2 \ldots q_N$ represents the N number of states, where q_i represents the state at time step i, $a_{q_i q_j}$ represents the probability of transition from state q_i to state q_j, and $b_{q_j}(O_k)$ represents the probability of observing the symbol (O_k) in state q_j.

HMM uses a Gaussian Mixture Model(GMM) to identify human behavior in the proposed system. The GMM models the probability distribution of features extracted from video frames that capture human action, as shown in Equation 8, as a combination of M Gaussian distribution.

$$b_j(O) = \sum_{m=i}^{M} c_{jm}\mathfrak{N}[O, \mu_{jm}, U_{jm}], \quad 1 \le j \le N \tag{8}$$

Where O denotes the observation being modeled, c_{jm} represents the mixture weight for the m^{th} mixture in state j, and $\mathfrak{N}$ indicates the Gaussian density with the mean and covariance matrices μ_{jm} and U_{jm} associated with state j and the m_{th} mixture, respectively. Equation 9 represents the constraint to be satisfied by mixing the weights, c_{jm}.

$$\sum_{m=1}^{M} c_{jm} = 1, \quad 1 \le j \le N \qquad c_{jm} \ge 0, \quad 1 \le j \le N, 1 \le m \le M \tag{9}$$

After extracting feature vectors from all video signals in the dataset, human activities were modelled using the HMM. We evaluated the HMM models using the test signals to generate a confusion matrix. Finally, based on the confusion matrix, we clustered similar human activities in the first level. We provided them as input to the second level, where we used SVM as a classifier.

2.4. LEVEL TWO OF THE PROPOSED HIERARCHICAL MODEL

Based on the output from level one, activities are now grouped together using the confusion matrix for level one. The confusion matrix helps us understand the performance of the classification model by showing the number of correct and incorrect predictions for each activity. By analyzing this matrix, we can identify patterns and similarities between activities, allowing us to group them based on their classification results. This grouping will help us gain better insights and improve the accuracy of our classification process. At level two, the activities inside the group G_i, created after the first level, were classified using the SVM classifier, as shown in Figure 2. The SVM creates a hyperplane to classify data. It seeks to identify the appropriate hyperplane for classifying the data into distinct groups. We selected the hyperplane to have the largest possible distance between it and the nearest data points for each class. The data points closest to the hyperplane, also known as the maximum margin hyperplane, are called the support vectors. The given training set consists of n data points of the form $(\bar{x}_1,\bar{y}_1),\cdots,(\bar{x}_n,\bar{y}_n)$, where $\bar{x}_i \in R^p$, p- dimensional input feature vector, and $\bar{y}_i$ is the target label for a binary classifier with values, {1,-1} are used for training the SVM. The values of $\bar{y}_i$, show the class to which point $\bar{x}_i$ belongs to. The SVM algorithm searches for the maximum-margin hyperplane that separates the data points belonging to the class, $\bar{y}_i$=1 from $\bar{y}_i$=-1. The hyperplane constraint, which requires data to be on the proper side of the margin, is represented by Equation 10.

$$\overline{y_i}(x_i \cdot w - b) \ge 1 \tag{10}$$

where b represents the offset of the hyperplane from the origin, and vector w depicts the orientation of the hyperplane. We can formulate the optimization problem as shown in Equation 11.

$$\text{Minimize} \parallel w \parallel^2 \text{ subject to } y_i(x_i \cdot w - b) \ge 1, \text{ for } i = 1, \ldots, n. \tag{11}$$

The classifier is determined by the w and b that solve the problem $x^{yields} \longrightarrow sgn(w \cdot x\text{-}b)$.

Let $R=\{R_1, R_2,\cdots,R_P\}$ be the P numbers of rows from the confusion matrix and let $G=\{G_1, G_2,\cdots,G_Q\}$ be the set of elements, where each element G_i is a set of similar activities.

Once we group identical activities from the output of the first level, we use the multi-class SVM, which is a collection of binary classifiers that distinguish between one of the classes and all the others (one-versus-all) or between every pair of classes (one-versus-one) to classify activities within each element G_i from the set G.

3. EXPERIMENTAL SETUP AND RESULT ANALYSIS

Four datasets were used to evaluate the proposed method: KTH [27], SFB588 Basic Kitchen Activity (BKA) [28], HMDB-51 [29], and UCF101 [30]. This section presents the results and findings of our Human Activity Recognition (HAR) study. We analyze the performance of our proposed model through the following subtopics:

1. Feature Extraction and Cross-Validation: We discuss the feature extraction process and the robust cross-validation techniques to ensure reliable results.
2. Selection of HMM Parameters: We discuss the empirical section of the number of states and the number of Gaussian mixers used in GMM for modeling the activities.
3. Confusion Matrix from Level 1 and Level 2: We present and interpret the confusion matrices from Level 1 and Level 2 classifications, revealing improved prediction accuracy.
4. Effect of Feature Length on the Model: We discuss how varying feature lengths influence the model's accuracy and efficiency.
5. Comparison with Previous Work: Our model is comprehensively compared with existing approaches, showcasing advancements and improvements.
6. Evaluation on Real-World Video-Based Dataset: We assess our model's real-world applicability and performance using video-based data, offering valuable insights for practical implementation.
7. Statistical Analysis: Key metrics, including precision and recall, are presented for quantitative evaluation.

By thoroughly examining these subtopics, we aim to provide a comprehensive understanding of our model's strengths and limitations, contributing to the advancement of HAR.

3.1. FEATURE EXTRACTION AND CROSS-VALIDATION

We extracted features from each frame of the input video sequence at 25 fps. Each frame yielded a feature vector of size 1×36, which was obtained by concatenating the extracted features. The feature matrix was created by storing features from all videos in the dataset. The feature matrix is divided into two parts for training and testing the activity model. We trained the HMM using the first portion of the feature set, whereas we used the second portion for the evaluation and cross-validation. For k-fold cross-validation, the feature set was randomly divided into k equally sized sub-parts.

During each iteration of the k-fold cross-validation, one sub-part was reserved as validation data, and the remaining k-1 sub-parts were utilized for training. This operation was performed k times, using each sub-part as validation data precisely once. Finally, the results from each k-fold were averaged or combined to estimate the model's performance.

3.2. SELECTION OF HMM PARAMETERS

The first level of the system utilizes the HMM with the GMM. HMM represents the activity being performed, and GMMs model the probability distribution of the features extracted from the video sequence. The parameters of the HMM with GMM are A, B, π, number of states (N), and Gaussians in the mixture model (M). An empirical analysis was performed to determine the number of states N and Gaussian in the mixture model (M) by experimenting with different parameter values and evaluating the model's performance. The optimal values of N and M are determined by analyzing the system's accuracy for various combinations of N and M, as shown in Fig. 5.

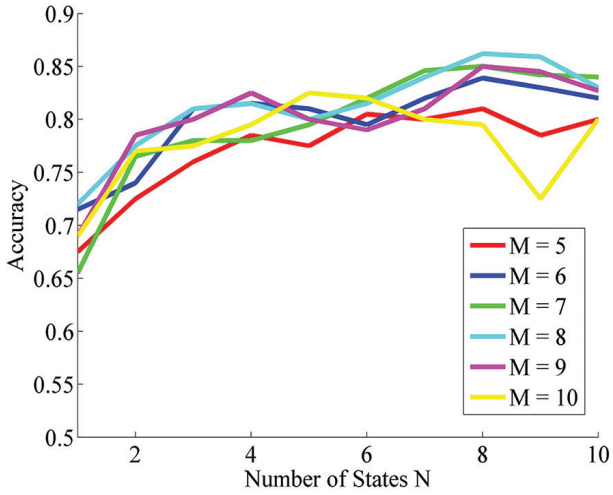

Fig. 5. Relationship between the accuracy of the system and the number of states.

3.3. CONFUSION MATRIX FROM LEVEL 1 AND LEVEL 2

Fig. 6 shows the confusion matrix from level one for the KTH and BKA datasets. In level one, activities are modelled using HMM, and then the probability of the observation sequence O given the model λ, P(O|λ) is calculated. Fig. 7 shows the confusion matrix from level two for the KTH and BKA datasets. In Level 2, the activities are grouped based on the confusion matrix obtained from Level one. For the KTH dataset, from the confusion matrix of Level one, as shown in Figure 6 (a), the activities related to the upper body's involvement were included in group one, and the activities involving the lower body were grouped in group two. Each group's activities were classified using a multi-class SVM at level two.

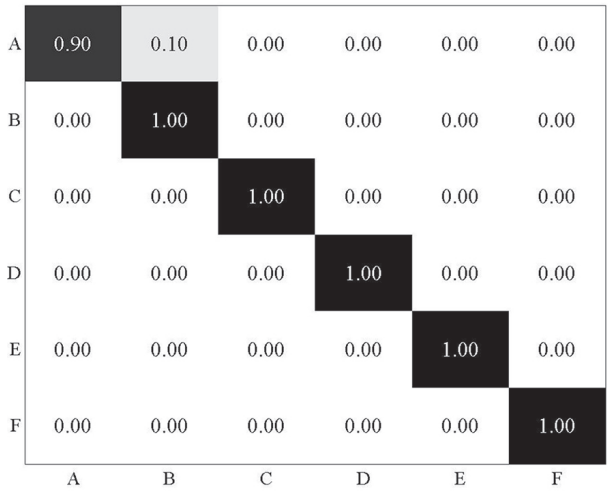

(a)

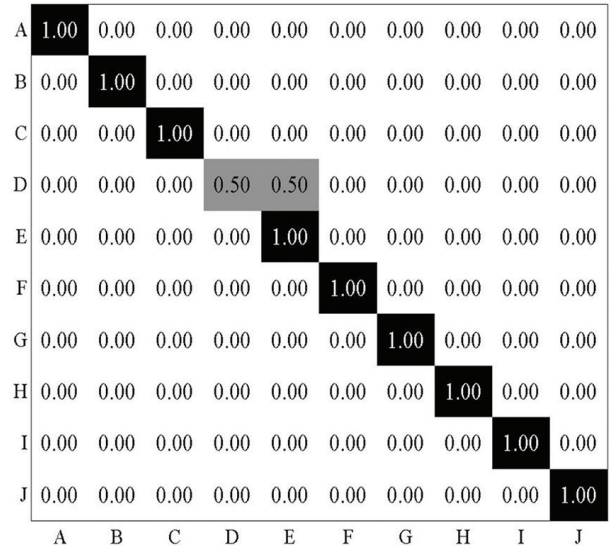

(b)

Fig. 6. Confusion matrix generated by Level 1 classification (a) KTH Dataset, where A: Boxing, B: Handwaving, C: Hand Clapping, D: Walking, E: Jogging, F: Running.(b) BKA Dataset, where 1. Chop, 2. Grate, 3. Mash, 4. Mill, 5. Pour, 6. Roll 7. Saw, 8. Slice, 9. Stir, 10. Sweep

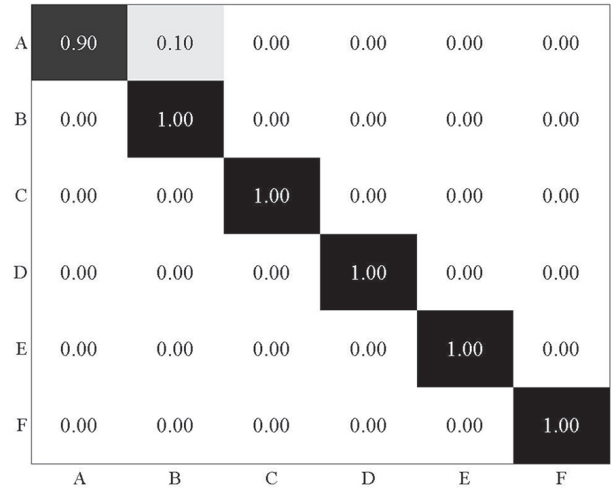

(a)

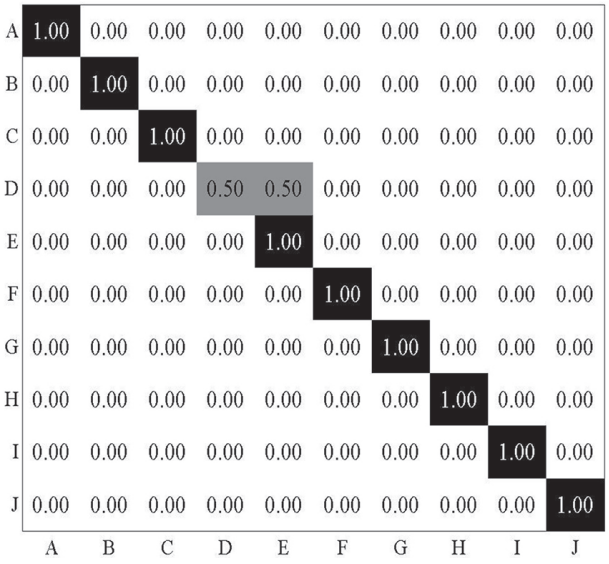

(b)

Fig. 7. Confusion matrix generated by Level 2 classification. (a) KTH Dataset, where A: Boxing, B: Handwaving, C: Hand Clapping, D: Walking, E: Jogging, F: Running. (b) BKA Dataset, where 1. Chop, 2. Grate, 3. Mash, 4. Mill, 5. Pour, 6. Roll 7. Saw, 8. Slice, 9. Stir, 10. Sweep

3.4. EFFECT OF FEATURE-LENGTH ON THE PROPOSED MODEL

Features are created by concatenating the features obtained from one frame, and the number of frames required to generate a feature determines its length. The length of the feature vector affected the overall effectiveness of the system. Table 1 shows the number of frames for the accuracy of the proposed system for the KTH dataset. The proposed system's accuracy increased with the feature vector's length. The accuracy of the proposed method decreases when fewer frames are utilized for the feature vector.

Table 1. Relationship between the number of frames and the accuracy of the system on the KTH dataset

Number of Frames	Accuracy
50	87.3
75	91.2
90	95.6
100	98.3

3.5. COMPARISON WITH PREVIOUS WORK

The proposed system was compared with a group of previously published studies. The results reveal that the proposed approach increases the accuracy rate for the KTH dataset by 0.4% compared to [31], as shown in Table 2. For the BKA dataset, Table 3 compares the proposed method with activity recognition using the Histogram of Oriented Optical Flow (HOOF) and Histogram of Feature Flow (HoFF) [28]. The accuracy of the proposed method is 97.1%.

Table 2. Performance comparison of the proposed method and other approaches on the KTH Dataset

Method	KTH Dataset
Schuldt [27]	71.72
Liu and Shah [32]	94.16
Bregonzio et al.[33]	94.33
Lin [34]	95.77
Moussa [31]	97.89
Proposed Method	98.3

Table 3. Comparison between Histogram of Optical Flow (HoOF) and Histogram of Feature Flow (HoFF) on the BKA Dataset

BKA dataset I	HoOF	HoFF
Unit recog. [27]	96.7	96.6
Proposed Method	97.1	

3.6. EVALUATION OF THE PROPOSED WORK ON REAL-WORLD VIDEO-BASED DATASET

The experimental results obtained for various realistic datasets, namely UCF101 and HMDB-51, are listed in Table 4 and Table 5, respectively. The accuracies obtained for UCF101 and HMDB-51 are 84.6% and 69.2%, respectively.

Table 4. Performance comparison of the proposed method and other approaches on the UCF101 Dataset

Model	Accuracy
3-dimensional (3D) Residual ConvNet [35]	85.9
Multi-region Two-Stream R-CNN [36]	91.1
Optical Flow Guided Feature [37]	96
Two-stream+LSTM [38]	88.6
Proposed Method	84.6

Table 5. Performance comparison of the proposed method and other approaches on the HMDB-51 Dataset

Model	Accuracy
Two-stream I3D [39]	80.9
Multi-stream I3D [40]	80.92
TVNet + IDT [41]	72.6
Proposed Method	69.2

3.7. STATISTICAL ANALYSIS OF THE PROPOSED SYSTEM

Table 6 presents a statistical analysis of the proposed two-level HAR system, which evaluates its performance using six metrics: accuracy, recall, specificity, precision, F1-score, and Matthews Correlation Coefficient (MCC). The first level of the model employed an HMM for classification, whereas the second level used an SVM for further classification.

The second level of the proposed system significantly outperformed the first level when tested on the KTH dataset, with improvements of 25%, 25%, 4%, 22%, 24%, and 30% in accuracy, recall, specificity, Precision, F1-score, and MCC, respectively. On the BKA dataset, the second level of the system shows improvements of 8.6%, 8.6%, 0.85%, 8.2%, 8.4%, and 9.5% for the same metrics compared to the first level.

The proposed system exhibits high precision and recalls to effectively identify activities and avoid false positives and negatives. The F1 score is a widely used metric for evaluating the performance of classification models because it considers both precision and recall. The F1 scores for the KTH and BKA datasets were 98.33% and 94.67%, respectively, representing increases of 24% and 8.4% compared to the first level. The results suggest that the proposed hierarchical system improves the classification ability of the system.

Table 6. Performance metrics of Level 1 and Level 2 classifiers on KTH and BKA datasets.

Performance Metrics	KTH Dataset		Basic Kitchen Activities	
	Level 1	Level 2	Level 1	Level 2
Accuracy	0.78	0.98	0.87	0.95
Error	0.21	0.02	0.126	0.05
Recall	0.79	0.98	0.874	0.95
Specificity	0.96	0.99	0.99	0.99
Precision	0.80	0.98	0.89	0.97
False Positive Rate	0.043	0.003	0.014	0.0056
F1-score	0.78	0.98	0.87	0.95
Matthew's Correlation Coefficient	0.75	0.98	0.87	0.95

4. CONCLUSION

The proposed system consists of a two-level hierarchical framework for activity recognition, with the first level using HMM to categorize activities and the second using SVM for classification. The system can recognize similar activities, and experiments on four datasets showed that the hierarchical model outperformed the HMM and SVM applied separately, resulting in higher accuracy. The number of frames utilized for modeling affects the system's precision, with fewer frames resulting in poorer accuracy. The F1 scores for the KTH and BKA datasets were 98.33% and 94.67%, respectively, which is 24%and 8.4% rise compared to level one. The increase in the F1 score indicates that the proposed model has low false-positive and false-negative values, and the system correctly identifies the classes. However, the system's performance on datasets such as HMDB-51 and UCF101 was lower because of factors such as the short video duration, cluttered backgrounds, multiple people in the frame, and the occlusion of body parts. The proposed method relies on hand-crafted features and pre-processing of video signals. Future work could explore using deep learning algorithms for feature extraction from real-world video signals.

5. REFERENCES

[1] W. Lin, M. Sun, R. Poovandran, Z. Zhang, "Human Activity Recognition for Video Surveillance", Proceedings of the IEEE International Symposium on Circuits and Systems, Seattle, WA, USA, 18-21 May 2008, pp. 2737-2740.

[2] P. Khatiwada, A. Chatterjee and M. Subedi, "Automated Human Activity Recognition by Colliding Bodies Optimization (CBO) -based Optimal Feature Selection with RNN", Proceedings of the IEEE 23rd Int Conf on High-Performance Computing & Communications, Haikou, Hainan, China, 2021, pp. 1219-1228.

[3] S.-R. Ke, H. Thuc, Y.-J. Lee, J.-N. Hwang, J.-H. Yoo, K.-H. Choi, "A Review on Video-Based Human Activity Recognition", Computers, Vol. 2, No. 2, 2013, pp. 88–131.

[4] H. S. Mojidra, V. H. Borisagar, "Article: A Literature Survey on Human Activity Recognition via Hidden Markov Model", IJCA Proceedings on International Conference on Recent Trends in Information Technology and Computer Science 2012, No. 6, 2013, pp. 1–5.

[5] N. Dalal, B. Triggs, "Histograms of oriented gradients for human detection", Proceedings of the IEEE Computer Society Conference on Computer Vision and Pattern Recognition, San Diego, CA, USA, 20-25 June 2005, pp. 886-893.

[6] P. Dollar, V. Rabaud, G. Cottrell, S. Belongie, "Behavior recognition via sparse spatio-temporal features", Proceedings of the IEEE International Workshop on Visual Surveillance and Performance Evaluation of Tracking and Surveillance, Beijing, China, 15-16 October 2005, pp. 65-72.

[7] M. S. Ryoo, J. K. Aggarwal, "Spatio-temporal relationship match: Video structure comparison for recognition of complex human activities", Proceedings of the IEEE 12th International Conference on Computer Vision, Kyoto, Japan, 2009, pp. 1593-1600.

[8] H. Kataoka, Y. Aoki, K. Iwata, Y. Satoh, "Evaluation of Vision-Based Human Activity Recognition in Dense Trajectory Framework", Advances in Visual Computing, 2015, pp. 634–646.

[9] H. Zhang, L. E. Parker, "CoDe4D: Color-Depth Local Spatio-Temporal Features for Human Activity Recognition From RGB-D Videos", IEEE Transactions on Circuits and Systems for Video Technology, Vol. 26, No. 3, 2016, pp. 541-555.

[10] X. Luo, T. Liu, B. Shen, J. Hong, Q. Chen, H. Chen, "Human Daily Activity Recognition Using Ceiling Mounted PIR Sensors", in Proceedings of the 2nd International Conference on Advances in Mechanical Engineering and Industrial Informatics, Hangzhou, Zhejiang, China, 2016, pp. 872–877.

[11] S. Ghabri, W. Ouarda, A. M. Alimi, "Towards human behavior recognition based on spatiotemporal features and support vector machines", Proceedings of the Ninth International Conference on Machine Vision, 2017, Vol. 10341, pp. 67–72.

[12] Z. Xiao, X. Xu, H. Xing, F. Song, X. Wang, B. Zhao, "A federated learning system with enhanced feature extraction for human activity recognition", Knowledge-Based Systems, Vol. 229, 2021.

[13] T. V. Duong, H. H. Bui, D. Q. Phung, S. Venkatesh, "Activity recognition and abnormality detection with the switching hidden semi-Markov model", Proceedings of the IEEE Computer Society Conference on Computer Vision and Pattern Recognition, San Diego, CA, USA, 20-25 June2005, pp. 838-845.

[14] N. T. Nguyen, D. Q. Phung, S. Venkatesh, H. Bui, "Learning and detecting activities from movement trajectories using the hierarchical hidden Markov model", Proceedings of the IEEE Computer Society Conference on Computer Vision and Pattern Recognition, San Diego, CA, USA, 20-25 June 2005, pp. 955-960 Vol. 2.

[15] H. Zhang, W. Zhou, L. E. Parker, "Fuzzy Temporal Segmentation and Probabilistic Recognition of Continuous Human Daily Activities", IEEE Transactions on Human-Machine Systems, Vol. 45, No. 5, pp. 598–611, 2015.

[16] A. Gaidon, Z. Harchaoui, C. Schmid, "Activity representation with motion hierarchies", International Journal of Computer Vision, Vol. 107, No. 3, 2014, pp. 219–238.

[17] Y. Song, L.-P. Morency, R. Davis, "Action Recognition by Hierarchical Sequence Summarization",

Proceedings of the IEEE Conference on Computer Vision and Pattern Recognition, Portland, OR, USA, 23-28 June 2013, pp. 3562-3569.

[18] M. Hasan, A. K. Roy-Chowdhury, "A Continuous Learning Framework for Activity Recognition Using Deep Hybrid Feature Models", IEEE Transactions on Multimedia, Vol. 17, No. 11, 2015, pp. 1909-1922.

[19] M. S. Ibrahim, S. Muralidharan, Z. Deng, A. Vahdat, G. Mori, "A Hierarchical Deep Temporal Model for Group Activity Recognition", Proceedings of the IEEE Conference on Computer Vision and Pattern Recognition, Las Vegas, NV, USA, 2016, pp. 1971-1980.

[20] J. Ni, A. H. Ngu, Y. Yan, "Progressive Cross-modal Knowledge Distillation for Human Action Recognition", Proceedings of the 30th ACM International Conference on Multimedia, 2022, pp. 5903–5912.

[21] S. W. Khan et al. "Anomaly Detection in Traffic Surveillance Videos Using Deep Learning", Sensors, Vol. 22, No. 17, 2022.

[22] S. Abbaspour, F. Fotouhi, A. Sedaghatbaf, H. Fotouhi, M. Vahabi, M. Linden, "A Comparative Analysis of Hybrid Deep Learning Models for Human Activity Recognition", Sensors, Vol. 20, No. 19, 2020, pp. 1–14.

[23] F. A. Dharejo et al. "FuzzyAct: A Fuzzy-Based Framework for Temporal Activity Recognition in IoT Applications Using RNN and 3D-DWT", IEEE Transactions on Fuzzy Systems, Vol. 30, No. 11, 2022, pp. 4578–4592.

[24] C. Weinreb et al. "Keypoint-MoSeq: parsing behavior by linking point tracking to pose dynamics", bioRxiv, 2023.

[25] Z. Gao, L. Wang, M. Z. Shou, "SparseFormer : Sparse Visual Recognition via Limited Latent Tokens", arXiv:2304.03768, 2023.

[26] L. R. Rabiner, "A tutorial on hidden Markov models and selected applications in speech recognition", Proceedings of the IEEE, Vol. 77, No. 2, 1989, pp. 257–286.

[27] C. Schuldt, I. Laptev, B. Caputo, "Recognizing human actions: a local SVM approach", Proceedings of the 17th International Conference on Pattern Recognition, Cambridge, UK, 26 August 2004, pp. 32-36

[28] H. Kuehne, D. Gehrig, T. Schultz, R. Stiefelhagen, "Online action recognition from sparse feature flow", Proceedings of the International Conference on Computer Vision Theory and Applications, Vol. 1, 2012, pp. 634–639.

[29] K. Soomro, A. R. Zamir, M. Shah, "UCF101: A Dataset of 101 Human Actions Classes From Videos in The Wild", arXiv:1212.0402, 2012.

[30] H. Kuehne, H. Jhuang, E. Garrote, T. Poggio, T. Serre, "HMDB: A large video database for human motion recognition", Proceedings of the International Conference on Computer Vision, Barcelona, Spain, 6-13 November 2011, pp. 2556–2563,.

[31] M. M. Moussa, E. Hamayed, M. B. Fayek, H. A. El Nemr, "An enhanced method for human action recognition", Journal of Advanced Research, Vol. 6, No. 2, 2015, pp. 163–169.

[32] J. Liu, M. Shah, "Learning human actions via information maximization", Proceedings of the IEEE Conference on Computer Vision and Pattern Recognition, Anchorage, AK, USA, 23-28 June 2008.

[33] M. Bregonzio, T. Xiang, S. Gong, "Fusing appearance and distribution information of interest points for action recognition", Pattern Recognition, Vol. 45, No. 3, 2012, pp. 1220–1234.

[34] Z. Jiang, Z. Lin, L. Davis, "Recognizing human actions by learning and matching shape-motion prototype trees", IEEE Transactions on Pattern Analysis and Machine Intelligence, Vol. 34, No. 3, 2012, pp. 533–547.

[35] D. Tran, J. Ray, Z. Shou, S.-F. Chang, M. Paluri, "ConvNet Architecture Search for Spatiotemporal Feature Learning", arXiv:1708.05038, 2017.

[36] X. Peng, C. Schmid, "Multi-region two-stream R-CNN for Action Detection", Proceedings of the European Conference on Computer Vision, 2016, pp. 744–759.

[37] S. Sun, Z. Kuang, L. Sheng, W. Ouyang, W. Zhang, "Optical Flow Guided Feature: A Fast and Robust Motion Representation for Video Action Recognition", Proceedings of the I IEEE/CVF Conference on Computer Vision and Pattern Recognition, Salt Lake City, UT, USA, 18-23 June 2018, pp. 1390–1399.

[38] J. Y. H. Ng, M. Hausknecht, S. Vijayanarasimhan, O. Vinyals, R. Monga, G. Toderici, "Beyond short snippets: Deep networks for video classification", Proceedings of the IEEE Conference on Computer Vision and Pattern Recognition, Boston, MA, USA, 7-12-June, 2015, pp. 4694–4702.

[39] K. Simonyan, A. Zisserman, "Two-stream convolutional networks for action recognition in videos", Advances in Neural Information Processing Systems, Vol. 1, No. January 2014, pp. 568–576.

[40] J. Hong, B. Cho, Y. W. Hong, H. Byun, "Contextual action cues from camera sensor for multi-stream action recognition", Sensors, Vol. 19, No. 6, pp. 1–13, 2019.

[41] L. Fan, W. Huang, C. Gan, S. Ermon, B. Gong, J. Huang, "End-to-End Learning of Motion Representation for Video Understanding", Proceedings of the IEEE/CVF Conference on Computer Vision and Pattern Recognition, Salt Lake City, UT, USA, 18-23 June 2018, pp. 6016–6025.

Advanced Human Activity Recognition through Data Augmentation and Feature Concatenation of Micro-Doppler Signatures

Original Scientific Paper

Djazila Souhila Korti
Belhadj Bouchaib University of Ain-Temouchent
Smart Structures Laboratory (SSL)
Faculty of Technology, Department of Telecommunication
Ain-Temouchent, Algeria
souhila.korti@univ-temouchent.edu.dz

Zohra Slimane
Abou Bekr Belkaid University of Tlemcen
Faculty of Technology, Department of Telecommunication
Tlemcen, Algeria
zoh_slimani@yahoo.fr

Abstract *–Developing accurate classification models for radar-based Human Activity Recognition (HAR), capable of solving real-world problems, depends heavily on the amount of available data. In this paper, we propose a simple, effective, and generalizable data augmentation strategy along with preprocessing for micro-Doppler signatures to enhance recognition performance. By leveraging the decomposition properties of the Discrete Wavelet Transform (DWT), new samples are generated with distinct characteristics that do not overlap with those of the original samples. The micro-Doppler signatures are projected onto the DWT space for the decomposition process using the Haar wavelet. The returned decomposition components are used in different configurations to generate new data. Three new samples are obtained from a single spectrogram, which increases the amount of training data without creating duplicates. Next, the augmented samples are processed using the Sobel filter. This step allows each sample to be expanded into three representations, including the gradient in the x-direction (Dx), y-direction (Dy), and both x- and y-directions (Dxy). These representations are used as input for training a three-input convolutional neural network-long short-term memory support vector machine (CNN-LSTM-SVM) model. We have assessed the feasibility of our solution by evaluating it on three datasets containing micro-Doppler signatures of human activities, including Frequency Modulated Continuous Wave (FMCW) 77 GHz, FMCW 24 GHz, and Impulse Radio Ultra-Wide Band (IR-UWB) 10 GHz datasets. Several experiments have been carried out to evaluate the model's performance with the inclusion of additional samples. The model was trained from scratch only on the augmented samples and tested on the original samples. Our augmentation approach has been thoroughly evaluated using various metrics, including accuracy, precision, recall, and F1-score. The results demonstrate a substantial improvement in the recognition rate and effectively alleviate the overfitting effect. Accuracies of 96.47%, 94.27%, and 98.18% are obtained for the FMCW 77 GHz, FMCW 24 GHz, and IR-UWB 10 GHz datasets, respectively. The findings of the study demonstrate the utility of DWT to enrich micro-Doppler training samples to improve HAR performance. Furthermore, the processing step was found to be efficient in enhancing the classification accuracy, achieving 96.78%, 96.32%, and 100% for the FMCW 77 GHz, FMCW 24 GHz, and IR-UWB 10 GHz datasets, respectively.*

Keywords*: human activity recognition, radar, micro-Doppler signature, data augmentation, preprocessing, feature concatenation*

1. INTRODUCTION

With the emergence of IoT and sensing technologies, Human Activity Recognition (HAR) has gained significant attention and found applications in various fields [1, 2]. Numerous sensing technologies have been investigated for HAR, including video devices, wearable sensors, and radars [3]. The key features of radar technology, including non-invasiveness, privacy preservation, low energy consumption, and environmental insensitivity, have made this technology very popular for HAR [4]. Non-contact radar sensors can continuously detect and monitor human activities, including gait, falls, gestures, and activities of daily living [4].

Two commonly employed radar sensors for the detection of human activities are Impulse Radio Ultra-Wide Band (IR-UWB) [5] and Frequency Modulated Continuous Wave (FMCW) [6]. Radar echoes caused by electromagnetic signals reflected from different parts of the body contain valuable information about human motion, known as the micro-Doppler effect. The Micro-Doppler signatures encompass frequency components derived from the translational motion of the body or the vibration and rotation of its non-rigid parts. These distinctive features can be directly exploited to identify various human activities [7-9].

Due to the ability of deep feature self-learning, Deep Neural Networks (DNNs) have been successfully applied for HAR based on micro-Doppler signatures [10]. DNNs mainly focus on automatic feature learning, which neither requires manual intervention nor relies on prior knowledge. Recent studies have shown that hybrid models like CNN-LSTM [8, 11, 12] are very useful and can improve performance over individual networks in identifying human activities. Although DNNs have been shown to be effective for micro-Doppler recognition, their performance is sometimes lacking due to data sparsity [13, 14]. DNNs are known to be data-intensive, requiring large amounts of labeled training samples to obtain satisfactory results [15]. Unfortunately, the requirement for a large amount of radar data is difficult to meet. Data acquisition and annotation remain complex, expensive, and time-consuming tasks.

Data augmentation is an effective technique used to increase the size and diversity of the training set by generating new synthetic samples from the original data. Several approaches in computer vision have been proposed, including geometric transformations and photometric transformations [16, 17]. However, in some cases, radar data cannot be augmented by performing transformations as it might distort the signature patterns [18, 19]. Advanced approaches, including Generative Adversarial Network (GAN), have emerged as a popular class of modern deep learning models for synthetically generating image data [20]. Various works on GAN extensions, such as Deep Convolution GANs (DCGANs), Auxiliary Classifier GAN (AC-GAN), CycleGANs, and Progressively-Growing GANs [21, 22], have been adopted in the radar area and have shown a great ability to mimic complex real-world data. However, the fidelity of the generated data is not guaranteed. Moreover, training GANs is very challenging and requires a lot of effort for implementation. Another alternative workaround in situations where large training data are difficult to access is by using transfer learning (TF) and Domain Adaptation (DA) [23, 24]. These approaches involve training models on a large dataset and then fine-tuning their weights on a small target dataset. However, the required accuracy cannot be met only by directly transferring the features. The models may exhibit unpredictable performance when a mismatch occurs between the source and target training content.

This work aims to develop an automated HAR system that achieves both lower computational requirements and high classification accuracy with small micro-Doppler datasets, with two main objectives in mind. The first objective is to propose a simple and efficient strategy for generating micro-Doppler spectrograms used for training classification algorithms. The main contribution of this research lies in the creation of new samples derived from the original dataset with non-overlapping features. Our focus is on developing an augmentation process that ensures the preservation of essential features in the micro-Doppler signatures without introducing unintended distortions. Additionally, we strive to establish a robust and adaptable augmentation strategy that can be applied to various datasets, rather than relying on a specific one. In contrast to previous studies [13], our approach stands out through its exclusive utilization of image manipulation techniques directly applied to micro-Doppler signatures. Instead of resorting to conventional image transformations [25], we propose the application of Discrete Wavelet Transform (DWT) as a novel alternative. This unique approach sets our work apart and contributes to the advancement in the context of data augmentation strategies.

The original micro-Doppler spectrograms are projected onto the DWT subspace. From this projection, spectrograms are decomposed, resulting in different sub-band images. Next, the decomposition components returned by the DWT process are used in different configuration to generate new samples. From a single spectrogram, three samples are generated, increasing the number of training data without creating duplicates. This approach makes it possible to enhance human motion characteristics to improve the accuracy of the final classifier without adding prior knowledge or re-acquiring data. The second objective is to extend our previous work [26] based on Hand Gesture Recognition (HGR) to the HAR application. Our previous contribution consisted of extending a single sample to three representations by extracting low-level feature images using the Sobel filter.

The generated low-level feature images are then used as independent input for the model. We used a lightweight CNN-LSTM-SVM to classify hand gestures using IR-UWB. Compared to existing models, our approach provides simplicity with significantly high performance.

The remainder of the paper is organized as follows: Section 2 briefly reviews scholarly works related to data augmentation for Micro-Doppler signatures. Section 3 describes the proposed approach. Section 4 provides the evaluation datasets and implementation details. Section 5 presents the experimental results and comparative analysis. The discussion is presented in Section 6, and Section 7 concludes the paper.

2. RELATED WORKS

In order to significantly reduce the cost and effort of data measurement, several data augmentation strategies have been proposed. Researchers in the radar-based HAR field have attempted to use Transfer Learning (TL) and Domain Adaptation (DA) methods [27, 28]. These greatly reduce the dependence of models on large training samples, improve recognition accuracy, and convergence speed. Several DNN models pre-trained on the ImageNet dataset have been used to classify limited micro-Doppler signatures for human activities [29, 30]. Du *et al*. [29] presented a transfer-learned residual network to classify human activity based on micro-Doppler spectrograms. The performance of the model was evaluated on the CMU Mocap dataset. Du *et al*. [30] proposed using pretrained VGG-19 on the ImageNet dataset for the classification of micro-Doppler measurements. The experimental results demonstrate that transfer-learned VGG-19 outperforms the trained model from scratch and gives a reduction in the number of parameters and computing operations. However, the required accuracy cannot be met only by directly transferring the features. The characteristics of radar signatures differ widely from those of optical images.

The models may exhibit unpredictable performance when a mismatch occurs between the source and target training content. Another approach for dealing with low sample support is the simulation of micro-Doppler signatures using motion capture [31]. This approach enables generating a large number of micro-Doppler signatures with different postures and motion speeds of the human model. Moreover, different technical aspects of the radar are supported, such as frequency, angle, and location of the radar. However, the main drawback of this approach is that the generated data is too clean and perfect, while in real scenarios the data is affected by various environmental factors, sensor parameters, and target characteristics. For example, variations introduced by the surrounding environment such as obstructions caused by walls, objects, or movements that are not related to the target. The gap between the real world and the simulation can considerably deteriorates the performance of the models. To tackle this problem, GAN has been proposed as a means to generate highly realistic simulated images [32, 33]. An early effort at applying GAN to synthesize new micro-Doppler signatures was first proposed in [34] for walking gaits at different speeds. A similar approach has been proposed in [35] to generate different human actions, extended to other movements than simply walking. Gurbuz *et al.* [13] used a GAN to synthesize micro-Doppler signatures collected from three radars for cross-frequency training. Results show an increase in the overall classification accuracies. Erol *et al.* [36] used ACGAN to generate more diverse and crisp synthetic micro-Doppler signatures. The results showed the effectiveness of synthetic ACGAN data adapted to different detection locations and environments. Zhong *et al.* [37] proposed using DCGAN to achieve data augmentation of the micro-Doppler samples set. Experimental studies have shown that the combination of GAN and CNN can achieve effective recognition. However, the experimental simulation is set up in an ideal environment without other target interference. A major drawback of the synthetic data generated by GAN is that its fidelity is not guaranteed. Although GAN has demonstrated its ability to generate realistic synthetic data, their fidelity is not guaranteed. Micro-Doppler signatures generated by GAN have been found to correspond to kinematically impossible behaviors or to classes of motions different from those expected [38, 39].

3. PROPOSED METHODOLOGY

The proposed methodology comprises three steps: data augmentation, data preprocessing, and classification. In the data augmentation step, DWT is applied to the original samples for the decomposition process. The obtained components are manipulated and used in different configurations to generate new samples to enrich the training set. In the preprocessing step, the Sobel filter is applied to each sample to expand the dataset and generate low-level image features to be used as independent input for the classification model. In the classification phase, a three-input CNN-LSTM-SVM is applied to classify the processed data into the corresponding activity.

The schematic diagram of the proposed methodology is depicted in Fig. 1.

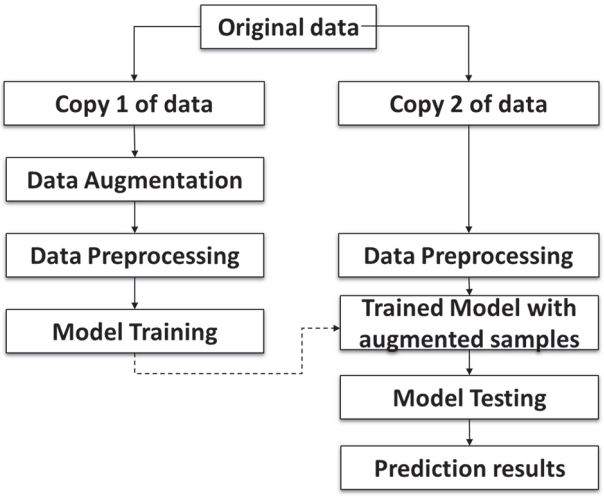

Fig. 1. Schematic diagram of the proposed methodology

3.1. DWT AUGMENTATION

In this work, we focus on the generation of 2D micro-Doppler samples to enrich the training set. We propose to use DWT with the aim of investigating its notable feature that allows the decomposition of an image into components. The DWT scheme is shown in Fig. 2.

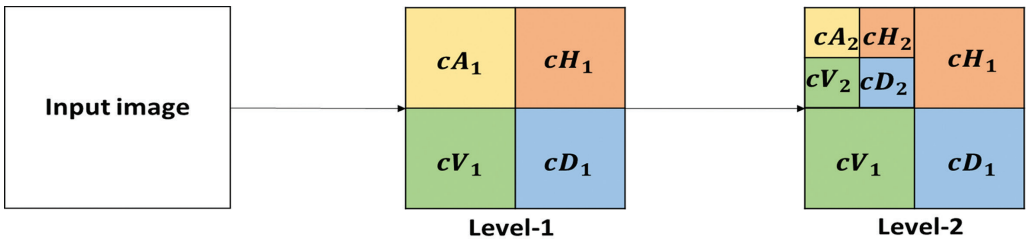

Fig. 2. 2D discrete wavelet decomposition process

3.1. DWT AUGMENTATION

In this work, we focus on the generation of 2D micro-Doppler samples to enrich the training set. We propose to use DWT with the aim of investigating its notable feature that allows the decomposition of an image into components. The DWT scheme is shown in Fig. 2. The DWT applies two filter banks, the low-pass filter, and the high-pass filter, to hierarchically decompose the input image into sub-bands, resulting in a single-level high and low-frequency parts. The low-frequency part is further divided into high and low-frequency parts for further levels of decomposition. The decomposition process is achieved by means of small waves called wavelets, of variable frequency and limited duration. There are many types of wavelet functions, including Haar, Daubechies, Symlets, and Coifflets [40]. Due to its low computing requirements, the Haar transformation has been primarily used for image processing and pattern recognition and is adopted in this work. By employing the DWT with the Haar wavelet, we can effectively decompose the micro-Doppler signatures into different frequency sub-bands, enabling further manipulation to enrich the training set.

Starting with the original image of size NxN, the Micro-Doppler signatures augmentation process is as follows:

- The low-pass and high-pass filters are applied to each row of the image and then sampled by a factor of 2, giving two half-images. One with scaling coefficients and the other with wavelet coefficients. Both images correspond to half the line width of the original image (N/2xN).
- The low-pass and high-pass filters are applied in the column direction of the image generated by the first step. This results in four quarter sub-bands representing different frequency ranges and spatial orientations within the original image. The quarter sub-bands refer to the single-level decomposition coefficients including approximation cA1, diagonal cD1, horizontal cH1, and vertical coefficients of size N/2 x N/2 as shown in Fig. 3. We consider a single-level decomposition to be an appropriate size, as additional levels of decomposition may result in the loss of useful information.
- The important information is concentrated in the approximation coefficient cA1. The horizontal cH1, vertical cV1, and diagonal cD1 coefficients can easily be perturbed by noises. Therefore, we propose to inject each of these coefficients on the cA1 and sum the pixels between the two images as shown in Fig. 3. This way three new images are generated as follows:

cA1 + cD1
cA1 + cV1
cA1 + cH1

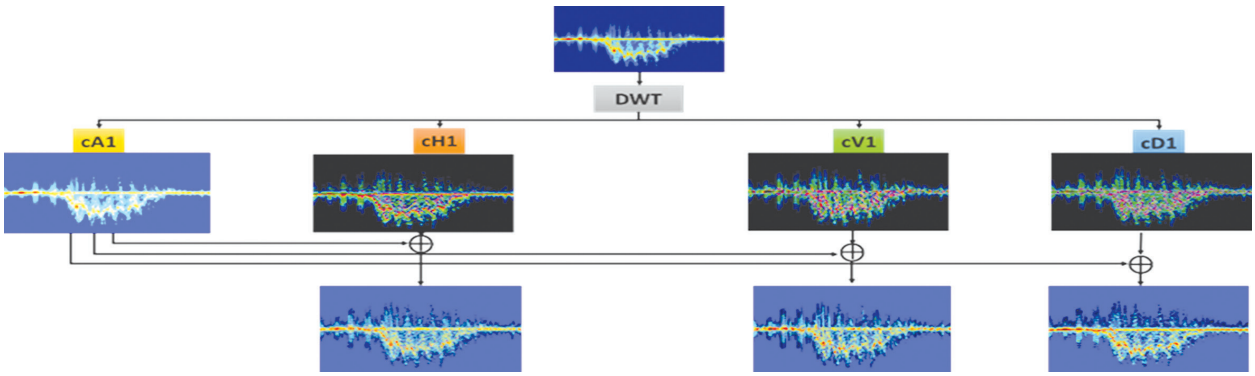

Fig. 3. Proposed augmentation process

3.2. PREPROCESSING

For the preprocessing phase, we adopt the proposed approach in [26]. This method is designed to improve the image content in order to extract and learn discriminative features. It makes use of the Sobel filter to generate low-level image features to be used as independent inputs for the model. These features include the image gradient in the x-direction (Dx), y-direction (Dy), and both x and y-directions (Dxy). The samples are first binarized and then extended using the Sobel

filters. The latter uses two directional filters to convolute the input image, respectively, to obtain Dx, Dy and Dxy. More details about the data preprocessing can be found in [26].

3.3. CLASSIFICATION

Micro-Doppler signatures are, by nature, variable time series data. They represent the time-varying velocity of different parts of the human body. Therefore, it is necessary to involve a process that exploits the temporal correlations of spatial features rather than simply detecting the global geometric shape.

For the classification stage, the three-input CNN-LSTM-SVM model [26] is considered for activity classification. The results from our previous work have demonstrated the effectiveness of combining CNN and LSTM for automatic spatiotemporal feature learning. The spatiotemporal feature extraction is carried out by the Three-input CNN-LSTM. The CNN part consists of three branches with similar layer configurations. Each of the Dx, Dy and, Dxy images is processed in a separate branch by performing multiple convolution operations to extract spatial features. The three CNN branches operate in parallel, and their outputs are combined for further processing by the LSTM. The concatenated features are reshaped and provided as input to the LSTM for temporal feature extraction. The LSTM captures and memorizes how the features extracted by the CNN layers change over time. The output of the LSTM is put into vector form and fed into the multiclass SVM. The SVM uses the OneVsRest strategy and gives the prediction result.

4. MATERIALS AND METHOD

4.1. DATASET

We evaluate the proposed approach on the Multi-Frequency Sensor Network Human Activity Database proposed by Gurbuz *et al.* [13]. The database consists of three datasets acquired from three synchronized radar sensors operating in monostatic mode. The sensors include the 77 GHz FMCW radar IWR1443 from Texas Instruments, the 24 GHz FMCW radar from Ancortek, and the 10 GHz XeThru X4 UWB pulse radar from XeThru. Each dataset comprises 11 classes of human activities, namely WLKT (walking towards the radar), WALKA (walking away from the radar), PICK (picking up an object from the ground), BEND (bending over), SIT (sitting on a chair), KNEEL (kneeling), CRWL (crawling towards the radar), LIMP (limping with a stiff right leg), WTOES (walking on both toes), SHTEPS (walking with small steps), and SCSSR (walking with scissors). Data acquisition involved six participants of various ages, heights, and weights. Each activity is performed 10 times by a participant, resulting in 60 signatures per class per sensor. The micro-Doppler signatures from all three radar sensors for all eleven activities are shown in Fig. 4.

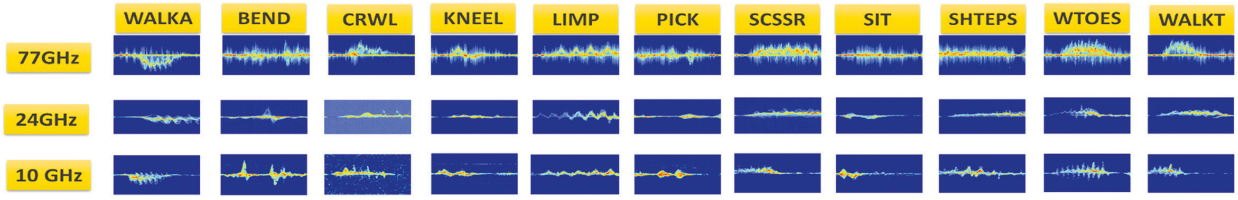

Fig. 4. Micro-Doppler signatures for each human activity class/radar

4.2. IMPLEMENTATION

The implementation of the proposed augmentation technique is performed using Matlab R2021 on a machine running an environment with an Intel (R) Core (TM) i5 2.40 GHz CPU, 16GB of RAM, 1TB of hard disk, and Windows 10. To consistently visualize the impact of the augmentation strategy on the model's generalization ability, we divided the datasets into three subsets: training, validation, and test. The validation set is used as an intermediary checkpoint, allowing us to assess the model's behavior during the training phase. When using the original datasets with a restricted number of samples, the validation set serves the purpose of identifying overfitting. Furthermore, when utilizing augmented samples, the validation set serves a dual purpose. Firstly, it enables us to ensure that the model effectively learns from the augmented samples. Secondly, it assists in ensuring that the augmented samples closely match the characteristics of the test data. The operations of training, validation, and testing were conducted on Google Collaboratory.

To evaluate our proposal in the experimental analysis, four experiments are performed for each dataset.

- **Experiment 1**: use the original datasets without augmentation or preprocessing. Each dataset is split into 80% for training, 10% for validation, and 10% for test. The same sample is simultaneously provided to all three CNN branches. To facilitate a concise comparison, we utilize the same test set across all experiments. To achieve this, we employ the random seed parameter to ensure consistent partitioning.
- **Experiment 2**: use the preprocessed original datasets without augmentation. Each dataset is split into 80% for training, 10% for validation, and 10% for test similar to experiment 1. Each CNN branch is fed with Dx, Dy, and Dxy, respectively.

- **Experiment 3**: use the augmented samples for training and the original samples for testing. The augmented samples are binarized and split into 90% for train and 10% for validation. Two tests are realized. Test (a): Use only a 10% portion of the original dataset as the test set, as mentioned in Experiment 1. Test (b): To prevent biased evaluation, we test the model on the entire original dataset, including all samples.
- **Experiment 4**: use the processed augmented samples for training and the processed original samples for testing. The model is trained using extended augmented images, where each CNN branch is fed with Dx, Dy, and Dxy, respectively. For the test, we follow the same procedure as Experiment 3. The test process of Experiment 3 is replicated.

Note that the model for all experiments is trained from scratch for 100 epochs with a batch size of 16 using the Adam optimizer with a learning rate set to 0.001. All the default configurations of the model are left intact as mentioned in [26]. Except for the LSTM layer, the number of units is changed to 300. For the SVM classifier, the number of binary classifiers is set to 11 corresponding to the number of class activities. We use the same SVM hyperparameters as mentioned in [26]. By keeping hyperparameters constant over all datasets for all experiments, we can demonstrate that the mitigation of overfitting is attributed to data augmentation rather than hyperparameter tuning.

4.3. EVALUATION METHOD

To evaluate the classification performance of the model, five assessment measures are used, including accuracy, precision, recall, F1-score, and the confusion matrix. These metrics are calculated based on the number of true positives (T_P), true negatives (T_N), false positives (F_P), and false negatives (F_N) using the following equations:

$$Accuracy = \frac{T_P + T_N}{T_P + T_N + F_P + F_N} \quad (1)$$

$$Precision = \frac{T_P}{T_P + F_P} \quad (2)$$

$$Recall = \frac{T_P}{T_P + F_N} \quad (3)$$

$$F1\text{-}score = \frac{2T_P}{2T_P + F_P + F_N} \quad (4)$$

5. EXPERIMENTAL RESULTS

The results of each experiment within the proposed framework will be provided in this section. Each subsection will display the results separately for each dataset.

5.1. 77 GHZ DATASET

The results are presented in Table 1. The confusion matrix and the classification report obtained from the combination of augmentation and preprocessing applied to the test data are depicted in Fig. 5 (A) and Fig. 6 (A), respectively.

Table 1. Comparative classification performance on the 77 GHz dataset

Experiment		Train Acc %	Val Acc %	Test Acc %	Precision %	Recall %	F1-score %
Exp 1		100	93.32	92.36	92.58	92.33	92.30
Exp 2		100	95.44	93.93	95.12	93.94	93.82
Exp 3	(a)	100	98.01	95.45	97.47	95.45	94.73
	(b)	100	98.01	96.47	96.61	96.42	96.40
Exp 4	(a)	100	98.21	98.48	98.99	98.18	98.45
	(b)	100	98.21	96.78	96.97	96.71	96.67

5.2. 10 GHZ DATASET

The results are presented in Table 2. The confusion matrix and the classification report obtained from the combination of augmentation and preprocessing applied to the test data are depicted in Fig. 5 (B) and Fig. 6 (B), respectively.

Table 2. Comparative classification performance on the 10 GHz dataset

Experiment		Train Acc %	Val Acc %	Test Acc %	Precision %	Recall %	F1-score %
Exp 1		100	88.29	81.33	86.58	81.82	80.33
Exp 2		100	91.52	83.33	88.71	83.33	82.80
Exp 3	(a)	100	99.48	100	100	100	100
	(b)	100	99.48	98.18	98.23	98.15	98.17
Exp 4	(a)	100	100	100	100	100	100
	(b)	100	100	100	100	100	100

5.3. 24 GHZ DATASET

The results are presented in Table 3. The confusion matrix and the classification report obtained from the combination of augmentation and preprocessing applied to the test data are depicted in Fig. 5 (C) and Fig. 6 (C), respectively.

Table 3. Comparative classification performance on the 24 GHz dataset

Experiment		Train Acc %	Val Acc %	Test Acc %	Precision %	Recall %	F1-score %
Exp 1		100	86.44	84.84	85.12	87.86	85.25
Exp 2		100	88.41	86.63	86.49	86.64	85.87
Exp 3	(a)	100	95.91	92.42	92.10	94.60	92.81
	(b)	100	95.91	94.27	94.50	94.14	94.14
Exp 4	(a)	100	98.09	98.18	98.18	98.18	97.98
	(b)	100	98.09	96.32	96.40	96.30	96.30

5.4. COMPARISON TO STATE-OF-THE-ART APPROACHES

Our proposed model results can be directly compared with those of Gurbuz *et al*. [13] and Vishwakarma *et al*. [25] as they also used the same 77 GHz dataset. The results are shown in Table 4.

Table 4. Comparative classification performance on the 77 GHz dataset with state of art methods.

Reference	Model	Accuracy
Gurbuz et al. [13]	CAE	85.40%
Vishwakarma et al. [25]	Modified Alexnet	96.44%
Our approach	Three input-CNN-LSTM-SVM	96.78%

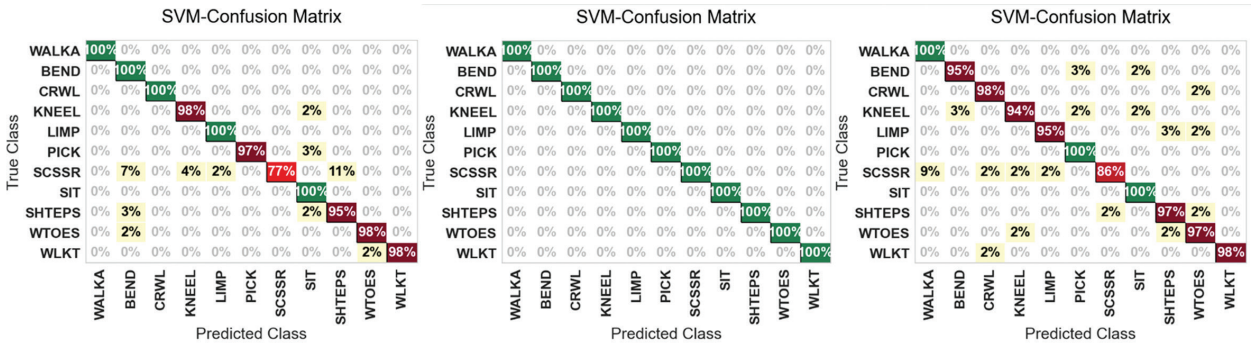

(a) (b) (c)

Fig. 5. Confusion matrix exp 4 (b) : (a) 77 Ghz, (b) 10 GHz, (c) 24 GHz, dataset

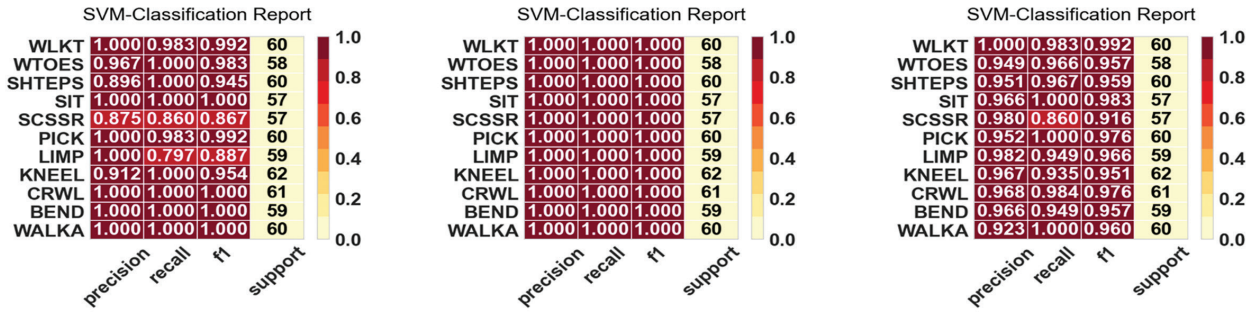

(a) (b) (c)

Fig. 6. Classification report exp 4 (b) : (a) 77 Ghz, (b) 10 GHz, (c) 24 GHz, dataset.

6. DISCUSSION

The results of Experiment 1 in Tables 1, 2, and 3 demonstrate that the model is suffering from overfitting. During the training phase, the model exhibits exceptional accuracy, reaching 100% on all three datasets. Nevertheless, when validated/tested on new, unseen data, the model's accuracy drops significantly and remains notably lower than its training accuracy. This discrepancy between training and validation/test accuracy is due to the limited size of the training set, which causes a lack of generalization. With restricted training data, the model is unable to capture all possible patterns and variations in the data. As a result, it tends to memorize rather than learn generalizable patterns.

From Experiment 2 in Tables 1, 2, and 3, we observe that using preprocessed data helps to enhance the model's accuracy on all datasets. An improvement rate in the test accuracy of 1.52%, 2%, and 2.2% is noticed for the 77 GHz, 10 GHz, and 24 GHz datasets, respectively. The preprocessing stage plays a crucial role in enhancing the content of images and facilitating the extraction and concatenation of additional features. Despite these benefits, the model's generalization ability remains limited. This is due to insufficient exposure to variations necessary for learning robust features that can effectively generalize to new data.

As observed from Experiment 3, the inclusion of the augmentation process during the training phase enhanced robustness and improved the model's performance. After conducting test (a) from Experiment 3, as shown in Tables 1, 2, and 3, a significant improvement in accuracy across all three datasets is observed. This noteworthy progress is primarily attributed to introducing higher variability among training samples. This variation enables the model to effectively discern patterns and overcome the limitations associated with generalization. Consequently, the model becomes better at making accurate predictions on unseen data, reducing the detrimental effects of overfitting that were apparent in the results of Experiments 1 and 2. The analysis of test (b) results from Experiment 3, as presented in Tables 1, 2, and 3, highlights the comparative performance with the results of test (a). The model achieved an accuracy of 96.43%, 98.18%, and 94.27% on the 77 GHz, 10 GHz, and 24 GHz datasets, respectively. This indicates that the model is well-generalized and has the potential to perform effectively on large new unseen data. This further

substantiates the reliability of the proposed augmentation approach. However, when comparing the model's performance on test (a) and test (b) from Experiment 3, employing a larger test set yielded superior accuracy for both the 77 GHz and 24 GHz datasets. This difference in accuracy suggests that using only a fraction of samples, often obtained through random splitting, might introduce greater variability. This issue arises from the possibility that the selected instances may not accurately represent the entire dataset, leading to biased evaluations. To address this concern, it is more appropriate to consider evaluating the model on a larger number of test samples, promoting a fair assessment.

Following Experiment 4, further improvement is achieved by combining data augmentation and preprocessing. The classification reports depicted in Fig.6 shows consistent results in terms of precision, recall, and F1-score for all three datasets. The model achieved accuracies of 96.78%, 100%, and 96.32% on the 77 GHz, 10 GHz, and 24 Ghz datasets, respectively. The analysis of the confusion matrices (A) and (C) in Fig. 5, corresponding to the 77 GHz and 24 GHz datasets respectively, reveals slight overfitting. The model encounters difficulty in accurately distinguishing between different activities within the various classes. This challenge can be attributed to the presence of highly similar features shared among these classes. The existence of common characteristics leads to confusion and misclassification, contributing to the model's limitations in differentiation. We believe that a review of the model's architecture and parameters could contribute to enhancing its ability to discern between activities. The classification report (B) presented in Fig. 6 indicates that the model performs better on the 10 GHz dataset in terms of classification metrics. Moreover, upon examining the confusion matrix (B) depicted in Fig. 5, it becomes apparent that the number and percentage of false positives and false negatives in the test set are zero. This achievement gains even greater significance as the dataset includes more discriminating patterns, enabling the model to effectively distinguish between different activities. This advantage stems from the high resolution of the IR-UWB, which allows for the detection of subtle motion patterns. As a result, the model achieves superior accuracy and the capacity to capture unique patterns associated with distinct activities and individuals.

To justify the relevance of the proposed approach, a comparative analysis of the performances with those reported in the literature using the same dataset is carried out. The results are reported in Table 4.

Gurbuz *et al.* [13] proposed to use GAN-synthesized data from the 77 GHz dataset to train a Convolutional AutoEncoder (CAE). Their model achieved a modest accuracy of 85.40%. The authors attributed this suboptimal performance to a mismatch between the distributions of synthetic and real data. In contrast, our model provided an improvement rate of 11.38%, reaching an accuracy of 96.78%. Through our approach, we successfully mitigated the mismatch problem by introducing an augmentation strategy that fosters better generalization on unseen data. Vishwarkarma *et al*. [25] proposed to artificially add Additive White Gaussian Noise (AWGN) to the 77 GHz dataset samples and use them to train a modified AlexNet with an attention mechanism. Compared to their model, which reached an accuracy of 96.44%, ours provided a slight improvement of 0.34%. In contrast to our approach, which makes use only of augmented samples, the authors in [25] utilized a combination of original and augmented samples for training purposes. Introducing original samples likely contributed to their improved performance as these samples share the same distribution as the test samples. Additionally, the authors employed a complex architecture with millions of parameters, while our model consists of a simple and lightweight structure maintained with 635397 trainable parameters. Furthermore, it is important to acknowledge that their approach has solely been evaluated on the 77 GHz dataset, and therefore, its generalizability to other datasets remains uncertain.

In conclusion, the proposed approach has been demonstrated to enhance data efficiency during the training process. The generated augmented samples exhibit significant attributes, as affirmed by the outcomes of Experiment 3. These results provide robust validation of the efficacy of the augmentation mechanism. As a result, we can infer that the predictive performance of the model, trained with augmented images using wavelet decomposition, showcases favorable characteristics pertaining to generalization and relevance.

7. CONCLUSION

The significance of this paper lies in offering a practical and effective solution to tackle the scarcity of micro-Doppler signatures for HAR. Our DWT-based augmentation strategy along with preprocessing mitigates the need for extensive data collection and complex models, making it feasible to achieve high performance. Future work in this research aims to explore the impact of using different wavelet basis functions on classification performance and investigate the design of a new architecture to further enhance the classification performance.

8. REFERENCES

[1] G. Diraco, G. Rescio, P. Siciliano, A. Leone, "Review on Human Action Recognition in Smart Living: Sensing Technology, Multimodality, Real-Time Processing, Interoperability, and Resource-Constrained Processing", Sensors, Vol. 23, No. 11, 2023, p. 5281.

[2] I. Ullmann, R. G. Guendel, N. C. Kruse, F. Fioranelli, A. Yarovoy, "A Survey on Radar-Based Continuous Human Activity Recognition", IEEE Journal of Microwaves, Vol. 3, No. 3, 2023, pp. 938-950.

[3] M. M. Islam, S. Nooruddin, F. Karray, G. Muhammad, "Human activity recognition using tools of convolutional neural networks: A state of the art review, data sets, challenges, and future prospects", Computers in Biology and Medicine, Vol. 149, 2022, p. 106060.

[4] A. Dey, S. Rajan, G. Xiao, J. Lu, "Radar-based Human Activity Recognition: Is it Ready for Aging in Place?", TechRxiv, 2023.

[5] J. Maitre, S. Bouchard, K. Gaboury, "Data filtering and deep learning for enhanced human activity recognition from UWB radars", Journal of Ambient Intelligence and Humanized Computing, Vol. 14, No. 6, 2023, pp. 7845-7856.

[6] Z. Wang, A. Ren, Q. Zhang, A. Zahid, Q. H. Abbasi, "Recognition of Approximate Motions of Human Based on Micro-Doppler Features", IEEE Sensors Journal, Vol. 23, No. 11, 2023, pp. 12388-12397.

[7] S. Hassan, X. Wang, S. Ishtiaq, N. Ullah, A. Mohammad, A. Noorwali, "Human Activity Classification Based on Dual Micro-Motion Signatures Using Interferometric Radar", Remote Sensing, Vol. 15, No. 7, 2023, pp. 1–21.

[8] F. Luo, E. Bodanese, S. Khan, K. Wu, "Spectro-temporal modelling for human activity recognition using a radar sensor network", IEEE Transactions on Geoscience and Remote Sensing, Vol. 61, 2023, pp. 1-13.

[9] L. Jiang, M. Wu, L. Che, X. Xu, Y. Mu, Y. Wu, "Continuous Human Motion Recognition Based on FMCW Radar and Transformer", Journal of Sensors, Vol. 2023, 2023.

[10] X. Li, Y. He, X. Jing, "A survey of deep learning-based human activity recognition in radar", Remote Sensing, Vol. 11, No. 9, 2019, p. 1068.

[11] S. Huan, L. Wu, M. Zhang, Z. Wang, C. Yang, "Radar Human Activity Recognition with an Attention-Based Deep Learning Network", Sensors, Vol. 23, No. 6, 2023, p. 3185.

[12] H. Zhou, Y. Zhao, Y. Liu, S. Lu, X. An, Q. Liu, "Multi-Sensor Data Fusion and CNN-LSTM Model for Human Activity Recognition System", Sensors, Vol. 23, No. 10, 2023, p. 4750.

[13] S. Z. Gurbuz, M. M. Rahman, E. Kurtoglu, T. Macks, F. Fioranelli, "Cross-frequency training with adversarial learning for radar micro-Doppler signature classification (Rising Researcher)", Radar Sensor Technology XXIV, Vol. 11408, 2020, pp. 58-68.

[14] M. Mahbubur Rahman, S. Z. Gurbuz, "Multi-Frequency RF Sensor Data Adaptation for Motion Recognition with Multi-Modal Deep Learning", Proceedings of the IEEE Radar Conference, Atlanta, GA, USA, 07-14 May 2021, pp. 1-6.

[15] L. Alzubaidi et al. "A survey on deep learning tools dealing with data scarcity: definitions, challenges, solutions, tips, and applications", Journal of Big Data, Vol. 10, No. 1, 2023, p. 46.

[16] G. Zhou, Y. Chen, C. Chien, "On the analysis of data augmentation methods for spectral imaged based heart sound classification using convolutional neural networks", BMC Medical Informatics and Decision Making, Vol. 22, No. 1, 2022, p. 226.

[17] X. Hao, L. Liu, R. Yang, L. Yin, L. Zhang, X. Li, "A Review of Data Augmentation Methods of Remote Sensing Image Target Recognition", Remote Sensing, Vol. 15, No. 3, 2023. p. 827.

[18] S. Yang et al. "The Human Activity Radar Challenge: benchmarking based on the Radar signatures of human activities dataset from Glasgow University", IEEE Journal of Biomedical and Health Informatics, Vol. 27, No. 4, 2023, pp. 1813-1824.

[19] R. Bravin, L. Nanni, A. Loreggia, S. Brahnam, M. Paci, "Varied Image Data Augmentation Methods for Building Ensemble", IEEE Access, Vol. 11, 2023, pp. 8810-8823.

[20] Y. Yang, Y. Zhang, C. Song, B. Li, Y. Lang, "Omnidirectional Spectrogram Generation for Radar-based Omnidirectional Human Activity Recognition", IEEE Transactions on Geoscience and Remote Sensing, Vol. 61, 2023, pp. 1-13.

[21] A. Oubara, F. Wu, A. Amamra, G. Yang, "Survey on Remote Sensing Data Augmentation: Advances, Challenges, and Future Perspectives", Proceedings of the 5th International Conference on Computing Systems and Applications, Algiers, Algeria, 17-18 May 2022, pp. 95-104.

[22] D. Bathe, K. Patil, N. Sanjay, "Leveraging Potential of Deep Learning for Remote Sensing Data", Proceedings of the International Conference on

Intelligent Systems and Human Machine Collaboration, Maharashtra, India, 8-9 July 2022, pp. 129–145.

[23] O. Pavliuk, M. Mishchuk, C. Strauss, "Transfer Learning Approach for Human Activity Recognition Based on Continuous Wavelet Transform", Algorithms, Vol. 16, No. 2, 2023, p. 77.

[24] A. Alkasimi, A. V. Pham, C. Gardner, B. Funsten," Geolocation tracking for human identification and activity recognition using radar deep transfer learning", IET Radar, Sonar & Navigation, Vol. 17, No. 6, 2023, pp. 955-966.

[25] S. Vishwakarma, W. Li, C. Tang, K. Woodbridge, R. R. Adve, K. Chetty, "Attention-enhanced Alexnet for improved radar micro-Doppler signature classification", IET Radar, Sonar & Navigation, Vol. 17, No. 4, 2023, pp. 652-664.

[26] D. S. Korti, Z. Slimane, K. Lakhdari, "Enhancing Dynamic Hand Gesture Recognition using Feature Concatenation via Multi-Input Hybrid Model", International journal of electrical and computer engineering systems, Vol. 14, No. 5, 2023, pp. 535–546.

[27] Y. Lang, Q. Wang, Y. Yang, C. Hou, D. Huang, W. Xiang, "Unsupervised Domain Adaptation for Micro-Doppler Human Motion Classification via Feature Fusion", IEEE Geoscience and Remote Sensing Letters, Vol. 16, No. 3, 2018, pp. 392–396.

[28] H. Du, T. Jin, Y. Song, Y. Dai, "Unsupervised Adversarial Domain Adaptation for Micro-Doppler Based Human Activity Classification", IEEE Geoscience and Remote Sensing Letters, Vol. 17, No. 1, 2019, pp. 62-66.

[29] H. Du, Y. He, T. Jin, "Transfer Learning for Human Activities Classification Using Micro-Doppler Spectrograms", Proceedings of the IEEE International Conference on Computational Electromagnetics, Chengdu, China, 26-28 March 2018, pp. 1-3

[30] H. Du, T. Jin, Y. Song, Y. Dai, M. Li, "Efficient human activity classification via sparsity-driven transfer learning," IET Radar, Sonar & Navigation, Vol. 13, No. 10, 2019, pp. 1741-1746.

[31] M. S. Seyfioglu, B. Erol, S. Z. Gurbuz, M. G. Amin, "Diversified radar micro-Doppler simulations as training data for deep residual neural networks", Proceedings of the IEEE Radar Conference, Oklahoma City, USA, 23-27 April 2018, pp. 612-617.

[32] Y. Lang, C. Hou, H. Ji, Y. Yang, "A Dual Generation Adversarial Network for Human Motion Detection Using Micro-Doppler Signatures", IEEE Sensors Journal, Vol. 21, No. 16, 2021, pp. 17995-18003.

[33] L. Qu, Y. Wang, T. Yang, Y. Sun, "Human Activity Recognition Based on WRGAN-GP-Synthesized Micro-Doppler Spectrograms", IEEE Sensors Journal, Vol. 22, No. 9, 2022, pp. 8960-8973.

[34] X. Shi, Y. Li, F. Zhou, L. Liu, "Human Activity Recognition Based on Deep Learning Method", Proceedings of the IEEE International Conference on Radar, Brisbane, QLD, Australia, 27-31 August 2018, pp. 1-5.

[35] I. Alnujaim, S. S. Ram, D. Oh, Y. Kim, "Synthesis of Micro-Doppler Signatures of Human Activities from Different Aspect Angles Using Generative Adversarial Networks", IEEE Access, Vol. 9, 2021, pp. 46422-46429.

[36] B. Erol, S. Z. Gurbuz, M. G. Amin, "Motion Classification Using Kinematically Sifted ACGAN-Synthesized Radar Micro-Doppler Signatures", IEEE Transactions on Aerospace and Electronic Systems, Vol. 56, No. 4, 2020, pp. 3197-3213.

[37] Y. J. Zhong, Q. S. Li, "Human Motion Recognition in Small Sample Scenarios Based on GAN and CNN Models", Progress in electromagnetics research M, Vol. 113, 2022, pp. 101-113.

[38] B. Erol, S. Z. Gurbuz, M. G. Amin, "Synthesis of micro-doppler signatures for abnormal gait using multi-branch discriminator with embedded kinematics", Proceedings of the IEEE International Conference on Radar, Washington DC, USA, 28-30 April 2020, pp. 175-179.

[39] M. M. Rahman, E. A. Malaia, A. C. Gurbuz, D. J. Griffin, C. Crawford, S. Z. Gurbuz, "Effect of Kinematics and Fluency in Adversarial Synthetic Data Generation for ASL Recognition with RF Sensors", IEEE Transactions on Aerospace and Electronic Systems, Vol. 58, No. 4, 2022, pp. 2732-2745.

[40] E. Guariglia, R. C. Guido, G. J. P. Dalalana, "From Wavelet Analysis to Fractional Calculus: A Review", Mathematics, Vol. 11, No. 7, 2023, pp. 1-12.

Correlation Coefficients and Adaptive Threshold-Based Dissolve Detection in High-Quality Videos

Original Scientific Paper

[1]**Kamal S. Chandwani**
Sarvepalli Radhakrishnan University
Bhopal, Madhya Pradesh, India
chandwani1@rediffmail.com

[2]**Varsha Namdeo**
Department of Computer Science & Engineering
Sarvepalli Radhakrishnan University
Bhopal, Madhya Pradesh, India
varsha_namdeo@yahoo.com

[3]**Poonam T. Agarkar**
Department of Electronics & Telecommunication Engineering
Yeshwantrao Chavan College of Engineering
Nagpur, Maharashtra, India
poonamagarkar71@gmail.com

[4]**Sanjay M. Malode**
Department of Computer Science & Engineering
K. D. K. College of Engineering
Nagpur, Maharashtra, India
malodesanjay14@gmail.com

[5]**Prashant R. Patil**
Department of Management Studies
Smt. Radhikatai Pandav College of Engineering
Nagpur, Maharashtra, India
patilnagpur@gmail.com

[6]**Narendra P. Giradkar**
Department of Electronics & Telecommunication Engineering
Smt. Radhikatai Pandav College of Engineering
Nagpur, Maharashtra, India
giradkarnaresh@gmail.com

[7]**Pratik R. Hajare**
Mansarovar Global University
Bhopal, M.P., India
pratikhajare8@gmail.com

Abstract *– Rapid enhancements in Multimedia tools and features day per day have made entertainment amazing and the quality visual effects have attracted every individual to watch these days' videos. The fast-changing scenes, light effects, and undistinguishable blending of diverse frames have created challenges for researchers in detecting gradual transitions. The proposed work concentrates to detect gradual transitions in videos using correlation coefficients obtained using color histograms and an adaptive thresholding mechanism. Other gradual transitions including fade out, fade in, and cuts are eliminated successfully, and dissolves are then detected from the acquired video frames. The characteristics of the normalized correlation coefficient are studied carefully and dissolve are extracted simply with low computational and time complexity. The confusion between fade in/out and dissolves is discriminated against using the adaptive threshold and the absence of spikes is not part of the case of dissolves. The experimental results obtained over 14 videos involving lightning effects and rapid object motions from Indian film songs accurately detected 22 out of 25 gradual transitions while falsely detecting one transition. The performance of the proposed scheme over four benchmark videos of the TRECVID 2001 dataset obtained 91.6, 94.33, and 92.03 values for precision, recall, and F-measure respectively.*

Keywords*: Multimedia tools, gradual transitions, correlation coefficients, color histograms, adaptive thresholding, fade out, fade in, cuts, and dissolve*

1. INTRODUCTION

The challenges in video summarization and then retrieval had become the foremost need owing to rapid development in Multimedia technology. The development introduced extremely high-quality techniques in video processing and certainly made it difficult to extract meaningful segments from a video called shots. The greatest challenges introduced include uneven illuminations, camera movements, object rotations, low-contrast backgrounds, low-frequency transitions, etc. The most common approach used in video summarization involves pre-processing the video frames, extracting and selecting optimum features, finding correlation coefficients between successive or neighboring frames, detecting transitions, identifying key frames, detecting and tracking objects, classification, etc. Shots carry vital information regarding specific scenes and can be differentiated by detecting abrupt transitions and gradual

transitions. Abrupt transitions are even perceptual and can be easily detected using simple algorithms when the correlation between successive frames is evaluated. Gradual transitions are hard to isolate due to several effects introduced such as dissolves, fade in and out, and wipes. Unlike abrupt transitions, the correlation between successive frames in the case of gradual transitions is very low that is the neighboring frames show high similarity. In detecting such gradual transitions, the transition effects have to be compensated and movements pertaining to objects and camera had to be cautiously handled. Various approaches as studied from the literature used key point detection in frames before finding the similarity between two successive frames. Patch matching with neighboring patches is another sort of technique to perfectly locate the moving patch or region in the frames but requires high computational and time complexity.

Recently, researcher have focused their research on dissolve detection due to unacceptably high false hit rate. Most of them are based on histograms, pixels, edges, etc. Histograms offer an advantage since they are invariant to local motions or small global motions. The authors in [1] used threshold to determine transitions when it was applied to the sum of the absolute difference between two successive frames. The transition was declared when the sum was greater than the threshold. A similar approach was used by [2-4]. The work suggested by [5] used an adaptive threshold instead of a fixed threshold based on a sliding window. Region-based matching was proposed in [6] to determine the best match between two neighboring frames. The frames were divided into 12 patches or regions to ensure the extraction of motion vectors and the weighted sum of sorted pixel difference was considered as the correlation between two frames. A twin comparison method [4] was introduced to compare two histograms based on the histogram difference metric. A block-based histogram over RGB color frames was used in [7]. The method in [8] used histograms with 64 bins and block-based histograms in two stages. In the first stage, global histograms were subtracted and their absolute value was compared with a threshold while in the subsequent stage, the histogram difference metric was compared. The number of region differences exceeding the difference threshold when exceeded the count threshold, a transition was observed [9-10]. An inter-frame difference histogram based on the Poisson model to detect abrupt and gradual transitions was proposed in [11]. The work proposed in [12] introduced scale-invariant feature transform to RGB color space while the method in [13] compared different Shot boundary detection schemes using color histograms as features. HSV histogram with level 5 difference was used to detect a gradual transition in [14].

This paper is organized with the following headings: Related work covers state of art work contributed by different researchers: Methods and Materials deals with the proposed work and covers algorithm and complete description of the system: Results and Discussion includes experimental results obtained over two different dataset videos under test and performance parameters: and Conclusion focuses on the summary of the work, loopholes and future scope for the work.

The paper is organized in the following sections. Section 2 summarizes state of art work by other researchers. Section 3 deals with the dataset and the proposed methodology to detect dissolve transitions. Section 4 includes results and discussion while the last section 5 concludes the work.

2. RELATED WORK

Frame features were extracted using principal component analysis to uplift prominent features and then subjected to distance calculating algorithm [15]. The detection accuracy was then improved by reviewing false detection boundaries to convolutional neural networks. The work by [16] suggested improving false detections of transitions and extracting multiple invariant features such as scale-invariant feature transform, color layout descriptor, and edge change ratio. These features compensate for the effect of variations in illumination, motion, scaling, and rotation. The feature set was classified using the SVM classifier to obtain an F1-score of 97% over the TRECVid 2001 dataset. The frames were segmented in [17] into primary and candidate segments to analyze the transition behavior in frames. Segmentation was obtained using the color feature and local adaptive threshold of each part or segment. Speeded Up robust features extracted from boundary segments were utilized to fine-tune the transitions from the candidate segments over TRECVid 2001 dataset to achieve a 90.8% F1-score in case of gradual transitions. A two-stage shot detection technique was presented in [18] employing a fusion of color histogram and deep features for distinguishing hard cuts and C3D-based deep analysis to locate gradual cuts. Abrupt shots are used to partition the video into segments and 3D-convolutional neural networks are used to classify the clips into specific gradual transitions. Merging techniques were used to know the positions of the gradual transitions.

Work introduced in [19] used the three-stage process to detect candidate boundaries, and instant and gradual transitions through deep CNN. They improved the performance by filtering out many non-boundaries and introduced a scheme to locate the start, mid and end points of the gradual transitions. Authors in [20] introduced a two-phased approach to detect candidate dissolves and filter candidates based on a threshold. The first stage involves identifying parabolic patterns in the mean fuzzy entropy of the frames and the second stage uses an ensemble of four parameters for filtering, respectively. The work suggested in [21] detected abrupt shots using Binarized edge information through a linear binary pattern and estimated the Euclidean distance of the histogram features and then applied an adaptive threshold. For key frame extraction, a Sobel operator was used to get the magnitude gra-

dient of frames under a segmented shot and transformed into z-scores. The frame possessing the highest value corresponding to the coefficient of variation was selected as the key frame for the shot.

2.1. OUR CONTRIBUTION

We propose a simple and efficient method to detect dissolve transitions in high-quality videos using correlation coefficients obtained from color histograms. The approach includes:

1. Calculation of Adaptive threshold based on correlation coefficients found over color histograms for isolating other transitions (fade in and fade out) from dissolve transitions.
2. Automatic detection of dissolved transition frames based on width and subsequently the peaks inside the transition.

3. PROPOSED WORK

The proposed work is concentrated on detecting dissolve transitions in videos based on calculating the consecutive frame differences and then thresholding the histogram. The histogram is obtained from the correlated values between two consecutive frames. Histograms for all three color components of two consecutive frames are considered for evaluating the correlated values. It is obtained by subtracting the histograms of individual color components, followed by taking the absolute values, and finally finding the sum. The average value of all three color components across the video clip is then averaged and normalized using the maximum value, and a histogram corresponding to (N-1) correlated values is obtained. The maximum values in the (N-1) correlated values are used as a threshold for the (N-1) values. Finally, the threshold correlated values are normalized again concerning the maximum value. The flowchart of the proposed algorithm for detecting the dissolve transitions is shown in Fig. 1 below. N represents the total number of frames in the clip or video.

Considering the $frame_m$ to represent one of the two consecutive frames, the histogram h_c for any of the color components is given by expression (1), where H represents the histogram.

$$h_c = H\,(frame_m)_{\,frame\,\epsilon\,(R,\,G,\,B)} \tag{1}$$

The correlation between two consecutive frames is thus obtained by the following expression (2), where (i) and (i+1) are any two consecutive frames, and m represents any of the channels including the R, G, and B.

$$C_{m\,\epsilon\,(R,\,G,\,B)} = sum\,(abs\,(h_{im} - h_{(i+1)m})) \tag{2}$$

The correlated values are stored in an array D which can be represented by,

$$D = \cup_{m=1}^{n=N-1}[C_R; C_B; C_G] \tag{3}$$

The correlation coefficients are obtained by taking the average value of all three components and expressed using the following equation (4),

$$M = \frac{1}{3}\sum_{i=1}^{N-1} D_{R,G,B} \tag{4}$$

The normalizing coefficient M_{max} is obtained by finding the maximum value from M. Equation (5) finds the maximum value.

$$M_{max} = Max\,(M) \tag{5}$$

The correlation coefficients are normalized using the expression (6),

$$F = \frac{M}{M_x} \tag{6}$$

Now we find the histogram of the normalized correlation coefficients using expression (7).

$$G = H\,(F) \tag{7}$$

The adaptive threshold is then calculated using the maximum value in the histogram which is given by the following equation (8).

$$T = Max\,(G) \tag{8}$$

With this adaptive threshold T, the values in F are subjected to the threshold using the expression (9).

$$S = \begin{cases} 1 & if\ F > T \\ 0 & Otherwise \end{cases} \tag{9}$$

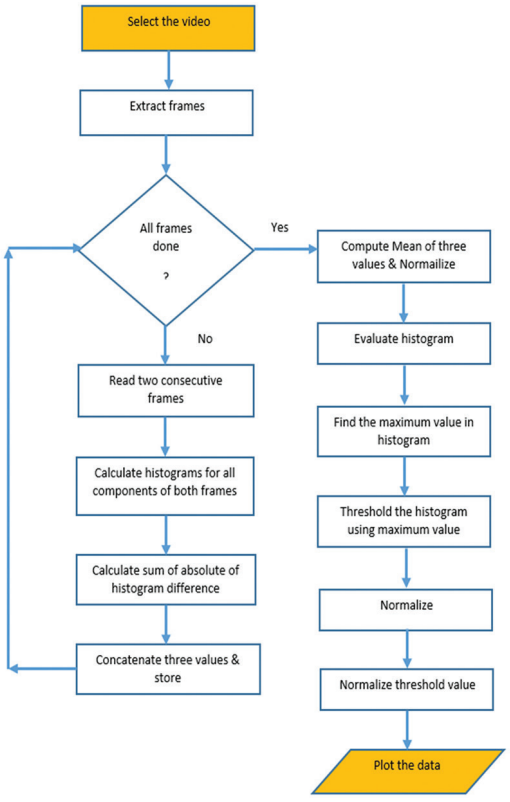

Fig. 1. Flowchart for the proposed algorithm to detect the Dissolve transitions

The original values remaining after thresholding are obtained by multiplying the result obtained using equation (9) by F again, which can be represented by equation (10).

$$S = S\ x\ F \tag{10}$$

Finally, the threshold T is made consistent with the values in S by dividing the threshold T by value 256.

$$T = T/256 \quad (11)$$

Histogram of normalized values is obtained further and the maximum value in the histogram is considered as a threshold. The threshold value is used to threshold the values of the histogram and multiplied by values in the histogram again. The threshold value is normalized by dividing it by value 256 to make it consistent with the histogram obtained in the previous stage.

The following Fig. 2 depicts the plot for one of video clips 4 from the Ashiqui2 song.

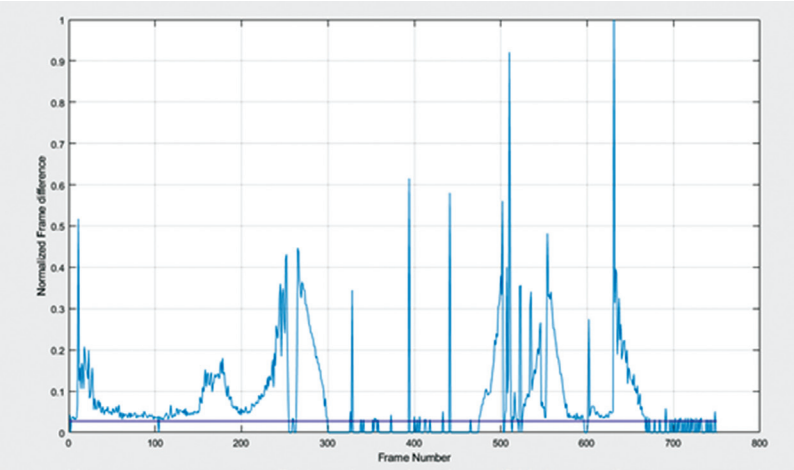

Fig. 2. Final plot obtained by our proposed algorithm on video clip 4 with a horizontal blue line as adaptive threshold

The following algorithm explains the steps to find the correlation coefficients and the adaptive threshold to detect gradual transitions in high-quality videos.

Algorithm 1 – Dissolve Detection

Input: Video Clip V

Output: Frames containing Dissolves F_n

Find the number of frames in the video clip V; N

For m =1 to N-1; N-Number of frames in the video clip

  Read two successive frames

  Evaluate the histogram for each color component; h

  Calculate the sum of absolute values for each component; C

  Store the sum of color component sum; D

End loop; m

Compute the Mean of each color component M and Normalize

Evaluate the histogram from the normalized mean value; G

Compute the Adaptive Threshold; T

Find the Occurrence of gradual transitions

Differentiate Fades and Dissolve Transitions based on Peaks

Find the start and end frames involving dissolve transitions; F_n

After eliminating the fade transitions, the transitions above the threshold line are found using the threshold. The starting frame is noted concerning the transition from low to high transition concerning the threshold line. The transition should remain high for at least 6 frames for a true dissolve. The cut-off value of 6 frames is found from experimental analysis and found to agree with more than 98% of cases. The other 2% of cases include fast camera motion accompanied by low illuminations and are confused with dissolves. The ending frame involves a high-to-low transition concerning the threshold. Similarly, other gradual transitions are found.

3.1. DATASET

We examined two video songs from Hindi movies *Ashiqui2* and *Once Upon a Time in Mumbai* and the other four videos from the benchmark dataset TRECVID 2001 for comparison. The song videos were cut into smaller videos consisting of 500 to 800 frames. The reason behind this is to reduce the computations and time complexity. The videos are so selected to test the effectiveness of our proposed algorithm since the songs are subjected to many objects plus camera motions and varying illuminations and include many dissolve, fade in, fade out, and cuts transitions. We also separated video clips involving wipe transitions but not covered their detection in this work. Fig. 3 shows a short dissolve transition from the song *Ashiqui2*. The number of frames is displayed at a slower rate reduced by 5 but the actual number of frames containing dissolve is 13, which starts with the 696th frame and ends at the 715th frame. All the videos have an original frame rate of 25 frames per second.

The video clips used in this work and the manual results obtained for dissolve transitions are given in Table 1 in the result and discussion section. For simplicity, we have not mentioned other transitions as those are not part of this work such as fade, fade-outs, and cuts. We have dealt with fade-in and fade-out in our earlier work [22]. We obtained 100% accuracy in detecting cuts, fade-in, and fade-out transitions.

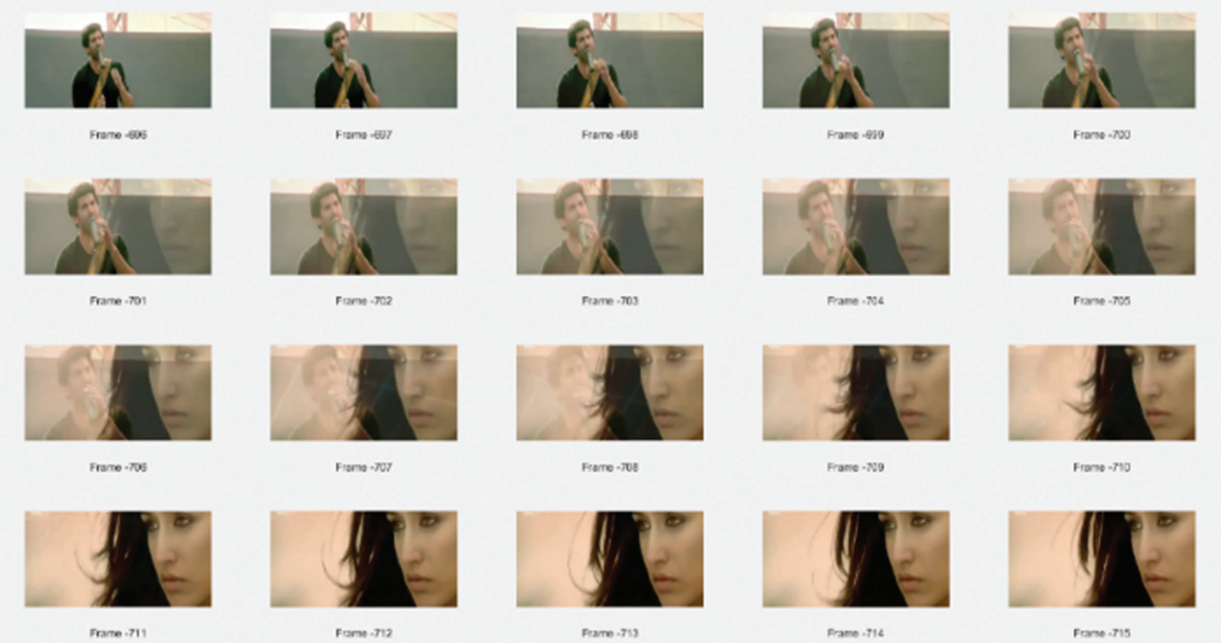

Fig. 3. A short dissolve (13 frames length) from the HINDI movie *ASHIQUI2* from frames 696 to 715

4. RESULTS AND DISCUSSION

Experimental evaluations carried out on 14 different clips containing rapid object/camera motions and uneven illumination showed that our technique was able to detect the gradual transitions with high accuracy except in some cases. The nature of variation in normalized correlation coefficients using the histogram technique as discussed earlier is presented in Fig. 4. The correlation coefficients touch the adaptive threshold line during the start and end of the gradual transition and remain above the threshold during the dissolve transition. The same effect is observed in the case of fade-in and fade-out transitions but there is an abrupt transition during the start and end frame which can be seen in figure 4. The effect of object motion and uneven illuminations are compensated using this technique. Slight spikes resulting from the object motion in dissolve transitions are unable to reach the threshold and thus can be detected as dissolves.

As seen from Figure 4, fade out followed by fade in as acquired by the correlated coefficients have different characteristics as compared to dissolve transitions. Dissolve transitions never touches the adaptive threshold line (Red) during the complete transition. Cuts are one-frame spikes as indicated by the green arrow. The small spikes occurring between the start and end of any of the transitions are effects of object motion or due to differences of illuminations between successive frames. The following figures from 5 to 11 represent the nature of correlation coefficient plots obtained for other videos.

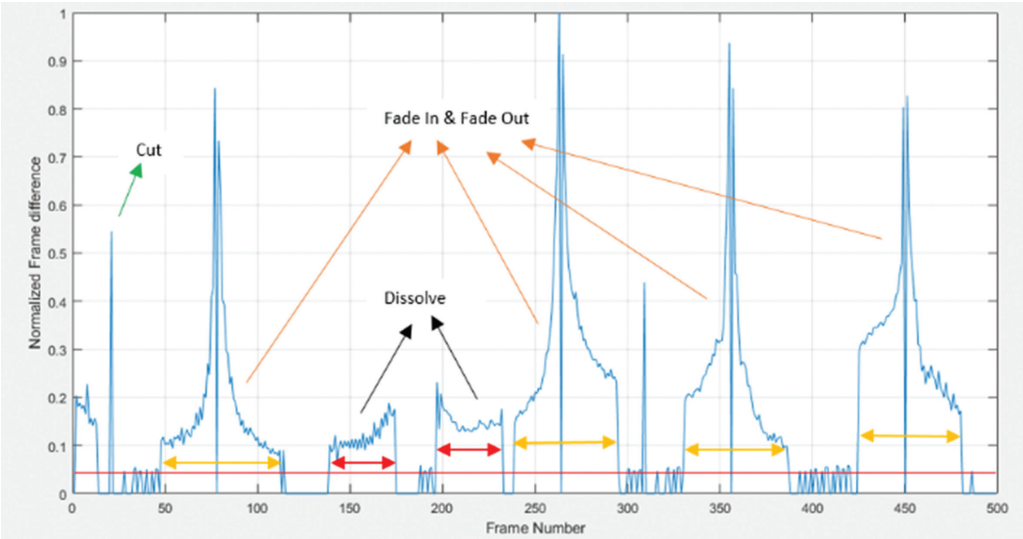

Fig. 4. Final plot obtained by our proposed algorithm on video clip 13. The correlation coefficient characteristics for cut (green), dissolve (black), and fade in and fade out (orange).

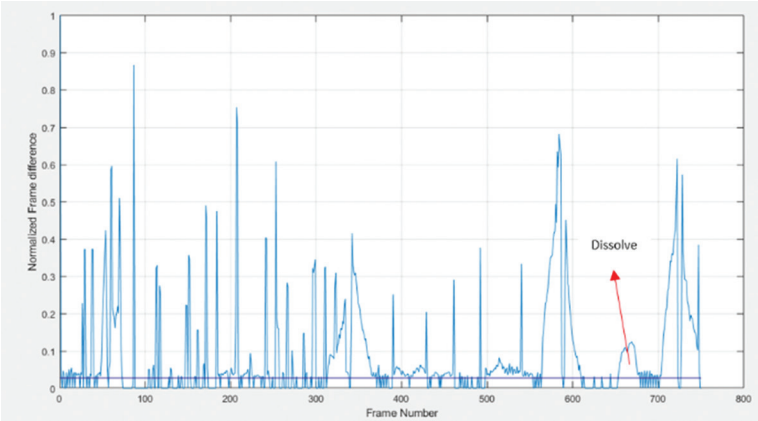

Fig. 5. Video clip 1 and the detected dissolve

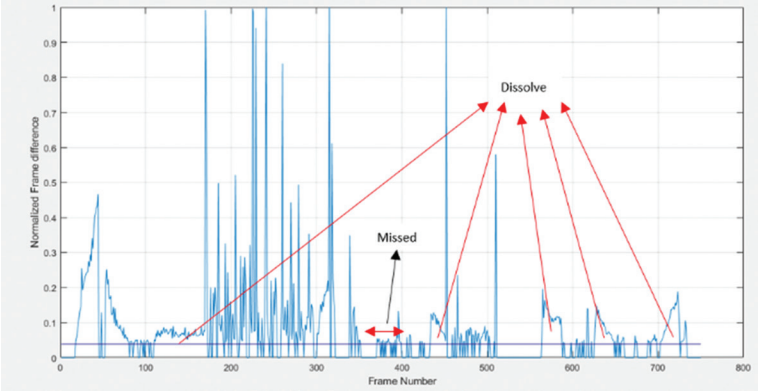

Fig. 6. Video clip 2 with Missed and detected dissolves

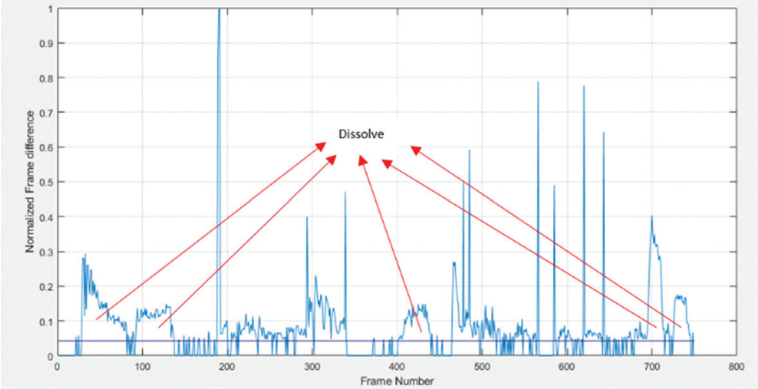

Fig. 7. Video clip 3 with detected dissolves

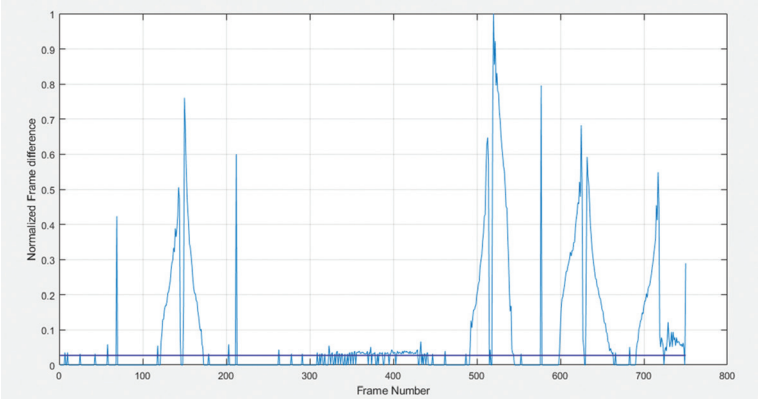

Fig. 8. Video clip 5 with no dissolve transitions

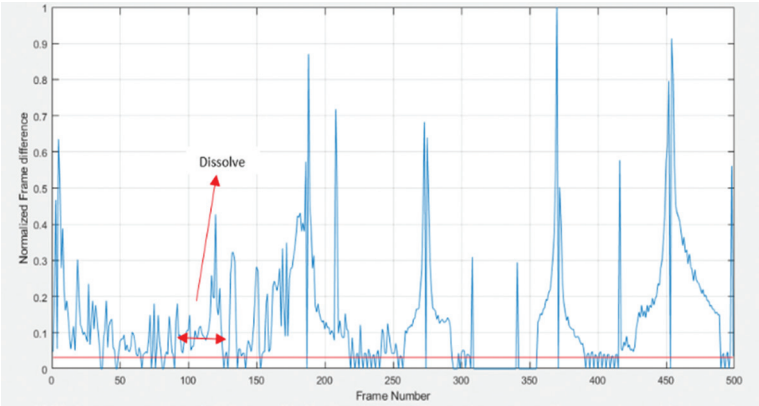

Fig. 9. Video clip 12 with no dissolve transitions

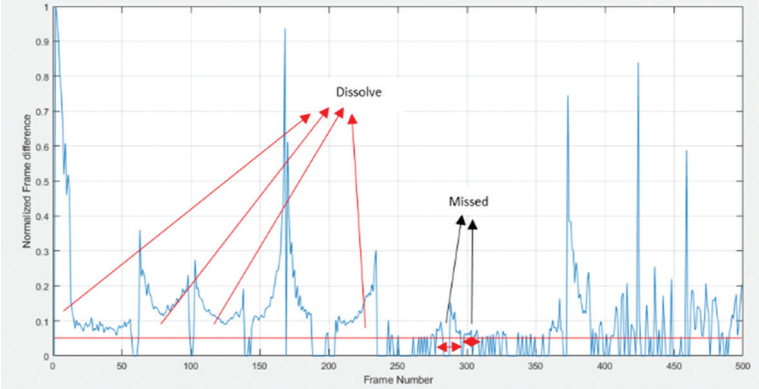

Fig. 10. Video clip 15 with Missed and detected dissolves

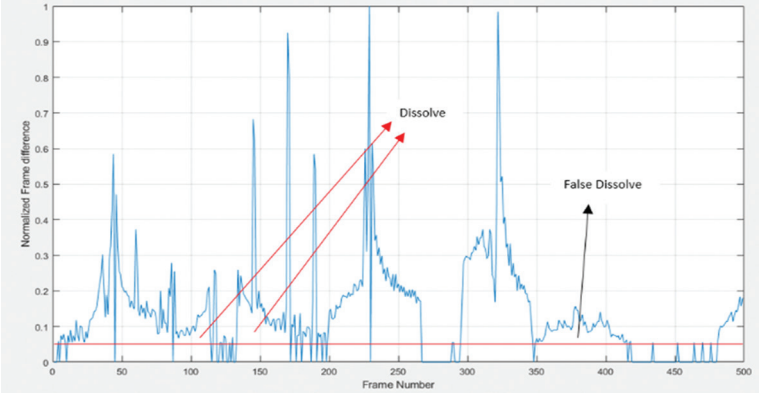

Fig. 11. Video clip 16 with False and True dissolves

Video Clips 6, 7, 8, 9, 10, 11, 13, 14, and 17 are not shown since they have no dissolve transitions and video Clip 18 has two dissolve transitions but are accurately detected by our proposed system. Video clip 2 (Missed dissolve from frame 380 to 400) shows missed dissolved transitions due to the reasons that there exist extreme lightning changes and rapid camera motion. The undetected dissolves in video clip 15 (244-280 & 290-325) were due to densely populated objects and very slow transitions of similar types of frames at the beginning and end of the transition. The similarity is due to the old frame being closely associated with the new frame as shown in Fig. 12.

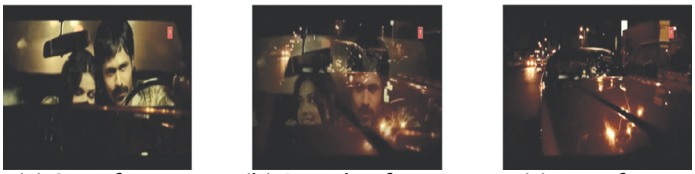

(a) Start frame (b) Dissolve frame (c) Next frame

Fig. 12. Dissolve scene from video clip 15, where the start frame and the next frame are closely associated concerning illumination and background (dark)

The false dissolve in video clip 16 is due to the motion of a large object covering almost 80% of the significant frame. Advancements in multimedia technology no matter had improved the perceptual quality of videos and made the entertainment eye-catching but at the same time increased the challenge of detecting gradual transitions and was almost impossible in some cases where the blending is done within a few frames (less than 5-6 frames). Table 1 shows the results obtained using our technique.

Table 1. Comparison between dissolve detected with the proposed technique and the ground truth

Sr. No.	Video Song	Video Clip	Actual Dissolve transition (Ground Truth)	Dissolve transition detected	Discrepancies
1	Aashiqui 2	Video Clip 1	655-690	✓	
2		Video Clip 2	110-130 380-400 431-450 561-585 630-650 700-721	✓	Missed – (380-400)
3		Video Clip 3	30-80 100-135 413-440 696-711 728-750	✓	
4		Video Clips 4,5 and 6	None	✓	
5	Once upon a time in Mumbai	Video Clip 11, 14 and 17	None	✓	
6		Video Clip 12	99-120	✓	
7		Video Clip 13	140-175 197-235	✓	
8		Video Clip 15	25-55 64-100 105-140 204-235 244-280 290-325	✓	Missed – (244-280, 290-325)
9		Video Clip 16	81-110 135-120	✓	False dissolve – (345-420)
10		Video Clip 18	1-20 618-645		

Assuming TP for True positive samples, FP for false positive samples, and FN for false negative samples.

$$\text{Then, } Precision\ P = \frac{TP}{(TP+FP)} \tag{12}$$

$$Recall\ R = \frac{TP}{(TP+FN)} \tag{13}$$

$$\text{And, } F\text{-}Measure\ F = \frac{2*P*R}{(P+R)} \tag{14}$$

Therefore, $TP = 22$, $FP = 1$, $FN = 3$ gives

$P = 22/24 = 0.9167$,

$R = 22/(22+3) = 0.88$ and

$F = (2x0.9167x0.88)/(0.9167 + 0.88) = 0.90$.

The performance of the proposed scheme is compared with other state of artwork techniques based on quantitative analysis concerning the standard TECHVID 2001 dataset and includes Eigenvalue decomposition and Gaussian transition detection method [23], Walsh-Hadamard transforms kernel-based method [24], temporal segmentation method [25], Multimodal visual feature method [26], 3D convolutional network method [27], visual color information [28], Adaptive thresholds and gradual curve point [29] and SURF feature descriptor [30]. The work proposed in [26] obtained multimodal features using frame-based SURF features thus increasing complexity and ignoring the illumination changes. Work done in [28] however tracked the illumination variations in the L*a b color space but was unable to cope with tracking due to poor features on account of rotation and scaling. The adaptive threshold estimated in [30] is estimated over the full-length video which affects the generalization ability of the algorithm when videos involve rapid scene changes.

The work suggested in [29] relies on the average edge image. Deep fine edge detection operators increase the chances of misclassification and considering only hard edges increases the probability of transition elimination. The analysis in Table 2 shows that the proposed scheme is comparable concerning a precision score of 91.6 with the SURF feature-based approach in [30] while it outperforms in terms of Recall and F1-measure.

Table 2. A Quantitative Analysis of the Proposed Method on the TRECVID 2001 Dataset

Method	Video	Precision	Recall	F1-Score
Eigen Value Decomposition and Gaussian Transition Detection Method [23]	anni006	85.2	93.8	89
	anni009	82.1	84.5	81.5
	anni010	78.4	91.2	83.5
	nad58	92	93	91.4
	Average	**84.5**	**92.3**	**87**
Walsh–Hadamard Transform Kernel-Based Method [24]	anni006	90	87.1	88.5
	anni009	88.7	85.9	87.3
	anni010	84.6	80	82.2
	nad58	88.5	88.5	88.5
	Average	**88.0**	**85.4**	**86.6**
Temporal Segmentation Method [25]	anni006	92.2	84.3	91.1
	anni009	86	87.9	84.2
	anni010	84.2	88.5	85.0
	nad58	91.5	92.8	93.7
	Average	**86.7**	**89.1**	**89.0**
Multi-Modal Visual Features Method [26]	anni006	77.8	90.3	83.6
	anni009	89.6	67.2	76.8
	anni010	65.5	65.5	65.5
	nad58	80.4	82.2	81.3
	Average	**78.3**	**76.3**	**76.8**
3D Convolutional Network Method [27]	anni006	95.5	92.8	90.2
	anni009	80.6	94.3	88.2
	anni010	85.6	84.5	88.9
	nad58	90.6	90.2	92.1
	Average	**87.3**	**91.7**	**89.7**
Visual Colour Information Method [28]	anni006	83.3	88.2	85.7
	anni009	84.8	87.5	86.2
	anni010	81.7	89.1	85.2
	nad58	90.9	87	88.9
	Average	**85.2**	**88.0**	**86.5**
Adaptive Thresholds And Gradual Curve Point [29]	anni006	77.3	83.9	83.6
	anni009	90.2	85.5	87.5
	anni010	93.6	87.3	92.4
	nad58	94.1	90.2	92.5
	Average	**91.7**	**86.5**	**89.6**
SURF Feature Descriptor [30]	anni006	92.3	88.9	90.6
	anni009	92.7	91.1	91.9
	anni010	89.1	100	94.2
	nad58	92.7	90.5	91.6
	Average	**91.7**	**92.6**	**92.1**
Proposed Scheme	anni006	92.3	90.6	90.0
	anni009	91.6	100	90.4
	anni010	89.5	95.4	94.6
	nad58	93.1	91.3	93.1
	Average	**91.6**	**94.33**	**92.03**

The color depth-based approach using the correlation between successive frames can track illumination changes and camera motions. However, our approach failed when the gradual transition is fast and abrupt involving a transition of less than 6 frames. Also, dissolve transitions occurring in high proportionate dark backgrounds with low-intensity frames are missed since the frame lacks proper color features.

5. CONCLUSIONS

Out of 18 video clips, with 25 dissolve transitions, the novel approach presented in this work was able to detect dissolve transitions in 11 videos having 22 dissolves with 100% accuracy. The video clips 4, 5, 6, 11, 14, and 17 were accurately determined by our technique which contained no dissolve transitions. The reason for missed detection and false detection for videos 2, 15, and 16 had been quoted in the previous section. Thus our system for detecting gradual transitions in videos was successful in detecting 22 out of 25 transitions with an accuracy of approximately 92%. The precision, recall, and F-measure are 0.9167, 0.88, and 0.90 respectively. The detection can be improved if the effect of illumination changes is compensated using any of the state of art contrast correction methods and the effect of object motion is properly handled using the robust correlation between neighboring frames. The proposed work achieved remarkable results over the TRECVID 2001 dataset outperforming another state of the artwork. The precision, recall, and F1 measure were found to be 91.6, 94.33, and 92.03 respectively average over four videos from the dataset. Future work will be concentrated to improve the detection accuracy and eliminate false detection using extracting optimum features from the frames for finding correlations between neighboring frames and deducing the feature vector for optimum detection.

6. REFERENCES

[1] M. S. Lee, Y. M. Yang, S. W. Lee, "Automatic video parsing using shot boundary detection and camera operation analysis", Pattern Recognition, Vol. 34, 2001, pp. 711-719.

[2] T. Kikukawa, S. Kawaguchi, "Development of an automatic summary editing system for the audio-visual resources", The Transactions of the Institute of Electronics, Information and Communication Engineers, Vol. 75, 1992, pp. 204-212.

[3] A. Nagasaka, Y. Tanaka, "Automatic video indexing and full-video search for object appearances. In Visual Database Systems II", North-Holland Publishing Co., 1992, pp. 113-127.

[4] H. Zhang, A. Kankanhalli, S. W. Smoliar, "Automatic partitioning of full-motion video", Multimedia Systems, Vol. 1, 1993, pp. 10-28.

[5] B. L. Yeo, B. Liu, "Rapid Scene Analysis on Compressed Video", IEEE Transaction on Circuits and Systems, Video Technology, Vol. 5, 1995, pp. 533-544.

[6] B. Shahraray, "Scene change detection and content-based sampling of video sequences", Proceedings of the IS&T/SPIE's Symposium on Electronic Imaging: Science & Technology; International Society for Optics and Photonics, San Jose, CA, USA, 1995, pp. 2-13.

[7] D. Swanberg, C. F. Shu, J. R. Jain, "Knowledge-guided parsing in video databases", Proceedings of the IS&T/SPIE's Symposium on Electronic Imaging: Science and Technology; International Society for Optics and Photonics, San Jose, CA, USA, 1993, pp. 13-24.

[8] J. S. Boreczky, L. A. Rowe, "Comparison of video shot boundary detection techniques", Journal of Electronics and Imaging, Vol. 5, 1996, pp. 122-128.

[9] J. Yuan, H. Wang, L. Xiao, W. Zheng, J. Li, F. Lin, B. Zhang, "A formal study of shot boundary detection", IEEE Transaction on Circuits & Systems for Video Technology, Vol. 17, 2007, pp. 168-186.

[10] S. H. Abdulhussain, A. R. Ramli, M. I. Saripan, B. M. Mahmmod, S. A. R. Al-Haddad, W. A. Jassim, "Methods and challenges in Shot boundary detection: a review", Entropy, Vol. 20, No. 4, 2018, p. 214.

[11] Y. Huo, Y. Wang, H. Hu, "Effective algorithms for video shot and scene boundaries detection", Proceedings of the IEEE/ACIS 15th International Conference on Computer and Information Science, Okayama, Japan, 26-29 June 2016, pp. 1-6.

[12] Z. El Khattabi, Y. Tabii, A. Benkaddour, "Video shot boundary detection using the scale-invariant feature transform and RGB color channels", International Journal of Electrical and Computer Engineering, Vol. 7, 2017, pp. 2565-2573.

[13] U. Gargi, R. Kasturi, S. H. Strayer, "Performance characterization of video-shot-change detection methods", IEEE Transaction on Circuits & Systems for Video Technology, Vol. 10, No. 1, 2000, pp. 1-13.

[14] Z. Li, X. Liu, S. Zhang, "Shot boundary detection based on the multilevel difference of color histograms", Proceedings of the First International Conference on Multimedia and Image Processing, Bandar Seri Begawan, Brunei, June 2016, pp. 15-22.

[15] D. Chakraborty, W. Chiracharit, K. Chamnongthai, "Semantically Relevant Scene Detection Using Deep Learning", Proceedings of the Asia-Pacific Signal and Information Processing Association Annual Summit and Conference, Tokyo, Japan, 14-17 December 2021, pp.1576-1579.

[16] T. J. Jose, S. Rajkumar, M. R. Ghalib, A. Shankar, P. Sharma, M. R. Khosravi, "Efficient Shot Boundary Detection with Multiple Visual Representations", Mobile Information Systems, Vol. 2022, 2022.

[17] M. R. Suguna, A. Kalaivani, S. Anusuya, "The Detection of Video Shot Transitions Based on Primary Segments Using the Adaptive Threshold of Colour-Based Histogram Differences and Candidate Segments Using the SURF Feature Descriptor", Symmetry, Vol. 14, No. 10, 2022, p. 2041.

[18] L. Wu, S. Zhang, M. Jian, Z. Lu, D. Wang, "Two-stage Shot Boundary Detection via Feature Fusion and Spatial-Temporal Convolutional Neural Networks", IEEE Access, Vol. 7, 2019, pp. 77268-77276.

[19] T. Wang, N. Feng, J. Yu, Y. He, Y. Hu, Y.-P. P. Chen, "Shot boundary detection through Multi-stage Deep Convolution Neural Network", Proceedings of the 27th International Conference, Multimedia and Multimodal Analytics in the Medical Domain and Pervasive Environments, Prague, Czech Republic, 22-24 June 2021.

[20] B. Hrishikesh, M. Chakraborty, S. Bhattacharya, S. Chakraborty, "Detection of Gradual Transition in Videos: Approaches and Applications", Intelligent Analysis of Multimedia Information, IGI Global, 2017, pp. 282-318.

[21] H. M. Nandini, H. K. Chethan, B. S. Rashmi, "Shot-based key-frame extraction using edge-LBP approach", Journal of King Saud University, Computer and Information Science, Vol. 34, 2022, pp. 4537-4545.

[22] K. Chandwani, V. Namdeo, N. Giradkar, P. Patil, "Multilevel wavelet-based features for detecting gradual transitions in High-Quality Videos", NeuroQuantology, Vol. 20, No. 13, 2022, pp. 2805-2812.

[23] A. Amiri, M. Fathy, "Video shot boundary detection using generalized eigenvalue decomposition and Gaussian transition detection", Computing and Informatics, Vol. 30, No. 3, 2012, pp. 595-619.

[24] G. G. L. Priya, S. Domnic, "Walsh-Hadamard Transform Kernel-Based Feature Vector for Shot Boundary Detection", IEEE Transaction on Image Processing, Vol. 23, 2014, pp. 5187-5197.

[25] E. Santos, A. C. Sousa, H. Pedrini, "Shot boundary detection for video temporal segmentation based on the Weber local descriptor", Proceedings of the IEEE International Conference on Systems, Man, and Cybernetics, Banff, AB, Canada, 5-8 October 2017, pp. 1310-1315.

[26] S. Tippaya, S. Sitjongsataporn, T. Tan, M. M. Khan, K. Chamnongthai, "Multi-Modal Visual Features-Based Video Shot Boundary Detection", IEEE Access, Vol. 5, 2017, pp. 12563-12575.

[27] T. Liu, Y. Lu, X. Lei, L. Zhang, H. Wang, W. Huang, Z. Wang, "Soccer video event detection using 3D convolutional networks and shot boundary detection via deep feature distance", Proceedings of the International Conference on Neural Information Processing, Guangzhou, China, 14-18 November 2017, pp. 440-449.

[28] S. Chakraborty, D. M. Thounaojam, N. Sinha, "A Shot boundary Detection Technique based on Visual Colour Information", Multimedia Tools & Applications, Vol. 80, 2021, pp. 4007-4022.

[29] N. Kumar, D. Raj, "Shot Boundary Detection Framework for Video Editing Via Adaptive Thresholds and Gradual Curve Point", Turkish Journal of Computer and Mathematics Education, 2021, Vol. 12, No. 11, pp. 3820-3828.

[30] M. Raja Suguna, A. Kalaivani, S. Anusuya, "The Detection of Video Shot Transitions Based on Primary Segments Using the Adaptive Threshold of Colour-Based Histogram Differences and Candidate Segments Using the SURF Feature Descriptor", Symmetry, Vol. 14, 2022, p. 2041.

Gravitational Deep Convoluted Stacked Kernel Extreme Learning Based Classification for Face Recognition

Original Scientific Paper

Gowri A.
Department of Information Technology,
Hindusthan College of Arts and Science,
Coimbatore, Tamilnadu, India
Department of Computer Science,
Government Arts College, Udumalpet,
Tiruppur, Tamilnadu, India.
gowrihindusthan@gmail.com

J. Abdul Samath
Department of Computer Science,
Chikkanna Government Arts College,
Tiruppur, Tamilnadu, India

Abstract *– In recent times, researchers have designed several deep learning (DL) algorithms and specifically face recognition (FR) made an extensive crossover. Deep Face Recognition systems took advantage of the hierarchical framework of the DL algorithms to learn discriminative face characterization. However, when handling severe occlusions in a face, the execution of present-day methods reduces appreciably. Several prevailing works regard that, when face recognition is taken into consideration, affinity materializes to be a pivotal recognition feature. However, the rate of affinity changes when the face image for recognition is found to be illuminated, and occluded, with changes in the age of the subject. Motivated by these issues, in this work a novel method called Gravitational Deep Convoluted Stacked Kernel Extreme Learning-based (GDC-SKEL) classification for face recognition is proposed for human face recognition problems in frontal views with varying age, illumination, and occlusion. First, with the face images provided as input, Gravitational Center Loss-based Face Alignment model is proposed to minimize the intra-class difference, which can overcome the influence of occlusion in face images. Second, Deep Convoluted Tikhonov Regularization-based Facial Region Feature extraction is applied to the occlusion-removed face images. Here, by employing the Convoluted Tikhonov Regularization function, salient features are said to be extracted with an age-invariant representation. Finally, Stacked Kernel Extreme Learning-based Classification is designed. The extracted features are given to the Stacked Kernel Extreme Learning-based Classification and to identify testing samples Stacked Kernel is utilized. The performance of GDC-SKEL is evaluated on Cross-Age Celebrity Dataset. Experimental results are compared with other state-of-the-art classifiers in terms of face recognition accuracy, face recognition time, PSNR, and False Positive Rate which shows the effectiveness of the proposed GDC-SKEL classifier.*

Keywords*: Face Recognition, Gravitational Convoluted, Gravitational Center Loss, Face Alignment, Tikhonov Regularization*

1. INTRODUCTION

Over the past few years, different types of biometric methods have been employed for authentication purposes in security priority systems wherein facial image recognition is one of the most utilized of them. Siamese Neural Network based on Local Binary Pattern (also called LBP) and Frequency Feature Perception (SN-LF) was proposed and applied the Uniform LBP algorithm and Frequency Feature perception to recognize faces under non-restricted conditions. With the application of the LBP algorithm, the influence of lighting on the image was discarded, and that in turn provided vector-level input to the network model. Next, the frequency feature was split into low-frequency features and high-frequency features. The human factor is considered to be probably the weakest element in the security chain because the internal threat is among the top informa-

tion security issues [1]. Here, the low-frequency features were compressed for improving recognition significance while exchanging information to preserve feature data while discarding noisy data. As a result, the recognition rate was said to be maintained and therefore resulted in the improvement of network computational speed. Though improvement was said to be found in recognition accuracy and robustness, the running time or the recognition time involved in face recognition was not focused.

An age-invariant face recognition system was designed in [2] that was split into four distinct steps, namely, preprocessing, feature extraction, feature fusion, and classification. First, employing Viola-Jones algorithm preprocessing was performed for aligning the frontal face. Second, feature extraction was done using CNN architecture to extract compact face features. The resultant extracted features were then fused utilizing feature-level multi-discriminant correlation analysis to minimize the feature dimensions and therefore obtain the most relevant features.

Current facial recognition methods are designed based on deep neural networks that are found to be efficient but expensive in training. In [3], a lightweight neural network was designed that consisted of fewer factors than the conventional deep neural networks. Moreover, an inhibitory layer was also introduced in the last layer that by reducing the number of trainable parameters also improved the overall performance.

With the prevailing COVID-19 pandemic, wearing masks has become mandatory in our day-to-day life. However, the usage of masks resulted in several issues concerning facial recognition accuracy owing to the reason that most of the facial features were hidden by the mask. To address this issue, a new method for masked face recognition integrating cropping-based models with an enhanced VGG-16 architecture was designed [4].

Yet another method integrating deep learning with Local Binary Pattern (LBP) features was proposed in [5] to identify the masked face. Moreover, multi-task learning integrating joint extra-supervised and self-supervised face detectors was also employed for concentrating on numerous scales of faces. The convolutional neural network was applied in [6] for face detection in the presence or absence of a face mask. Deep learning and parallelism were utilized in [7] for distinct facial expression recognition.

The main contributions of the proposed Gravitational Deep Convoluted Stacked Kernel Extreme Learning-based (GDC-SKEL) classification for face recognition are:

- The design of a face alignment model minimizes the intra-class difference that can control the impact of occlusion. A novel Gravitational Center Loss-based Face Alignment model is presented in this study and the proposed Gravitational Center Loss is utilized for face alignment. To calculate numerical results of the proposed Gravitational Center Loss-based Face Alignment, 100 face images are chosen and three widely used face recognition methods are utilized for comparisons.
- A model called Deep Convoluted Tikhonov Regularization-based Facial Region Feature extractor has been implemented. The main aim of the proposed Reference Convoluted Tikhonov Regularization-based Facial Region Feature extractor is to extract significant facial region features for further processing across years from facial images.
- The design of a Stacked Kernel Extreme Learning-based Classification to make training easier and improve the recognition accuracy.
- We conduct a series of experiments on the Cross-Age Celebrity Dataset and a comparison analysis is also made. The results show that the proposed method achieves state-of-the-art performance and outperforms the conventional learning methods in terms of face recognition accuracy, face recognition time, PSNR, and false positive rate.

The rest of the paper is organized as follows. Section 2 briefly introduces the related works in face recognition using machine and deep learning algorithms. The proposed WKSRC algorithm is released in Section 3 in detail, and Section 4 gives the experimental results of SRC, KSRC, and WKSRC with the public databases to confirm the better performance of our proposal. And Section 5 concludes this paper and gives some future directions.

2. RELATED WORKS

The face is the most pivotal feature utilized by humans for the recognition process. Hence, Face recognition (FR) is said to be the classical issue and is still very active in image processing. This is owing to the reason that face recognition has become a major necessity in authentication systems for ensuring both safety and security factors. The novice facial format and non-intrusive characteristics have gained a large amount of attention from research communities upon comparison with biometric features like fingerprint, iris, palm, and so on.

Deep learning, in specific the deep convolutional neural networks, has gained immense attention in face recognition, and so enormous deep learning methods have been designed. A summarization of about 330 distinct contributions was provided in [8]. Major deep learning concepts for the analysis of face and recognition were provided and also a precise overview of face recognition issues concerning age, illumination, and expression were provided. In [9], related research on face recognition from numerous angles was investigated. Also, face recognition development stages and related algorithms were provided. Recent advancements in efficient and significant deep learning-based solutions for face recognition were presented in [10].

Video retrieval based on the face images refers to the task of video retrieval consisting of a similar face.

In [11], a comparison of video retrieval based on face images was done using deep learning.

In [12], a wide exploration of face recognition techniques, their advantages, and menaces was surveyed in detail. This survey paper proposes a novel taxonomy to represent potential face identity threats. In [13], a detailed survey of current deep learning-based two dimensions and three dimension representations of face images were analyzed for face recognition.

Face recognition enhancement makes these tasks simpler and quicker. A holistic review of the issue of Facial Kinship Verification to determine the individuals automatically from their facial images provided as input was surveyed in [14]. Numerous facets of three dimension face reconstruction algorithms were explored in [15].

With the evolution of sophisticated environments, the necessity for identifying faces has become significant. Also, face detection and identification have been increasing globally. It necessitates the requirement of security like authorization, authentication, and other crucial inferences. Several algorithms have been designed in the recent past for facial detection. In [16], two face recognition mechanisms using Haar Cascade and Local Binary Pattern were utilized for classification. Many researchers considered a recognition system to detect and recognize individual face images with minimum recognition time [17]. Here, the face recognition process is developed when there are variations in attributes and behaviors both surrounded by different persons. Though, the systems are mostly used to overcome the challenging issues of recognizing the face image [18]. It protects individual human information with efficient recognition. Previously designed algorithms are unable to enhance recognition with minimum time and high accuracy. The above-described methods have minimum accuracy in the recognition of human faces with minimum time and complexity. On considering the above limitations, the following proposed work is developed to provide a better solution to solve these issues.

3. METHODOLOGY

The human face is a critical facet as far as social communication and interaction are concerned. Humans are required to identify others' faces for these purposes. Over the past few years, it is also extensively utilized in providing access control, security concerns, surveillance, and so on. Face recognition enhancement makes those tasks effortless and quicker. Moreover, different robust face recognition methods have been presented to address issues making an appearance for face recognition due to face illumination, occlusion, and age in distinct scenarios [19]. In this section, a method called, Gravitational Deep Convoluted Stacked Kernel Extreme Learning-based (GDC-SKEL) classification for face recognition is designed. Fig.1. shows the block diagram of the GDC-SKEL method for face recognition.

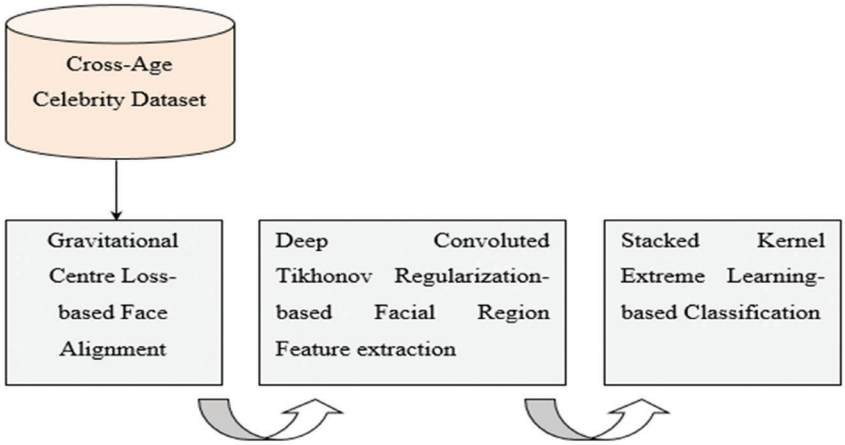

Fig. 1. Block diagram of Gravitational Deep Convoluted Stacked Kernel Extreme Learning-based (GDC-SKEL) classification for face recognition

As shown in Fig.1. Above the GDC-SKEL method is split into three sections. They are face alignment, feature extraction, and classification. First, with the distinct face images obtained as input from the Cross-Age Celebrity Dataset (CACD) dataset, the alignment of the face is made employing Gravitational Center Loss-based Face Alignment model. Second with the aligned faces, salient features are extracted by utilizing Deep Convoluted Tikhonov Regularization-based Facial Region Feature extraction. Finally, with the extracted features, Stacked Kernel Extreme Learning-based Classification is performed for face recognition. A detailed description of the GDC-SKEL is provided in the following sections.

3.1 GRAVITATIONAL CENTER LOSS-BASED FACE ALIGNMENT MODEL

With the evolution of deep learning, several deep models are presented for face alignment and achieve a great deal of performance by referring to various techniques [20]. In this work, a new loss function, namely

Gravitational Center Loss, significantly improves the discriminative potentiality of deeply learned features in neural networks. To be more specific, a center for deep features of each class is learned according to the Gravitational Force. Here, the training process is utilized for updating features to recognize face images. During training, each image feature is determined through estimation, motivation, plan, release, and evaluation. With the result of the training process, center portions are updated and therefore minimize the distances between deep features and their equivalent class centers.

The Gravitational Center Loss in turn significantly obtains the deep features of the same class to their centers. With the integrated management process, not only the interclass features contrasts are augmented but also the intra-class features contrasts are minimized. In this manner, the discriminative potentiality of deeply learned features is said to be improved to a greater extent, therefore enhancing the recognition accuracy with minimum time also. Fig 2 shows the block diagram of the Gravitational Center Loss-based Face Alignment model.

In Fig. 2. the Face alignment model is explained. First, the Cross-Age Celebrity Dataset (CACD) dataset is provided as input with several images. After that, the face image center pixel is obtained and then with the test elements, gravitation force is first applied. According to Gravitation Law, every body mass M_i attracts every other body mass M_j based on the force directing in a straight line l between mass centers, and hence this Gravitation Force is said to be correlative to body masses and inversely proportional to the square of their disjunction. The Gravitational Force is mathematically stated as given below.

$$GF = G * \frac{(M_i * M_j)}{l} \tag{1}$$

From the above equation (1), Gravitational Force GF is presented. Here, G refers to the gravitational constant (i.e., 6.67269 * 10^{-11}), M_i specifies every body mass, and M_j indicates attracted every body mass.

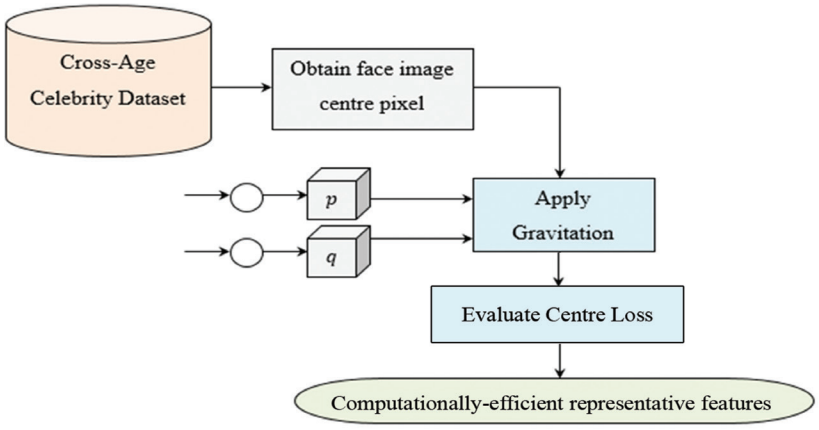

Fig. 2. Block diagram of Gravitational Center Loss-based Face Alignment model

Let us consider a face image FI, face image center pixel as $FI(C)$ of face, (i.e., $FI(C)$) is encircled by eight adjacent pixels, FI_i. Then, the gravitational force applied on $FI(C)$ by the 'th adjacent pixel is denoted by $GFI(C)$, and the p and q elements of GFI_{ip} (C) and GFI_{iq} (C) is mathematically stated as given below.

$$GFI_{ip}(C) = GFI_i(C) * sin\ sin\ \varphi \tag{2}$$

$$GFI_{iq}(C) = GFI_i(C) * cos\ cos\ \varphi \tag{3}$$

Then, based on the application of gravitation force to the face image center pixel concerning the p and q elements is mathematically stated as given below.

$$GFI_{ip}(C) = \sum_{i=1}^{N} \quad G\left[\frac{FI(C) * FI_i}{l_i^2(C)} * sin\ sin\ \varphi\right] \tag{4}$$

$$GFI_{iq}(C) = \sum_{i=1}^{N} \quad G\left[\frac{FI(C) * FI_i}{l_i^2(C)} * cos\ cos\ \varphi\right] \tag{5}$$

From the above equations (4) and (5), N denotes the total number of adjacent pixels, and 'l_i^{2}' represents the square distance between the ith pixel and center pixel C of face image FI respectively. The face image center pixel is denoted as $FI(C)$, the face image with i^{th} pixel is indicated as FI_i, and G specifies the Gravitational function. Next, for the face alignment process, the main issue is to eliminate the influence of the intra-class similarity and therefore enhance the discriminative potentiality of deeply learned features. Hence, in this work, a Gravitational Center Loss function is proposed to minimize the intra-class variations and retain sufficient useful information. With this, the influence of occlusion can be minimized to a greater extent. The Gravitational Center Loss function is then mathematically stated as given below.

$$CLoss = \frac{1}{2}\sum_{i=1}^{N} \quad (FI_i - C_{CLi})^2 \tag{6}$$

From the above equation (6), the Gravitational Center Loss function $CLoss$ is evaluated based on the 'i-th' deep feature of face image FI, the $CLi\text{-}th$ class center of deep features, and the N number of adjacent pixels respectively. With this model, the face image is reconstructed to minimize the intra-class difference to discard the impact of occlusion, therefore improving recognition accuracy. The pseudo-code representation

of Gravitational Center Loss-based Face Alignment is given below.

Input: Dataset DS, Face Image FI=FI_1, FI_2,…, FI_n

Output: Computationally-efficient face aligned images

1: **Initialize** n, angle φ
2: **Begin**
3: **For** each Dataset DS with Face Image FI
4: Formulate Gravitation Force as given in equation (1)
5: Evaluate p and q elements for an angle of φ as given in equations (2) and (3)
6: Evaluate gravitation force concerning the p and q elements as given in equations (4) and (5)
7: Evaluate Gravitational Center Loss function as given in equation (6)
8: **Return** occlusion-removed face images OFI
9: **End for**
10: **End**

Algorithm 1 Gravitational Center Loss-based Face Alignment

As given in Algorithm 1 above with the Cross-Age Celebrity Dataset (CACD) dataset provided as input, the objective here remains in improving the face recognition accuracy even in case of the presence of occlusion. With this objective, Gravitation Force is applied to the raw face images to obtain the edge of the image. Next, the resultant image is subjected to distinct elements concerning angle φ to eliminate the disparities arising due to intra-class variations. Finally, Gravitational Center Loss function is applied wherein the most discriminative or representative features are obtained for further processing, therefore addressing the aspects involved during occlusion.

3.2. DEEP CONVOLUTED TIKHONOV REGULARIZATION-BASED FACIAL REGION FEATURE EXTRACTION

Despite obtaining the pivotal points feature information in the feature extraction module, it is nevertheless a great dispute to recognize facial features with illuminative, occlusion, and age-differing faces. Salient features have to be extracted from occlusion-removed face images for representation. In the proposed method, Deep Convoluted Tikhonov Regularization-based Facial Region Feature extraction is used. The Deep here represents the utilization of Max Pooling Aggregation (MPA) for aggregating representations across different years or ages and on the other hand, the Tikhonov regularization is applied to the occlusion-removed face images to extract salient features. Fig 3 shows the block diagram of Deep Convoluted Tikhonov Regularization-based Facial Region Feature extraction. As shown in Fig.3. above with the occlusion-removed face images provided as input, batch normalization is performed using reference convolute operation. Followed by which pooling is done using the Tikhonov Regularization function, Finally, the Max Pooling Aggregation function is applied to extract salient features.

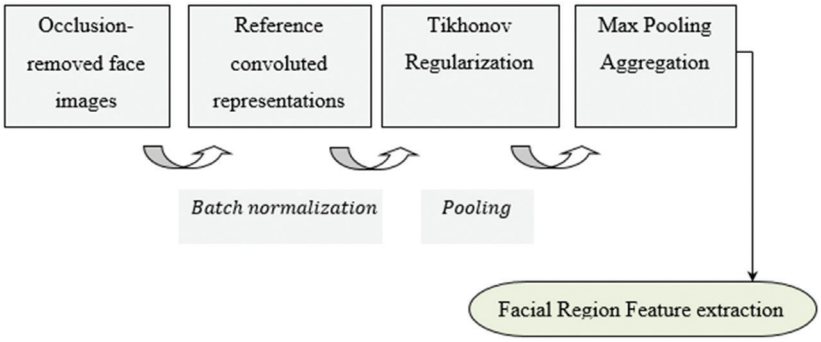

Fig. 3. Block diagram of Deep Convoluted Tikhonov Regularization-based Facial Region Feature extraction

In the proposed Tikhonov regularization model, a novel local structure is provided which is referred to as Max Pooling Aggregation (MPA). Utilizing the occlusion-removed face images, the Deep Convoluted Representations are mathematically stated as given below.

$$DC_i^j = \frac{1}{N_{ij}} \sum \quad OFI_i, \forall\, i = 1,2,\ldots,n; j = 1,2,\ldots,m \quad (7)$$

From the above equation (7), the Deep Convoluted representations DC_i^j are attained for each occlusion-removed face image OFI based on the number of images N and number of years m respectively. Given a set of RR_i^j={RR_1^j, RR_2^j,…, RR_n^j } Reference occlusion-removed face images representation Reference Convoluted representations (i.e., for batch normalization) to encode the new feature is mathematically stated as given below.

$$DC_i^j = \left(OFI_i - RR_i^j \alpha^j\right)^2 + \gamma(\alpha^j)^2 \quad (8)$$

The application of Deep Convoluted temporal relationships between representations across different years is not considered. To address this issue, a temporal constraint employing the Tikhonov Regularization function is employed so that the reconstruction error or the false positive rate can be reduced to a greater extent. To model this function, first, a diagonal matrix DM is formulated as given below.

$$DM=|0\ 0\ 0\ 0\ 1\ 0\ 0\ 0\ 1\ 0\ 0\ 0\ 1\ 0\ 0\ 0\ 1\ 0\ 0\ 0\ 1\ 0\ 0\ 0\ 0| \quad (9)$$

Then, with the above diagonal matrix DM (9), the Deep Convoluted temporal relationship employing the Tikhonov Regularization function (i.e., pooling) between representations across different years is mathematically formulated as given below.

$$\left[\left(OFI_i - RR_i^j \alpha^j\right)^2 + \gamma_1(\alpha^j)^2\right]_{\alpha^j} + \gamma_2(DMOF_i)^2 \quad (10)$$

From the above equation (10), the result of the Deep Convoluted representations DC_i^j is used to reduce the false positive rate (FPR) whereas the second part of the equation is designed with the purpose of face recognition across adjacent years of age to become similar for a subject and vice versa. Finally, Max Pooling Aggregation (MPA) is employed to aggregate representations across different years or ages as given below.

$$a_i = \left(\alpha_i^{(1)} \alpha_i^{(2)}, \ldots, \alpha_i^{(m)}\right) \quad (11)$$

From the above equation (11), aggregate representations are provided as $\alpha i^{(1)}$ $\alpha i^{(2)}$,…,$\alpha i^{(m)}$. By employing MPA, with the presence of two face images of the same person at different ages, face images at a smaller age have a higher response than the older image and vice versa. As a result, face recognition with occlusion-removed face images as input can even result in age-invariant face recognition with a minimum false positive rate. The pseudo-code representation of Deep Convoluted Tikhonov Regularization-based Facial Region Feature extraction is given below.

Input: Dataset DS, Face Image FI=FI_1, FI_2,…, FI_n

Output: Error minimized face extracted TF

1: **Initialize** n, m, occlusion-removed face images OFI
2: **Begin**
3: **For** each Dataset DS with occlusion-removed face images OFI
4: Evaluate Reference Convoluted representations as given in equation (7)

//Batch normalization

5: Obtain Reference Convoluted representations to encode the new feature as given in equation (8)
6: Formulate a diagonal matrix as given in equation (9)

//Pooling

7: Evaluate the Tikhonov Regularization function between representations as given in equation (10)
8: Evaluate Max Pooling Aggregation (MPA) is employed to aggregate representations across different years as given in equation (11)
9: **Return** occlusion-removed age-invariant face extracted TF
10: **End for**
11: **End**

Algorithm 2 Deep Convoluted Tikhonov Regularization-based Facial Region Feature Extraction

As given in the above algorithm, salient features are extracted from occlusion-removed face images using the Deep Convoluted Tikhonov Regularization function. First, Reference Convoluted Representations are evaluated from the occlusion-removed face images provided as input. Second, Tikhonov Regularization functions between representations to generate image results across years. Finally, with the aid of Max Pooling Aggregation aggregate representations across different years are evolved to reduce the false positive rate.

3.3. STACKED KERNEL EXTREME LEARNING-BASED CLASSIFICATION

Numerous robust face recognition methods have been presented in the literature to address the issues arising from face recognition due to face occlusion and illumination in different scenarios. Finally, in this section, the Stacked Kernel Extreme Learning-based (SKEL) classifier is presented. In SKEL, the input weights and biases are selected arbitrarily and output layer weights are ascertained based on the inverse function on the hidden layer output nodes. This in turn generates the learning process very fast and better recognition results upon comparison with the traditional learning algorithms. In SKEL, Stacked Kernel is utilized at the hidden layer to obtain the output.

The SKEL classifier comprises of 'n' input layer's unit, 'M' hidden layer neurons, and the 'K' output layer's unit. In SKEL, the hidden layer output weights post-training are mathematically stated as given below.

$$Res\beta = O \quad (12)$$

From the above equation (12), β denotes the hidden layer output weights post-training, Res denotes the hidden layer output matrix, and O represents the expected classifier output respectively. Also, SKEL classifier output weights are mathematically obtained as given below.

$$\beta = Res^T(ResRes^T)^{-1}O \quad (13)$$

From equation (13), the result of hidden layer output β is estimated. Based on the estimated result, the output of the SKEL classifier for test face TF is obtained using the mathematical formulation as given below.

$$y = h(TF)\beta = h(TF)[Res^T(ResRes^T)^{-1}O] = \varphi^{EL_{ij}} \quad (14)$$

From the above output of SKEL classifier results (14), the kernel matrix is formulated as given below.

$$\varphi^{EL_{ij}} = Kernel\left(TF_i, TF_j\right) \quad (15)$$

Finally, the proposed SKEL classifier utilizes the Stacked Kernel function φ to measure the output function of the classifier. The expression for Stacked Kernel functions is given below.

$$Kernel\left(TF_i, TF_j\right) = \sum \left(log\ log\ [TF(p,q)] - log\ log\ [TF(p,q) * \alpha_i]\ \right) \quad (16)$$

$$Kernel(TF_i) = \sum \left(log\ log\ (TF_i) - log\ log\ (TF_i * \alpha_i)\ \right) \quad (17)$$

$$Kernel(TF_j) = \sum \left(log\ log\ (TF_j) - log\ log\ (TF_j) * \alpha_i \right) \quad (18)$$

From the above equations (16), (17), and (18), TF represent the original test face image, and α_i represents the aggregate representations across different years respectively. The pseudo-code representation of Stacked Kernel Extreme Learning-based Classification is given below.

Input: Dataset DS, Face Image FI=FI_1, FI_2,…, FI_n

Output: Accuracy improved face recognition

1: **Initialize** n, m, occlusion-removed age-invariant face extracted TF
2: **Begin**
3: **For** each Dataset DS with occlusion-removed age-invariant face extracted TF
4: Formulate hidden layer output weights post-training as given in equation (12)
5: Formulate SKEL classifier output weights as given in equation (13)
6: Evaluate the output of the SKEL classifier for test face TF as given in equation (14)
7: Evaluate kernel matrix as given in equation (15)
8: Formulate output function via Stacked Kernel as given in equations (16), (17), and (18)
9: **Return** face-recognized results
10: **End for**
11: **End**

Algorithm 3 Stacked Kernel Extreme Learning-based Classification

As given in Algorithm 3 above, to enhance the face recognition accuracy, Stacked Kernel is introduced that utilizes insightful information for identifying and testing sample images. First, with the n input layer's unit, M hidden layer neurons, and K output layer's unit, extreme learning is performed to obtain hidden layer output weights and classifier output weights separately. Second, the output of the SKEL classifier for the test face is obtained by employing the kernel matrix. Finally, a Stacked Kernel is utilized to measure the output function of the classifier that considers occlusion in kernel feature space and provides results with a higher recognition rate.

4. EXPERIMENTS, RESULTS, AND DISCUSSION

The experimental evaluation of the proposed Gravitational Deep Convoluted Stacked Kernel Extreme Learning-based (GDC-SKEL) classification for face recognition is conducted by comparing with two existing methods. The methods are namely Siamese Neural Network based on Local Binary Pattern (also called LBP) and Frequency Feature Perception (SN-LF) [1] and Age-invariant face recognition system [2] is implemented using MATLAB simulator. To conduct a fair analysis, the comparison is made with the GDC-SKEL and existing methods [1], [2] using Cross-Age Celebrity Dataset (CACD) dataset [*https://bcsiriuschen.github.io/CARC/*].

The experimental evaluation of GDC-SKEL classification for face recognition is carried out using factors such as face recognition accuracy, face recognition time, PSNR, and False Positive Rate concerning different numbers of face images and sizes. First qualitative analysis is presented followed by which a depth discussion with state-of-the-art methods, using graphs and tabulation is provided in detail.

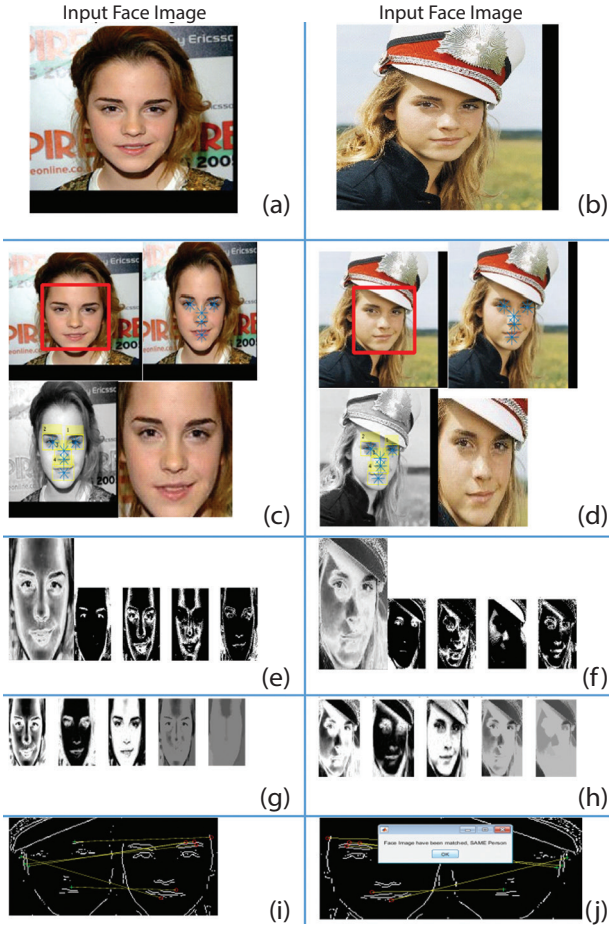

Fig. 4. Illustration of GDC-SKEL classifications for face recognition

In this section, qualitative analysis of Gravitational Deep Convoluted Stacked Kernel Extreme Learning-based (GDC-SKEL) classification for face recognition is done. Fig. 4 given below shows the illustrative details of GDC-SKEL classification for face recognition. As illustrated in the above Fig.4, first, input face images (a) (i.e., original face image) and (b) (i.e., occluded face image) obtained as input fromCross-Age Celebrity Dataset (CACD) dataset are utilized. Next, to the input face image face alignment is performed by applying Gravitational Center Loss-based Face Alignment model (i.e., as in (c) and (d)). Here, by applying this model, the intra-class difference is minimized that in turn eliminates the impact of occlusion in the face image during the recognition process. In the recognition process, 80% oc-

clusion is attained with higher face recognition rates. Second, to the computationally-efficient face-aligned images as input, salient features are extracted by utilizing the Deep Convoluted Tikhonov Regularization-based Facial Region Feature extraction algorithm.

Utilizing this algorithm, error-minimized facial images are obtained as output (i.e., as in (e) and (f)). Finally, the actual classification process for face recognition is done using the Stacked Kernel Extreme Learning-based (SKEL) classifier. With this type of classifier, accurate face recognition is made (i.e., as in (g) and (h)). The detected output is provided in (i) and (j).

The quantitative analysis of four distinct performance metrics, face recognition accuracy, face recognition time, PSNR, and False Positive Rate are analyzed in detail.

4.1. FACE RECOGNITION ACCURACY

In this section, the comparative result analysis of face recognition accuracy is provided. Higher the accuracy, the more efficient the method is said to be. The face recognition accuracy is mathematically formulated as given below.

$$FRA = \left[\frac{NICR}{n}\right] * 100 \quad (19)$$

From the above equation (19), face recognition accuracy FRA is measured based on the number of face images correctly recognized $NICR$ to the face images involved in the simulation process n. It is measured in terms of percentage (%). The table reports the simulation of different results of face recognition accuracy of GDC-SKEL, SN-LF [1], and Age invariant face recognition systems [2] for different numbers of face images.

Table 1. Comparative analysis of face recognition accuracy using GDC-SKEL, SN-LF [1], and Age invariant face recognition system [2]

Face Images	Face recognition accuracy (%)		
	GDC-SKEL	SN-LF	Age-invariant face recognition system
100	95	91	89
200	93.25	88.35	86.35
300	91	85.25	82
400	89.15	83	80
500	86	81.55	78.25
600	83.25	78	76
700	81	75.25	73
800	78.45	72	71.05
900	73.15	70	67
1000	70	68	64.35

Fig. 5 given below shows the face recognition accuracy concerning the face images varying between 100 and 1000 of different sizes. A decrease in accuracy rate is observed using all three methods. However, the number of face images correctly recognized using the GDC-SKEL method was found to be comparatively better therefore also improved the face recognition accuracy than [1] and [2]. The improvement in face recognition accuracy can be attributed to the application of the Stacked Kernel Extreme Learning-based Classification algorithm. By applying this algorithm, the first extreme learning was applied to obtain hidden layer output weights and classifier output weights separately. Next, the kernel matrix was employed separately to obtain the output for each test face. With the resultant output only, Stacked Kernel was utilized for classifying that in turn considered occlusion in kernel feature space, therefore improving the face recognition accuracy using the GDC-SKEL method by 6% compared to [1] and 10% compared to [2] respectively.

Fig. 5. Graphical representation of face recognition accuracy

4.2. FACE RECOGNITION TIME

A small proportion of time is said to be consumed in recognizing the face images. To be more specific, face recognition time refers to the time consumed in recognizing the face images even in the presence of occlusion, highly illuminated across years. This is mathematically formulated as given below.

$$FRT = n * Time\left[\varphi^{EL_{ij}}\right] \quad (20)$$

Table 2 Comparative analysis of face recognition time using GDC-SKEL, SN-LF [1], and Age invariant face recognition system [2]

Face images	Face recognition time (ms)		
	GDC-SKEL	SN-LF	Age-invariant face recognition system
100	25	33	41
200	28.15	35.15	43.15
300	31	38	45
400	34.25	39.55	48.25
500	38	42.55	50.15
600	45.25	55.25	57.35
700	53.51	59.15	63.25
800	60.55	70	75.25
900	71.35	74.55	78
1000	78	85.15	87.15

From the above equation (20), the face recognition time *FRT* is measured based on the number of face images involved in the simulation process 'n' and the time consumed in recognizing the face based on classification via extreme learning *Time* $[\varphi^{(EL_{ij})}]$. It is measured in terms of milliseconds (ms). The table reports the simulation of different results of face recognition time of three different methods concerning different numbers of face images.

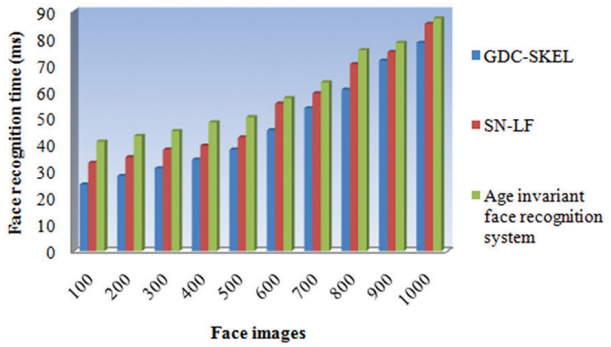

Fig. 6. Graphical representation of face recognition time

Fig. 6 given above shows the face recognition time. But when performed with simulations using 100 face images, the time consumed in recognizing face images using the three methods for the single face was 0.25 ms, 0.33 ms [1], and 0.41 ms [2] respectively. From this simulation results the overall face recognition time was observed to be 25 ms using GDC-SKEL, 33 ms using [1], and 41 ms using [2]. From this, the face recognition time was observed to be comparatively better in GDC-SKELthan [1] and [2]. The reason behind the improvement was due to the application of the Gravitational Center Loss-based Face Alignment algorithm. By applying this algorithm, the influence of intra-class similarity was said to be eliminated, which in turn improved the discriminative potentiality of deeply learned features. This in turn reduced the face recognition time using the GDC-SKEL method by 14% compared to [1] and 23% compared to [2] respectively.

4.3. PSNR

The peak signal-to-noise ratio (PSNR) is evaluated based on the mean square error that denotes the difference between the original face image and the processed face image. The formula for computing the PSNR is formulated below,

$$PSNR = 10\left[\frac{M^2}{S_{ME}}\right] \tag{21}$$

$$S_{ME} = \left[size_{preprocessed} - size_{original}\right]^2 \tag{22}$$

From the above equation (21) and (22), the peak signal-to-noise ratio '*PSNR*' is measured based on the processed size $size_{preprocessed}$ and the original size $size_{original}$ respectively. It is measured in terms of decibels (dB). The table given below shows the performance results of the PSNR concerning varying face image sizes obtained from the CACD dataset. The results obtained confirm that the PSNR of the GDC-SKEL method is improved upon comparison with the other existing methods [1], [2].

Table 3 Comparative analysis of PSNR using GDC-SKEL, SN-LF [1], and Age invariant face recognition system [2]

Sizes of face images (KB)	PSNR (dB)		
	GDC-SKEL	SN-LF	Age-invariant face recognition system
16.3	52.23	46.20	48.70
14.1	54.72	44.27	48.70
19.4	48.70	42.68	46.20
20.2	49.60	44.27	46.65
22.9	48.70	43.14	44.27
21.6	49.30	42.68	46.20
24.9	46.20	43.14	41.35
26.8	48.70	44.27	46.20
25.5	52.64	46.20	48.70
27.2	48.70	42.68	44.27

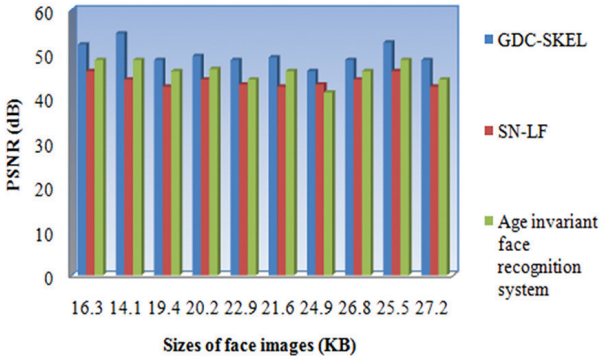

Fig. 7. Graphical representation of PSNR

Fig. 7 given above illustrates the PSNR concerning 10 distinct numbers of face images of varying sizes. However, simulations performed with a 16.3 KB size image saw a PSRN rate of 52.23 dB using the proposed GDC-SKEL, 46.20 dB using [1] and 48.70 dB using [2] respectively. From this result, it is inferred that the PSNR rate is found to be better when applied with the GDC-SKEL method upon comparison with [1] and [2]. The reason behind the improvement was due to the application of the Gravitational Center Loss-based Face Alignment algorithm. By applying this algorithm, the Gravitational Center Loss function was utilized that in turn not only reduced the intra-class variations but also retained useful information. As a result, the occlusion was minimized and in turn, aided in face recognition. Owing to this the peak-signal-to-noise-ratio (PSNR) was found to be improved significantly using the GDC-SKEL method by 14% compared to [1] and 8% compared to [2] respectively.

4.4. FALSE POSITIVE RATE

False Positive Rate (TPR) or specificity denotes the percentage ratio of several face images that were incorrectly recognized during the face recognition process. The false positive rate is measured as given below

$$Rate_{fp} = \left[\frac{NIICR}{n}\right] * 100$$

From the above equation (23), the false positive rate $Rate_{fp}$ is evaluated based on many face images that were incorrectly recognized $NIICR$ concerning the sample face images provided as input for simulation n. It is measured in terms of percentage (%). The table given below provides the performance results of the false positive rate versus the number of face images collected from the database. For conducting the simulation, 1000 numbers of distinct face images in the range of 100 to 1000 were utilized.

Table 4 Comparative analysis of false positive rate using GDC-SKEL, SN-LF [1], and Age invariant face recognition system [2]

Face images	False positive rate (%)		
	GDC-SKEL	SN-LF	Age-invariant face recognition system
100	4	7	9
200	6	9	10
300	7	11	12
400	9	10	11
500	5	8	9
600	3	6	7
700	4	7	8
800	7	8	10
900	5	6	8
1000	4	5	7

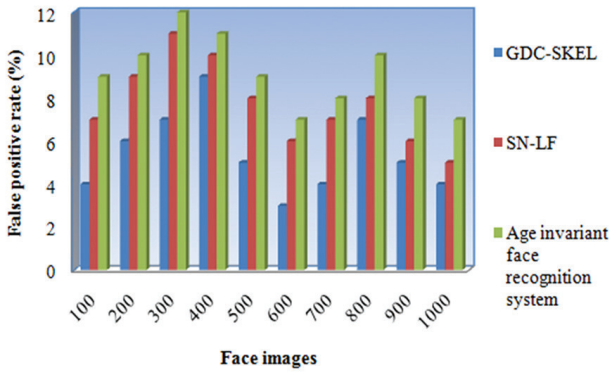

Fig. 8. Graphical representation of false positive rate

Fig 8 given above shows the graphical presentation of the false positive rate concerning ten numbers of face images with varying sizes provided as input. This in turn would result in a significant proportion of falsification of face recognition. But comparative analysis performed with 100 face images found 4 face images incorrectly recognized using GDC-SKEL, 7 face images incorrectly recognized using [1], and 9 face images incorrectly recognized using [2] respectively. From this analysis, the false positive rate using GDC-SKEL, [1] and [2] were found to be 4%, 7%, and 9% respectively. As a result, improvement was found in terms of false positive rates using the GDC-SKEL method. The reason behind the improvement was the application of the Deep Convoluted Tikhonov Regularization-based Facial Region Feature extraction algorithm. By applying this algorithm, Max Pooling Aggregation (MPA) was applied to aggregate representations across different years or ages. By applying this function face image at a smaller age had a high response upon comparison with the older image and vice versa. With this, the false positive rate using the GDC-SKEL method was found to be reduced by 30% compared to [1] and 42% compared to [2] respectively.

5. CONCLUSION

An efficient face recognition method from face images called, GDC-SKEL is designed by exploring and inspecting the affinity points selected from the given dataset. To minimize the face recognition time and improve the face recognition accuracy, therefore, paving the means for face recognition, Gravitational Center Loss-based Face Alignment is first applied to the selected face input image, focusing on occluded images. Second with the occlusion-removed face images provided as input salient features for further processing are extracted using the Convoluted Tikhonov Regularization function. Finally, with the extracted facial regions, Stacked Kernel Extreme Learning-based Classification is performed to obtain the final face image recognition output. For the experimentation, the Cross-Age Celebrity Dataset (CACD) dataset is used. The performance of the GDC-SKEL method is evaluated with different metrics such as face recognition accuracy, face recognition time, PSNR, and False Positive Rate. From the result, it is clearly understood that the proposed GDC-SKEL method outperforms well in the face recognition process with a higher detection rate and minimum time when compared to the state-of-the-art methods. In general, face recognition is only suitable for offline applications. To recognize human faces in online applications, a higher computing system is required. Thus, future work is developed for recognizing the human face in online applications

6. REFERENCES:

[1] C. Song, S. Ji, "Face Recognition Method Based on Siamese Networks under Non-Restricted Conditions", IEEE Access, Vol. 10, 2022, pp. 40432-40444.

[2] A. A. Moustafa, A. Elnakib, N. F. F. Areed, "Age-invariant face recognition based on deep features analysis", Signal, Image, and Video Processing, Vol. 14, 2020, pp. 1027-1034.

[3] P. Barros, N. Churamani, A. Sciutti, "The FaceChannel: A Fast and Furious Deep Neural Network for Facial Expression Recognition", SN Computer Science, No. 321, 2020, pp. 1-10.

[4] O. K. Sikha, B. Bharath, "VGG16-random Fourier hybrid model for masked face recognition", Ap-

plication of Soft Computing, Vol. 26, 2022, pp. 12795-12810.

[5] H.N. Vu, M. H. Nguyen, C. Pham, "Masked face recognition with convolutional neural networks and local binary patterns", Applied Intelligence, Vol. 52, No. 5, 2021, pp. 1-16.

[6] H. Goyal, K. Sidana, C. Singh, A. Jain, S. Jindal, "A real-time face mask detection system using convolutional neural network", Multimedia Tools and Applications, Vol. 81, 2022, pp. 14999-15015.

[7] M.A. Hossain, B. Assiri, "Facial expression recognition based on the active region of interest using deep learning and parallelism", Peer Journal of Computer Science, Vol. 8, 2022, pp. 1-38.

[8] G. Guo, N. Zhang, "A survey on deep learning based face recognition", Computer Vision and Image Understanding, Elsevier, Vol. 189, 2019, p. 102805.

[9] L. Li, X. Mu, S. Li, H. Peng, "A Review of Face Recognition Technology", IEEE Access, Vol. 8, 2020, pp. 139110-139120.

[10] A. Martın, D. Camacho, "Recent advances on effective and efficient deep learning-based solutions", Neural Computing and Applications, Vol. 34, 2022, pp. 10205-10210.

[11] G. Ciaparrone, L. Chiariglione, R. Tagliaferri, "A comparison of deep learning models for end-to-end face-based video retrieval in unconstrained videos", Neural Computing and Applications, Vol. 34, 2022, pp. 7489-7506.

[12] M. K. Rusia, D. K. Singh, "A comprehensive survey on techniques to handle face identity threats: challenges and opportunities", Multimedia Tools and Applications, Vol. 82, 2023, pp. 1669-1748.

Healthcare Critical Diagnosis Accuracy: A Proposed Machine Learning Evaluation Metric for Critical Healthcare Analysis

Original Scientific Paper

Deepali Pankaj Javale
School of Computer Engineering and Technology, Dr. Vishwanath Karad MIT World Peace University, Pune, India
deepali.javale@mitwpu.edu.in

Sharmishta Desai
School of Computer Engineering and Technology, Dr. Vishwanath Karad MIT World Peace University, Pune, India
sharmishta.desai@mitwpu.edu.in

Abstract *– Since at least a decade, Machine Learning has attracted the interest of researchers. Among the topics of discussion is the application of Machine Learning (ML) and Deep Learning (DL) to the healthcare industry. Several implementations are performed on the medical dataset to verify its precision. The four main players, True Positive (TP), True Negative (TN), False Positive (FP), and False Negative (FN), play a crucial role in determining the classifier's performance. Various metrics are provided based on the main players. Selecting the appropriate performance metric is a crucial step. In addition to TP and TN, FN should be given greater weight when a healthcare dataset is evaluated for disease diagnosis or detection. Thus, a suitable performance metric must be considered. In this paper, a novel machine learning metric referred to as Healthcare-Critical-Diagnostic-Accuracy (HCDA) is proposed and compared to the well-known metrics accuracy and ROC_AUC score. The machine learning classifiers Support Vector Machine (SVM), Logistic Regression (LR), Random Forest (RF), and Naive Bayes (NB) are implemented on four distinct datasets. The obtained results indicate that the proposed HCDA metric is more sensitive to FN counts. The results show, that even if there is rise in %FN for dataset 1 to 10.31 % then too accuracy is 83% ad HCDA shows correlated drop to 72.70 %. Similarly, in dataset 2 if %FN rises to 14.80 for LR classifier, accuracy is 78.2 % and HCDA is 63.45 %. Similar kind of results are obtained for dataset 3 and 4 too. More FN counts result in a lower HCDA score, and vice versa. In common exiting metrics such as Accuracy and ROC_AUC score, even as the FN count increases, the score increases, which is misleading. As a result, it can be concluded that the proposed HCDA is a more robust and accurate metric for Critical Healthcare Analysis, as FN conditions for disease diagnosis and detection are taken into account more than TP and TN.*

Keywords*: Machine Learning, Performance Metrics, Accuracy, ROC_AUC, Healthcare, True Positive, True Negative, False Negative*

1. INTRODUCTION

Machine learning has proved beneficial in a variety of fields. The analysis of healthcare data is also gathering popularity. But it also has its difficulties [1]. Different Ensemble methods [2] have also proven superior for achieving high precision. When discussing Machine Learning, performance evaluation metrics play an important role in determining how closely the parameters influence the target field. In supervised learning, we specify a target field, train the model with various classifiers, and test it on a small sample of records using the same parameters. The performance metrics accuracy, F1-Score, Precision, Recall, and ROC_AUC Score play a crucial role in classifier implementation comparisons based on performance metrics. When discussing these metrics, the perplexity matrix is used to calculate their scores. True Positive (TP), True Negative (TN), False Positive (FP), and False Negative (FN) are the four key actors from the confusion matrix that aid in calculating the metric scores. Accuracy [2] and ROC_AUC score metrics are typically used in healthcare data analytics [3-6]. When discussing these metrics, it is observed that false negative counts are not taken into account, which should be one of the most important considerations when dealing with essential healthcare analytics. The ROC_AUC score takes into account the number of false negatives and is therefore superior. In addition, the Recall and F1-Score metrics can be considered because they include FN as one of their key decision-making parameters.

When all of the aforementioned metrics are considered, it is observed that although the number of FNs increases,

the metric value also increases, which is contradictory. The number of false negatives in a critical healthcare analysis should be minimal. For instance, if a heart attack prediction is made and the false negative readings indicate that even though it is a heart attack state, it was not correctly predicted, this is extremely dangerous for the patient. The false positive state is tolerable because it may be a false alarm for a critical situation, but it may not pose a life-threatening threat. Taking all of these factors into account.

Further, the study was to explore more performance metrics in machine learning. Just relying on an accuracy score was not a good choice. In one of the articles, the authors have given a comparative study of different metrics used in machine learning for imbalanced datasets. The difference in majority and minority class affects the metrics like accuracy and F1-score, while s Area Under the Receiver Operating Characteristic Curve metric shows no effect. [7]

Different ensemble approaches for machine learning viz. bagging, Breiman boosting, and Freund boosting. Imbalanced datasets are mainly to be taken into consideration. Different metrics for imbalanced datasets were discussed and experimented with. AUC was considered to be the most robust [8]. When the results of various implementations for different metric values such as accuracy, ROC_AUC score, F1 score, Precision score, and Recall score were compared, it was discovered that the percentage of False Negatives was increasing while the accuracy was increasing. Consequently, the Health-Critical-Diagnosis-Accuracy (HCDA) metric was conceived. Using various classifiers of Machine Learning, four distinct healthcare datasets were implemented. Comparing the implementation results for metrics accuracy, ROC_AUC Score, and the HCDA state-of-the-art metric revealed that HCDA produced more accurate results.

The paper includes below given contributions,

- Four different datasets are used for disease or medical condition detection for which the statistics are given in section 2.1.
- Different Machine Learning performance evaluation metrics are discussed in section 2.2 which are further used for results and conclusions.
- A state-of-art metric is proposed, Healthcare-Critical-Diagnosis-Accuracy(HCDA) which is given in section 2.3
- Comparative analysis of different machine metrics from section 2.2 and HCDA metric from 2.3 are compared together.
- In section 3 results for all experimentation are given and discussion on it is done.
- Lastly, a conclusion is stated which shows the significance of the proposed work.

Need for Proposed Work :

Despite the various performance evaluation metrics provided by the machine learning community, it has been observed that critical areas, such as Critical Healthcare Analysis, require additional attention and development. In numerous instances, an ensemble approach utilising machine learning proves to be beneficial. In critical healthcare analysis, emphasis must be placed not only on True positive and True negative cases, but also on False negative cases. False negative contricution must be understood when calculating the metric value. Therefore, the proposed work is an effort to focus more on False Negative counts in order to achieve greater accuracy in Healthcare Analytics, thereby reducing the risk of death in critical conditions such as stroke and heart attack.

2. METHOD

2.1. DATASETS USED

Machine learning implementation was done on 4 different datasets. The first 2 datasets used were the diabetes dataset while the 3rd dataset was the stroke prediction dataset and the 4th was the Heart Failure Clinical Record dataset.

The statistics and description of the four different datasets used are given in Table 1.

Table 1. Summary of Datasets Used

Dataset Number	Title	Attributes	Fields considered	Number of Records	Description
1.	Dataset for People For Their Blood Glucose Level With Their Superficial Body Feature Readings [9]	10	Diastolic BP,Systolic BP, Heartrate, Shivering BodyTemperature, Hypoglycemia(Target Field)	70000	The given Dataset is a record of different age groups of people either diabetic or non-diabetic for their blood glucose level reading with superficial body features like body temperature, heart rate, blood pressure, etc.
2.	Diabetes Data Set [10]	9	Pregnancies,BloodGlucose blood pressure, SkinThickness, Outcome (Target Field)	2000	Predict a Model to detect Whether Person has Diabetes or Not
3.	STROKE PREDICTION DATASET [11]	12	Id, Gender, Age, Hypertension, Heart disease, Ever marrried, Worktype Stroke(Target Field)	5111	11 clinical features for predicting stroke events
4.	HEART FAILURE PREDICTION [12]	13	Age, anaemia, high blood pressure, creatinine, phosphokinase, diabetes, ejection fraction, platelets, sex, serum creatinine, serum sodium, smoking, [target] death event(Target Field)	300	12 clinical features for predicting death events

Taking into consideration the comparative analysis from Table 2 for supervised machine learning classifiers, four machine learning classifiers viz. Random Forest (RF), Support Vector Machine(SVM), Naïve Bayes (NB) and Logistic regression(LR) [13-17] were used for supervised classification using Machine Learning [2, 18,19] on the above datasets. The train test method with Stratified Crossfold with k=10 strategy was used for classifier experimentation. The chances of missing any of the train or test records are eliminated in Stratified Crossfold [20-24] mechanism of Machine Learning. The commonly used machine learning evaluation metrics based on the confusion matrix are Accuracy, F1-Score, Precision, Recall, and ROC_AUC. Here according to confusion matrix TP means True Poistive which means correct prediction for true/positive values. TN means True predictions for False/Negative values. FP means wrong predictions for True/Positive values. FN means wrong predictions for False/Negative Values

$$Accuracy = \frac{(\mathrm{TP+TN})}{(\mathrm{TP+TN+FP+FN})} \quad (1)$$

$$Precision = \frac{TP}{(\mathrm{TP+FP})} \quad (2)$$

$$Recall = \frac{TP}{(\mathrm{TP+FN})} \quad (3)$$

$$F1 - Score = \frac{(2(\mathrm{P*Q}))}{(\mathrm{P+Q})} \quad (4)$$

$$TPR = \frac{TP}{(\mathrm{TP+FN})} \quad (5)$$

$$FPR = \frac{FP}{(\mathrm{FP+TN})} \quad (6)$$

$$ROC\_AUC = (Eq\ (5))/(Eq\ (6))$$

The evaluation metrics used for comparative analysis were Accuracy, F1-Score, Precision, Recall, and ROC_AUC from Machine Learning. Along with these metrics, the proposed HCDA metric is also used. The Accuracy, F1-Score, Precision, Recall, and ROC_AUC are then compared with HCDA a state-of-art metric used.

$$HCDA = \frac{(\mathrm{TP+TN*100}}{(\mathrm{TP+TN+FP+FN})} - \frac{(\mathrm{FP*100})}{(\mathrm{TP+TN+FP+FN})} \quad (7)$$

Based on the confusion matrix parameters TP, TN, FP and FN consideration for the value calculation of respective metrics, the metrics and their mapping [25-27] are shown in Table 3.

Table 3. Machine Learning and HCDA metric mapping with the confusion matrix key players

Metric	True Positive (*TP*)	True Negative (*TN*)	False Positive (*FP*)	False Negative (*FN*)
Accuracy	√	√	√	√
Precision	√	-	√	-
Recall	√	-	-	√
F1-Score	√	-	√	√
ROC_AUC	√	√	√	√
HCDA	√	√	√	√

The above table shows the use of TP, TN, FP, or FN for the metric value calculation. In further discussions, False Negative (FN) is considered to be an important player as in critical healthcare analysis the condition of false negative is considered to be more alarming. If the critical health state is taking place and it's not indicated then such a situation is termed false negative which should not be tolerated.

If we consider a dataset for stroke diagnosis, then

TP- The patient is undergoing stroke and is correctly diagnosed

TN- The patient is not undergoing a stroke and is correctly diagnosed.

FP- The patient is wrongly diagnosed as undergoing a stroke.

FN – The patient is wrongly diagnosed as not undergoing a stroke.

If we look at the above case study of healthcare critical analysis, then it is observed that TP and TN are correct to be found but along with it, the most important is the FN count. If the FN count goes high it means the system is failing in classifying critical health conditions. Compared to it if FP count goes high then too it may not be a risk to the patient.

Thus, from Table 3, it is clear that for healthcare analysis metrics like Precision and Recall should not be considered for Critical Healthcare Analysis. The methodology implementations are done on the datasets given in Table 1 and we continued with metrics Accuracy, Precision, Recall, F1-Score, ROC_AUC [28,29] and HCDA proving that how HCDA is a better metric for critical healthcare analysis as compared to all other metrics. The significance of TP, TN and FN is to be justified using a mathematical model or graph comparison.

2.3. PROPOSED METRIC

The state-of-art metric is proposed named HCDA (Healthcare-Critical-Diagnosis-Accuracy). The HCDA is the percentage difference between the sum of true positives and true negatives and the percentage of false negatives. In critical healthcare diagnosis along with true positive and true negative more importance should be given to false negative. The false negative state mentions that even the critical state is occurring then diagnosis is not done which is considered to be more dangerous. The false positive count can be neglected as false alarms can be tolerated. When we use other Machine Learning Metrics then it is observed that we need to get the values of various metrics like precision, accuracy, F1-Score, Recall, and ROC_AUC score. Either of the strategies have to be used to come to conclude like stacking-C, Max vote, or Average. If we use HCDA the only metric gives accurate results.

Where,

$HCDA$ - Healthcare - Critical - Diagnosis - Accuracy (Proposed metric value)

TP - True Positive (Correct Diagnosis counts. Critical State occurring with proper indication)

TN - True Negative(Correct Diagnosis Count. Critical State occurring with no indication)

FN – False Negative (Wrong Diagnosis. Critical State occurring but no indication)

The HCDA metric focuses on true positive and true negative for calculating accuracy and in the same way removes the percentage of false negative counts to get more accurate results.

The steps for calculating HCDA metric score are given in Algorithm 1.

Algorithm 1 :

Result: HCDA Metric score

List: Support Vector Machine, Logistic Regression, Naïve Bayes and Random Forest

Dataset: 4 Datasets from Table 1

Steps:

for <for each algorithm in **List**> ***do***

for <for each dataset from **Dataset**> ***do***

Implement Machine Learning Algorithm

Get Confusion Matrix Parameter values for TP, TN, FP, and FN

Calculate HCDA by the given formula

$$HCDA = \frac{TP + TN * 100}{TP + TN + FP + FN} - \frac{FP * 100}{TP + TN + FP + FN}$$

end

end

2.4. COMPARATIVE ANALYSIS

Comparative analysis was done between the evaluation metric values obtained for Machine Learning metrics used and HCDA, the state-of-art metric proposed.

The comparative analysis proposes the effectiveness of the HCDA metric

The workflow architecture for the proposed work and experimentation is shown in Fig 1.

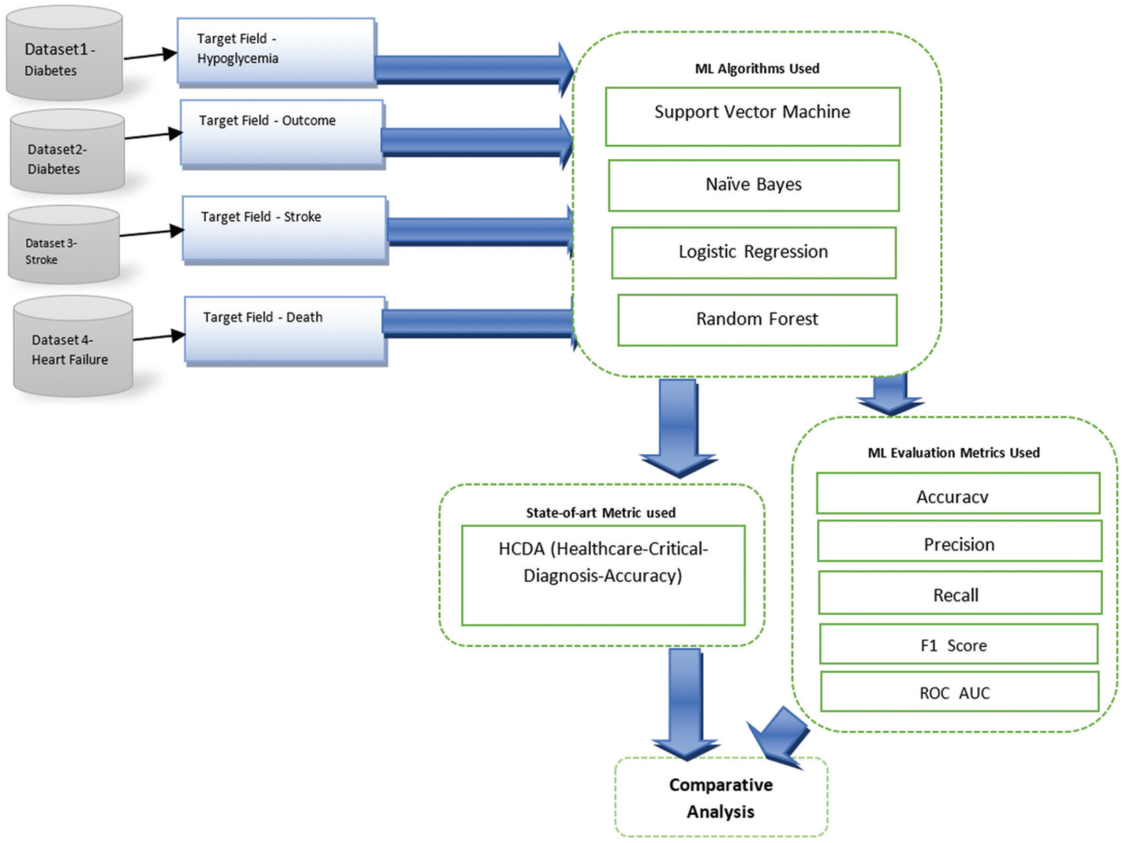

Fig 1. The Workflow Architecture of the Implementation Done

3. RESULTS AND DISCUSSION

The results obtained were the comparative chart for the values of different metric values after the implementation of classifier execution on the four different healthcare datasets used. The datasets were picked up from the Kaggle repository and IEEE data port.

Table 4 shows the true positive, true negative, false negative, and false positive counts obtained after classifier execution on the respective dataset.

Based on the values of TP, TN, FP, and FN the metric values for ML classifier execution were calculated for different machine learning metrics and the HCDA metric proposed. All the metric values are considered to be in percentage.

Table 5 shows the %(TP+TN) and %FN values along with the value generated for the HCDA metric and the standard machine learning metrics viz. accuracy, precision, recall, F1-Score, and ROC_AUC score. Though the accuracy score gives a good score, it can be seen that the accuracy score is directly correlating with %(TP+TN) only. The FN value rise does not affect the accuracy score, while HCDA shows variations accordingly.

Table 4. The TP, TN, FN, and FP values for different machine learning classifier implementations

Dataset / Metric	Classifier	TN	TP	FP	FN
D1 (Base Dataset)	RF	61869	8673	19	382
	SVM	57157	1738	4731	7317
	LR	61603	8259	285	796
	NB	60912	8091	976	964
D2 - Diabetes	RF	1303	642	13	42
	SVM	708	363	608	321
	LR	1177	388	139	296
	NB	1032	468	284	216
D3 - Stroke	RF	4841	5	20	244
	SVM	4534	21	327	228
	LR	4852	2	9	247
	NB	4673	46	188	203
D4 - Heart Failure	RF	179	66	24	30
	SVM	185	52	18	44
	LR	184	61	19	35
	NB	182	69	21	27

Table 5. Different metric values obtained for Machine Learning classifier implementations

Dataset/ Metric	Classifier	%(Tp+TN)	%FN	HCDA	Accuracy	Precision	Recall	F1score	ROC
D1 (Base Dataset)	RF	99.43	0.54	98.90	99.4	99.4	99.4	99.4	99.4
	SVM	83.02	10.31	72.70	83	80.8	83	81.8	61.6
	LR	98.48	1.12	97.35	98.5	98.5	98.5	98.5	99.6
	NB	97.27	1.36	95.91	97.3	97.3	97.3	97.3	99.5
D2 - Diabetes	RF	97.25	2.10	95.15	97.3	97.3	97.3	97.2	99
	SVM	53.55	16.05	37.50	53.5	58.1	53.5	54.7	56.5
	LR	78.25	14.80	63.45	78.2	77.8	78.2	77.5	83.3
	NB	75.00	10.80	64.20	75	75.7	75	75.3	82.3
D3 - Stroke	RF	94.83	4.77	90.06	94.8	91.5	94.8	92.8	74.5
	SVM	89.14	4.46	84.68	89.1	90.9	89.1	90	56.8
	LR	94.99	4.83	90.16	95	91.4	95	92.8	65.5
	NB	92.35	3.97	88.38	92.3	92.1	92.3	92.2	80.6
D4 - Heart Failure	RF	81.94	10.03	71.91	81.9	81.7	81.9	81.8	88
	SVM	79.26	14.72	64.55	79.3	78.7	79.3	78.3	84
	LR	81.94	11.71	70.23	81.9	81.5	81.9	81.5	85.5
	NB	83.95	9.03	74.92	83.9	83.7	83.9	83.8	90.8

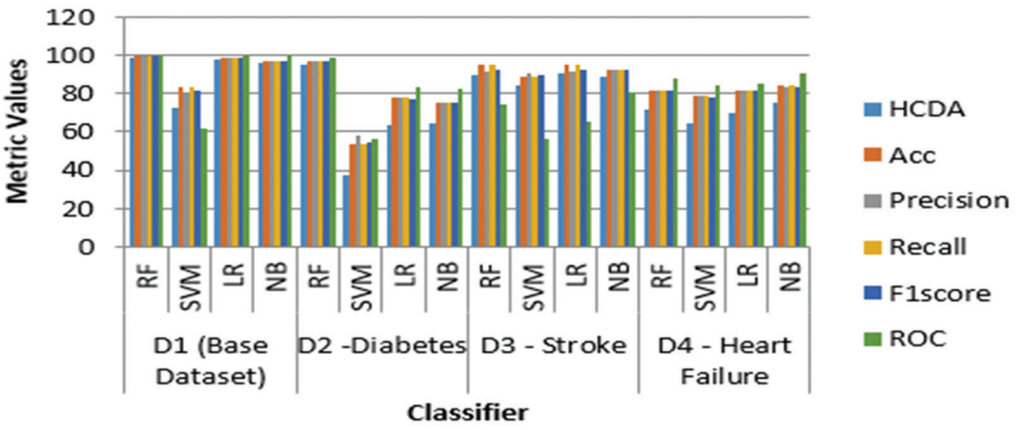

Fig. 2. Comparison of HCDA metric with Machine Learning Metric values.

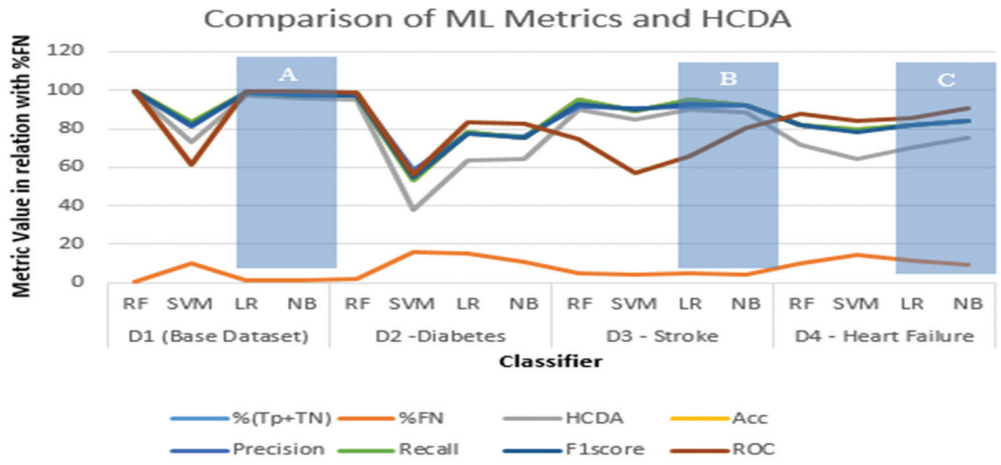

Fig 3. Comparison of HCDA metric with Machine Learning Metric values.

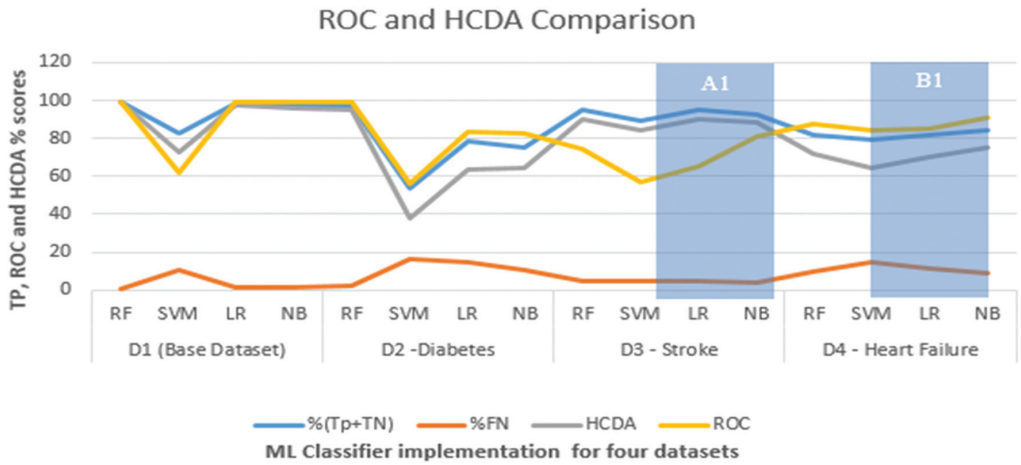

Fig 4. Comparative Analysis for ROC and HCDA metric

Discussion 1 : Fig. 2 compares various metrics, including precision, accuracy, F1-score, Recall, and ROC score, to the proposed HCDA metric. In healthcare diagnosis, precision, accuracy, F1-score, Recall, and ROC score metrics are likely adopted to reach a conclusion [4,5]. The HCDA value differs from the machine learning metrics' values. The HCDA metric value is relatively low compared to other metric values. The ROC is regarded as the most reliable metric for healthcare analysis. However, if we observe the ROC and HCDA scores attentively, we will notice that in many instances the HCDA score is greater than the ROC score. The primary topic of discussion is not achieving a higher accuracy score, but rather achieving the most accurate score in relation to the percentages of True Positives and True Negatives as well as False Negatives.

Observing Fig. 3 closely reveals that the HCDA score is highly correlated with $\%FN$ values. The greater the value of $\%FN$, the lower the HCDA score, whereas there is no correlation between $\%FN$ value and ROC score. The shaded area A in Fig. 3 indicates that the $\%FN$ count is greater. Under this condition, the ROC score and HCDA score both decrease significantly. In addition, the shaded portion B reveals that the $\%FN$ score is significantly lower than the ROC score, while the HCDA score has a much stronger correlation with the $\%FN$ count. The shaded section C indicates an increase in $\%FN$. In such a scenario, the accuracy score should decrease, but the ROC score is high and the HCDA score remains stable in correlation with $\%FN$.

Here the $\%FN$ score means,

For Dataset 1 – A hypoglycemia state occurs but is not detected

For Dataset 2 - Diabetes positive but not detected

For Dataset 3 - Stroke occurs but is not detected

For Dataset 4 – A heart failure state occurs but is not detected

From the above four respective FN states for 4 different datasets, it is clear that the FN count should be the most important parameter along with TP and TN.

Discussion 2: ROC is typically regarded as the most reliable metric, and healthcare is no exception. Figure 4 depicts a comparison of the ROC score and HCDA score in relation to the percentage of true positive, true negative, and false negative scores. It demonstrates that the %(true positive + true negative) score and %false negative score, despite being identical in many instances,

reflect distinct ROC scores, whereas HCDA indicates a very close correlation between them.

Observing Fig. 4, part A1 reveals that the percentage of FN is relatively low compared to the percentage of $TP+TN$. In this scenario, a high accuracy score should be reflected by the HCDA score and not the ROC score. In addition, the shaded portion B1 displays an increase in $\%FN$ and a minor decrease in $\%(TP+TN)$, which should result in a decrease in the accuracy score. However, this is best reflected by the HCDA score and not the ROC score. Fig. 4 demonstrates that the HCDA metric is consistent with respect to the %false negative score. For Acute/Critical healthcare, detection $\%FN$ is a very essential factor, and HCDA is a self-sufficient metric for determining the classifier's performance.

4. CONCLUSION

Consequently, the implemented research demonstrates that the proposed state-of-the-art metric HCDA is more robust and superior for critical healthcare analysis than other machine Learning metrics such as Accuracy, Precision, Recall, F1-Score, and ROC. The execution of various classifiers, namely Random Forest, Nave Bayes, Support Vector Machine, and Logistic Regression, leads to the conclusion that the HCDA metric is more accurate for critical healthcare diagnosis. The four datasets employed were the datasets for critical healthcare analysis in which acute state detection is the primary objective. All experiments demonstrated that the proposed HCDA metric is the only self-sufficient metric capable of producing accurate classification decisions. For the proposed metric HCDA, the accuracy will increase if the number of false negatives decreases. The HCDA demonstrates a very strong correlation with the True Positive, True Negative, and False Negative values, which is essential for conducting critical healthcare analyses. The minority class, which is represented by the false negative count, should therefore be weighed equally with the true positive and true negative tallies. If the HCDA metric is used for decision-making in critical healthcare analysis, such as heart failure or stroke, then putting more emphasis on false negative cases will prevent or reduce the occurrence of severe conditions that are not detected. This demonstrates that the HCDA metric has the potential to revolutionise acute state detection analysis in healthcare. Despite the fact that the scope of this study is limited to Critical Healthcare Analysis, the HCDA metric can be applied in sectors such as the aerospace and military that place a premium on false-negative conditions.

5. REFERENCES

[1] A. Qayyum, J. Qadir, M. Bilal, A. Al-Fuqaha, "Secure and Robust Machine Learning for Healthcare: A Survey", IEEE Reviews in Biomedical Engineering, Vol. 14, 2021, pp. 156-180.

[2] M.-P. Hosseini, A. Hosseini, K. Ahi, "A Review on Machine Learning for EEG Signal Processing in Bioengineering", IEEE Reviews in Biomedical Engineering, Vol. 14, 2021, pp. 204-218.

[3] N. Y. Philip, M. Razaak, J. Chang, S. M. M. O'Kane, B. K. Pierscionek, "A Data Analytics Suite for Exploratory Predictive, and Visual Analysis of Type 2 Diabetes", IEEE Access, Vol. 10, 2022, pp. 13460-13471.

[4] M. Habib, Z. Wang, S. Qiu, H. Zhao, A. S. Murthy, "Machine Learning Based Healthcare System for Investigating the Association Between Depression and Quality of Life", IEEE Journal of Biomedical and Health Informatics, Vol. 26, No. 5, 2022, pp. 2008-2019.

[5] N. Reamaroon, M. W. Sjoding, K. Lin, T. J. Iwashyna, K. Najarian, "Accounting for Label Uncertainty in Machine Learning for Detection of Acute Respiratory Distress Syndrome", IEEE Journal of Biomedical and Health Informatics, Vol. 23, No. 1, 2019, pp. 407-415.

[6] Y. Dong et al. "A Polarization-Imaging-Based Machine Learning Framework for Quantitative Pathological Diagnosis of Cervical Precancerous Lesions", IEEE Transactions on Medical Imaging, Vol. 40, No. 12, 2021, pp. 3728-3738.

[7] T. Hasanin, T. M. Khoshgoftaar, J. L. Leevy, "A Comparison of Performance Metrics with Severely Imbalanced Network Security Big Data", Proceedings of the IEEE 20th International Conference on Information Reuse and Integration for Data Science, Los Angeles, CA, USA, 2019, pp. 83-88.

[8] M. Naghshvarianjahromi, S. Kumar, M. J. Deen, "Brain-Inspired Intelligence for Real-Time Health Situation Understanding in Smart e-Health Home Applications", IEEE Access, Vol. 7, 2019, pp. 180106-180126.

[9] D. Javale, S. Desai, "Dataset for People for their Blood Glucose Level with their Superficial body feature readings", IEEE Dataport, 2021.

[10] "Diabetes Data Set (Version 1) [Predict a Model to detect Person has Diabetes or Not]", https://www.kaggle.com/datasets/vikasukani/diabetes-dataset (accessed: 2023)

[11] "Stroke Prediction Dataset (Version 1) [11 clinical features for predicting stroke events]", https://

www.kaggle.com/datasets/fedesoriano/stroke-prediction-dataset (accessed: 2023)

[12] D. Chicco, G. Jurman, "Machine learning can predict survival of patients with heart failure from serum creatinine and ejection fraction alone", BMC Medical Informatics and Decision Making, Vol. 20, No. 16, 2020.

[13] J. P. Li, A. U. Haq, S. U. Din, J. Khan, A. Khan, A. Saboor, "Heart Disease Identification Method Using Machine Learning Classification in E-Healthcare", IEEE Access, Vol. 8, 2020, pp. 107562-107582.

[14] J. Faouzi et al. "Machine Learning-Based Prediction of Impulse Control Disorders in Parkinson's Disease From Clinical and Genetic Data", IEEE Open Journal of Engineering in Medicine and Biology, Vol. 3, 2022, pp. 96-107.

[15] S. A. -F. Sayed, A. M. Elkorany, S. Sayed Mohammad, "Applying Different Machine Learning Techniques for Prediction of COVID-19 Severity", IEEE Access, Vol. 9, 2021, pp. 135697-135707.

[16] J. R. Campos, E. Costa, M. Vieira, "Improving Failure Prediction by Ensembling the Decisions of Machine Learning Models: A Case Study", IEEE Access, Vol. 7, 2019, pp. 177661-177674.

[17] M. Gramajo, L. Ballejos, M. Ale, "Seizing Requirements Engineering Issues through Supervised Learning Techniques", IEEE Latin America Transactions, Vol. 18, No. 07, 2020, pp. 1164-1184.

[18] M. Alkhodari et al. "Screening Cardiovascular Autonomic Neuropathy in Diabetic Patients With Microvascular Complications Using Machine Learning: A 24-Hour Heart Rate Variability Study", IEEE Access, Vol. 9, 2021, pp. 119171-119187.

[19] G. Wang, K. W. Wong, J. Lu, "AUC-Based Extreme Learning Machines for Supervised and Semi-Supervised Imbalanced Classification", IEEE Transactions on Systems, Man, and Cybernetics: Systems, Vol. 51, No. 12, 2021, pp. 7919-7930.

[20] N. W. S. Wardhani, M. Y. Rochayani, A. Iriany, A. D. Sulistyono, P. Lestantyo, "Cross-validation Metrics for Evaluating Classification Performance on Imbalanced Data", Proceedings of the International Conference on Computer, Control, Informatics and its Applications, Tangerang, Indonesia, 2019, pp. 14-18.

[21] R. Ghorbani, R. Ghousi, A. Makui, A. Atashi, "A New Hybrid Predictive Model to Predict the Early Mortality Risk in Intensive Care Units on a Highly Imbalanced Dataset", IEEE Access, Vol. 8, 2020, pp. 141066-141079.

[22] E. R. Fernandes, C. P. L. F. A. De Carvalho, X. Yao, "Ensemble of Classifiers Based on Multiobjective Genetic Sampling for Imbalanced Data", IEEE Transactions on Knowledge and Data Engineering, Vol. 32, No. 6, 2020, pp. 1104-1115.

[23] N. Liu, X. Li, E. Qi, M. Xu, L. Li, B. Gao, "A Novel Ensemble Learning Paradigm for Medical Diagnosis With Imbalanced Data", IEEE Access, Vol. 8, 2020, pp. 171263-171280.

[24] M. S. Santos, J. P. Soares, P. H. Abreu, H. Araujo, J. Santos, "Cross-Validation for Imbalanced Datasets: Avoiding Overoptimistic and Overfitting Approaches [Research Frontier]", IEEE Computational Intelligence Magazine, Vol. 13, No. 4, pp. 59-76.

[25] K. Anam, H. Ismail, F. S. Hanggara, C. Avian, S. B. Worsito, "Cross Validation Configuration on k-NN for Finger Movements using EMG signals", Proceedings of the International Conference on Instrumentation, Control, and Automation, Bandung, Indonesia, 25-27 August 2021, pp. 17-21.

[26] M. Panda, A. A. A. Mousa, A. E. Hassanien, "Developing an Efficient Feature Engineering and Machine Learning Model for Detecting IoT-Botnet Cyber Attacks", IEEE Access, Vol. 9, 2021, pp. 91038-91052.

[27] J.-G. Choi, I. Ko, J. Kim, Y. Jeon, S. Han, "Machine Learning Framework for Multi-Level Classification of Company Revenue", IEEE Access, Vol. 9, 2021, pp. 96739-96750.

[28] T. Hasanin, T. M. Khoshgoftaar, J. L. Leevy, "A Comparison of Performance Metrics with Severely Imbalanced Network Security Big Data", 2019 IEEE 20th International Conference on Information Reuse and Integration for Data Science, Los Angeles, CA, USA, 2019, pp. 83-88.

[29] U. R. Salunkhe, S. N. Mali, "Classifier Ensemble Design for Imbalanced Data Classification: A Hybrid Approach", Procedia Computer Science, Vol. 85, 2016, pp. 725-732.

Software Reliability Prediction using Correlation Constrained Multi-Objective Evolutionary Optimization Algorithm

Original Scientific Paper

Neha Yadav
KIET Group of Institutions, Delhi-NCR, Ghaziabad, India
nehayadav1508@gmail.com

Vibhash Yadav
Rajkiya Engineering College, Banda, India
vibhashds10@gmail.com

Abstract *– Software reliability frameworks are extremely effective for estimating the probability of software failure over time. Numerous approaches for predicting software dependability were presented, but neither of those has shown to be effective. Predicting the number of software faults throughout the research and testing phases is a serious problem. As there are several software metrics such as object-oriented design metrics, public and private attributes, methods, previous bug metrics, and software change metrics. Many researchers have identified and performed predictions of software reliability on these metrics. But none of them contributed to identifying relations among these metrics and exploring the most optimal metrics. Therefore, this paper proposed a correlation-constrained multi-objective evolutionary optimization algorithm (CCMOEO) for software reliability prediction. CCMOEO is an effective optimization approach for estimating the variables of popular growth models which consists of reliability. To obtain the highest classification effectiveness, the suggested CCMOEO approach overcomes modeling uncertainties by integrating various metrics with multiple objective functions. The hypothesized models were formulated using evaluation results on five distinct datasets in this research. The prediction was evaluated on seven different machine learning algorithms i.e., linear support vector machine (LSVM), radial support vector machine (RSVM), decision tree, random forest, gradient boosting, k-nearest neighbor, and linear regression. The result analysis shows that random forest achieved better performance.*

Keywords*: Reliability, Faults, Bugs, Object-oriented, Evolutionary optimization, Machine learning*

1. INTRODUCTION

Software development involves creating software with potential flaws, leading to negative consequences and financial losses [1]. To address these risks, decision-makers use software defect prediction (SDP) to anticipate faulty modules through testing and coding inspection [2]. Ensuring software reliability during development is challenging, especially with constant changes in the software engineering sector. Estimating models' accuracy can vary with different datasets, and improving reliability requires finding a suitable reliability allocation paradigm within constraints [3-6]. Software reliability refers to a system or component's probability of functioning properly in a specific environment for a certain period [7-10]. Evaluating software reliability during the design phase compares current reliability to previous performance, using models to analyze release time and estimate future reliability [11-17]. However, testing complex software becomes difficult, impacting the effectiveness of software models [18-24]. Various approaches, including machine learning techniques, have been explored to model software reliability and quality [25-27]. Throughout the software development lifecycle, estimation techniques are used in the early stages, while reliability growth models are used during testing to reduce failure rates and predict defect density after deployment. Inference techniques fit the curve to the data for software reliability forecasting and estimation, with failure intensity being a simpler measure often derived from the reliability estimate. Estimating software reliability is challenging due to unbalanced and inaccurate data. Researchers are exploring machine learning algorithms for software defect prediction but haven't delved into it extensively. Software reliability prediction aims to identify fault-prone components early, reducing costs and time while ensuring desired quality. Various prediction approaches for effort, privacy, quality, defect, cost, and reusability are still in the early stages of development [24]. Software Reliability Prediction (SRP) involves using machine learning to find problematic classes/modules before testing [6,25]. Neural networks and statistical approaches like logistic regression are used, but they lack optimal parameter selection for software fault determination. This paper proposes a novel multi-objective evolutionary-based strategy that integrates machine learning algorithms to predict software reliability by anticipating

errors during testing using past failure data [27]. Therefore, the major contribution of the paper is:

- The paper presented a novel approach using a machine learning algorithm for software reliability prediction using software metrics correlation-constrained multi-objective evolutionary optimization algorithm. The algorithm is based on the identification of the software metrics based on certain hypotheses.
- The paper presented the comparative performance evaluation of the presented hypothesis on different classification techniques.
- The comparative state-of-art is presented to show the effectiveness of the proposed method.

The rest of the paper is organized as section 2 presents the related contributions of researchers for software reliability prediction using optimization. Section 3 presented an overview of the proposed evolutionary optimization algorithm and a detailed flowchart and working of the proposed methodology along with a hypothesis description. Section 4 describes the result analysis and comparative analysis. Section 5 presents the discussion of the proposed method and the result obtained. Finally in section 6 conclusion and future scope are presented.

2. RELATED WORK

Dhavakumar and Gopalan [5] proposed a Chaotic-GWO. It uses the Pham-Zhang model to forecast parameters and improves reliability by approximating SRGM parameters using TEF and chaotic maps. The findings show a good convergence rate and a link between selected variables and the fitness criterion. The desired outcome is an automated SRGM using CGWO, eliminating the need for customer involvement. Rani and Mahapatra [22] presented the exponential software reliability model to quantify numerous aspects, particularly fault initiation and time-varying fault diagnosis frequency. To optimize software reliability while lowering allocation costs, an expanded particle swarm optimization (EPSO) is presented. Researchers do trials utilizing completely random testing-resource sets and the entropy function to modify performance. Gupta et al. [9] proposed a nonlinear MO-optimizer regarding data envelopment analysis (DEA) for choosing software systems in the context of optimum redundancy to assure software reliability. Kumar et al. [18] presented a novel comparison analysis to determine the most appropriate and accurate artificial neural network. In this study, we present a backpropagation-based feed-forward neural network for improving software reliability and accuracy. Jaiswal et al. [13] used machine learning techniques such as the adaptive neuro-fuzzy system (ANFIS), and other techniques are used to predict software reliability on a variety of datasets derived from the operating system. Sangeeta et al. [27] proposed a novel technique for optimizing parameter values depending on the Ant Colony Optimizer with differential evolutions idea of ecological space has boosted the exploration capabilities of the ABC algorithm. The suggested algorithm's efficiency is further validated by comparing it to hybrid PSO algorithms. The newly proposed ABCDE algorithm estimates the system's reliability to be up to 85 percent. Diwaker et al. [4] proposed a novel quantitative model is provided that uses series and parallel reliability frameworks to calculate the SR. To compare the best reliability value, the performance of the proposed method is assessed to the output of soft computing approaches PSO and Fuzzy logic. The development of a big combination of parameters increases the complexity of the suggested model as more components are included. Jabeen et al. [12] proposed a highly precise error iteration analysis technique (HPEIAM) based on error-residuals is suggested to improve the predictive performance of current PSRGMs. SRGMs compute residual errors repeatedly, improving and correcting prediction accuracy to the intended level. HPEIAM's performance is evaluated using various PSRGMs and two sets of actual software failure data, with three quality criteria in mind. Table 1 presents the comparative feature of related works with the presented work.

Table 1. Recent Contribution

Ref	Objectives	Contribution	Research Gaps
[6]	The aim is to cover all finite paths of the control flow graph of the software under the test.	Presents a memetic algorithm for automatically generating test data	To solve the software cost problem because Software testing is very time-consuming and expensive
[8]	To predict future software faults by deploying the classifier algorithms	Build the model and predict the occurrence of the software bugs based on historical data by deploying the classifiers Logistic regression, Naive Bayes, and Decision Tree	To solve Software bug prediction issues as bugs are a serious challenge for system consistency and efficiency
[11]	To estimate the software release time and cost of the testing effort	A high-precision error iterative analysis method (HPEIAM) Proposes to enhance the prediction accuracy	Limitations of them mean that their predictive capacities differ from one dataset to others
[12]	To predict software reliability and evaluate them based on selected performance criteria	Applied ML including (ANFIS), feed forward back propagation neural network, SVM, etc	To solve various challenges in developing highly reliable software.
[13]	The aim is to provide software reliability within the allotted time & budget.	Presents a genetic programming-based decision tree model which facilitates a multi-objective optimization in the context of the software quality classification problem	Improved by the allocated software quality-improvement resources, and on the project-specific costs of misclassifications.
[19]	Aims to remove the wrong solution during the algorithm execution process, and adds knowledge to improve the solution accuracy	Proposes parameter estimation method of software reliability model based on hybrid PSO-ABC	The existing software reliability models are nonlinear, and the parameter estimation of these models is difficult.

[21]	The aim is to provide an extensive comparison of the explanative and predictive power of well-known bug prediction approaches	Present a benchmark for defect prediction	Low Accuracy
[23]	Aim to predict bugs in software using machine learning	Used dynamic classifier for detection	Low Accuracy

3. METHODOLOGY

In this paper, we have designed an evolutionary algorithm-based software reliability prediction. For these object-oriented metrics are considered and some hypotheses are designed. These hypotheses are considered objective functions for evolutionary algorithms. The below sub-section describes the steps and working model of the proposed methodology.

3.1. MULTI-OBJECTIVE EVOLUTIONARY ALGORITHM

We apply evolutionary algorithms, which are a kind of artificial intelligence, in our suggested study. These algorithms optimize problems through mutation and recombination. Multi-objective evolutionary optimization improves machine learning performance. The algorithms simulate natural evolution, where solutions represent humans and the problem specification represents the environment. A population of solutions is created and evaluated using objective functions. Better solutions have a higher chance of being selected for recombination. Crossover and mutation are key reproduction phases. The population is regulated through replacement. The process is repeated until a stop criterion is met. These algorithms follow natural processes and focus on populations rather than individual solutions. The first generation is randomly initialized and evaluated. Traditional optimization approaches vary from evolutionary algorithms in the following ways:

- While some CCMOEO scans a population concurrently, some just look for a specific position.
- Just the objectives functional part and fitness level are required for CCMOEO, without derivation variables.
- It utilizes probability ideas.
- Because there were minimal restrictions on the definition of objective functional area, CCMOEO is often simple to use.

Natural selection for resources in the environment is what drives evolution. Those kids who are more likely to survive to live longer and pass on their genetic material. Asexual reproduction is used to encode genetic information, resulting in kids that are genetically identical to their parents. Nowadays, evolutionary algorithms may be found everywhere, having been effectively applied to a variety of issues in fields such as social systems, automated programming, signal processing, and bioinformatics. These methods are highly beneficial for optimizing outcomes from many domains [3]. There are several evolutionary algorithms strategies, such as ant colonies, bee colonies, and so on. We may utilize these types of algorithms to optimize the outcome in the area of software quality optimization. There are numerous stages to the optimization: i) An initialization of random solutions is formed, referred to as individuals. ii) The simulation model evaluates each individual's goal functions.

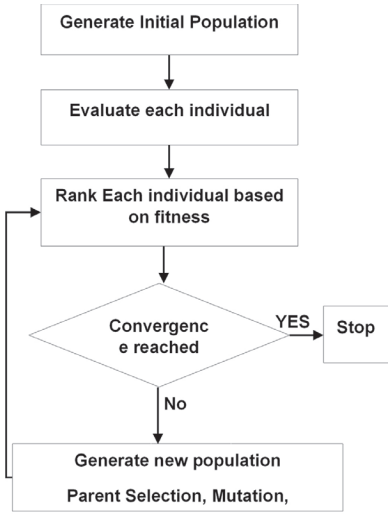

Fig. 1. Multi-Objective Evolutionary Algorithm

All software functionality, processing time, profiles, and costs are fixed input factors in our scenario since they do not vary throughout the optimization. iii) Each person is graded based on their "fitness," or the values of their goal functions. iv) Following the ranking of all individuals, the MOEA develops a new population of people (the next "generation") using the standard genetic algorithm operators of parent selection, crossover, and mutation. v) The MOEA generates a Pareto front after a certain number of generations (see Fig. 1).

3.2 OBJECT-ORIENTED DESIGN METRICS (OODMS)

One of the commonly used metrics in existing software reliability models is object-oriented design metrics (OODMs). Apart from this, there are several other Metrics also that can help determine software reliability growth. In the literature review, we have analyzed that there are several machine learning, optimization, and statistical techniques that are being used to predict software reliability. Many researchers also presented the correlation between OODMs and defective and non-defective classes of software. But relations among other metrics are still not that enlightening. For this, some hypotheses are presented in this paper which are discussed in the below sub-section. To prove this hypothesis, the paper proposed a software metrics correlation-constrained multi-objective evolutionary optimization algorithm whose steps are discussed below (Fig 2).

The methodology is divided into three basic steps: (a) pre-processing, (b) Correlation-Constraint Multi-objective Evolutionary Optimization, and (c) classification. These steps are described in detail below sub-sections.

3.2.1. Preprocessing

In this paper, the dataset contains a mixed set of data i.e., numerical and categorical parameters. Due to the dynamic nature of software reliability parameters, it is required to distinguish between parameters. For this pre-processing step is required. As machine learning can only handle numerical data. Therefore, for the proper estimation of the hyperparameter's performance, these mixed data are converted into an array of numerical data.

Transformation of Hyperparameters: In this step, a set of data features is used to estimate the reliability level of software. Fig 2 represents the pre-processing steps used for reliability prediction.

Data Type detection: In this step, a simple, type of data is detected i.e., numeric, categorical, and boolean. Some samples of datasets and their type are presented in Table 2.

Mapping: In this step, two major works are performed. In the first step, the redundant data are removed and in the second step, unnamed columns are removed. As it is known that data redundancy generally occurs when some parameters or Metrics are stored multiple times in the database. These redundant data don't seem a big issue but when the size of data increases, then these redundant data create unnecessary computational complexity for the learning model. Therefore, these data must be removed. Another major issue that occurs while the learning/analytics process is the presence of unnamed or unknown columns (software parameters) in the dataset. If these data are not removed then it will result in ambiguous analysis.

Merging: In this step, parameters related to software metrics are selected i.e., Object-Oriented Design Metrics, Previous Bug Metrics, Methods Metrics, and Entropy Metrics. These Metrics are most important for analytical purposes.

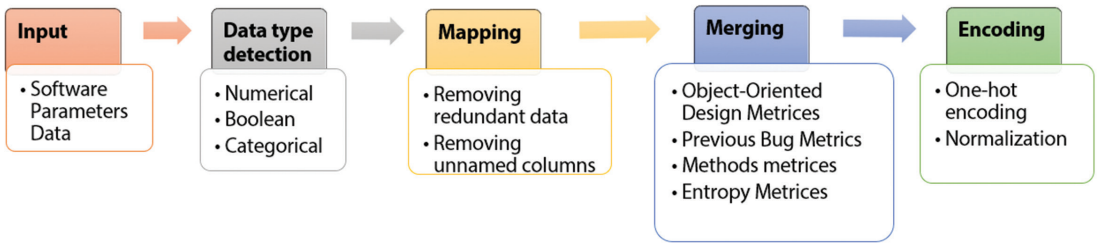

(a) Pre-processing

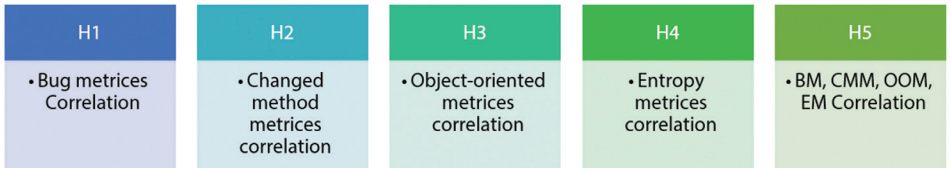

(b) Correlation-Constraint Multi-objective Evolutionary Optimization

(c) Classification

Fig. 2. Proposed Methodology

Table 2. Data Type Detection

Bug Metrices		Object-Oriented Metrics		Entropy Metrics	
Parameters	Type	Parameters	Type	Parameters	Type
class name	Mixed	CBO	Mixed	CvsEntropy	Mixed
Bugs Found	Integer	Fin	Decimal	CvsWEntropy	Decimal
Trivial bugs	Integer	Fout	Decimal	LinEntropy	Decimal
Major Bugs	Integer	No. of attributes	Decimal	LogEntropy	Decimal
Critical Bugs	Integer	No. of LOC	Decimal	ExpEntropy	Decimal
Priority Bugs	Integer	No of Methods	Decimal	Defect	Boolean
Defect	Boolean	Defect	Boolean	-	-

Encoding In this step, the one-hot encoding method is used to convert the merged data so that they can result in me better prediction results. so they can be provided to machine learning algorithms to improve predictions. This method is adopted because it of better prediction results of machine learning with those data that show no relationship to each other. After encoding data normalization is performed. Normalizing an attribute by evaluating the percentage of a value to the attribute's summation value is known as frequency normalization. It's described as:

$$x_i = \frac{x_i}{\sum_i x_i} \quad (1)$$

Frequency normalization also scales an attribute into [0,1].

3.2.2. Correlation-Constraint Multi-objective Evolutionary Optimization

In this section, an MOEA algorithm is proposed based on correlation constraints on the following hypothesis:

- Hypothesis 1 (H1): Previous bug metrics (BM) is unable to predict defect in the software.
- Hypothesis 2 (H2): Changed method metrics (CMM) is unable to predict defect in the software.
- Hypothesis 3 (H3): Object-oriented metrics (OOM) is unable to predict defect in the software.
- Hypothesis 4 (H4): Entropy metrics EM) is unable to predict defect in the software.
- Hypothesis 5 (H5): Bug matrices (BM), object-oriented metrics (OOM), changed method metrics CMM) and entropy metrics (EM) correlate them to predict defects in the software.

Scientific application is generally formulated as constrained optimization problems and mathematically it is represented as:

$$min\{f(X)\}=X=\{x_1, x_2,...x_n\} \; such \; that \; LB<x_n<UB$$
$$subjects \; to: \; g(X)\leq 0 \; \{inequality \; constraints\} \quad (2)$$
$$subjects \; to: \; h(X)=0 \; \{equality \; constraints\}$$

Where, $f(X)$= objective function,
$\{x_1, x_2,...x_n\}$ = decision vectors

LB and UB = *lower* and *upper bound* respectively

The equality constraint violation on all constraints is mathematically represented as:

$$G(X) = \sum_{i=1}^{n} G_i(X) \quad (3)$$

Where, i= inequality constraints

The solution that satisfies G(X) is termed a feasible solution. Therefore, the target of any constraint-oriented optimization is to locate optimal G(X). The evolutionary algorithm possesses a powerful searching ability that can solve above mentioned constraint problem efficiently. Therefore, this paper has adopted evolutionary optimization as a solution. The framework of the proposed correlation-constrained multi-objective evolutionary optimization algorithm (CCMOEO) is given in Fig. 3. Two basic steps are performed in this algorithm: learning and evolution. In the learning stage, five hypotheses are designed to establish a correlation between constraints and objective function. As a result, in the evolving stage, the correlation is used to direct the evolution process. To avoid a local optimum induced by complex constraints, correlation is employed to determine how much information of the objective function is utilized. As a result, the inhabitants can more easily enter the area. Constraint and goal function variation tendencies are more important to us in this work. That's why it's possible to catch a trend early on since the population is spread out throughout a large area. Learning is followed by evolution, which uses the rest of the computer's processing power.

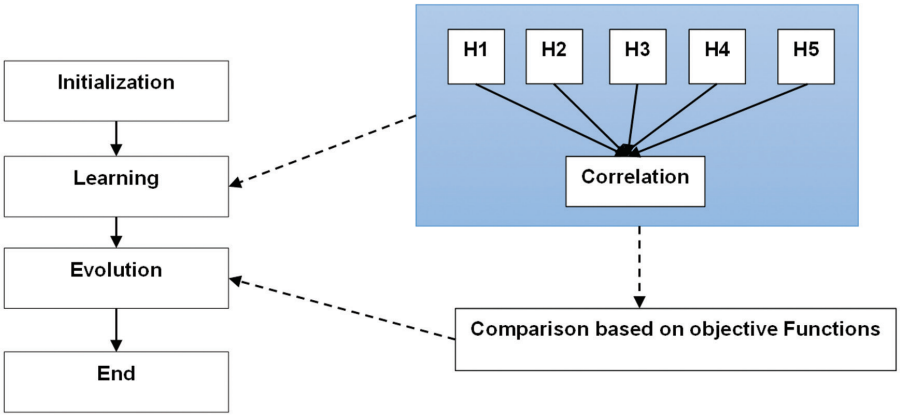

Fig. 3. CCMOEO Architecture

In the stage of learning, the notion of correlation index (CI) is proposed to mine the correlation between the variables. The closer the value of CI is to one, the greater the degree to which the constraints and the goal function are correlated. During the period of development, two different approaches are designed. The first method is referred to as the weighted sum updating strategy, and it states that the fitness value of an individual is determined by the weighted sum of normalized G(X) and normalized f.(X).

3.2.3. Classification

In this step, the optimized data is fed into a classifier for learning the pattern of failure and success of software metrics. For classification, the paper analyzed the performance of seven classifiers. These are discussed below:

Linear support vector machine (LSVM): A support vector machine is a machine learning model that is capable to simplify between two dissimilar classes if the fixed of categorized data is provided in the training set to the algorithm. The key purpose of the SVM is to distribute the data samples according to hyperplane and distinguish among different classes. Linearly Separable 2D Data is a two-dimensional database separated by line if we can distinguish positive from negative objects by a straight line. It does not matter if there is more than one such line. If data cannot be categorized, linearization cannot completely separate these two categories. For many non-linear databases, the line separator will still be "good enough" and segment multiple cases correctly.

Radial support vector machine (RSVM): The RBF kernel is one of the most popular kernels because it is the most general form of the kernel and resembles a Gaussian distribution. The RBF kernel function for two points Y_1 and Y_2 computes the similarity or how close they are to each other. An RBF kernel is a function whose value depends on the origin or distance from some point.

Decision tree: In machine learning, a decision tree is a predicting approach. It's a flowchart-like layout where every other block contains an attribute "test." Classification rules are represented by the results from one block to the next. Nodes may be classified into three categories: Squares are used to symbolize decision nodes. Ending nodes are depicted by triangles, whereas chance nodes are depicted by circles. The following is how a decision tree works: begin with the root node, which holds the whole dataset. By using Attribute Selection Measure, discover the perfect attribute in the dataset. Divide the root node into subgroups that include the best attribute's potential values. Create the node of the decision tree that holds the best attribute. Make new decision trees recursively using subsets of the dataset, Repeat this procedure till the nodes could no longer be classified and the last node is designated as a leaf node. It's utilized in data mining research. This is the most effective instrument for forecasting. The decision tree has a few benefits, like being easy to use and requiring minimal data preparation. The following are some disadvantages: it may result in too complicated trees, which is known as overfitting.

Random forest: It is a commonly used ML method that is classified as supervised learning. It may be used in ML for both classifiers and as well as for regression data. It is based on the notion of supervised methods, which is the act of combining numerous classifications to tackle a difficult problem and increase the individual's effectiveness. This approach consists of some decision trees, each of which can be built up of datasets retrieved from a training dataset, referred to as the bootstrap sample. The RF considers each tree's forecast and generates an outcome based on the plurality of predictions. The forest's enormous number of trees provides greater precision, avoiding the issue of overfitting.

Gradient boosting: Gradient boosting is an ML boosting technique. It is based on the assumption that combining the best subsequent modeling with the prior model reduces the total estimation error. To reduce mistakes, the key concept is to define target outcomes for the following concepts. To decrease bias error, the GB Algorithm is often utilized. Both prediction and classification techniques may benefit from the gradient-boosting approach. MSE is the cost function in a regression problem, and function Loss is the cost function in a classifier. GB Machine integrates results from many decision trees to create a final prediction. Take into account that in a gradient-boosting machine, each learning rate is a decision tree.

k-nearest neighbor: K-Nearest Neighbors (KNN) is a machine learning method that uses case similarities to classify data points. It is a non-parameterized approach that relies on comparing the characteristics of data points to determine their classifications. The process involves selecting a value for K, calculating the Euclidean distance between the K nearest neighbors, and then assigning a category based on the majority of the neighbors. The KNN algorithm identifies the closest data points in terms of feature similarity, with K representing the number of data points used in the analysis. The distance measure, typically Euclidean distance, and the corresponding values play a crucial role in the KNN classifier. By considering the K nearest neighbors and their associated labels, KNN can classify new data points in the feature space.

Logistic regression: The most widely used ML algorithm is logistic regression. It is a statistical technique that is also known as the Logit model. Depending on the dataset of independent factors, it calculates the likelihood of an event occurring. In binary logistic regression, there is just one binary dependent variable, coded by an indicator variable, with two parameters labeled 0 and 1, and the independent variables may be either binary or continuous. Important assumptions to keep in mind are that the dependent variable has to be categorized and that the independent variable should not be multi-collinear. The dependent variable is confined between 0 and 1 since the outcome is a probability. A logit transformation is performed to the odds in logistic regression, which is the likelihood of success divided by the probability of failure.

4. RESULTS AND DISCUSSIONS

In this section, the paper presents the results obtained after prediction. Section 4.1 describes dataset taken in this paper for evaluation. Section 4.2 describes the implementation details. Section 4.3 describes the data visualization and finally in section 4.4 results are analyzed with a comparative state-of-art.

4.1. DATASET DESCRIPTION

This paper introduces a software fault dataset designed for comparing bug prediction models [21]. The dataset includes information necessary for estimating bugs based on source code measures, historic measurements, and access to data. The dataset covers several software systems, including Eclipse, PDE, Equinox, Lucene, and Mylyn. It provides historical information, biweekly versions of systems, source code metrics, and post-release defect numbers for each class. A sample of the dataset is presented in Table 3.

Table. 3. Dataset Representation

Dataset	Samples
Eclipse	5372
Equinox	325
PDE	1492
Lucene	692
Mylyn	1863

4.2. IMPLEMENTATION DETAILS

This paper has implemented and trained the models in the Keras framework with TensorFlow. The proposed model was trained using GPU on Google colab. Following the performance, parameters are used to evaluate the model's efficiency in terms of Accuracy, precision, and recall.

$$Accuracy = \frac{TP + TN}{TP + TN + FP + FN} \tag{4}$$

$$\frac{Recall}{Sensitivity} = \frac{TP}{TP + FN} \tag{5}$$

$$Precision = \frac{TP}{TP + FP} \tag{6}$$

Where, TP = True Positive, FP= False Positive, FN= False Negative and TN = True Negative

4.3. EXPLORATORY DATA VISUALIZATION

Fig. 4 shows the feature correlation map using the eclipse dataset considering all the pre-determined conditions and variables and this map shows the correlation coefficient for different variables for all the possible pair of variables and helps in visualizing the given eclipse dataset.

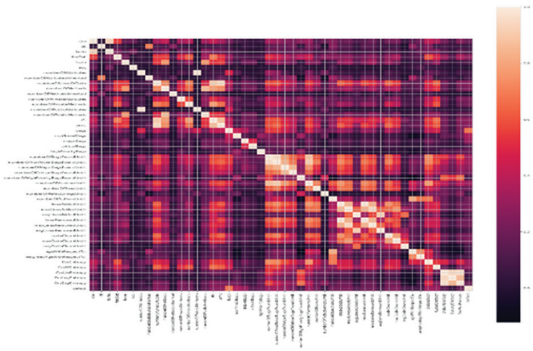

Fig. 4. Feature Correlation Map

4.4. RESULT ANALYSIS

Table 4 shows the accuracy, precision, and recall comparison of for eclipse dataset for different classifiers. The Accuracy of the Random Forest Classifier is maximum and it is minimum for the K-neighbors classifier. Precision is maximum for the Linear SVM classifier and minimum for the logistic regression classifier. The recall is maximum for the Decision Tree classifier and minimum for the Radial SVM classifier. Table 5 shows the accuracy, precision, and recall comparison of for equinox dataset for different classifiers. The Accuracy of Linear SVM, Random Forest, and Gradient Boosting is maximum and it is minimum for the K-Neighbors classifier. Precision is maximum for Linear SVM and Gradient Boosting classifier and minimum for logistic regression classifier. The recall is maximum for the Decision Tree classifier and minimum for the Decision Tree classifier. Table 6 shows the accuracy, precision, and recall comparison of for equinox dataset for different classifiers. The Accuracy of Linear SVM, Random Forest, and Gradient Boosting is maximum and it is minimum for the Logistic Regression classifier. Precision is maximum for different classifiers and minimum for Decision Tree classifiers. The recall is maximum for the Decision Tree classifier and minimum for Random Forest and K-Neighbors classifier. Table 7 shows the accuracy, precision, and recall comparison of for Mylyn dataset for different classifiers. The Linear SVM, Random Forest is maximum and it is minimum for Radial SVM classifier. Precision is maximum for the Linear SVM classifier and minimum for the K-Neighbors classifier. The recall is maximum for the Decision Tree classifier and minimum for the Gradient Boosting classifier. Table 8 shows the accuracy, precision, and recall comparison of for PDE dataset for different classifiers. The Accuracy of the Linear SVM Classifier is maximum and it is minimum for the Radial SVM classifier. Precision is maximum for the Linear SVM classifier and minimum for the Decision Tree classifier. The recall is maximum for 4 classifiers and minimum for the Logistic Regression classifier. Fig 5 represents the comparative state-of-art. In Fig 5, the paper compares with works presented by [16] and [23]. [16] proposed a Hyperparameter optimization algorithm and achieved an average of 87% accuracy whereas [23] proposed a dynamic parameter selection algorithm and achieved an accuracy of approx. 76%. From the result, we can observe that the proposed multi-constraint multi-optimization algorithm achieves better accuracy of approx. 99%.

Table 4. Parameter Comparison for Eclipse Dataset

Classifier	Accuracy	Precision	Recall
Decision Tree	99.39 %	66.66 %	97.47 %
Random Forest	99.47 %	95.85 %	96.46 %
Logistic Regression	86.07 %	46.4 %	96.46 %
Linear SVM	98.43 %	100 %	93.43 %
Gradient Boosting	99.18 %	56.93 %	26.26 %
K-Neighbors	84.66 %	97.94 %	22.72 %
Radial SVM	86.37 %	97.96 %	15.15 %

Table 5. Parameter Comparison for Equinox Dataset

Classifier	Accuracy	Precision	Recall
Linear SVM	97.53 %	100 %	100 %
K-Neighbors	80.24 %	100 %	93.54 %
Random Forest	97.53 %	86.95 %	93.54 %
Logistic Regression	80.23 %	74.14 %	93.54 %
Decision Tree	97.53 %	82.60 %	74.19 %
Gradient Boosting	97.53 %	100 %	64.51 %
Radial SVM	82.17 %	100 %	61.29 %

Table 6. Parameter Comparison Lucene Dataset

Classifier	Accuracy	Precision	Recall
Linear SVM	100 %	100 %	100 %
Logistic Regression	91.3 %	100 %	100 %
Radial SVM	90.17%	100 %	100 %
Decision Tree	100 %	83.3 %	100 %
Gradient Boosting	100 %	100 %	26.13 %
Random Forest	100 %	100 %	10.5 %
K-Neighbors	90.17%	100 %	10.5 %

Table 7. Parameter Comparison for Mylyn Dataset

Classifier	Accuracy	Precision	Recall
Linear SVM	99.78 %	100 %	98.8 %
Radial SVM	81.9 %	97.67 %	98.8 %
Decision Tree	99.57 %	87.87 %	98.8 %
K-Neighbors	83.4 %	63.33 %	98.8 %
Logistic Regression	87.12 %	98.8 %	34.11 %
Random Forest	99.78 %	66.66 %	22.3 %
Gradient Boosting	99.35 %	100 %	2.3 %

Table 8. Parameter Comparison for PDE Dataset

Classifier	Accuracy	Precision	Recall
Linear SVM	100 %	100 %	100 %
Random Forest	99.46 %	96.7 %	100 %
Gradient Boosting	100 %	55.17 %	100 %
Decision Tree	100 %	12.5 %	100 %
K-Neighbors	82.13 %	100 %	27.11 %
Radial SVM	82.66 %	31.8 %	11.86 %
Logistic Regression	85.066 %	100 %	1.6 %

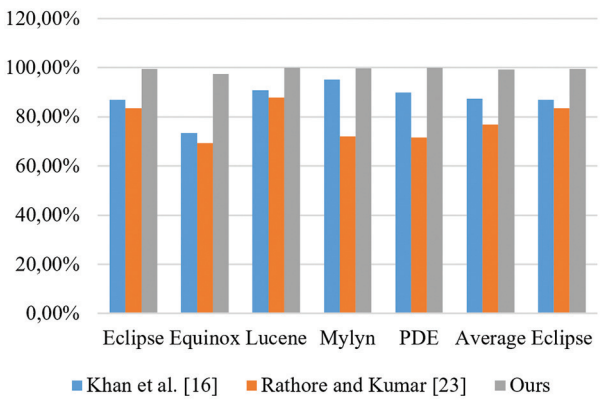

Fig 5. Comparative Accuracy Evaluation

5. DISCUSSION

Based on the information provided, the final result suggests that the proposed multi-constraint multi-optimization algorithm achieves a significantly higher accuracy of approximately 99% compared to other classifiers and state-of-the-art approaches. This is because the CCMOEO algorithm combines the power of evolutionary optimization with the incorporation of correlations between metrics and defect prediction. By leveraging these correlations, the algorithm aims to improve the accuracy of defect prediction in software and find better solutions to the constrained optimization problem. This indicates that the algorithm is highly effective in accurately classifying the datasets used in the study (Eclipse, Equinox, Mylyn, and PDE). The algorithm's superior performance in terms of accuracy, precision, and recall makes it a promising solution for the classification tasks considered in the study.

6. CONCLUSION

Software systems have a significant impact on society, and ensuring their trustworthiness is crucial. Bug-free software is a key factor in achieving trust, and reliability models are used to assess software reliability and predict faults. Researchers are exploring computational intelligence methods, including machine learning and optimization, to improve prediction models. In this paper, a software reliability prediction model is developed using a software metrics correlation multi-objective evolutionary algorithm-based model proposed for the identification of defect metrics for establishing the reliability of software. The result analysis was observed on seven classifiers and achieved an average accuracy of 99% which is approx. 13% improvement over comparative state-of-art. Future research can focus on training the algorithm on larger datasets, identifying failure points in AI software, and identifying weak reliable points that may lead to attacks.

Data Availability Statement:
All data are made available in the manuscript.

Conflict of Interest:
The authors declare no conflict of interest.

Funding Information: None.

7. REFERENCES

[1] A. K. Behera, M. Panda, S. C. Nayak, C. S. K. Dash, "An Artificial Electric Field Algorithm and Artificial Neural Network-Based Hybrid Model for Software Reliability Prediction", Computational Intelligence in Data Mining, Springer, 2022, pp. 271-279.

[2] X. Chen, Y. Shen, Z. Cui, X. Ju, "Applying Feature Selection to Software Defect Prediction Using Multi-objective Optimization", Proceedings of the IEEE

41st Annual Computer Software and Applications Conference, Turin, Italy, 4-8 July 2017, pp. 54-59.

[3] C. A. Coello Coello, S. González Brambila, J. Figueroa Gamboa, M. G. Castillo Tapia, R. Hernández Gómez, "Evolutionary multiobjective optimization: open research areas and some challenges lying ahead", Complex & Intelligent Systems, Vol. 6, No. 2, 2020, pp. 221-236.

[4] C. Diwaker et al. "A New Model for Predicting Component-Based Software Reliability Using Soft Computing", IEEE Access, Vol. 7, 2019, pp. 147191-147203.

[5] P. Dhavakumar, N. P. Gopalan, "An efficient parameter optimization of software reliability growth model by using chaotic grey wolf optimization algorithm", Journal of Ambient Intelligence and Humanized Computing, Vol. 12, No. 2, 2021, pp. 3177-3188.

[6] S. K. Dubey, B. Jasra, "Reliability assessment of component based software systems using fuzzy and ANFIS techniques", International Journal of Systems Assurance Engineering and Management, Vol. 8, No. 2, 2017, pp. 1319-1326.

[7] F. El Hajj Chehade, R. Younes, "Structural reliability software and calculation tools: a review", Innovative Infrastructure Solutions, Vol. 5, No. 1, 2020, p. 29.

[8] M. Esnaashari, A. H. Damia, "Automation of software test data generation using genetic algorithm and reinforcement learning", Expert Systems with Applications, Vol. 183, 2021, p. 115446.

[9] P. Gupta, M. K. Mehlawat, D. Mahajan, "Data envelopment analysis based multi-objective optimization model for evaluation and selection of software components under optimal redundancy", Annals of Operations Research, Vol. 312, No. 1, 2022, pp. 193-216.

[10] D. D. Hanagal, N. N. Bhalerao, "Literature Survey in Software Reliability Growth Models", Software Reliability Growth Models, Springer Singapore, 2021, pp. 13-26.

[11] S. Delphine Immaculate, M. Farida Begam, and M. Floramary, "Software Bug Prediction Using Supervised Machine Learning Algorithms", Proceedings of the International Conference on Data Science and Communication, 2019, pp. 1-7.

[12] G. Jabeen, P. Luo, W. Afzal, "An improved software reliability prediction model by using high precision error iterative analysis method", Software Testing, Verification and Reliability, Vol. 29, No. 6-7, 2019, p. e1710.

[13] A. Jaiswal, R. Malhotra, "Software reliability prediction using machine learning techniques", International Journal of Systems Assurance Engineering and Management, Vol. 9, No. 1, 2018, pp. 230-244.

[14] A. Jindal, A. Gupta, Rahul, "Comparative Analysis of Software Reliability Prediction Using Machine Learning and Deep Learning", Proceedings of the Second International Conference on Artificial Intelligence and Smart Energy, 2022, pp. 389-394.

[15] M. Job, S. Battista, R. Stanzani, A. Signori, M. Testa, "Quantitative Comparison of Human and Software Reliability in the Categorization of Sit-to-Stand Motion Pattern", IEEE Transactions on Neural Systems and Rehabilitation Engineering, Vol. 29, 2021, pp. 770-776.

[16] F. Khan, S. Kanwal, S. Alamri, B. Mumtaz, "Hyper-Parameter Optimization of Classifiers, Using an Artificial Immune Network and Its Application to Software Bug Prediction", IEEE Access, Vol. 8, 2020, pp. 20954-20964.

[17] T. M. Khoshgoftaar, Y. Liu, "A Multi-Objective Software Quality Classification Model Using Genetic Programming", IEEE Transactions on Reliability, Vol. 56, No. 2, 2007, pp. 237-245.

[18] P. Kumar, S. K. Singh, S. Deo Choudhary, "Reliability prediction analysis of aspect-oriented application using soft computing techniques", Materials Today: Proceedings, Vol. 45, 2021, pp. 2660-2665.

[19] Z. Li, M. Yu, D. Wang, H. Wei, "Using Hybrid Algorithm to Estimate and Predicate Based on Software Reliability Model", IEEE Access, Vol. 7, 2019, pp. 84268-84283.

[20] K. Lwin, R. Qu, G. Kendall, "A learning-guided multi-objective evolutionary algorithm for constrained portfolio optimization", Applied Soft Computing, Vol. 24, 2014, pp. 757-772.

[21] M. D'Ambros, M. Lanza, R. Robbes, "An extensive comparison of bug prediction approaches", Proceedings of the 7th IEEE Working Conference on

Mining Software Repositories, Cape Town, South Africa, 2-3 May 2010, pp. 31-41.

[22] P. Rani, G. S. Mahapatra, "Entropy based enhanced particle swarm optimization on multi-objective software reliability modelling for optimal testing resources allocation", Software Testing, Verification and Reliability, Vol. 31, No. 6, 2021, p. e1765.

[23] S. S. Rathore, S. Kumar, "Software fault prediction based on the dynamic selection of learning technique: findings from the eclipse project study", Applied Intelligence, Vol. 51, No. 12, 2021, pp. 8945-8960.

[24] S. K. Rath, M. Sahu, S. P. Das, S. K. Mohapatra, "Hybrid Software Reliability Prediction Model Using Feature Selection and Support Vector Classifier", Proceedings of the International Conference on Emerging Smart Computing and Informatics, Pune, India, 9-11 March 2022, pp. 1-4.

[25] K. Sahu, R. K. Srivastava, "Revisiting Software Reliability", Data Management, Analytics and Innovation, Springer, 2019, pp. 221-235.

[26] S. P. Sahu, B. R. Reddy, D. Mukherjee, D. M. Shyamla, B. S. Verma, "A hybrid approach to software fault prediction using genetic programming and ensemble learning methods", International Journal of Systems Assurance Engineering and Management, Vol. 13, 2022, pp. 1746-1760.

[27] Sangeeta, K. Sharma, M. Bala, "An ecological space based hybrid swarm-evolutionary algorithm for software reliability model parameter estimation", International Journal of Systems Assurance Engineering and Management, Vol. 11, No. 1, 2020, pp. 77-92.

Power Flow Control of the Grid-Integrated Hybrid DG System using an ARFMF Optimization

Original Scientific Paper

Saleem Mohammad
Electrical and Electronics Engineering,
Sathyabhama Institute of Science & Technology
Chennai-119, India
saleem238@gmail.com

S.D Sundarsingh Jeebaseelan
Electrical and Electronics Engineering, Sathyabhama
Institute of Science & Technology
Chennai-119, India
Sundarsingh.eee@sathyabama.ac.in

Abstract *– A power flow control scheme for a grid-integrated Hybrid DG System (HDGS) is presented in this work, utilizing an advanced random forest algorithm combined with the moth-flame optimization (ARFMF) approach. The proposed control scheme combines the random forest algorithm (RFA) and moth-flame optimization algorithm (MFO) for consolidated execution. The random forest algorithm (RFA), an AI technique, is well-suited for nonlinear systems due to its accurate interpolation and extrapolation capabilities. It is an ensemble learning method that combines multiple decision trees to make predictions. The algorithm constructs a forest of decision trees and aggregates their predictions to produce the final output. The moth-flame optimization (MFO) process is a meta-heuristic optimization procedure inspired by the transverse orientation of moths in nature. It improves initial random solutions and converges to superior positions in the search area. Similarly, the MFO is effective in nonlinear systems as it accurately interpolates and extrapolates arbitrary information. In the proposed technique, the RFA performs the calculation process to determine precise control gains for the HDGS through online implementation based on power variation between the source side and the load side. The recommended dataset is used to implement the AI approach for online execution, reducing optimization process time. The learning process of the RFA is guided by the MFO optimization algorithm. The MFO technique defines the objective function using system information based on equal and unequal constraints, including the accessibility of renewable energy sources, power demand, and state of charge (SOC) of storage systems. Storage devices such as batteries stabilize the energy generated by renewable energy systems to maintain a constant, stable output power. The proposed model is implemented on the MATLAB/Simulink platform, and its execution is compared to previous approaches.*

Keywords*: moth-flame optimization, random forest algorithm, Microgrid, optimization, nonlinear systems*

1. INTRODUCTION

The evolution of the energy sector is being driven by the urgent need to address environmental issues and reduce reliance on fossil fuels for electricity generation. This shift towards sustainable energy sources requires the integration of innovative approaches to facilitate the transformation. As renewable energy sources and distributed generators become more prevalent, it is imperative to devise new strategies for effectively managing and operating the power grid. The objective is to ensure the consistent and high-quality delivery of electricity while maintaining or enhancing the reliability of the power supply. This entails the development of robust frameworks and technologies that can accommodate the increasing complexity and variability associated with renewable energy integration while upholding grid stability and performance. By leveraging innovation in grid management, we can pave the way for a sustainable and resilient energy future. [1]

The need for energy storage devices in the DC link arises from the growing adoption of renewable energy sources driven by the transition to clean and sustainable energy. However, renewable energy sources, such as solar (PV) and wind, are characterized by their variability and unpredictability. This variability poses challenges in effectively harnessing these energy sources, necessitating the use of energy storage devices to balance power and ensure a smooth and reliable power supply. [2]

Inverter reactive power compensation alone is insufficient to handle load variations, resulting in voltage sag, which can lead to operational issues [3]. To overcome this limitation, additional measures and strategies are required to effectively manage load variations and maintain stable voltage levels within the system. The complementarity and unpredictability of PV and wind energy further compound the challenges of effectively harnessing these energy sources [4]. Fluctuating PV irradiation and wind speed make it difficult to predict and optimize their power generation. However, technological advancements, such as the utilization of double-fed induction generators in wind turbine systems, enable multiple wind turbines to operate at variable speeds [5]. This flexibility allows for better control and regulation of the generator's torque, aligning it with the desired power factor or generator terminal voltage. This regulation takes into account various factors, including the availability of wind, PV, hydro, and energy storage devices, to optimize the overall system performance.

Achieving power flow balance and minimizing the impacts of atmospheric conditions in a hybrid generation system with multiple renewable energy sources is essential. Power flow balance ensures a consistent meeting of energy demand by the hybrid generation system. Balancing the power flow between renewable energy sources helps maintain a stable and reliable power supply, reducing the risk of blackouts or disruptions in the electrical grid. By achieving power flow balance, the hybrid generation system can optimize the utilization of renewable energy resources. During periods of high PV irradiation, more power can be generated from the PV source, while in times of high wind speed, the wind turbines can contribute a larger share of the power. This balanced approach maximizes the use of available resources and improves the overall efficiency of the system. Atmospheric conditions, such as variations in PV irradiance and wind speed, can significantly impact the power output of renewable energy sources. Effective management of these variations and balancing the power flow enables the hybrid generation system to minimize the negative impacts caused by fluctuations in atmospheric conditions. This reduction in sudden power output changes allows for better control and integration of renewable energy into the grid.

The proposed hybrid technique, referred to as ARFMF, combines the Random Forest Algorithm (RFA) and Moth Flame Optimization (MFO) algorithms for hybrid optimization. This proposal aims to achieve a balance in power flow and minimize impacts. The work is structured as follows: Section 2 provides a review of recent research, Section 3 discusses control strategies for Hybrid DG Systems, Section 4 presents the recommended ARFMF approach, Section 5 presents simulation results, and finally, Section 6 concludes the paper.

2. RECENT RESEARCH WORK

In their study, T. P. Kumar [6] put forward an optimal control strategy for Hybrid DG Systems (HDGS) that combines RNN and ANN with lighting search optimization, referred to as ANNLSA. To achieve optimal power flow management in Hybrid DG Systems (HDGS), a technique that balances real and reactive power involves a parallel connection of solar, wind, fuel cells, and batteries. The incorporation of solar and wind energy into an electric grid is examined, and the effectiveness of the compensation strategy of the DC-DC converter is evaluated using the ANNLSA technique. In optimising active power management, the Lightning Search Algorithm (LSA) is utilized, while optimal reactive power management is achieved using a Recurrent Neural Network (RNN). T. F. Shatter [7] introduced a system that integrates 3 renewable sources—solar, wind, and fuel cells—with the primary objective of controlling and maximising the productivity of the renewable sources. The primary aim of the PV, wind, and FC energy sources is to be efficiently controlled and operated. To attain MPPT for both solar and wind systems, Fuzzy Logic Control is employed, directing the peak power to a regulated DC voltage bus. This fixed voltage bus is responsible for powering the load, and any surplus energy is utilised for the electrolysis of water to produce hydrogen for fuel cells.

Tazvinga [8] put forward an ideal power management model for an HDGS designed for isolated applications. The system combines solar photovoltaic, diesel, and battery power, and a controlling strategy is implemented to regulate the power flow between system components to meet the varying load demands throughout the day. In the proposed model, the main objective is to meet the load demand while satisfying system constraints. To achieve this, the model aims to determine the optimal power flow while minimising fuel and battery wear costs. This is accomplished by taking into consideration the availability of photovoltaic power, the battery bank's state of charge, and the varying load demand. The optimal solutions are evaluated for two different scenarios: one where objectives have equal weight and another where a higher weight is given to battery wear. Giving a higher weight to battery wear leads to a noticeable rise in system operational costs, primarily due to increased usage of the diesel generator. In their research, N. Bizon [9] proposes a new Energy Management Unit (EMU) control strategy that relies on the LF approach. The EMU control strategy is designed to maintain a charge-sustaining mode for the Energy Storage System (ESS), effectively minimizing battery stack capacity when directly connected to the DC bus.

K. Venkatesan and colleagues [10] have presented an optimal control strategy for Hybrid DG Systems (HDGSs), which incorporate photovoltaic and wind turbine systems alongside energy storage. The aim of the presented optimal control strategy is to optimise power flow control in HDGSs. To achieve this, K. Venkatesan et al. [10] propose combining the Whale Optimization

Algorithm (WOA) with an Artificial Neural Network (ANN) to create a more effective and efficient control strategy. In the proposed optimal control strategy by K. Venkatesan et al. [10], the Whale Optimization Algorithm (WOA) is incorporated into the Artificial Neural Network (ANN) learning process to minimise the error in the objective function. This results in the development of the WOANN approach, which combines the WOA and ANN. The WOANN approach predicts control gain parameters for HDGS to regulate power flow, taking into account factors such as renewable energy availability, storage device charge levels, and load power demand. It accomplishes this by examining active and reactive power variation at the load side.

2.1. BACKGROUND OF THE RESEARCH WORK

It is evident that the energy management of Hybrid DG Systems with energy storage devices involves the integration of multiple renewable sources, such as PV and wind power generators, along with a diesel power generator. Determining the appropriate size of PV, wind, and diesel power plants is a complex task in energy management. While the use of a fuzzy logic controller for a wind turbine, PV, hydrogen, or battery HDGS in energy management has demonstrated improved results, it does not fully capture the unique characteristics of fuzzy systems theory. The complexity of the problem, the variability of renewable energy sources and load demand, and the interdependence among multiple variables all contribute to the difficulty of achieving optimal energy management in hybrid DG systems. To address this challenge, various traditional energy management strategies, such as fuzzy logic, neuro-fuzzy, and optimization algorithms, have been employed. However, the stochastic nature of the velocity equation in the Particle Swarm Optimization (PSO) algorithm makes it difficult to determine the global best value. The need for an integrated MG system arises to tackle this challenge. However, there are only a few existing works in literature that address this issue, highlighting the importance and motivation for the present research.

3. CONTROL METHODS OF HYBRID DG SYSTEM

The HDGS control structure is established through the implementation of the ARFMF technique, as depicted in Fig. 1. The HDGS comprises a wind turbine, photovoltaic (PV), fuel cell (FC), and battery, which together ensure the energy transmission of the DC bus. Dynamic optimal power flow management is used to determine the optimal load and grid parameters, and the electrical energy produced by the system is evaluated. A circuit diagram is provided to illustrate the control modules of the HDGS unit with a VSI-based design [11].

The power flow management and control modules of the HDGS unit are designed based on the load and grid operational modes. In the case of grid-connected mode, the HDGS unit's active and reactive output powers are regulated based on their respective reference values. Thus, the VSI-based control system must adopt the appropriate power control mode to ensure optimal performance.

To meet changing load demands, the power supplied by the main grid and HDGS must be adjusted accordingly. Effective regulation of power flow between the HDGS and the utility is necessary to keep a constant supply of active and reactive power, and a proper connection between the power from the main grid and the PV array is needed to meet the load demand, as shown in [12].

The DC-link and PCC must satisfy the power balance equation, as expressed in the following equation.

$$P_{hres}(t)=P_{windturbine}(t)+P_{photovoltaic}(t)+P_{FuelCell}(t)+P_{battery}(t) \quad (1)$$

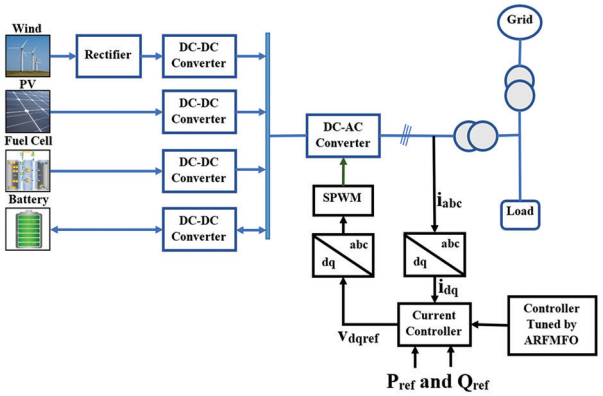

Fig. 1. Management Structure of HDGS with the Proposed Controller

Equation 1 is utilized to determine the power flow balance in the system, which accounts for the total power flow model. It involves calculating the power balance using the output from the HDGS and the demand from the load. PGRID (t) and PLOAD (t) are computed using equations 2 and 3, while QLOAD (t) and QGRID (t) are determined using equations 4 and 5.

$$P_{GRID}(t)=[P_{LOAD}(t)-P_{HRES}(t)] \quad (2)$$

$$P_{LOAD}(t)=[P_{HRES}(t)+P_{GRID}(t)] \quad (3)$$

$$Q_{GRID}(t)=[Q_{LOAD}(t)-Q_{HRES}(t)] \quad (4)$$

$$Q_{LOAD}(t)=[Q_{HRES}(t)+Q_{GRID}(t)] \quad (5)$$

The storage unit's battery power is determined by the discharge time as an energy source and the charging time as a load. However, due to the nonlinear variations in load demand and the uncertainty of renewable energy, it is challenging to maintain a consistent power balance [13]. To address this issue, a high-performance operation mode is necessary for effective power control in the HDGS unit. The measured values of active and reactive power are represented by Equations 6 and 7.

$$P_l(t)=3/2\,[v_d*i_d+v_q*i_q] \quad (6)$$

$$Q_l(t)=3/2\,[v_q*i_d+v_d*i_q] \quad (7)$$

Improvement of the current control scheme is necessary for better power tracking in the HDGS unit, as relying solely on it is insufficient to achieve high-performance operation.

3.1. CURRENT CONTROL STRATEGY

The power controller presented in Section 3.1 introduces two PI controllers to achieve controlled dynamic and reactive power to the load by controlling the power flow between the grid and the utility. Equations (8) and (9) illustrate the reference current for the control objective. The two PI controllers in the power controller communicate with the external control loop to generate the reference current vectors ID and IQ. Even a slight change in the reference current direction can ensure high-quality inverter output control, highlighting the attainment of the control objective.

$$i_d^*(t)=P_{error}(t)*(K_p^P+(K_p^P/S)) \quad (8)$$

$$i_q^*(t)=Q_{error}(t)*(K_p^Q+(K_p^Q/S)) \quad (9)$$

where $P_{error}(t)=[P_{ref}(t)-P_l(t)]$ and $Q_{error}(t)=[Q_{ref}(t)-Q_l(t)]$

The controller's output needs to be evaluated to ensure accurate tracking and minimize inverter drift. This is achieved by using two PI controllers to eliminate current error along with an inverter current feedback and grid voltage feedforward loop to enhance steady-state and dynamic performance. The PWM system is utilized by the controller to produce voltage vectors with reduced harmonic distortion. Equation (10) represents the transformation of Clarke's transformation equation into the stationary frame. In addition to the PWM system, the controller employs a current feedback loop and a grid voltage feedforward loop to enhance steady-state and dynamic performance, eliminate current error, and ensure accurate tracking while minimizing the drift of the inverter.

$$\begin{bmatrix} v_\alpha \\ v_\beta \\ v_0 \end{bmatrix} = \frac{2}{3}\begin{bmatrix} v_a \\ v_b \\ v_c \end{bmatrix}.\begin{bmatrix} 1 & -\frac{1}{2} & -\frac{1}{2} \\ 0 & \frac{\sqrt{3}}{2} & -\frac{\sqrt{3}}{2} \\ \frac{1}{2} & \frac{1}{2} & \frac{1}{2} \end{bmatrix} \quad (10)$$

In grid-connected mode, the HDGS unit regulates the amplitude and phase angle of the inverter current to provide the specified active and reactive power values to the grid. The control strategy for active and reactive power is based on frequency and voltage regulation. In figuring out how well the HDGS unit works, the outputs of the PV irradiance, wind turbine, and battery are considered. [15-17].

3.2. POWER CONTROL STRATEGY

The DC/DC converter of the HDGS unit is controlled by the PI controller to manage the grid power flow, as discussed in [18-20]. Real-time and reactive power optimization is performed using the controller parameters to achieve optimal power flow operations. The proposed technique generates optimal real and reactive power values for a three-phase grid-connected VSI system using the proposed controller.

3.3. PMSG WITH DC-DC CONVERTER

Wind power accessible from a wind turbine having a cross sectional area of A is

$$P_{wind}=1/2\ \rho A V_w^3 \quad (11)$$

The air density is denoted by ρ in kg/m^3 and the wind speed is represented by V_w in m/s.

Power coefficient C_p describes quantity of power obtainable after wind turbine for conversion is given as

$$P_w=C_p P_{wind} \quad (12)$$

Maximum value of C_p is Betz limit 0.593.

P_w is power extracted from rotor of the wind turbine given as

$$P_w=1/2\ \rho A V_w^3 C_p(\beta,\lambda) \quad (13)$$

λ is tip speed ratio given as

$$\lambda=(w_r R)/V_w \quad (14)$$

R is radius of rotor in m, w_r is rotor speed in rad/s, β is the pitch angle.

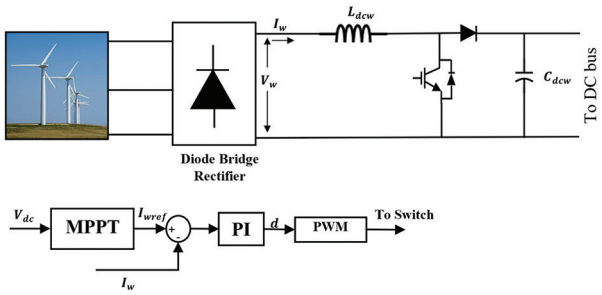

Fig. 2. PMSG based wind generation with DC-DC converter

Fig. 2 depicts a PMSG that is linked to the DC microgrid through a diode bridge rectifier and a DC-to-DC boost converter. The diagram also highlights the control procedure of the IGBT switch in the DC-to-DC converter. The MPPT is used to manage the reference inductor current Iwref generated from the rectifier to achieve maximum power from the wind generation system at a specific DC bus voltage V_{dc}.

PI controller in control system of DC-DC converter will administer duty cycle of switching pulses to be given to IGBT switch to maintain I_{wref} current through inductor. I_{wref} is the current determined by MPPT algorithm for a particular V_{dc}. Maximum power extraction from wind turbine can be possible at $(dP_w)/(dW_r)=0$, and as back emf is directly proportional to rotor speed hence

$$(dP_w)/(dV_{dc})=0 \quad (15)$$

The MPPT algorithm is used to determine the optimal value of the reference inductor current, Iwref, for a particular DC bus voltage, V_{dc}, to extract the maximum power from the PMSG. This involves adjusting the value of Iw based on the variation in the DC link voltage for a specific wind speed.

3.4. PV WITH MPPT BASED DC-DC CONVERTER

A DC-DC boost converter is employed to connect the PV panels to the DC microgrid, which utilizes an INC-based MPPT algorithm to operate at the maximum power point. The use of the MPPT algorithm helps to

extract the maximum amount of solar energy from the PV arrays by regulating the operating point. Fig. 4 illustrates the connection of the PV system to the DC bus through the DC-DC converter.

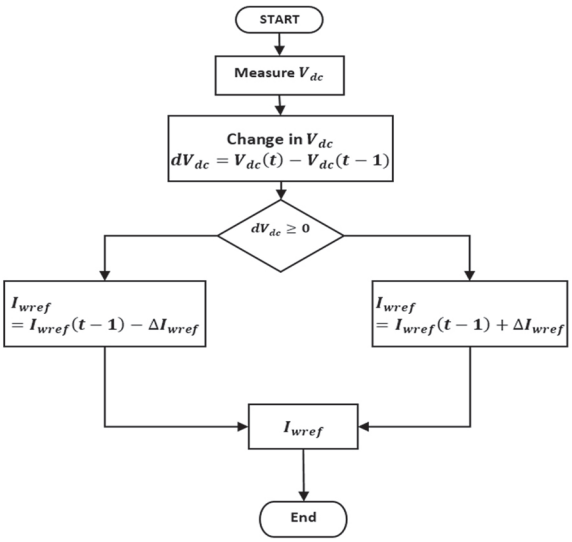

Fig. 3. Flow chart for MPPT algorithm of PMSG DC-DC converter

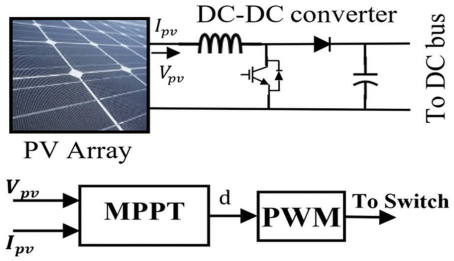

Fig. 4. PV with MPPT operated DC-DC converter

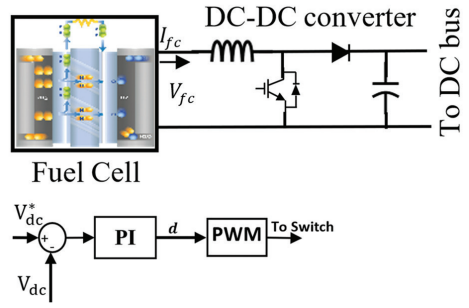

Fig. 5. FC system with DC-DC converter

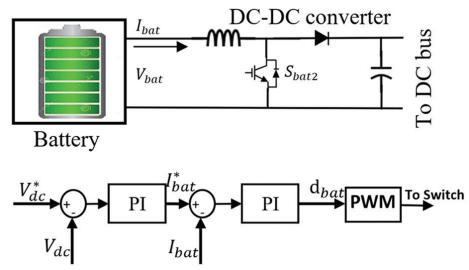

Fig. 6. Battery Storage system with DC-DC converter

Figs. 5 and 6 show the fuel cell system with DC converter and battery storage with DC converter.

4. PROPOSED APPROACH OF ARFMF

4.1. MOTH FLAME OPTIMIZATION ALGORITHM (MFO)

The Moth-Flame Optimization Algorithm is a metaheuristic optimization technique that imitates the navigation behavior of moths in low-light conditions using a mechanism called transverse orientation. This algorithm is inspired by the behavior of over 160,000 moth species found in nature. Moths have a two-stage life cycle consisting of the larval and adult stages.

Step 1: Parameter set

A parameter defines the operation of a system and is a constant value in an equation. Parameters are not limited to mathematical equations, as any system can have parameters that set its boundaries and conditions.

Step 2: Population Initialization

In the Moth-Flame Optimization Algorithm, moths serve as potential solutions for a given problem, with their positions representing the parameters of the problem. These moths can move through spaces of different dimensions, including 1-D, 2-D, 3-D, or even hyper-dimensional spaces, by exchanging their position vectors.

Step 3: Fitness Function

The fitness function determines the quality of a single solution in a population by evaluating its performance. At each iteration's end, to evaluate the effectiveness of the search process in the Moth-Flame Optimization Algorithm, the fitness value of each agent is computed. This fitness value serves as a measure of the quality of the search conducted by the agent.

Step 4: Optimal Selection

The positions of the moths are adjusted in relation to the best solutions they've encountered so far, which they do by flying in hyperspheres around them. The pattern of the flames, used as reference points, changes in each iteration based on the best solutions, causing the moths to update their positions accordingly [21-23].

4.2. RANDOM FOREST ALGORITHM (ARF)

Random subspace selection, a technique used in the design of random forests, helps forests of trees maintain accuracy as they grow without overtraining by restricting the trees to randomly selected feature dimensions [24].

To use the trained random forest algorithm for prediction, we need to apply the rules of each of the 100 random decision trees to the test features [25-29].

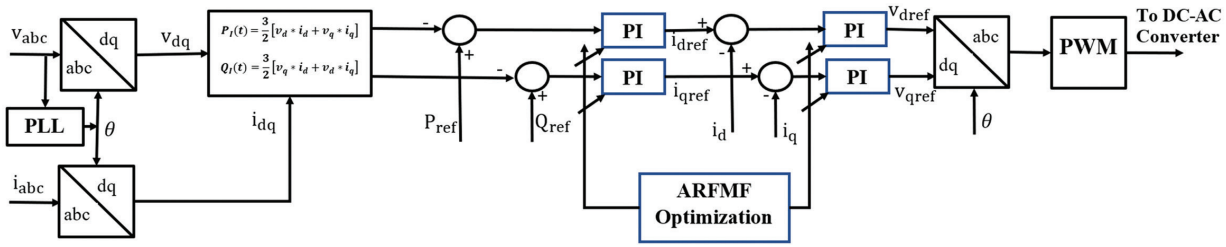

Fig. 7. Controlling Strategy of DC-AC Converter

The random forest algorithm calculates a predicted target by considering the votes of each unique target predicted by the 100 random decision trees. The votes of each target (e.g., x, y, and z) are determined by counting the number of trees that predict that target. For example, if 60 of the 100 decision trees predict target x, then x is returned as the final prediction of the random forest [30-32].

The following are the steps involved in RFA algorithm.

Step 1: Data Preparation

The algorithm begins by preparing the training data, which consists of input features (available power, load demand and control gains) and their corresponding target values (error between actual and reference values). Each sample in the training data contains a set of features and a known target value.

Step 2: Random Sampling

Random Forest uses a technique called bootstrap aggregating, or "bagging," to create multiple subsets of the training data. Each subset is obtained by sampling with replacement from the original data. This process creates different training sets, each potentially containing duplicate samples.

Step 3: Building Decision Trees

For each subset of the data, a decision tree is constructed. Decision trees are built using various algorithms, such as CART (Classification and Regression Trees). During the tree-building process, at each node, the algorithm selects the best feature to split the data based on certain criteria, typically the Gini impurity or information gain.

Step 4: Random Feature Selection

One of the distinguishing characteristics of Random Forest is that it randomly selects a subset of features at each node when building each decision tree. This random feature selection helps to introduce diversity among the trees and prevent overfitting by reducing the correlation between the trees.

Step 5: Tree Construction

The decision trees are constructed recursively by partitioning the data based on the selected features until reaching leaf nodes. Each leaf node represents a class label in the case of classification or a predicted value in the case of regression.

Step 6: Aggregating Predictions

Once the ensemble of decision trees is built, predictions are made by aggregating the individual predictions of each tree. For classification tasks, the class with many votes among the trees is chosen as the final prediction. For regression tasks, the average of the predicted values from all trees is taken.

Step 7: Evaluation and Generalization:

The performance of the Random Forest model is evaluated using evaluation metrics specific to the task at hand, such as accuracy, precision, recall, or mean squared error. The model's ability to generalize to unseen data is assessed using cross-validation or separate test datasets.

5. RESULT AND DISCUSSION

This section presents a discussion on the outcomes achieved by applying the proposed techniques in three distinct test cases, accompanied by a comparison with various existing techniques. The effectiveness of the proposed approach is emphasized by comparing its results to those obtained through the implementation of existing techniques in the MATLAB/Simulink platform. The main goal of the proposed method is to minimize power generation deviation and optimize the flow of active and reactive power in the Hybrid Distributed Generation System (HDGS) unit. The control strategy of the proposed technique is depicted in Fig. 7.

To assess the efficiency of the suggested system, it underwent testing with two specific scenarios: changes in irradiance and changes in load. The outcomes obtained from these tests were then compared to the results obtained using other techniques, namely MFO, LSA, and BAT optimization.

The system comprises various renewable energy sources, including Photovoltaic (PV) panels, wind turbines, Fuel Cells (FC), and batteries. To evaluate the effectiveness of the proposed method, it was subjected to three separate analytical cases, each representing a distinct set of conditions or parameters. These cases were designed to comprehensively assess the system's performance and measure its capabilities in handling different situations related to renewable energy generation and load management.

Table 1. Parameters of the System

PV Array	
Series connected modules	5
Parallel Strings	44
Maximum Power of Module	305 W
Open Circuit Voltage (V_oc)	64.2 V
Short Circuit Current (I_sc)	5.96 A
MPP voltage (V_mpp)	54.7 V
MPP Current (I_mpp)	5.58 A
Wind Turbine and PMSG	
Base Wind Speed	8 m/s
Nominal mechanical output power	50 kW
PMSG Stator Resistance and Inductance	0.425 ohm and 8.5 mH
Torque constant and inertia	3.2475 and 0.01197 kg.m2
Fuel Cell	
Power and Voltage	6 kW and 45 Vdc
Battery	
Nominal Voltage	100 V
Rated Capacity	60 Ah

- **Case 1:** Unbalanced source along with balanced load with PV Irradiance Pattern 1
- **Case 2:** Stable source along with unbalanced load with PV Irradiance pattern 2
- **Case 3:** Supply in balance with an unbalanced load.

An analysis was conducted on a case involving actual and volatile control limits in a microgrid system using existing methods such as MFO, LSA, and BAT, along with the proposed technique. The results obtained from the proposed technique were found to be optimal, and their significance is explained in detail below.

Case 1: Distorted supply with balanced load with PV Irradiance Pattern 1

In Case 1, conducted an analysis of the Hybrid Distributed Generation System (HDGS) under the conditions of unbalanced PV power supply and a balanced load. Throughout the analysis, the load power remained constant, while the PV power and wind speed were subject to variation. To illustrate this, Figs. 8(a) and 8(b) were utilized to showcase the analyses of PV irradiance and wind speed, respectively. In Fig. 8(a), the analysis of PV irradiance is given. The PV power output initiates at 1000 w/m2 and remains constant from 0 to 0.6 seconds, reflecting specific irradiation conditions. However, at 0.75 seconds, there is a sudden drop in PV irradiance, leading to a reduction in PV power output to 500 w/m2. This change in irradiation conditions significantly impacts the performance of the HDGS.

Fig. 8(b) represents the wind speed, which remains constant at 8 m/s throughout the analyzed time. Figs. 9(a) to 9(d) present a comparative analysis of PV, wind, Fuel Cell (FC), and battery power. The performance of the proposed ARFMF method is compared to existing methods such as MFO, LSA, and BAT.

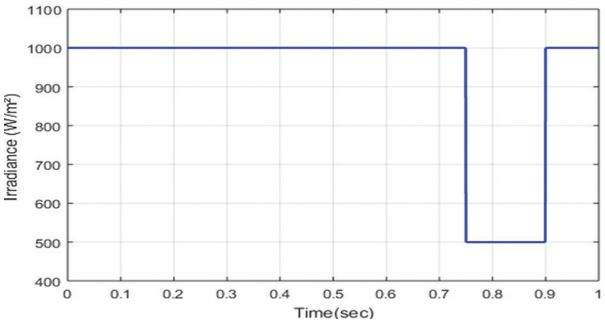

(a)

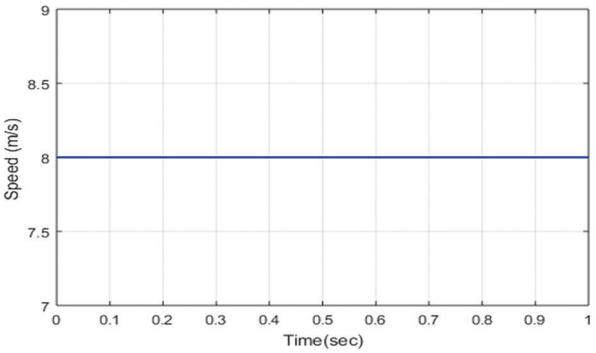

(b)

Fig. 8. Input Data to PV and wind (a) Solar Irradiance profile (b) Wind speed profile

In Fig. 9(a), the analysis focuses on PV power. It shows that the peak PV power of 5000 W is attained between 0.21 and 0.75 seconds. However, there is a reduction in PV power to 1100 W between 0.75 and 0.9 seconds, followed by a rise back up to 5000 W between 0.9 and 1 second. This fluctuation in PV power output demonstrates the dynamic nature of the system and the ability of the proposed ARFMF method to adapt to changing conditions and optimize power generation.

Fig. 9(b) presents the performance of the wind generation system. It achieves a maximum power output of 3300 kW, surpassing the performance of existing techniques such as MFO, LSA, and BAT. This comparison highlights the superior performance of the proposed ARFMF method in harnessing wind energy and maximizing power generation. The performance of the Fuel Cell (FC) power is depicted in Fig. 9(c). The analysis shows a maximum power output of 2503 W between 0.3 and 1 second. The proposed ARFMF method outperforms the existing techniques in terms of FC power generation, further emphasizing its effectiveness in optimizing power production from different sources within the HDGS.

Fig. 9(d) illustrates a comparison between the proposed and existing battery power methods. The ARFMF approach achieves a maximum battery power of 7000 W between 0.7 and 1 second, outperforming the other techniques. This result indicates that the proposed method is capable of effectively managing and utilizing battery storage to optimize power flow within the HDGS.

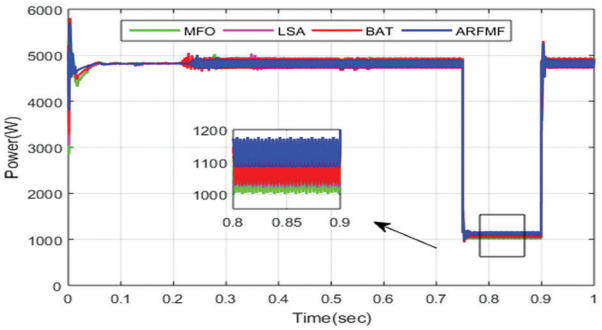

(a)

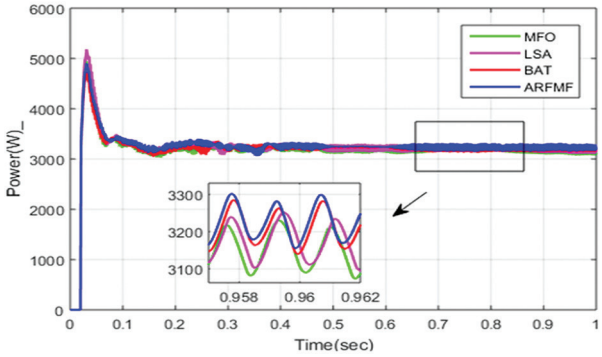

(b)

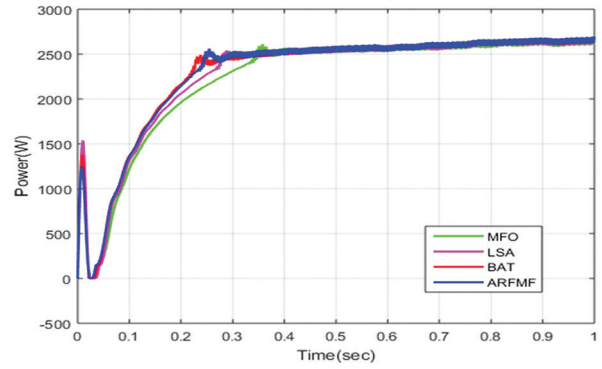

(c)

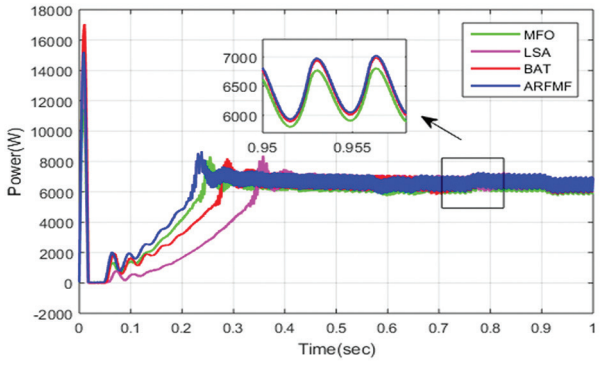

(d)

Fig 9. Power Comparison of (a) PV (b) wind (c) FC (d) Battery

Figs. 10(a) to 10(d) present a comparison of grid power, load power, total power, and fitness between the proposed ARFMF method and existing techniques.

In Fig. 10(a), the analysis compares the grid power achieved by the proposed ARFMF method with that of existing techniques. It is observed that the proposed method achieves the highest grid power of 4450 W between 0.8 and 1 second, surpassing the performance of the existing techniques. Fig. 10(b) focuses on the comparison of load power. The proposed ARFMF method achieves the highest load power of 20 kW between 0.3 and 1 second, outperforming the existing techniques. The total power analysis is depicted in Fig. 10(c). It shows the overall power output, considering all the generation sources in the HDGS. The analysis reveals that the total power starts at 0.5 kW at time 0 and increases to 2.4 kW. It then drops to 0.5 kW again from 2.4 kW, followed by a rise back to 2.4 kW. Between 0.75 and 0.9 seconds, there is a temporary decrease in total power due to a decrease in irradiance. Finally, the total power rises back to 2.4 kW. Fig. 10(d) illustrates the comparison of fitness between the proposed ARFMF method and existing techniques. Fitness represents the measure of how well a solution meets the desired objectives. The analysis reveals that the proposed technique achieves convergence at 17 iterations, outperforming the existing methods. The MFO technique converges at 20 iterations, LSA at 18 iterations, and BAT at 19 iterations.

In summary, Fig. 10(a) to 10(d) provide a comprehensive comparison of grid power, load power, total power, and fitness between the proposed ARFMF method and existing techniques. The findings emphasize the superior performance of the proposed method in terms of power generation, load fulfillment, overall power optimization, and convergence speed. These results validate the effectiveness and efficiency of the proposed ARFMF method in managing and optimizing power generation in the HDGS.

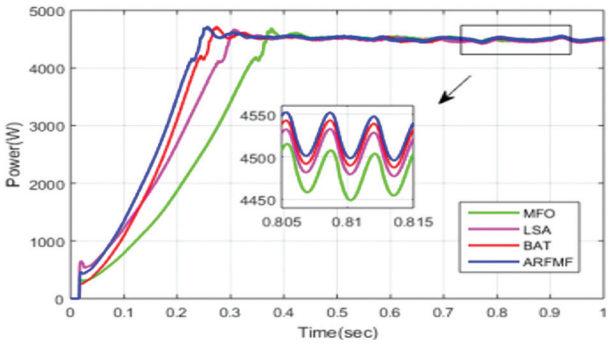

(a)

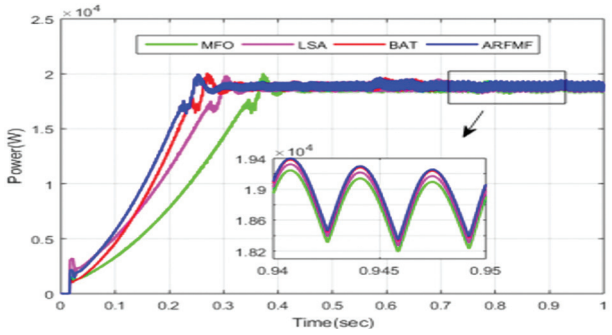

(b)

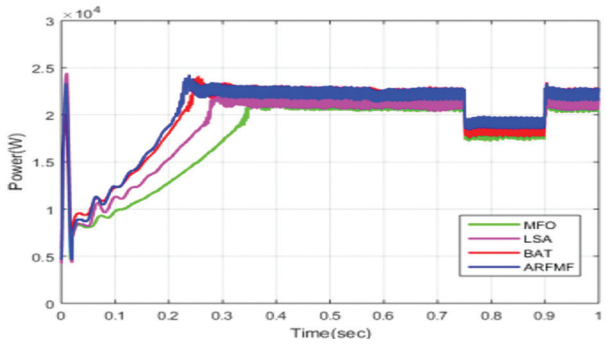

(c)

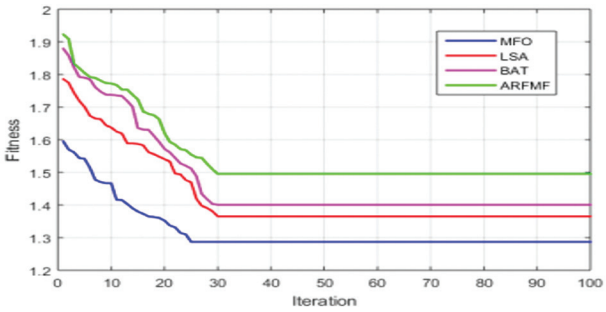

(d)

Fig 10. Evaluation assessment of (a) Grid power (b) Load power (c) Total power (d) Fitness

Case 2: Balanced supply with unbalanced load with PV irradiance pattern 2

In Case 2, the HDGS unit is analysed with an unbalanced PV power supply and a balanced load under the second pattern of PV irradiance. In this scenario, the load power remains constant while the PV power changes, and the wind speed is constant. The analyses of PV irradiance and wind speed are shown in Figs. 11(a) and 11(b), respectively. In Fig. 11(a), the PV irradiation is 1000w/m2 from 0 to 0.7 seconds then suddenly dropped to 0 w/m2 from 0.75 to 1 second. Throughout the analysis, wind speed is constant at 8 m/s as shown in Fig. 11(b).

Figs. 12(a) to 12(d) showcase the power generated from PV, wind, Fuel Cell (FC), and battery, comparing the proposed ARFMF technique with existing methods such as MFO, LSA, and BAT. In Fig. 12(a), the analysis focuses on the power generated from PV. It demonstrates that the peak PV power of 5000 watts occurs between 0.21 and 0.7 seconds. From 0.75 to 1 second, the PV power decreases and remains constant, as indicated in the figure.

Fig. 12(b) illustrates the power generated from the wind source. The proposed ARFMF technique achieves a higher wind power of 3300 watts between 0.878 and 0.882 seconds compared to the existing methods. The performance of FC power is depicted in Fig. 12(c). The proposed ARFMF method delivers a maximum power output of 2503 watts between 0.3 and 1 second, outperforming the existing techniques. Lastly, Fig. 12(d) presents a comparison between the proposed ARFMF technique and existing methods for battery power. The proposed technique achieves a maximum battery power of 1600 watts between 0.3 and 1 second.

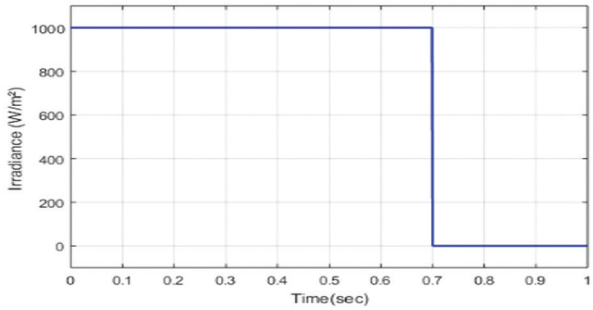

(a)

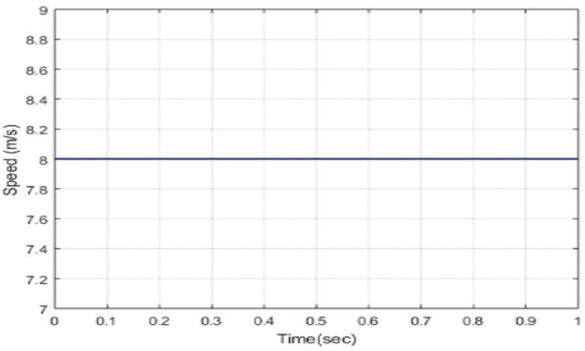

(b)

Fig. 11. Input Data to PV and wind (a) Solar Irradiance profile (b) Wind speed profile

Overall, the analysis in Figs. 12(a) to 12(d) underscores the superior performance of the proposed ARFMF technique in generating power from PV, wind, FC, and battery sources. These findings highlight the efficiency and effectiveness of the proposed technique in optimizing power generation and maximizing the output from different sources, outperforming the existing methods.

Figs. 13(a) to 13(d) provide a comparative analysis of grid power, load power, total power, and fitness between the proposed ARFMF technique and existing methods. In Fig. 13(a), the analysis focuses on grid power and compares the performance of the proposed ARFMF technique with existing methods. It is observed that the highest grid power of 4450W, achieved by the ARFMF technique, is observed between 0.8 and 0.81 seconds. Fig. 13(b) presents the assessment of load power, comparing the proposed ARFMF method with existing techniques. The highest load power of 20 kW, generated by the ARFMF method, occurs between 0.3 and 1 second. The analysis of total power is depicted in Fig. 13(c).

It shows the overall power output, considering all the generation sources in the system. The plot starts at 0.5 kW at time 0 seconds, then increases to 2.4 kW, followed by a decrease to 0.5 kW from 2.4 kW, and then a rise back to 2.4 kW. At 0.7 seconds, there is a decrease

in total power due to a decrease in irradiance. Fig. 13(d) compares the fitness of the proposed ARFMF technique with that of other methods. This result highlights the efficiency and effectiveness of the proposed ARFMF technique in finding optimal solutions and converging towards the desired objectives.

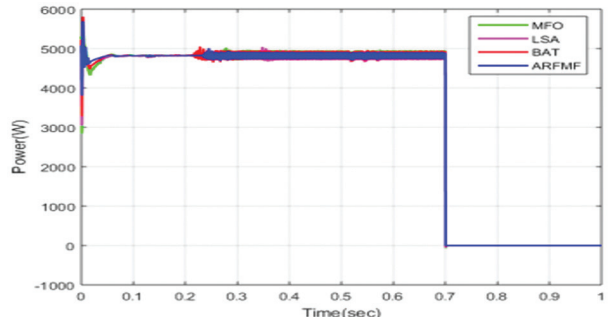

(a)

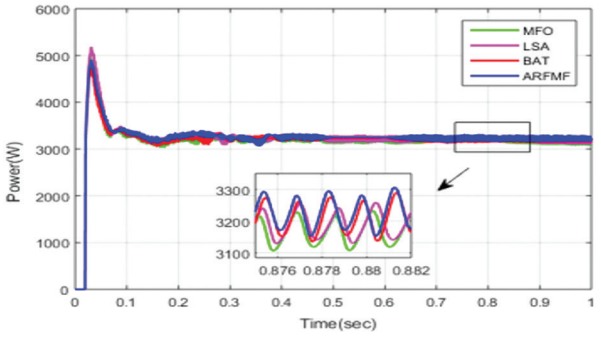

(b)

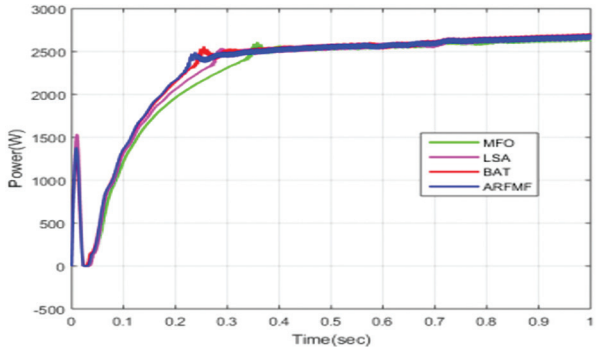

(c)

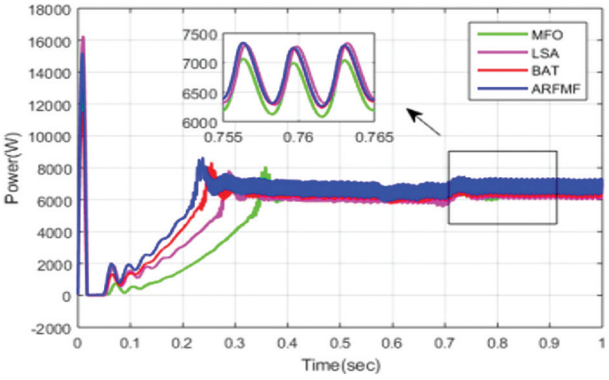

(d)

Fig. 12. Power Evaluation of (a) PV (b) wind (c) FC (d) Battery

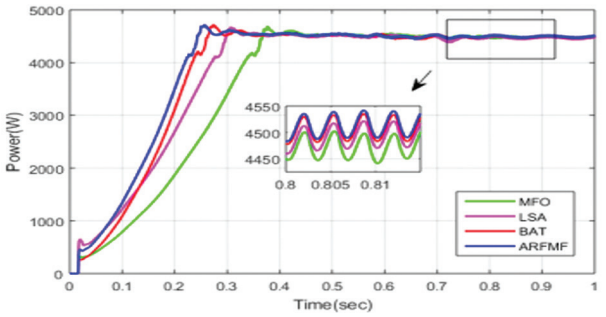

(a)

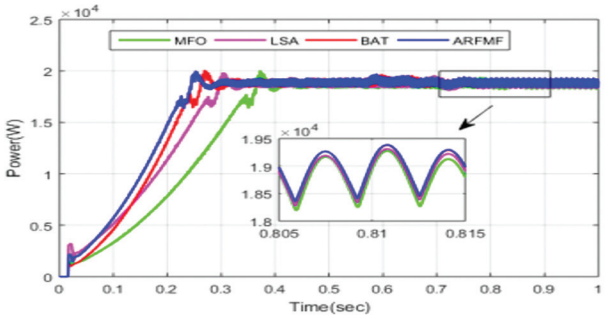

(b)

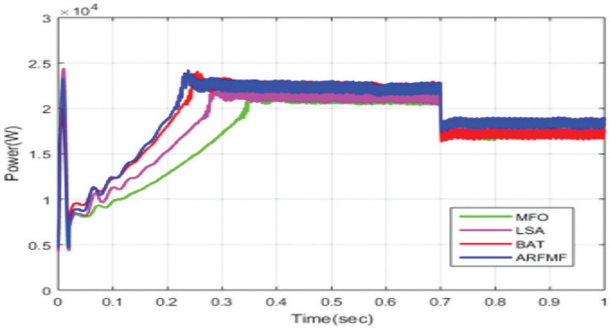

(c)

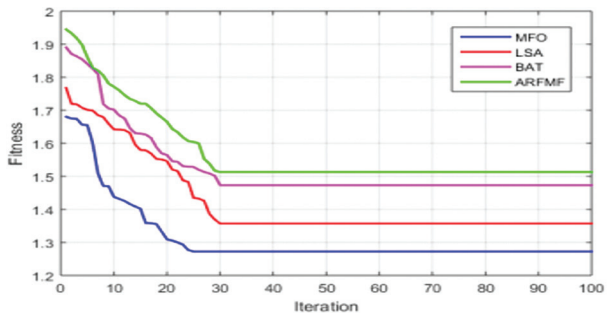

(d)

Fig. 13. Evaluation of (a) Grid power (b) Load power (c) Total power (d) Fitness

Case 3: Balanced supply with unbalanced load

Case 3 examines the HDGS under a balanced PV power supply, and in this scenario, an unbalanced load condition is considered where the load power is kept constant, while the PV power and wind speed are varied. Figs. 14(a) and 14(b) depict the analysis of PV irradiance and wind speed, respectively. As shown in Fig. 14(a), the irradiance remains constant from 0 to 1 second. Mean-

while, Fig. 14(b) shows that the wind speed remains constant at 8 m/s throughout the analysis.

Fig. 15(a) presents a comparison of PV power performance between the proposed ARFMF method and existing methods, including MFO, LSA, and BAT. The proposed method achieves a maximum PV power of 3800 W between 0.5 and 0.9 seconds, surpassing the power outputs of the other techniques. Between 0.25 and 1 second, the highest PV power of 5000 W is achieved.

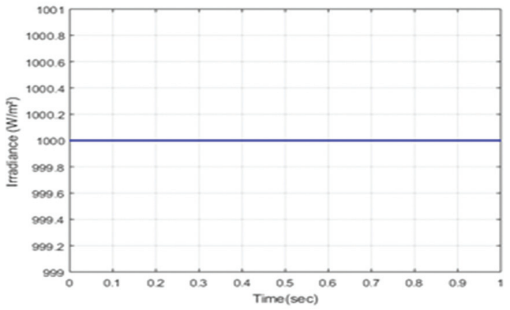

(a)

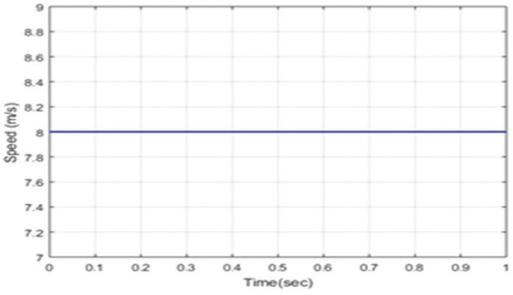

(b)

Fig. 14. Input Data to PV and wind (a) Solar Irradiance profile (b) Wind speed profile

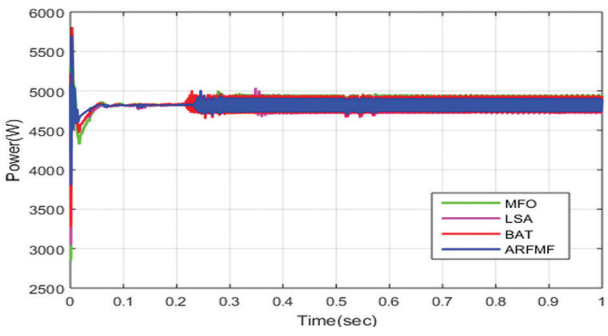

(a)

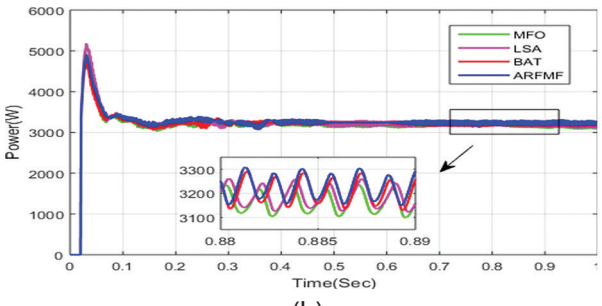

(b)

Fig. 15. Power Comparison of (a) PV (b) wind

Notably, the PV power decreases from 0.75 to 0.9 seconds and then rises again to 5000 W from 0.9 to 1 second. Fig. 16(a) illustrates the performance of FC power. The proposed ARFMF technique outperforms existing methods, achieving the highest FC power of 2503 W between 0.2 and 1 second. Fig. 16(b) compares the battery power between the proposed ARFMF method and other techniques.

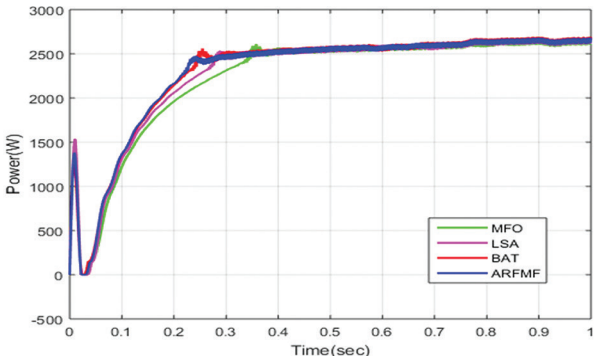

(a)

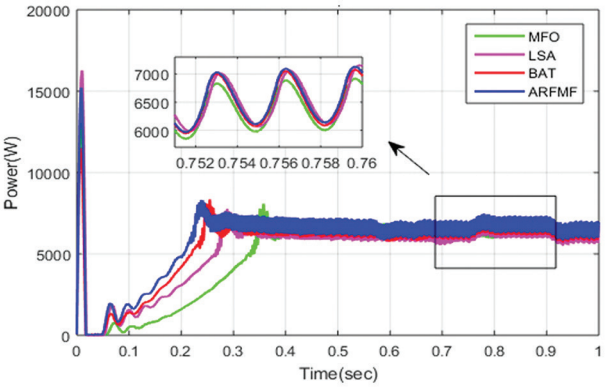

(b)

Fig. 16. Power Comparison of (a) FC (b) Battery

The ARFMF method generates the highest battery power of 7000 W between 0.7 and 1 second. In summary, Fig. 15(a) highlights the higher PV power achieved by the proposed ARFMF method compared to existing techniques, showcasing its effectiveness in adapting to changing conditions and optimizing PV power generation. Fig. 16(a) demonstrates the superior performance of the proposed technique in maximizing FC power output, and Fig. 16(b) highlights its ability to generate the highest battery power. These results validate the superiority of the proposed ARFMF method in optimizing power generation and overall system performance.

In Figs. 17(a)–17(b) and 18(a)-18(b) the comparison of grid power, load power, total power, and fitness is presented. Fig. 17(a) specifically shows the comparison of grid power between the proposed ARFMF technique and existing methods. The highest grid power of 4450W is achieved by the ARFMF method between 0.8 to 1 sec, making it the most powerful technique compared to others.

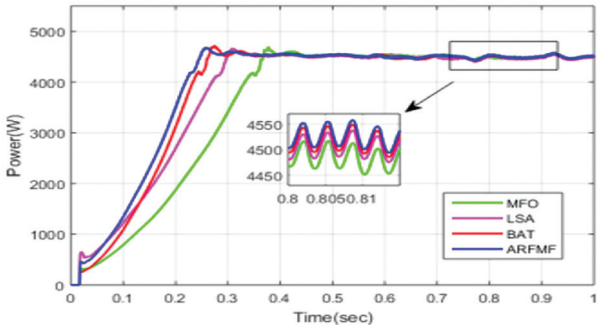

(a)

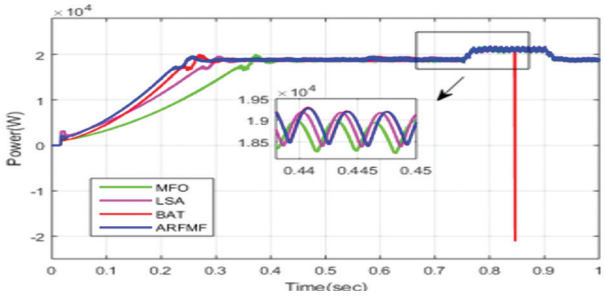

(b)

Fig. 17. Comparison of (a) Grid power (b) Load power

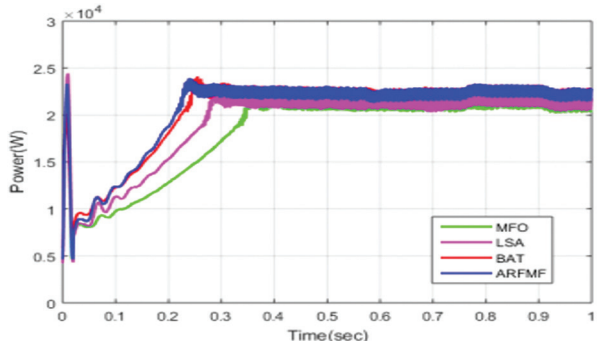

(a)

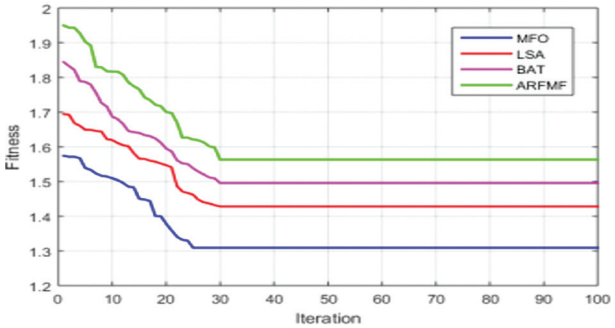

(b)

Fig. 18. Comparison of (a) Total power (b) Fitness

6. CONCLUSION

The paper proposes an energy management system for hybrid distributed generation systems (HDGS) that incorporates an energy storage device. The proposed model is implemented using the MATLAB/Simulink platform, and its performance is compared against existing methods. The energy system comprises various sources of renewable energy, including photovoltaic panels and wind generators, in addition to a diesel generator. The proposed energy management system faces challenges in determining the size of PV, wind, and diesel generators. It employs a combined approach using the Random Forest Algorithm (RFA) and Moth-Flame Optimization Algorithm (MFO). The effectiveness of this technique, called ARFMF, is evaluated under both balanced and unbalanced supply scenarios with changing loads. The proposed control scheme takes into account equal and unequal constraints, including the accessibility of renewable energy sources, power demand, and state of charge (SOC) of storage systems. By stabilizing the energy generated by renewable sources through storage devices such as batteries, the system maintains a constant and stable output power. The implementation of the proposed model on the MATLAB/Simulink platform demonstrates its efficacy compared to previous approaches. By utilizing an AI-based approach for online execution and reducing the optimization process time, the scheme enhances the efficiency and reliability of power flow control in the HDGS. The proposed controller's performance was compared with the MFO, LSA, and BAT techniques. The proposed model's accuracy, efficiency, and ability to handle nonlinear systems make it a valuable contribution to the field of power system control and optimization. The proposed control scheme should be further evaluated for its robustness and resilience against various system uncertainties, such as fluctuating renewable energy generation, varying load demands, and grid disturbances. Robust optimization techniques and advanced control strategies can be explored to enhance the system's ability to withstand and recover from such uncertainties while maintaining stable and reliable power supply.

7. REFERENCES:

[1] Y. Riffonneau, S. Bacha, F. Barruel, S. Ploix, "Optimal Power Flow Management for Grid Connected PV Systems With Batteries", IEEE Transactions on Sustainable Energy, Vol. 2, No. 3, 2011, pp. 309-320.

[2] G. Boukettaya, L. Krichen, "A dynamic power management strategy of a grid connected hybrid generation system using wind, photovoltaic and Flywheel Energy Storage System in residential applications", Energy, Vol. 71, 2014, pp. 148-159.

[3] K. Kusakana, "Optimal scheduled power flow for distributed photovoltaic/wind/diesel generators with battery storage system", IET Renewable Power Generation, Vol. 9, No. 8, 2015, pp. 916-924.

[4] S. Koko, K. Kusakana, H. Vermaak, "Optimal energy management of a grid-connected micro-hydroki-

netic with pumped hydro storage system", Journal of Energy Storage, Vol. 14, pp. 8-15, 2017

[5] N. Mbungu, R. Naidoo, R. Bansal, M. Bipath, "Optimisation of grid connected hybrid photovoltaic–wind–battery system using model predictive control design", IET Renewable Power Generation, Vol. 11, No. 14, 2017, pp. 1760-1768.

[6] T. Praveen Kumar, N. Subrahmanyam, M. Sydulu, "Power Flow Management of the Grid-Connected Hybrid Renewable Energy System: A PLSANN Control Approach", IETE Journal of Research, Vol. 67, No. 4, 2019, pp. 569-584.

[7] T. El-Shatter, M. Eskander, M. El-Hagry, "Energy flow and management of a hybrid wind/PV/fuel cell generation system", Energy Conversion and Management, Vol. 47, No. 9-10, 2006, pp. 1264-1280.

[8] H. Tazvinga, B. Zhu, X. Xia, "Optimal power flow management for distributed energy resources with batteries", Energy Conversion and Management, Vol. 102, 2015, pp. 104-110.

[9] N. Bizon, "Load-following mode control of a standalone renewable/fuel cell hybrid power source", Energy Conversion and Management, Vol. 77, 2014, pp. 763-772.

[10] K. Venkatesan, U. Govindarajan, "Optimal power flow control of hybrid renewable energy system with energy storage: A WOANN strategy", Journal of Renewable and Sustainable Energy, Vol. 11, No. 1, 2019, p. 015501.

[11] M. Kabir, Y. Mishra, G. Ledwich, Z. Dong, K. Wong, "Coordinated Control of Grid-Connected Photovoltaic Reactive Power and Battery Energy Storage Systems to Improve the Voltage Profile of a Residential Distribution Feeder", IEEE Transactions on Industrial Informatics, Vol. 10, No. 2, 2014, pp. 967-977.

[12] C. Bhattacharjee, B. Roy, "Advanced fuzzy power extraction control of wind energy conversion system for power quality improvement in a grid tied hybrid generation system", IET Generation, Transmission & Distribution, Vol. 10, No. 5, 2016, pp. 1179-1189.

[13] G. Mehta, S. Singh, "Power quality improvement through grid integration of renewable energy sources", IETE Journal of Research, Vol. 59, No. 3, 2013, p. 210.

[14] S. Dasgupta, S. Mohan, S. Sahoo, S. Panda, "Lyapunov Function-Based Current Controller to Control Active and Reactive Power Flow From a Renewable Energy Source to a Generalized Three-Phase Microgrid System", IEEE Transactions on Industrial Electronics, Vol. 60, No. 2, 2013, pp. 799-813.

[15] W. Al-Saedi, S. Lachowicz, D. Habibi, O. Bass, "Power flow control in grid-connected microgrid operation using Particle Swarm Optimization under variable load conditions", International Journal of Electrical Power & Energy Systems, Vol. 49, 2013, pp. 76-85.

[16] B. Daryanian, R. Bohn, "Sizing of electric thermal storage under real time pricing", IEEE Transactions on Power Systems, Vol. 8, No. 1, 1993, pp. 35-43.

[17] G. Wang, R. Wai, Y. Liao, "Design of backstepping power control for grid-side converter of voltage source converter-based high-voltage dc wind power generation system", IET Renewable Power Generation, Vol. 7, No. 2, 2013, pp. 118-133.

[18] X. Yuan, F. Wang, D. Boroyevich, Y. Li, R. Burgos, "DC-link Voltage Control of a Full Power Converter for Wind Generator Operating in Weak-Grid Systems", IEEE Transactions on Power Electronics, Vol. 24, No. 9, 2009, pp. 2178-2192.

[19] A. Roy, S. Kedare, S. Bandyopadhyay, "Optimum sizing of wind-battery systems incorporating resource uncertainty", Applied Energy, Vol. 87, No. 8, 2010, pp. 2712-2727.

[20] K. Ishaque, Z. Salam, A. Shamsudin, M. Amjad, "A direct control based maximum power point tracking method for photovoltaic system under partial shading conditions using particle swarm optimization algorithm", Applied Energy, Vol. 99, 2012, pp. 414-422.

[21] A. Garces, "A quadratic approximation for the optimal power flow in power distribution systems", Electric Power Systems Research, Vol. 130, 2016, pp. 222-229.

[22] A. Hermann, Q. Wu, S. Huang, A. Nielsen, "Convex Relaxation of Optimal Power Flow in Distribution Feeders with Embedded Solar Power", Energy Procedia, Vol. 100, 2016, pp. 43-49.

[23] M. Rouholamini, M. Mohammadian, "Heuristic-based power management of a grid-connected hy-

brid energy system combined with hydrogen storage", Renewable Energy, Vol. 96, 2016, pp. 354-365.

[24] A. Aktas, K. Erhan, S. Ozdemir, E. Ozdemir, "Experimental investigation of a new smart energy management algorithm for a hybrid energy storage system in smart grid applications", Electric Power Systems Research, Vol. 144, 2017, pp. 185-196.

[25] Y. Ueda, K. Kurokawa, T. Tanabe, K. Kitamura, H. Sugihara, "Analysis Results of Output Power Loss Due to the Grid Voltage Rise in Grid-Connected Photovoltaic Power Generation Systems", IEEE Transactions on Industrial Electronics, Vol. 55, No. 7, 2008, pp. 2744-2751.

[26] S. Ko, S. Lee, H. Dehbonei, C. Nayar, "Application of Voltage- and Current-Controlled Voltage Source Inverters for Distributed Generation Systems", IEEE Transactions on Energy Conversion, Vol. 21, No. 3, 2006, pp. 782-792.

[27] R. Kadri, J. Gaubert, G. Champenois, "An Improved Maximum Power Point Tracking for Photovoltaic Grid-Connected Inverter Based on Voltage-Oriented Control", IEEE Transactions on Industrial Electronics, Vol. 58, No. 1, 2011, pp. 66-75.

[28] Y. Luo, Y. Shi, Y. Zheng, N. Cai, "Reversible solid oxide fuel cell for natural gas/renewable hybrid power generation systems", Journal of Power Sources, Vol. 340, 2017, pp. 60-70.

[29] J. Allison, "Robust multi-objective control of hybrid renewable microgeneration systems with energy storage", Applied Thermal Engineering, Vol. 114, 2017, pp. 1498-1506.

[30] G. Kasal, B. Singh, "VSC with zigzag transformer based electronic load controller for a stand-alone power generation", International Journal of Power and Energy Conversion, Vol. 1, No. 1, 2009, p. 1.

[31] L. Ju, Z. Tan, J. Yuan, Q. Tan, H. Li, F. Dong, "A bi-level stochastic scheduling optimization model for a virtual power plant connected to a wind–photovoltaic–energy storage system considering the uncertainty and demand response", Applied Energy, Vol. 171, 2016, pp. 184-199.

[32] V. Das, S. Padmanaban, K. Venkitusamy, R. Selvamuthukumaran, F. Blaabjerg, P. Siano, "Recent advances and challenges of fuel cell based power system architectures and control – A review", Renewable and Sustainable Energy Reviews, Vol. 73, 2017, pp. 10-18.

INTERNATIONAL JOURNAL OF ELECTRICAL AND COMPUTER ENGINEERING SYSTEMS

Published by Faculty of Electrical Engineering, Computer Science and Information Technology Osijek,
Josip Juraj Strossmayer University of Osijek, Croatia.

About this Journal

The International Journal of Electrical and Computer Engineering Systems publishes original research in the form of full papers, case studies, reviews and surveys. It covers theory and application of electrical and computer engineering, synergy of computer systems and computational methods with electrical and electronic systems, as well as interdisciplinary research.

Topics of interest include, but are not limited to:

- Power systems
- Renewable electricity production
- Power electronics
- Electrical drives
- Industrial electronics
- Communication systems
- Advanced modulation techniques
- RFID devices and systems
- Signal and data processing
- Image processing
- Multimedia systems
- Microelectronics
- Instrumentation and measurement
- Control systems
- Robotics
- Modeling and simulation
- Modern computer architectures
- Computer networks
- Embedded systems
- High-performance computing
- Parallel and distributed computer systems
- Human-computer systems
- Intelligent systems
- Multi-agent and holonic systems
- Real-time systems
- Software engineering
- Internet and web applications and systems
- Applications of computer systems in engineering and related disciplines
- Mathematical models of engineering systems
- Engineering management
- Engineering education

Paper Submission

Authors are invited to submit original, unpublished research papers that are not being considered by another journal or any other publisher. Manuscripts must be submitted in doc, docx, rtf or pdf format, and limited to 30 one-column double-spaced pages. All figures and tables must be cited and placed in the body of the paper. Provide contact information of all authors and designate the corresponding author who should submit the manuscript to https://ijeces.ferit.hr. The corresponding author is responsible for ensuring that the article's publication has been approved by all coauthors and by the institutions of the authors if required. All enquiries concerning the publication of accepted papers should be sent to ijeces@ferit.hr.

The following information should be included in the submission:

- paper title;
- full name of each author;
- full institutional mailing addresses;
- e-mail addresses of each author;
- abstract (should be self-contained and not exceed 150 words). Introduction should have no subheadings;
- manuscript should contain one to five alphabetically ordered keywords;
- all abbreviations used in the manuscript should be explained by first appearance;
- all acknowledgments should be included at the end of the paper:
- authors are responsible for ensuring that the information in each reference is complete and accurate. All references must be numbered consecutively and citations of references in text should be identified using numbers in square brackets. All references should be cited within the text;
- each figure should be integrated in the text and cited in a consecutive order. Upon acceptance of the paper, each figure should be of high quality in one of the following formats: EPS, WMF, BMP and TIFF;
- corrected proofs must be returned to the publisher within 7 days of receipt.

Peer Review

All manuscripts are subject to peer review and must meet academic standards. Submissions will be first considered by an editor-in-chief and if not rejected right away, then they will be reviewed by anonymous reviewers. The submitting author will be asked to provide the names of 5 proposed reviewers including their e-mail addresses. The proposed reviewers should be in the research field of the manuscript. They should not be affiliated to the same institution of the manuscript author(s) and should not have had any collaboration with any of the authors during the last 3 years.

Author Benefits

The corresponding author will be provided with a .pdf file of the article or alternatively one hardcopy of the journal free of charge.

Units of Measurement

Units of measurement should be presented simply and concisely using System International (SI) units.

Bibliographic Information

Commenced in 2010.
ISSN: 1847-6996
e-ISSN: 1847-7003

Published: semiannually

Copyright

Subscription Information

The annual subscription rate is 50€ for individuals, 25€ for students and 150€ for libraries.

Postal Address

Faculty of Electrical Engineering,
Computer Science and Information Technology Osijek,
Josip Juraj Strossmayer University of Osijek, Croatia
Kneza Trpimira 2b
31000 Osijek, Croatia

IJECES Copyright Transfer Form

(Please, read this carefully)

This form is intended for all accepted material submitted to the IJECES journal and must accompany any such material before publication.

TITLE OF ARTICLE (hereinafter referred to as "the Work"):

COMPLETE LIST OF AUTHORS:

The undersigned hereby assigns to the IJECES all rights under copyright that may exist in and to the above Work, and any revised or expanded works submitted to the IJECES by the undersigned based on the Work. The undersigned hereby warrants that the Work is original and that he/she is the author of the complete Work and all incorporated parts of the Work. Otherwise he/she warrants that necessary permissions have been obtained for those parts of works originating from other authors or publishers.

Authors retain all proprietary rights in any process or procedure described in the Work. Authors may reproduce or authorize others to reproduce the Work or derivative works for the author's personal use or for company use, provided that the source and the IJECES copyright notice are indicated, the copies are not used in any way that implies IJECES endorsement of a product or service of any author, and the copies themselves are not offered for sale. In the case of a Work performed under a special government contract or grant, the IJECES recognizes that the government has royalty-free permission to reproduce all or portions of the Work, and to authorize others to do so, for official government purposes only, if the contract/grant so requires. For all uses not covered previously, authors must ask for permission from the IJECES to reproduce or authorize the reproduction of the Work or material extracted from the Work. Although authors are permitted to re-use all or portions of the Work in other works, this excludes granting third-party requests for reprinting, republishing, or other types of re-use. The IJECES must handle all such third-party requests. The IJECES distributes its publication by various means and media. It also abstracts and may translate its publications, and articles contained therein, for inclusion in various collections, databases and other publications. The IJECES publisher requires that the consent of the first-named author be sought as a condition to granting reprint or republication rights to others or for permitting use of a Work for promotion or marketing purposes. If you are employed and prepared the Work on a subject within the scope of your employment, the copyright in the Work belongs to your employer as a work-for-hire. In that case, the IJECES publisher assumes that when you sign this Form, you are authorized to do so by your employer and that your employer has consented to the transfer of copyright, to the representation and warranty of publication rights, and to all other terms and conditions of this Form. If such authorization and consent has not been given to you, an authorized representative of your employer should sign this Form as the Author.

Authors of IJECES journal articles and other material must ensure that their Work meets originality, authorship, author responsibilities and author misconduct requirements. It is the responsibility of the authors, not the IJECES publisher, to determine whether disclosure of their material requires the prior consent of other parties and, if so, to obtain it.

- The undersigned represents that he/she has the authority to make and execute this assignment.
- For jointly authored Works, all joint authors should sign, or one of the authors should sign as authorized agent for the others.
- The undersigned agrees to indemnify and hold harmless the IJECES publisher from any damage or expense that may arise in the event of a breach of any of the warranties set forth above.

_____ _____

Author/Authorized Agent **Date**

CONTACT
International Journal of Electrical and Computer Engineering Systems (IJECES)
Faculty of Electrical Engineering, Computer Science and Information Technology Osijek
Josip Juraj Strossmayer University of Osijek
Kneza Trpimira 2b
31000 Osijek, Croatia
Phone: +38531224600,
Fax: +38531224605,
e-mail: ijeces@ferit.hr